A NOVEL APPROACH FOR PROPERTY MODIFICATION OF CAST ALUMINUM ALLOYS WITH NANOSTRUCTURED CHEMICAL ADDITIONS

By

Yang Lu

A DISSERTATION

Submitted to
Michigan State University
in partial fulfillment of the requirements
for the degree of

Materials Science and Engineering - Doctor of Philosophy

2019

ABSTRACT

A NOVEL APPROACH FOR PROPERTY MODIFICATION OF CAST ALUMINUM ALLOYS WITH NANOSTRUCTURED CHEMICAL ADDITIONS

By

Yang Lu

Continued weight reduction which involves replacing steel components with lightweight materials is one of the major strategies to achieve the average fuel economy standards in the automotive industry. Based on the significant success of aluminum alloys in non-structural components, aluminum alloys in structural applications attract particular interest. To this end, the ultimate objective is to achieve aluminum alloys with high ductility and strength. However, conventional aluminum-silicon (Al-Si) based casting alloys possess low ductility as compensation for the required high strength, since the presence of irregular eutectic silicon crystals in the as-cast condition promotes crack initiation and propagation. Strontium (Sr) is widely used to modify the Si eutectic in commercially available "high ductility" cast aluminum alloys. However, fading issues arise due to Sr oxidation at the casting temperature, and become major concerns for aluminum foundries. Therefore, it is important to develop a universal modifier that can be used in alloys with a larger range of Si content.

In this thesis, trisilanol polyhedral silsesquioxane (TSP) was first incorporated in Sn-based binary and ternary alloys, leading to microstructure refinement and high creep resistance. Based on these preliminary results, TSP was further applied to Al based alloys. First, TSP was coated on Al-12Si powders using dip-coating approach. After melting, the microstructure of both primary Al and eutectic microconstituents of Al-12Si ingots was refined. Ductility increased from 5% with no TSP treatment to 18% when treated with TSP. More interestingly, the modified structure was maintained with 150 ppm of TSP addition. The incorporation of TSP reduced the

undercooling and arrest temperatures of Al-Si eutectic during solidification. These results suggest TSP bonds with Al to slow down the Al segregation from Al-Si melt during eutectic reaction, leading to the microstructural refinement of Al-Si eutectic microconstituents.

Based on the laboratory-scale results, a new TSP master was produced to facilitate the incorporation of TSP into traditional foundry process. The optimized master composition contained 6%TSP in an Al-12Si alloy, and 10% Al-12Si-6TSP master was applied to modify Al-Si binary and commercial alloys at a 100 lbs. scale.

In Al-Si binary alloys, TSP addition results 50% improvement in ductility over the Al-7.5Si base alloy without sacrificing the strength. The microstructure of both primary Al and eutectic microconstituents of the Al-7.5Si alloy with TSP addition was refined. Minimal fade was observed up to a 192-hour hold at 720°C, which sheds light on the Sr fading issue. In Aural^{TM} 2 and W319 -type commercial alloys, TSP additions reduced the solidification shrinkage of castings. Metallography showed refined Si in the Al-Si eutectic microconstituent and reduced Al secondary dendrite arm spacing (SDAS), resulting in an 100% improvement in ductility without sacrificing strength. Besides microstructural refinement, the mass fraction of θ (Al_2Cu) increased while Q ($Al_4Cu_2Mg_8Si_7$) decreased with TSP addition, suggesting TSP changes the Cu intermetallic compounds (IMCs) to favor the formation of θ, which demonstrated its potential as a strengthening precipitate.

This study addresses fundamental questions on how the addition of TSP influences microstructure and solidification behavior of Al-Si based casting alloys, thus providing solutions to reinforce aluminum alloys in body structures for the environmental and fuel economy benefits.

This thesis is dedicated to the memory of my father, Xuhui Lu, who would have been happy to see me finish my Ph.D. degree. It is also dedicated to my mother, Xiuyun Mi, my wife, Chun Liu, and my daughter, Danica Lu, for their love and support.

ACKNOWLEDGEMENTS

The first person I would like to thank is my advisor, Prof. Andre Lee. I would like to express my sincere gratitude for his inspiring guidance and constant encouragement during my PhD studies. His knowledge, creativeness, and passion for research have not only earned him a reputation but also positioned him as a role model for his students, including me.

I would also like to thank my committee members—Prof. Martin Crimp, Prof. Yue Qi, and Prof. Patrick Kwon—for their intelligent questions and feedback for my research.

I have been extremely lucky to have Larry Godlewski, Jacob Zindel, and Mei Li who cared so much about my research, provided patient guidance, and responded to my questions so promptly during my Co-Op study at Ford Motor Company.

Special thanks to Drs. Tsung-Yu Pan and Allen Roche of Vinci Technology Corporation with whom I have had the pleasure of working on the NSF-SBIR project. I must, however, give special thanks to Dr. Pan, who truly went above and beyond in providing me with advice and support on matters both academic and otherwise.

Thanks to F. H. LePrevost and Aaron Morrow of Johnson Manufacturing Company for providing materials and advice for aluminum and solder experimentation.

Much appreciation must also go out to the ChEMS faculty that I took classes from, the ChEMS staff who facilitated my research and study needs, including Donna Fernandez, Jennifer Keddle, and Tiffany Owen, and my current lab mates for their support and friendship, including Yuxiang Zhong, Yuelin Wu, and David Vogelsang.

TABLE OF CONTENTS

LIST OF TABLES ..... **ix**

LIST OF FIGURES ..... **xi**

KEY TO ABBREVIATIONS ..... **xvii**

KEY TO SYMBOLS ..... **xviii**

Chapter 1 Introduction **1**
1.1 Solidification of Aluminum Silicon Alloys 1
1.1.1 Solidification of Primary Aluminum Phase *3*
1.1.2 Al-Si Eutectic Solidification *4*
1.2 Effects of grain refinement and chemical modification 6
1.2.1 Strengthening in Al-Si Alloys *6*
1.2.2 Ductility Improvement in Al-Si Alloys *13*
1.3 Development of Cast Aluminum Alloys Using Nano-structured Chemicals 19
1.3.1 Overall Goal *19*
1.3.2 Motivation *19*
1.3.3 Fundamental Idea and Specific Aims *26*

Chapter 2 Sn-Cu Binary Alloys Refinement **28**
2.1 Background 28
2.2 Experimental 29
2.2.1 Preparation of Sn/Cu Solder Wires *29*
2.2.2 Coil Creep Testing *30*
2.2.3 Polarized Optical Microscopy *30*
2.2.4 Differential Scanning Calorimetry *31*
2.2.5 Indentation Microhardness *31*
2.2.6 Orientation Imaging Microscopy *31*
2.3 Results and Discussions 32
2.3.1 Creep Behavior *32*
2.3.2 Microstructure *34*
2.3.3 Solidification of Eutectic Constituent *35*
2.3.4 Indentation Microhardness *37*
2.3.5 EBSD Results on Tin-rich Grains *38*
2.3.6 Texture of Tin-rich Grains *40*
2.4 Conclusions 41

Chapter 3 Sn-based Ternary Alloys **43**
3.1 Background 43
3.2 Experimental 44
3.2.1 Preparation of Solid Wires *44*
3.2.2 Coil Creep Testing *44*
3.2.3 Polarized Optical Microscopy *45*

3.3 Results and Discussions 45
3.3.1 Pure Tin *45*
3.3.2 Sn-Ag-Cu Alloys *47*
3.3.3 Sn-Cu-Sb Alloys *50*
3.3.4 Sn-Cu-Zn Alloys *53*
3.4 Conclusions 56

Chapter 4 Al-12Si Alloys with TSP Treatment 57
4.1 Background 57
4.2 Experimental 58
4.2.1 Materials *58*
4.2.2 Surface Treatment of A4047 powders *58*
4.2.3 Preparation of A4047 Ingots *58*
4.2.4 Microscopy *60*
4.2.5 Tensile Test *60*
4.2.6 Indentation Microhardness *60*
4.2.7 Thermal Analysis *60*
4.3 Results and Discussion 61
4.3.1 Mechanical Properties *61*
4.3.2 As-cast Microstructure *63*
4.3.3 Fracture Surface *67*
4.3.4 Solidification *70*
4.3.5 Influence of Treatment Time *74*
4.3.6 Sequential Dilution *77*
4.3.7 Proposed Modification Mechanism *83*
4.4 Conclusions 85

Chapter 5 Development of Al-Si-TSP Master Alloys 86
5.1 Background 86
5.2 Experimental 87
5.2.1 Materials and Melt Preparation *87*
5.2.2 TSP Incorporation Process *87*
5.2.3 Casting *87*
5.2.4 Characteristics *88*
5.3 Results and Discussion 88
5.3.1 Melt Characterization *88*
5.3.2 Form of Master *89*
5.3.3 TSP Concentration in Master *95*
5.3.4 Amount of Master *100*
5.5 Conclusions 103

Chapter 6 Aluminum Silicon Binary Alloys Modification 104
6.1 Background 104
6.2 Experimental 105
6.2.1 Materials *105*
6.2.2 TSP Master Alloy Preparation *105*
6.2.3 Casting *105*

6.2.4 Characteristics *107*
6.3 Results and Discussion 108
6.3.1 Melt Characterization *108*
6.3.2 Solidification and Melting *109*
6.3.3 As-cast Microstructures *113*
6.3.4 Tensile Properties *115*
6.3.5 Additive Stability *117*
6.4 Conclusions 125

Chapter 7 Commercial Cast Aluminum Silicon Based Alloys Modification 126
7.1 Background 126
7.2 Experimental 127
7.2.1 Materials *127*
7.2.2 TSP Master Alloy Preparation *127*
7.2.3 Casting *127*
7.2.4 Characteristics *128*
7.3 Results and Discussion 130
7.3.1 Melting Characterization *130*
7.3.2 Casting Properties *132*
7.3.3 Solidification and Melting *135*
7.3.4 As-cast Microstructures *144*
7.3.5 Tensile Properties *148*
7.3.6 High Cycle Fatigue *151*
7.4 Conclusions 153

Chapter 8 Summary and Future Work 154
8.1 Summary 154
8.2 Future Work 155
8.2.1 Understanding modification mechanism with TSP addition. *155*
8.2.2 Effect of TSP on the porosity distribution and fatigue in cast aluminum alloys *155*
8.2.3 Application of TSP in foundries *156*

APPENDIX 157

BIBLIOGRAPHY 172

LIST OF TABLES

Table 2-1 Comparison of Solidification Temperature, Melting Temperature, and Undercooling for Sn-Cu Wires. 35

Table 3-1 Chemical Composition in wt% of All Wires. 44

Table 3-2 Stress Exponent and Activation Energy of Pure Sn and TSP-treated Sn Wires. 46

Table 3-3 Stress Exponent and Activation Energy of Sn-4.7Ag-1.7Cu and TSP-treated Sn-4.7Ag-1.7Cu Wires. 49

Table 3-4 Stress Exponent and Activation Energy of Sn-3.5Cu-7.5Sb and TSP-treated Sn-3.5Cu-7.5Sb Wires. 52

Table 3-5 Stress Exponent and Activation Energy of Sn-15Cu-3Zn and TSP-treated Sn-15Cu-3Zn Wires. 55

Table 4-1 Overall Composition of TSP in the A4047 Ingots. 59

Table 4-2 Eutectic Reaction Temperatures for A4047 with and without TSP Extracted from Cooling Curves. 73

Table 4-3 Microhardness of the TSP-treated A4047 Alloys. 76

Table 4-4 Microhardness of the Diluted A4047 Alloys. 78

Table 4-5 Eutectic Reaction Temperatures Extracted from Cooling Curves. 82

Table 5-1 Chemical Composition in wt% of the Al-7.5Si Base Alloy. 88

Table 5-2 Naming Conventions of All Cast Specimens for Master Form Study. 89

Table 5-3 SDAS of the Al-12Si Alloys with and without TSP. 92

Table 5-4 Naming Conventions of All Cast Specimens for TSP Concentration Study. 95

Table 5-5 Naming Conventions of All cast Specimens for Master Content Study. 100

Table 6-1 Naming Conventions of All Cast Specimens. 106

Table 6-2 Chemical Composition in wt% of the Al-7.5Si Alloy with and without TSP. 108

Table 6-3 Selected Characteristic Temperatures Taken from Cooling Curves. 111

Table 6-4 Selected Characteristic Temperatures Taken from DSC Heating Curves. 112

Table 7-1 Chemical Composition in wt% of the Aural™ 2 Alloys. 131

Table 7-2 Chemical Composition in wt% of the W319 Alloys. 131

Table 7-3 Selected Characteristic Temperatures Taken from Cooling Curves. 140

Table 7-4 High Cycle Fatigue Stress of Heat-treated Aural™ 2 Alloys at Room Temperature. 152

LIST OF FIGURES

Figure 1-1 Aluminum Silicon Binary Phase Diagram [10]. 2

Figure 1-2 Type of Al-Si Eutectic Structures as a Function of Growth Rate (V) and Temperature Gradient (G): 5

Figure 1-3 The Aluminum Rich-side of the Al-Ti Phase Diagram [29]. 8

Figure 1-4 Al_3Ti Nucleates on Aluminum Grain [30]. 9

Figure 1-5 The Aluminum Rich-side of the Al-B Phase Diagram [31]. 12

Figure 1-6 Chemical Structure of (a) Polyhedral Oligomeric Silsesquioxane (POSS) and (b) Trisilanol POSS. 21

Figure 2-1 Creep Experimental Setup: (a) Stereo Micrographs of Wire Winding and (b) Schematic of Coil Creep Setup. 30

Figure 2-2 Stretch Rates at Various Temperatures: (a) Sn-0.7Cu Wire without and with TSP Additions and (b) Sn-3Cu Wire without and with TSP Additions. 33

Figure 2-3 Polarized Optical Micrographs of Sn-Cu Solder Wires: (a) Sn-0.7Cu Wire, (b) TSP-treated Sn-0.7Cu Wire, (c) Sn-3Cu Wire, and (d) TSP-treated Sn-3Cu Wire. 36

Figure 2-4 Knoop Hardness Values of Sn-Cu Wires. 37

Figure 2-5 C-axis orientation maps of Sn-Cu solder wires: (a) Sn-0.7Cu wire, (b) TSP-treated Sn-3Cu wire, (c) Sn-3Cu wire, and (d) TSP-treated Sn-3Cu wire 39

Figure 2-6 (001) and (100) discrete and density pole Fig.s of Sn-Cu solder wires: (a) Sn-0.7Cu wire, (b) TSP-treated Sn-3Cu wire, (c) Sn-3Cu wire, and (d) TSP-treated Sn-3Cu wire 41

Figure 3-1 Stretch Rates of Pure Sn and TSP-treated Sn Wires at Various Temperatures. 46

Figure 3-2 Optical Micrographs of Pure Tin Solder Wires: (a) Pure Sn Wire and (b) TSP-treated Sn Wire. 47

Figure 3-3 Stretch Rates of Sn-4.7Ag-1.7Cu and TSP-treated Sn-4.7Ag-1.7Cu Wires at Various Temperatures 48

Figure 3-4 Optical Micrographs of Sn-4.7Ag-1.7Cu Solder Wires: (a) Sn-4.7Ag-1.7Cu Wire and (b) TSP-treated Sn-4.7Ag-1.7Cu Wire. 50

Figure 3-5 Stretch Rates of Sn-3.5Cu-7.5Sb and TSP-treated Sn-3.5Cu-7.5Sb Wires at Various Temperatures 51

Figure 3-6 Optical Micrographs of Sn-3.5Cu-7.5Sb Solder Wires: (a) Sn-3.5Cu-7.5Sb Wire and (b) TSP-treated Sn-3.5Cu-7.5Sb Wire. 53

Figure 3-7 Stretch Rates of Sn-15Cu-3Zn and TSP-treated Sn-15Cu-3Zn Wires at Various Temperatures..... 54

Figure 3-8 Optical Micrographs of Sn-15Cu-3Zn Solder Wires: (a) Sn-15Cu-3Zn Wire and (b) TSP-treated Sn-15Cu-3Zn Wire. 56

Figure 4-1 Ultimate Tensile Strength (a) and Elongation to Failure (b) of Ingots Made of A4047 Powders without and with TSP Treatment. 62

Figure 4-2 Optical Micrographs of Al-Si Alloys Showing the Effect of TSP on the Primary Al and Eutectic Si Morphology of the as-Cast Ingot: (a) The A4047 Control with an Objective Lens of 5x, (b) The TSP-treated A4047 with an Objective Lens of 5x, (c) The A4047 Control with an Objective Lens of 20x, (d) The TSP-treated A4047 with an Objective Lens of 20x, (e) The A4047 Control with an Objective Lens of 100x, and (f) The TSP-treated A4047 with an Objective Lens of 100x. 64

Figure 4-3 Effect of TSP Treatment on the Secondary Dendrite Arm Spacing (SDAS) of the A4047 Ingots. 65

Figure 4-4 ImageJ Analysis of (a) the A4047 Ingot and (b) the TSP-treated A4047 Ingot. 66

Figure 4-5 A Fractured A4047 Tensile Bar: (a) Photograph of Fractured Sample, (b) Stereo Photograph of Fracture Surface, and (c) Back-scattered Electron Micrograph of Fracture Surface. 68

Figure 4-6 A Fractured TSP-treated A4047 Tensile Bar: (a) Photograph of Fractured Sample, (b) Stereo Photograph of Fracture Surface, and (c) Back-scattered Electron Micrograph of Fracture Surface. 69

Figure 4-7 Cooling Curves of A4047 and TSP-treated A4047 Alloys. 72

Figure 4-8 Optical Micrograph of an Ingot Made of the A4047 Powders: (a) without TSP Treatment, (b) 4-hour Treatment, (c) 8-hour Treatment, (d) 24-hour Treatment, and (e) 9-day Treatment. 75

Figure 4-9 Optical Micrographs of Diluted A4047 Ingots: (a) 50% Untreated A4047 + 50% Untreated A4047, (b) 50% Untreated A4047 + 50% TSP-treated A4047, (c) 75% Untreated A4047 + 25% TSP-treated A4047, (d) 94% Untreated A4047 + 6% TSP-treated A4047. 80

Figure 4-10 Cooling Curves of Diluted TSP-treated A4047 ingots. 82

Figure 4-11 Schematic Illustrating 2D View of the Twin Plane Re-entrant Edge Growth Mechanism. 85

Figure 5-1 Optical Micrographs of As-cast Al-12Si Alloys with and without TSP Using Cold-pressed Puck Process: (a) the Al-12Si-P Base Alloy with the Objective Lens of 20x, (b) the Al-12Si-TSP-P with the Objective Lens of 20x, (c) the Al-12Si-P Base Alloy with the Objective Lens of 100x, and (d) the Al-12Si-TSP-P with the Objective Lens of 100x. 90

Figure 5-2 Optical Micrographs of As-cast Al-12Si Alloys with and without TSP using Pre-melted Ingot Process: (a) the Al-12Si-I Base Alloy with the Objective Lens of 20x, (b) the Al-12Si-TSP-I with the Objective Lens of 200, (c) the Al-12Si-I Base Alloy with the Objective Lens of 100x, and (d) the Al-12Si-TSP-I with the Objective Lens of 100x. 91

Figure 5-3 Optical Micrographs of As-cast Al-7.5Si Alloys with and without TSP Using Cold-pressed Puck Process: (a) the Al-7.5Si-P Base Alloy with the Objective Lens of 20x, (b) the Al-7.5Si-TSP-P with the Objective Lens of 20x, (c) the Al-7.5Si-P Base Alloy with the Objective Lens of 100x, and (d) the Al-7.5Si-TSP-P with the Objective Lens of 100x. 93

Figure 5-4 Optical Micrographs of As-cast Al-7.5Si Alloys with and without TSP Using Pre-melted Ingot Process: (a) the Al-7.5Si-I Base Alloy with the Objective Lens of 20x, (b) the Al-7.5Si-TSP-I with the Objective Lens of 200x, (c) the Al-7.5Si-I Base Alloy with the Objective Lens of 100x, and (d) the Al-7.5Si-TSP-I with the Objective Lens of 100x. 94

Figure 5-5 Optical Micrographs of the A4047-TSP Master with Different Amount of TSP: (a) the A4047-2TSP with the Objective Lens of 20x, (b) the A4047-2TSP with the Objective Lens of 100x, (c) the A4047-4TSP with the Objective Lens of 20x, (d) the A4047-4TSP with the Objective Lens of 100x, (e) the A4047-6TSP with the Objective Lens of 20x, and (f) the A4047-6TSP with the Objective Lens of 100x. 97

Figure 5-6 Optical Micrographs of As-cast Al-7.5Si Alloys with and without TSP: (a) the Al-7.5Si Base Alloy with the Objective Lens of 20x, (b) the Al-7.5Si-TSP-i with the Objective Lens of 20x, (c) the Al-7.5Si Base Alloy with the Objective Lens of 100x, and (d) the Al-7.5Si-TSP-i with the Objective Lens of 100x. 98

Figure 5-7 Optical Micrographs of As-cast Al-7.5Si Alloys with TSP: (a) the Al-7.5Si-TSP-ii with the Objective Lens of 20x, (b) the Al-7.5Si-TSP-iii with the Objective Lens of 20x, (c) the Al-7.5Si-TSP-ii with the Objective Lens of 100x, and (d) the Al-7.5Si-TSP-iii with the Objective Lens of 100x. 99

Figure 5-8 Optical Micrographs of As-cast Al-7.5Si alloys with TSP: (a) Al-7.5Si with the Objective Lens of 20x, (b)Al-7.5Si-TSP-25 with the Objective Lens of 20x, (c) Al-7.5Si with the Objective Lens of 100x, (d) Al-7.5Si-TSP-25 with the Objective Lens of 100x. 101

Figure 5-9 Optical Micrographs of As-cast Al-7.5Si Alloys with TSP: (a) Al-7.5Si-TSP-10 with the Objective Lens of 20x, (b) Al-7.5Si-TSP-5 with the Objective Lens of 20x, (c) Al-7.5Si-TSP-10 with the Objective Lens of 100x, (d) Al-7.5Si-6TSP-5 with the Objective Lens of 100x. .. 102

Figure 6-1 Cooling Curve and its First Derivative of (a) Al-7.5Si and (b) Al-7.5Si-TSP-1.5h. 110

Figure 6-2 DSC Heating Curves of the Al-7.5Si Alloy with and without TSP. 112

Figure 6-3 Optical Micrographs of the Al-7.5Si Alloy with and without TSP: (a) Al-7.5Si, (b) Al-7.5Si with TSP Additions after 1.5-hour Hold in 720 ^{o}C Furnace. 114

Figure 6-4 Stress-strain Curves of the Al-7.5Si Alloy with and without TSP at Room Temperature. 115

Figure 6-5 Tensile Strength (a) and Ductility (b) of the Al-7.5Si Alloy with and without TSP. 116

Figure 6-6 Cooling Curves of the Al-7.5Si, Al-7.5Si-TSP-1.5h, and Al-7.5Si-TSP-4h Alloys. 118

Figure 6-7 DSC Heating Curves of the Al-7.5Si, Al-7.5Si-TSP-1.5h, and Al-7.5Si-TSP-4h Alloys. 119

Figure 6-8 Optical Micrographs of the Al-7.5Si and Al-7.5Si-TSP-4h Alloys. (a) Al-7.5Si, (b) Al-7.5Si With TSP Additions After 4-hour Hold in 720 ^{o}C Furnace. 120

Figure 6-9 Tensile Strength (a) and Ductility (b) of the Al-7.5Si, Al-7.5Si-TSP-1.5h, and Al-7.5Si-TSP-4h Alloys. 121

Figure 6-10 Cooling Curves of the Al-7.5Si, Al-7.5Si-TSP-4h, and Al-7.5Si-TSP-4h-R-X. X=24, 48, 72, and 192h. 123

Figure 6-11 Optical Micrographs of the Al-7.5Si, Al-7.5Si-TSP-4h, and Al-7.5Si-TSP-4h-R-X. X=24, 48, 72, and 192h: (a) Al-7.5Si, (b) Al-7.5Si with TSP Additions after 4-hour Hold in 720 ^{o}C Furnace, (c) Al-7.5Si with TSP Additions after Remelting 4-hour-hold Al-7.5Si-TSP Alloy and Additional **24-hour** Hold in 720 ^{o}C Furnace, (d) Al-7.5Si with TSP Additions after Remelting 4-hour-hold Al-7.5Si-TSP Alloy and Additional **48-hour** Hold in 720 ^{o}C Furnace, (e) Al-7.5Si with TSP Additions after Remelting 4-hour-hold Al-7.5Si-TSP Alloy and Additional **72-hour** Hold in 720 ^{o}C Furnace, (f) Al-7.5Si with TSP Additions after Remelting 4-hour-hold Al-7.5Si-TSP Alloy and Additional **192-hour** Hold in 720 ^{o}C Furnace. 124

Figure 7-1 A Top-view Image of Aural^{TM} 2 Castings: Aural^{TM} 2 Control, Aural^{TM} 2 – TSP, and Aural^{TM} 2 – Sr Alloys. 133

Figure 7-2 A Top-view Image of W319 Castings: W319 Control and W319-TSP Alloys. 134

Figure 7-3 Typical DSC Endothermic (Top) and Exothermic (Bottom) Curves of Aural^{TM} 2, Containing the Primary Al and Al-Si Eutectic Microconstituent. 136

Figure 7-4 DSC Results of Aural^{TM} 2 (Blue), Aural^{TM} 2-TSP(Red), and Aural^{TM} 2 -Sr (Green) during Heating (Top) and Cooling (Bottom) Cycles. 137

Figure 7-5 Cooling Curve and its First Derivative of (a) W319 and (b) W319-TSP. 139

Figure 7-6 Typical DSC Endothermic Curve of W319. Al: The Primary Al, Si: Al-Si Eutectic, θ: Al_2Cu, Q: $Al_4Cu_2Mg_8Si_7$ and α-Fe: $Al_{15}(Fe, Mn)_3Si_6$. 142

Figure 7-7 DSC Results of W319 (Blue), W319-TSP(Red), and W319-Sr (Green) during Heating Cycle. 143

Figure 7-8 Optical Micrographs of the As-cast Condition: (a) Aural™ 2 Base, (b) Aural™ 2 with TSP, and (c) Aural™ 2 with Sr. 144

Figure 7-9 SEM Micrographs of the Deep-etched Aural™ 2 Alloys: (a) Aural™ 2 Base, (b) Aural™ 2 with TSP, and (c) Aural™ 2 with Sr. 145

Figure 7-10 EBSD Micrographs of the As-cast Aural™ 2 Alloys: (a) Aural™ 2 Base, (b) Aural™ 2 with TSP, and (c) Aural™ 2 with Sr. 145

Figure 7-11 Optical Micrographs of the W319 Alloy with and without TSP: (a) W319 and (b) W319 with TSP Additions. 147

Figure 7-12 Stress-strain Curves of the Aural™ 2 Alloy with and without TSP at (a) Room Temperature and (b) 300ºC. 149

Figure 7-13 Yield Strength, Ultimate Tensile Strength, and Ductility of the Aural™ 2 Alloy with and without TSP Additions at Room Temperature and 300ºC. 150

Figure 7-14 S-N Curves of Heat-treated Aural™ 2 Alloys: (a) Aural™ 2 without Sr, (b) Aural™ 2 with TSP, and (c) Aural™ 2 with Sr. 151

Figure 7-15 Fracture Surface of Fatigue Specimen: (a) Aural 2 without Sr, (b) Aural 2 with TSP, and (c) Aural 2 with Sr Alloys. 152

Figure A-1 Cartoon of a Four-point Flexure Fixture. 159

Figure A-2 A Four-point Bend Fixture with a Bended Specimen: (a) Side-view and (b) Top-view. 160

Figure A-3 Macro of a Four-point Bend specimen: (a) A4047 and (b) A4047-TSP. 162

Figure A-4 Opical Micrographs of As-cast A4047 Alloys with and without TSP Treatment Using Dip-coating Process: (a) the A4047 Base Alloy with the Objective Lens of 20x, (b) the T4047-TSP with the Objective Lens of 20x, (c) the A4047 Base Alloy with the Objective Lens of 100x, and (d) the A4047-TSP with the Objective Lens of 100x. 163

Figure A-5 Stereo Micrographs of Bended A4047 Alloys with and without TSP Treatment Using Dip-coating Process: (a) the A4047 Base Alloy with the Objective Lens of 7x, (b) the A4047-TSP with the Objective Lens of 7x, (c) the A4047 Base Alloy with the Objective Lens of 10x, and (d) the A4047-TSP with the Objective Lens of 10x. 164

Figure A-6 Secondary (Left) and Backscattered (Right) Electron Images of the A4047 Ingots. A 1.9mm-long Crack was Formed from the Notch. 166

Figure A-7 Secondary (Left) and Backscattered (Right) Electron Images of the TSP-treated A4047 Ingots. A 0.78mm-long crack was formed from the notch. 167

Figure A-8 Strains Induced during Bending of a Beam. 169

Figure A-9 Stereo Micrographs of (a) the A4047 Ingot and (b) the TSP-treated A4047 Ingot Analyzed by ImageJ..... 170

KEY TO ABBREVIATIONS

Al	Aluminum
Cu	Copper
Mg	Magnesium
Si	Silicon
Sn	Tin
Sr	Strontium
FCC	Face-Centered Cubic
OM	Optical Microscope
SEM	Scanning Electron Microscopy
VH	Vickers Hardness
UTS	Ultimate Tensile Strength
POSS	Polyhedral Oligomeric Silsesquioxane
TSP	TriSilanol POSS
IMCs	Intermetallic Compounds
SDAS	Secondary Dendrite Arm Spacing

KEY TO SYMBOLS

a	Lattice parameter
r*	the critical radius for homogeneous nucleation
ΔH_f	the latent heat of fusion per unit volume of solid formation
γ_{SL}	the solid/liquid interfacial free energy
T_m	the equilibrium solidification temperature
ΔT	the undercooling
V	growth rate
G	temperature gradient
S	slope of the liquidus line
σ_y	Yield strength
ε	Strain
d	the average grain diameter
r_{het}^*	the critical nucleus radius for heterogeneous nucleation
ΔG_{het}^*	the free energy barrier
n_r	the number of clusters with radius r
ΔG_v	the free energy change per unit volume of solid formation
γ_{SL}	the solid/liquid interfacial free energy
θ	wetting angle
ΔG_r	cluster free energy
n_0	total number of atoms
k	Boltzmans constant

T	Temperature
λ	interparticle spacing
λ_{ex}	the lamellar spacing at the extremum undercooling point
ϕ	the ratio of mean to extremum spacing
$T_{Al\ nuc}$	the primary Al nucleation temperature
$T_{Al\ min}$	the primary Al temperature minimum (dT/dt=0).
$T_{Al\ max}$	the primary Al temperature maximum (dT/dt=0).
$T_{Al\text{-}Si\ nuc}$	the Al-Si eutectic nucleation temperature.
$T_{Al\text{-}Si\ arr}$	the Al-Si eutectic arrest temperature.
$T_{sol\ nuc}$	the Cu IMCs nucleation temperature.

Chapter 1 Introduction

Aluminum based casting alloys have been widely used in areas such as automotive, military, aerospace, and alternative energy industries, due to their light-weight and low life-cycle costs characteristics [1-4]. To meet future fuel standards and safety requirements, it is expected the demand for aluminum alloys in transportation applications will increase dramatically, including powertrain and structural components that were traditionally cast from iron. As compared with the eutectic transformation temperature of Al-Cu (548°C) [5] and Al-Mg(450°C) [6] binary alloys, Al-Si alloys have a higher eutectic temperature, 577°C [7]. Therefore, Al-Si alloys exhibit narrower solidification ranges, and offer greater fluidity [8, 9], which precede other aluminum casting alloys. The mechanical properties of Al-Si casting alloys, such as ductility and strength, are determined by the metallurgy of solidification. This chapter addresses the role the solidification plays in the Al-Si alloy development and discusses intrinsic effects of alloying elements on solidification and mechanical properties.

1.1 Solidification of Aluminum Silicon Alloys

The evolution of Al-Si alloy microstructure during solidification under both equilibrium and nonequilibrium conditions can be predicted from the phase diagram. Al atoms are arranged in a face-centered cubic structure with a lattice spacing of 0.40 nm, while Si crystallizes in a diamond cubic crystal structure with a lattice spacing of 0.54 nm [7]. The difference in these crystal structures results in three equilibrium states in terms of the minimum free energy at a given temperature: primary aluminum phase, Si phase, and Al-Si eutectic microconstituent. According to free energy curves of Al-Si alloys obtained at different temperatures, the equilibrium phase diagram is generated as shown in Figure 1-1 [10].

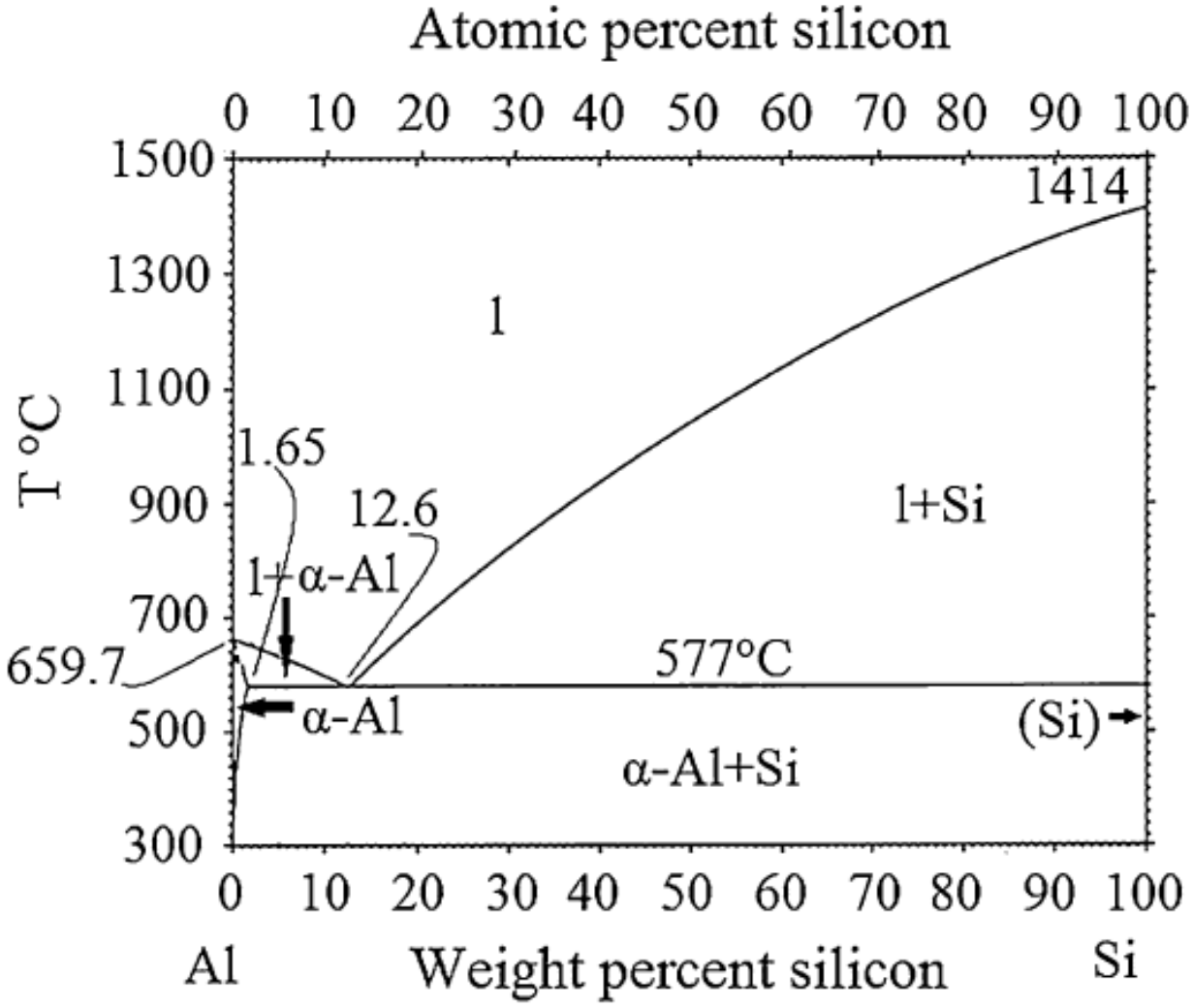

Figure 1-1 Aluminum Silicon Binary Phase Diagram [10].

In Figure 1-1, Al-Si alloys containing up to 12.6 wt. % Si and over 12.6 wt. % Si are referred to as hypoeutectic alloys and hypereutectic alloys, respectively. Hypoeutectic Al-Si alloys are more suitable for casting than the hypereutectic alloys, since the larger size and non-uniform distribution of the brittle primary Si phase in hypereutectic alloys result in very poor ductility. Typically, solidification of hypoeutectic Al-Si alloys consists of solidification of the primary Al phase followed by the Al-Si eutectic reaction.

1.1.1 Solidification of Primary Aluminum Phase

The solidification of primary aluminum occurs by two sequential microstructure evolutions: nucleation and formation of a dendritic network [11].

Nucleation is the formation of nuclei from molten material. Based on the free energy change from liquid state to solid state, classical nucleation theory was developed in the early twenty century [12-18]. There are two types of nucleation: homogeneous and heterogeneous. Homogeneous nucleation typically occurs when the undercooling becomes large enough to cause the formation of a stable nucleus [19]. The size of the critical radius r* for homogeneous nucleation [20] is given by

$$r^* = \frac{2\gamma_{SL}T_m}{\Delta H_f \Delta T} \qquad \text{Equation 1-1}$$

where ΔH_f is the latent heat of fusion per unit volume of solid formation, γ_{SL} is the solid/liquid interfacial free energy, T_m is the equilibrium solidification temperature, and $\Delta T = (T_m - T)$ is the undercooling when the liquid temperature is T.

Heterogeneous nucleation occurs when there are impurities, either suspended in the liquid or on the walls of the container that holds the liquid, providing a surface on which the solid can form. Therefore, much less undercooling is required to achieve the critical size in heterogeneous

nucleation. Homogeneous nucleation never happens in practice, while heterogeneous nucleation typically occurs for the primary aluminum phase [20].

Once the solid nuclei forms, growth starts as more atoms attach to the solid surface until fully solidify. The growing process generates heat due to the reduced enthalpy of the aluminum from solid solution to the melt [21, 22], which creates a negative thermal gradient in front of the solid/liquid interface. In the meantime, Si is partitioned into the liquid ahead of the solid/liquid interface as its solubility in the solid solution is much less than that in liquid, resulting in a corresponding variation in the liquidus temperature based on Figure 1-1. As a result of the supercooled liquid ahead of interface, a small solid protuberance forms [23]. The temperature drop from interface to protuberance drives the tip to grow, hence forming the primary dendrite arms. The Si partition perpendicular to the primary arms allows more protuberances to from along the primary arms, which leads to the formation of secondary dendrite arms. The fast growth directions are generally $< 100 >$ for aluminum, because of the anisotropic surface tension [24]. As solidification proceeds, dendritic tips become sharper so as to minimize the solid/liquid interfacial energy.

1.1.2 Al-Si Eutectic Solidification

The formation of the α-phase increases the Si level in the remaining liquid. The eutectic reaction takes place when the Si level in the liquid reaches 12.6 wt.%. Two solid phases, the Al-rich and the Si phase, form cooperatively as an anomalous structure from liquid during eutectic reaction [25]. Day and Hellawell [26] proposed the morphology and crystallography of Si in Al-Si alloys can be classified into regions A, B, and C, as shown in Figure 1-2, based on the growth rate (V) and temperature gradient (G).

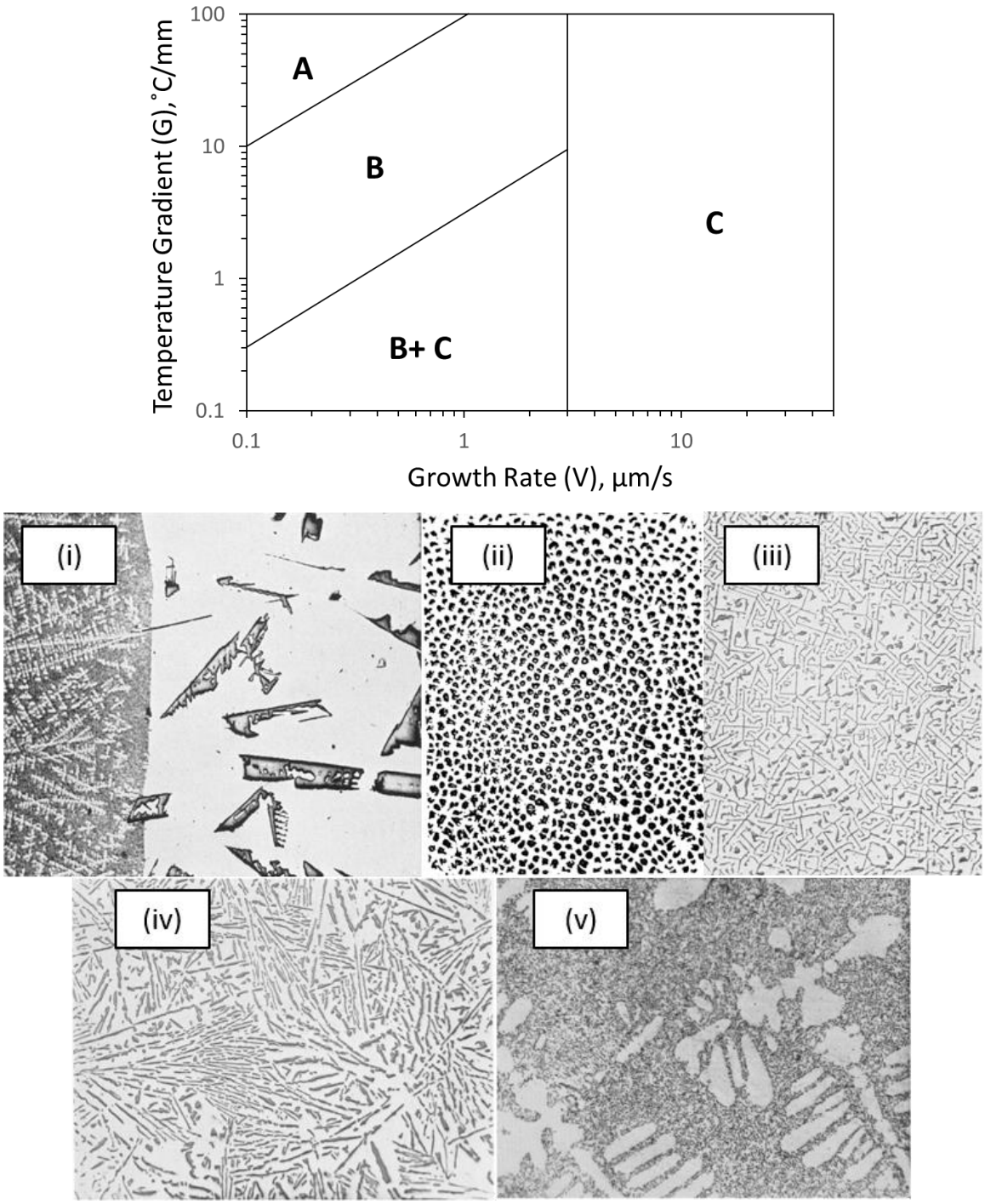

Figure 1-2 Type of Al-Si Eutectic Structures as a Function of Growth Rate (V) and Temperature Gradient (G):
(i) Region A (V=0.28µm/s and G=30°C/mm); (ii) Region B (V=0.28µm/s and G=20°C/mm); (iii) Region B (V=0.28µm/s and G=3°C/mm); (iv) Region C (V=3.7µm/s and G=3°C/mm); (v) Region C (water quenched) [26].

In Figure 1-2 (i), massive crystals of planar aluminum and faceted Si phases are growing by long-range diffusion in region A. The fiber-like Si with round cross-section typically occurs when the temperature gradient is less than 20 °C/mm (Figure 1-2 (ii)). However, the morphology of Si in region B is sensitive to G, and the fibrous Si forms lateral branches at the lower temperature gradient (Figure 1-2 (iii)). Irregular Si crystals form in region C when the growth rate and temperature gradients fall into a limited range of value (Figure 1-2 (iv)). Depending on the solidification conditions, finer structures form at rapid freezing rate of quenched alloy in Figure 1-2 (v). Day and Hellawell found that the Si structure grows at a fluctuating duplex solid-liquid front at a rapid freezing rate to form fibrous structure, whereas at relatively low rates these solid-liquid fronts are irregular and non-isothermal to form flaky structure. Nevertheless, the solidification condition in region C is similar to that commonly used in laboratory and industrial practice [26]. Therefore, the microstructure associated with region C is selected as target to study effects on solidification and mechanical properties.

1.2 Effects of grain refinement and chemical modification

To improve the overall mechanical properties of Al-Si alloys, it is important to understand the development of Al-Si microstructures with desirable properties. There are several approaches to alter the as-solidified microstructure of the alloys, which control the mechanical properties. The most significant of which are grain refinement of primary Al to enhance strength and chemical modification of eutectic Si to improve ductility.

1.2.1 Strengthening in Al-Si Alloys

Grain refinement is one of the fundamental strengthening approaches to enhance the hardness and strength of Al-Si alloys [27]. Fine-grained polycrystal have higher hardness and strength than coarse grained, because the dislocation motion during plastic deformation is

impeded by a greater total grain boundary area. The yield strength σ_y depends on grain size according to the Hall-Petch equation [28]

$$\sigma_y = \sigma_0 + k_y d^{-1/2} \quad \text{Equation 1-2}$$

where d is the average grain diameter, and σ_0 and k_y are material constant.

Grain refiners were typically inoculated in the melt before casting, resulting in a fine equiaxed microstructures. The refined microstructure was achieved by inoculation during the formation and growth of primary aluminum phase.

Titanium was first used to refine aluminum by the nucleation on Al_3Ti, which can be explained from the Al-Ti phase diagram in Figure 1-3 [29]. The system presents a peritectic reaction.

$$\text{Liquid} + Al_3Ti \rightarrow \text{Solid (FCC)} \quad \text{Equation 1-3}$$

Backerud explained how Ti_3Al nucleates aluminum grains, as shown in Figure 1-4 [30]. Al-Ti master alloys with many Al_3Ti particles were inoculated into the aluminum melt. The micro-sized Al_3Ti crystals in the master alloys start to dissolve into the liquid aluminum after a few minutes, as the black dot is shown in Figure 1-4 (1) and (2). Once the Ti concentration is enriched at the surface of liquid aluminum, Al_3Ti crystal solidifies first at hyperperitectic concentration according to the Al-Ti phase diagram. Therefore, the solid aluminum nucleates on the surface of Al_3Ti in Figure 1-4 (3). The Al_3Ti nuclei are typically located at the interface of the Al_3Ti crystals and liquid aluminum. After that the primary aluminum crystal grows around the interface, as shown in Figure 1-4 (4) and (5), small solid protuberances begin to grow (6) and dendrites forms (7) as solidification proceeds.

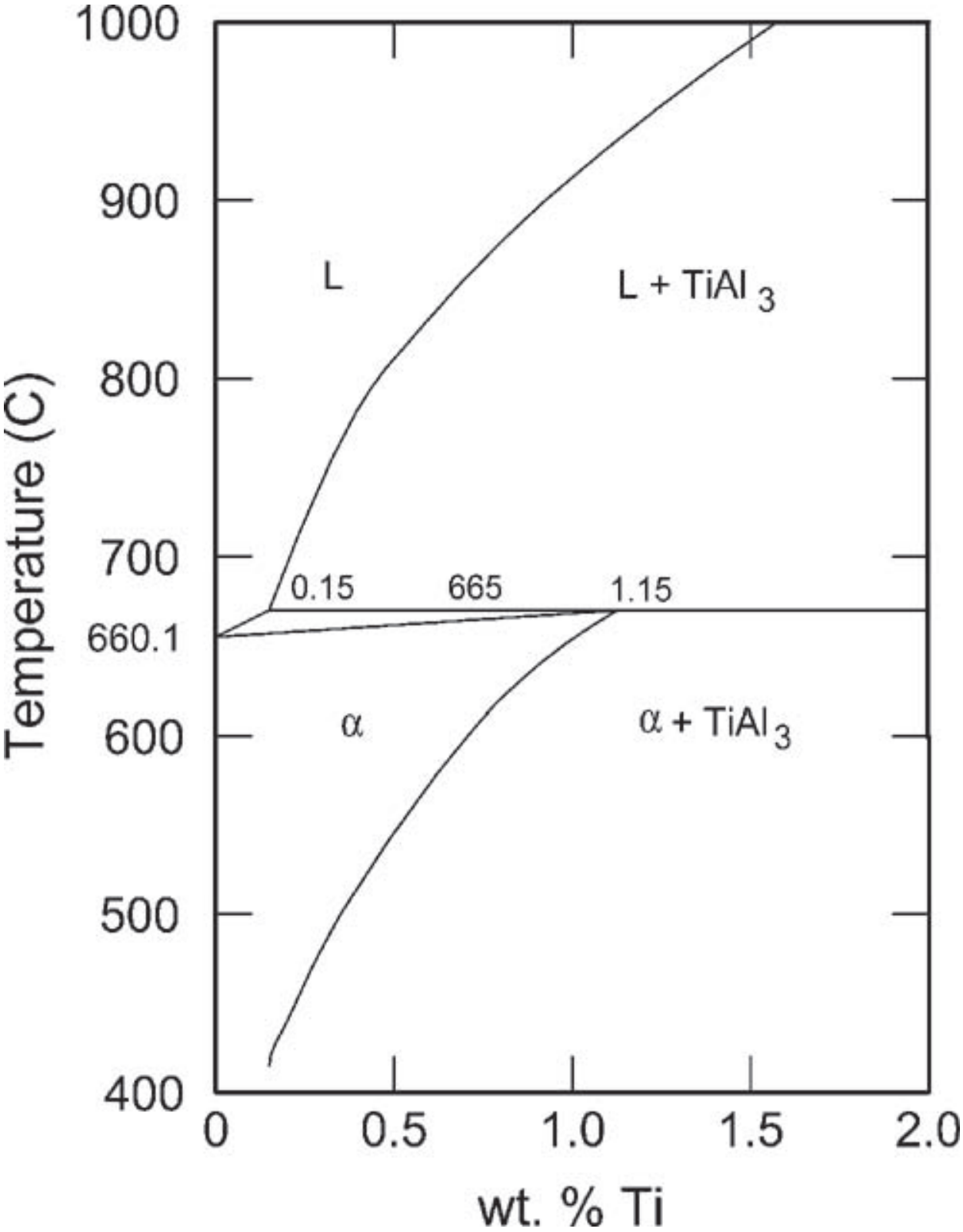

Figure 1-3 The Aluminum Rich-side of the Al-Ti Phase Diagram [29].

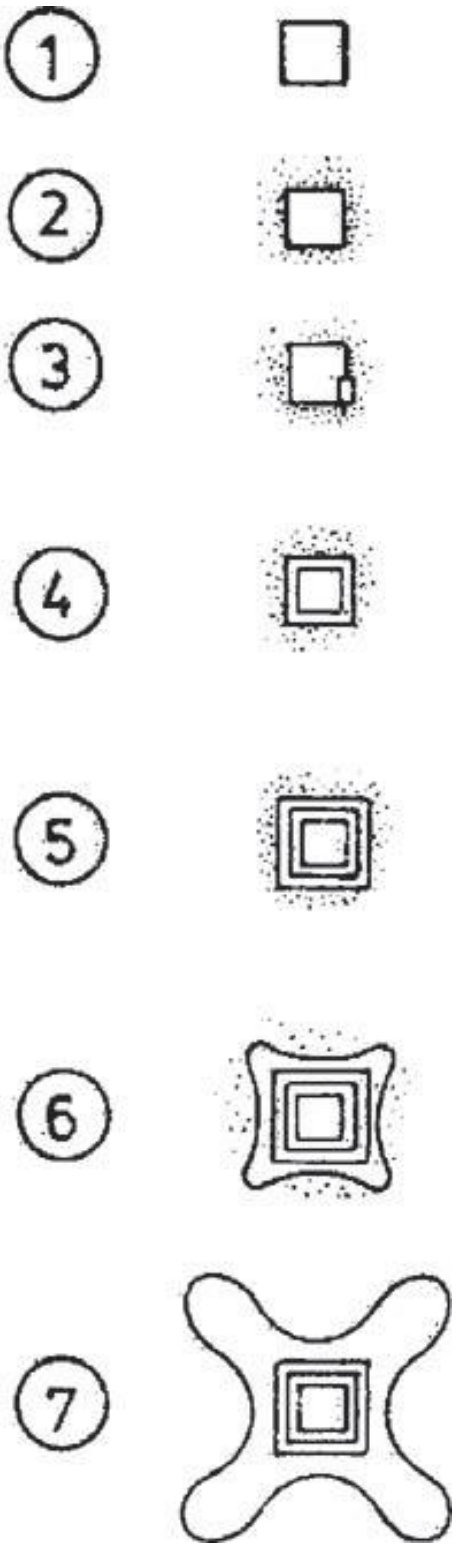

Figure 1-4 Al_3Ti Nucleates on Aluminum Grain [30].

There are some concerns about the dissolution of Al_3Ti crystals. Al_3Ti dissolves into aluminum when Ti contents fell below the peritectic composition, which causes the loss of refining ability [27]. The disappeared grain refining effect with time is known as fade.

To overcome this fading issue, Sigworth and Guzowski [31] used boron as an aluminum refiner, showing that AlB_2 is much more effective in refining aluminum grain size as compared to Al_3Ti. The refinement is caused by a eutectic reaction from the Al-B phase diagram in Figure 1-5 [31]. The AlB_2 nucleus produced much smaller grain than Al_3Ti. In other words, AlB_2 has a much greater nucleation potency than Al_3Ti. However, sludge was formed after inoculating B into the melt [32]. B has been found to react with other elements, such as Ti, Sr. The refiner-to-refiner/modifier reactions cause sludge or the loss of refinement, which is referred to as "poisoning effect". The B poisoning issues exhibited a devastating impact on the soundness of the final products.

To solve the Ti fading and B poisoning issues, a combination of B with Ti was developed. Al-Ti-B has been widely used as an excellent grain refiner in aluminum casting industry. However, there is a lot of debate about the mechanism of the Al-Ti-B grain refinement. The biggest argument focuses on the right nuclei in the Al-Ti-B master alloy, which is referred to as the "nucleant paradigm". Two theories under the nucleant paradigm were proposed, which are the nucleant-particle theory and the phase-diagram theory. The nucleant-particle theory proposed that aluminum nucleates on $(Ti/Al)B_2$ crystals [33, 34], while the phase diagram theory argued that aluminum nucleates on Al_3Ti crystals because of the peritectic reaction [35]. However, both theories have limitations. The nucleat-particle theory cannot explain why Al_3Ti was found at the center of grains at hyperperitectic concentrations. The phase-diagram theories cannot explain grain refinement at hypoperitectic Al-Ti concentrations, since Al_3Ti dissolves into aluminum for Ti contents below peritectic concentrations.

The nucleant paradigm did not provide comprehensive and consistent theories to explain grain refinement mechanisms. In 1990s, the nucleant paradigm was shifted toward the solute paradigm, suggesting that both the nucleant particles and the segregating elements affect the grain-refinement process. Easton and StJohn [36] found that TiB_2 nucleated 99.97% pure aluminum without the addition of solute Ti, but the refined macrostructure was still columnar with a few equiaxed grains. By adding 0.02% Ti to aluminum containing a TiB_2 substrate, a transition to an equiaxed microstructure was observed with significantly decreased grain size. They also found the same trend for the addition of TiB_2 and Si solute on the grain size of 99.97% pure aluminum. Similar results were observed by Johnson [37, 38]. Therefore, it has been experimentally confirmed that both effective nucleants and solute elements are required to obtain grain refinement. The effective nucleants removed the undercooling of substrate, and the solute causes the formation of a constitutional undercooling zone in front of the solidi/liquid interface to facilitate further nucleation. The solute paradigm can also clarify why Al_3Ti was found at the center of grains in refined aluminum grains at hypoperitectic Al-Ti concentrations, which cannot be explained by the nucleant paradigm.

The paradigm shift has been experimentally validated, however, there is almost no refinement if the Si content is higher than 3% in Al-Si casting alloys [39]. A new gain refiner needs to be developed to effectively refine Al-Si alloys with a large range of Si content.

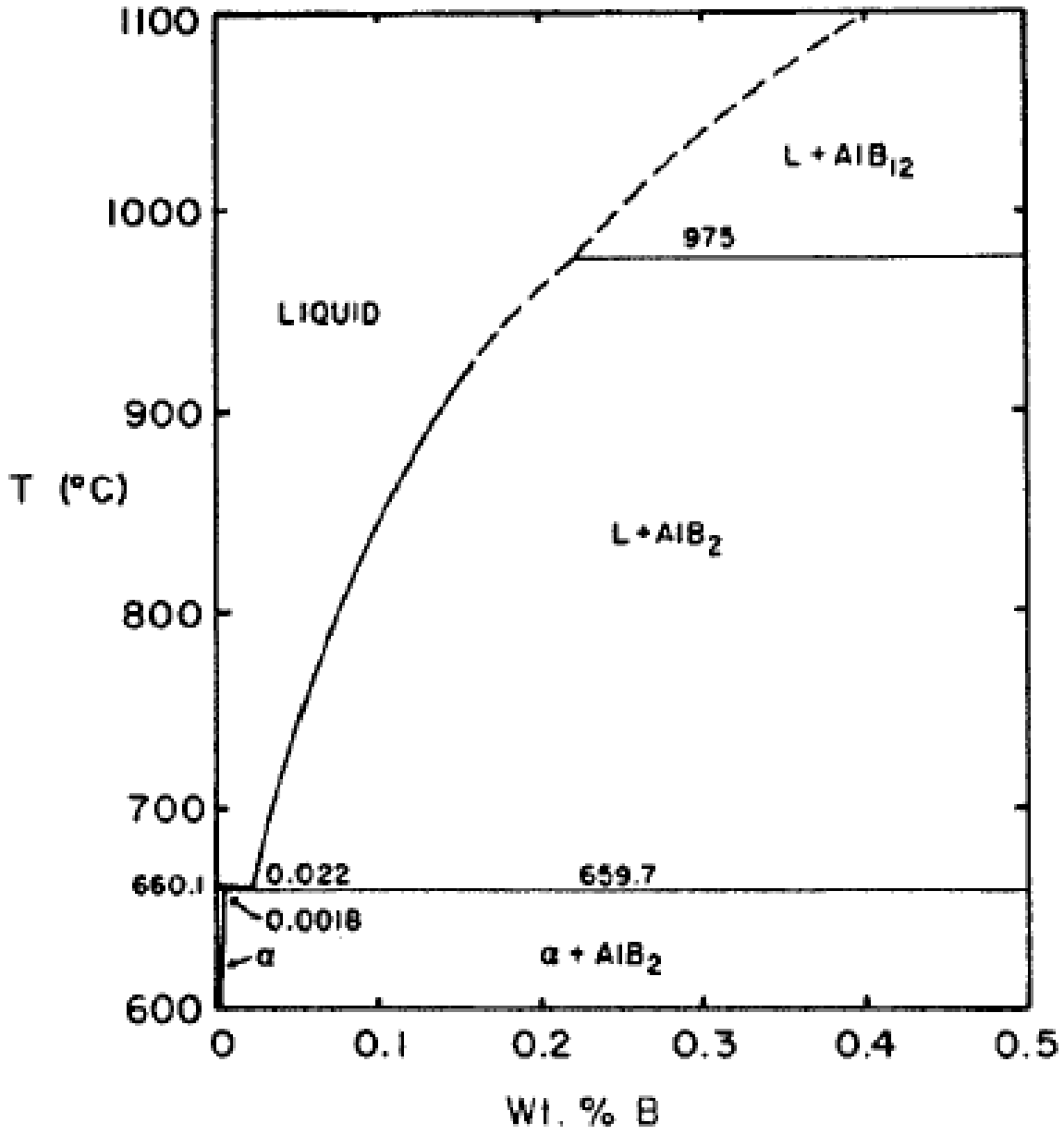

Figure 1-5 The Aluminum Rich-side of the Al-B Phase Diagram [31].

1.2.2 Ductility Improvement in Al-Si Alloys

The ductility of hypoeutectic Al-Si binary casting alloys is relatively low [40-43], as compared to steel. This is mainly because the presence of irregular eutectic Si crystals in the as-cast condition promotes crack initiation and propagation [44]. Therefore, the manner in which morphology of eutectic Si crystals develops during solidification is extremely important to optimize the overall mechanical properties for Al-Si casting alloys.

The morphology of irregular eutectic Si crystals is in flaky form, which results in low ductility. In order to increase the ductility without losing strength, trace elements, including alkaline or alkali earth metals such as Na [45], Ca [46, 47], or Sr [48-55], are intentionally added to modify the morphology of the Si crystals from the flake-like structure to a fibrous structure. It is difficult to control Na modifications due to its high vapor pressure and fast fading in molten aluminum [56]. Ca is less effective as a modifier than Na and Sr, while Ca additions are usually accompanied by an increase in the dissolved hydrogen levels, which adversely affects casting properties [57]. Sr has less fading effect in molten aluminum compared to Na and is more effective than Ca [58]. Therefore, Sr is the most widely used trace element addition for modifying the morphology of eutectic Si crystals to improve ductility. Considering that this modification through changes in the Si morphology only occurs in eutectic reaction, this section focuses on the Si microstructure evolution in eutectic colonies during solidification.

The solidification progress of eutectic Si crystals follows two stages: nucleation and growth. An understanding of the nucleation and growth mechanisms of eutectic Si crystals during solidification, with and without Sr additions, is critical to the fundamental knowledge of the modification mechanisms of Si crystals with Sr additions and how they relate to the improvement of ductility.

1) Nucleation Kinetics of Eutectic Si Crystals

It is generally accepted that the initial stages of eutectic reactions are controlled by heterogeneous nucleation [25, 59-61]. According to classical nucleation theory [20], the critical nucleus radius (r^*_{het}), the free energy barrier (ΔG^*_{het}), and the number of clusters with radius r (n_r) are

$$r^*_{het} = \frac{2\gamma_{SL}}{\Delta G_v},\ \Delta G^*_{het} = \frac{16\pi\gamma^3_{SL}}{3\Delta G^2_v}\left[{}^{(2+\cos\theta)(1-\cos\theta)^2}/_4\right] \quad \text{Equation 1-4}$$

$$n_r = n_0 e^{\left(-\frac{\Delta G_r}{kT}\right)} \quad \text{Equation 1-5}$$

where ΔG_v is the free energy change per unit volume of solid formation, γ_{SL} is the solid/liquid interfacial free energy, θ is the wetting angle, ΔG_r is the cluster free energy, n_0 is the total number of atoms, k is Boltzmans constant, and T is temperature.

Therefore, the critical nucleus radius is dependent on γ_{SL} and ΔG_v, while the energy barrier depends on γ_{SL}, ΔG_v, and θ. In the case of unmodified Al-Si eutectic, the random motion of atoms within the liquid results in small unstable clusters of Si atoms being formed. The transformation from unstable clusters to stable nuclei requires two conditions. First, a decahedron bounded by low energy facets of 111 planes is formed to minimize the surface energy resulting from the cluster formation. Second, additional undercooling supplies a driving force to overcome the free energy barrier. However, the nucleating site of the eutectic Si is still under discussion. Elliot [25] proposed that Si nucleates on nucleation centers within liquid, whereas Dahle [50] suggested that the eutectic Si could nucleate on Al dendrite tips or the nuclei within the interdendritic liquid.

2) Nucleation Kinetics of Sr-modified Si Crystals

The addition of trace elements increases the difficulty of the nucleation of the Si crystals. Solidification is therefore suppressed to lower temperatures. As mentioned above, the free energy barrier depends on the interfacial energy of liquid and the undercooling. It is reported

[62] that the addition of Sr decreases the interfacial energy between the eutectic liquid and solid Si, lowering the energy barrier and thus aiding nucleation of eutectic Si particles. In contrast, the addition of Sr decreases the number of Si-Si covalent bonds, reduces the number of Si nuclei in the melt, and increases the undercooling, hindering the nucleation of eutectic Si [63]. This effect dominates during the eutectic reaction [62]. Although this study can explain the increased undercooling temperature, modified Si morphology, and improved ductility with Sr addition, it is not clear whether the nucleation or growth processes controls the evolution of the Al-Si eutectic. In order to comprehensively understand modification mechanism of hypoeutectic Al-Si alloys with Sr additions, both nucleation and growth processes need to be considered.

3) Growth Kinetics of Eutectic Si Crystals

The flaky morphology of Si crystals in Al-Si eutectic colonies is dependent on both thermodynamic and kinetic parameters. There are two types of heat during solidification [20]: the specific heat of the liquid and the latent heat of fusion. The total interface undercooling (ΔT) of regular eutectics consists of thermal, curvature, and kinetic undercooling. Considering both the diffusion in the liquid and the thermodynamics of solid-liquid interfaces, the total interface undercooling is related to the growth velocity (V) and the interparticle spacing (λ). This relationship of the regular eutectic growth behavior was set up by Jackson and Hunt [64] for an isothermal interface and it can be shown that $\Delta T = K_1 V\lambda + K_2/\lambda$, where K_1 and K_2 are alloy constants determined from thermodynamic data. Three equations, calculated by differentiating the undercooling equation and setting $\partial\Delta T/\partial\lambda = 0$, describe the growth mechanisms of the regular eutectic:

$$\lambda_{ex}^2 V = K_1/K_2 \qquad \text{Equation 1-6}$$

$$\Delta T/\sqrt{V} = 2\sqrt{K_1 K_2} \qquad \text{Equation 1-7}$$

$$\Delta T\lambda_{ex} = 2K_2 \qquad \text{Equation 1-8}$$

where λ_{ex} is the lamellar spacing at the extremum undercooling point, which is presumed to be the operative point of the regular eutectic system. However, this model cannot properly predict the anisotropic growth behavior of irregular eutectics because of the non-isothermal interface. Magnin and Kurz [65] developed a model for irregular eutectic system by setting up a non-isothermal coupling condition over the whole interface and a morphological criterion for the branching behavior of the faceted phase. The growth behavior of the irregular eutectic is shown as follows:

$$\langle\lambda\rangle^2 V = \phi^2 K_1/K_2 \quad \text{Equation 1-9}$$

$$\langle\Delta T\rangle/\sqrt{V} = (\phi + 1/\phi)\sqrt{K_1 K_2} \quad \text{Equation 1-10}$$

$$\langle\Delta T\rangle\langle\lambda\rangle = (\phi^2 + 1)K_2 \quad \text{Equation 1-11}$$

where ϕ is the ratio of mean to extremum spacing. Thus, the growth velocity of faceted Si crystals increases exponentially with undercooling. Guzik and Kopycinski [66] developed a new model that modified the MK model to consider the effect of material constants on the interlamellar spacing and protrusion of the faceted phase. In this modified model, the characteristic depression of the nonfaceted phase and the protrusion of the faceted phase can be calculated. Material constants, such as the wetting angle, diffusion coefficient, and Gibbs-Thomson coefficient, play important roles in the irregular eutectic growth. All the modified models, however, are mostly focused on the two-dimensional parameterization of the irregular eutectic. The exact growth mechanism cannot be fully understood unless a mathematical model can be developed with three-dimensional parameterization. Nevertheless, the growth kinetics provide correlations between undercooling, growth velocity, and interparticle spacing, which are convenient for establishing the growth mechanism of eutectic Si crystals with and without trace element additions.

4) Growth Mechanism of Eutectic Si Crystals

The Si flakes in Al-Si eutectic colonies promote crack initiation and propagation and hence result in low ductility. The twin plane re-entrant growth edge (TPRE) mechanism is one of the established growth mechanisms of flaky Si, which was first proposed by Hamilton and Seidensticker [67] to explain the growth behavior of germanium dendrites. Kobayashi and Hogan [68] confirmed the growth of Si in Al-Si eutectic alloys by multiple twinning through the TPRE mechanism from the experimental evidence. The surface of the solid-liquid interface on the Si 111 plane is atomically smooth, and the equilibrium Si crystal is bounded by 111 habit planes with two parallel twins. Compared with 111 flat surfaces and the re-entrant ridge with the external angle of 219°, the re-entrant corner with an external angle of 141° is the most favorable site for Si crystals to nucleate, hence the growth of eutectic Si along $< 112 >$ directions take place rapidly at the reentrant corner. Silicon crystals with two twins can generate more re-entrant corners to continue growing. Once a triangular corner bounded entirely by ridges is formed, the Si growth stops due to the absence of any 141°extenal angles. Recently, Fujiwara et al. [23, 69] modified the growth model of Si crystal and claimed that Si crystal growth continues with the two new 141°extenal angles formed on the growth surface of a 219° external angle. According to these experimental results, there are two preferential growth directions of Si crystals: $< 112 >$and $< 110 >$. In the case of $< 112 >$directions, the Si can grow alternately at the re-entrant corners with a 141°extenal angle, while the Si crystal along $< 110 >$ directions can grow at both the re-entrant corners with 141°extenal angles and the re-entrant ridges with 219°extenal angles. Therefore, Si tips along $< 112 >$ directions become wider during growth, while these along $< 110 >$ directions become narrow. In this case, the faceting Si crystals in eutectic colonies grow independently and form flaky structures.

5) Growth Mechanism of Sr-modified Eutectic Si Crystals

With the Sr addition, the morphology of Si crystals is modified to form a fibrous structure and thus improves ductility. According to the TPRE mechanism, in the unmodified Al-Si system there are two different restricted growth theories for Al-Si eutectic colonies modified with trace elements. One of them [26, 68] refers to poisoning the re-entrant edges. Sr can sit at re-entrant edges, acting as a deactivator to inhibit Si growth rather than acting as a nucleation site to promote the growth process. Rather than the Si growing along $< 112 >$ directions anisotropically, isotropic growth along multiple directions takes place for the modified Al-Si eutectic colonies. Lu and Hellawell [70] claimed that Sr is rejected into the liquid ahead of the solidification front because of the extremely low solubility of Sr in both aluminum and Si. Therefore, Sr is absorbed at trace levels onto the Si layers, which can induce twinning by poisoning the growing ledges of Si. Lu and Hellawell also proposed that 1.65 is the ideal ratio of trace element to Si atom radii to induce twinning. Considering both unmodified and modified Al-Si eutectics, there are still two limitations corresponding to the experimental results that cannot be well explained by this model: the undercooling temperature of the Al-Si eutectic reaction is increased with Sr addition and eutectic structure without Sr addition is modified by a relatively high solidification rate. Nevertheless, it is generally accepted that Sr acts as deactivator to inhibit Si growth during solidification. Therefore, the morphology of eutectic Si crystals with Sr additions is fibrous in form, which improves the ductility of Al-Si casting alloys.

Deciphering the controlling mechanisms exerted by Sr over nucleation and growth is one of the central challenges, as it is crucial for understanding how fibrous Si crystals in Al-Si eutectic colonies are formed. This section has focused on two aspects that are central to the identification and analysis of important trends. Sr at trace levels decreases the number of Si-Si bonds that act as the nuclei of Si crystals in eutectic colonies. Hence, Sr hinders the nucleation process. Additionally, Sr sits at re-entrant edges of Si crystals, acting as a deactivator to inhibit

crystal growth. These two mechanisms provide a framework for relating the interactions between the modifier and the morphology of the eutectic colonies. Thus, the desired mechanical properties of Al-Si based alloy can be engineered.

1.3 Development of Cast Aluminum Alloys Using Nano-structured Chemicals

1.3.1 Overall Goal

The goal of the proposed work is to explore the role of nanostructured silanols and their effect on the solidification kinetics, microstructure, and mechanical properties of Al-Si based casting alloys.

1.3.2 Motivation

One of the major strategies to meet the new Corporate Average Fuel Economy (CAFE) standards for 2025 (54.5 mpg) [71] is to reduce vehicle weight by replacing steel with lightweight materials. The ultimate objective is to enhance aluminum alloys with both high ductility and strength. However, conventional Al-Si based casting alloys show low ductility as a compensation for high strength, since the presence of irregular flakes like eutectic Si crystals in the as-cast condition promotes crack initiation and propagation. To improve their overall mechanical behaviors, grain refiners or chemical modifiers have been added into the base alloy, which enhances the overall mechanical properties through microstructure refinement. For example, titanium (Ti)/ boron (B) can react with Al to form intermetallic compounds (IMCs)[72], such as Al_3Ti and TiB_2. These IMCs serve as heterogeneous nucleation sites for primary Al, resulting in refined grain size. The addition of strontium (Sr) can poison the re-entrant corner or growing ledges in eutectic Si in order to modify the morphology of eutectic Si from flaky to fibrous form[62, 70]. However, as the Si content is greater than 3%, the effect of the Al-Ti-B grain refiner on changing Al grain size diminishes significantly [39, 73], which results from the formation of TiSi and $TiSi_2$. Sr also suffers from an accelerated oxidation at

casting temperatures [56], leading to the loss of Si modification in Al-Si alloy after the second melt. Therefore, the issues of Ti poisoning and Sr fading after the addition of refiners/modifiers become major concerns for aluminum foundries and researchers. Thus, there is a need to develop new Al-based casting alloys with high ductility while not sacrificing strength for structural applications without the poisoning and fading effects of current methods.

This thesis relates to the use of nano-structured chemicals in the processing of lightweight aluminum alloys for structural applications. Polyhedral oligomeric silsesquioxane (POSS) are silsesquioxane-based nano-structural chemicals, as shown in Figure 1-6 (a) [74]. These chemicals are cage-like structures with repeating monomer units of $RSiO_{1.5,}$ where Si is the element silicon, O is oxygen, and R is a hydrocarbon group, e.g. ethyl, isobutyl, phenyl, etc. These hybrid structure links inorganics to organics with unique properties, such as high reactivity and thermal stability [74, 75]. Trisilanol POSS (TSP) are produced by replacing a Si atom at the corner of the POSS to form silanols, as shown in Figure 1-6 (b). These silanols have been revealed to form thermodynamically stable Si-O-M bonds with metals [75]. Silanols in TSP can react with reactive metals to make a salt and hydrogen.

$$2XSiOH^{-} + M^{X+} \rightarrow X(SiO)_{2/X}M + XH_2 \qquad \text{Equation 1-1}$$

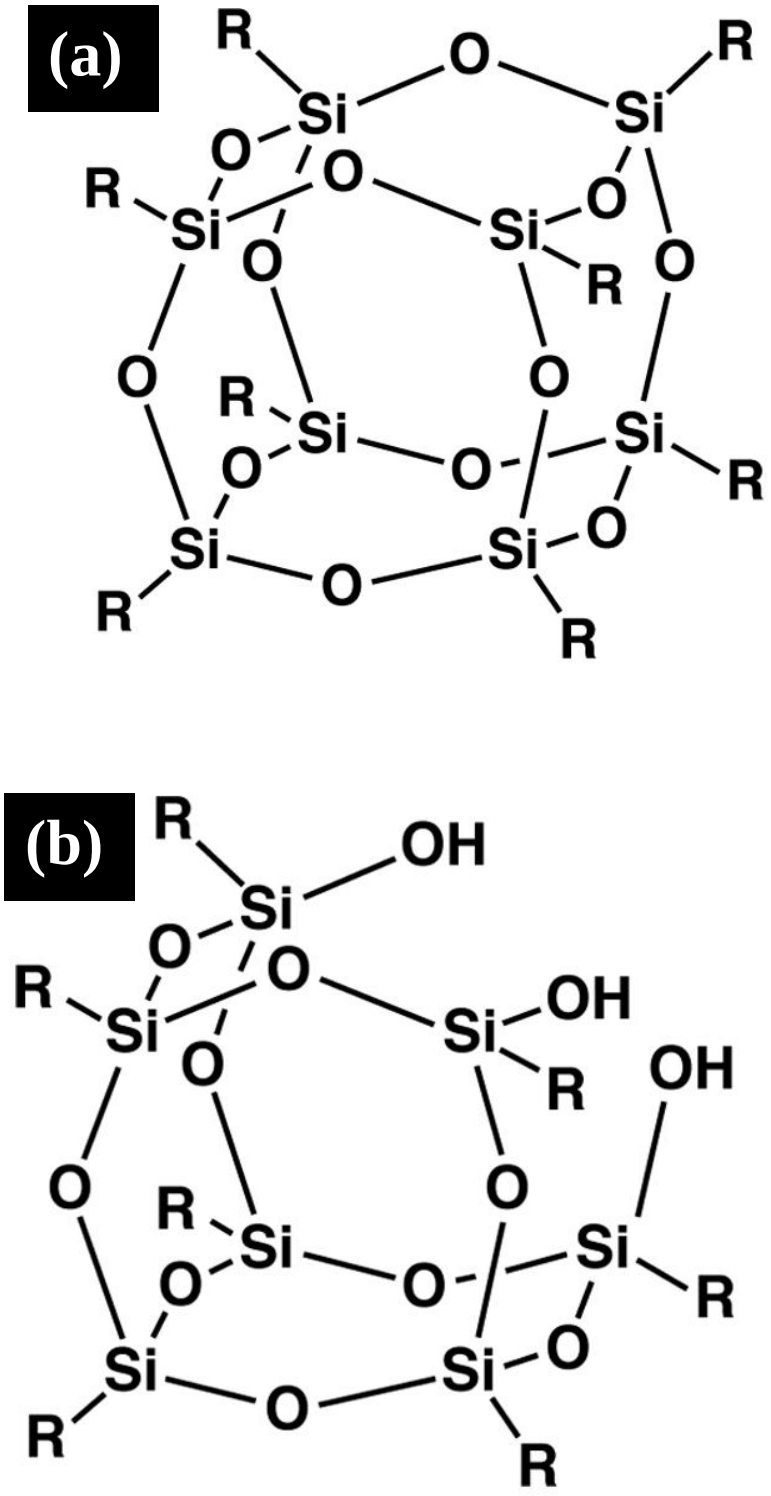

Figure 1-6 Chemical Structure of (a) Polyhedral Oligomeric Silsesquioxane (POSS) and (b) Trisilanol POSS.

Many metallic elements, such as Al [76, 77], Ti [76, 78], V [78], Zn [77], have been incorporated with TSP to form polyhedral oligomeric metallic silsesquioxane (POMS). Effect of TSP additions on the microstructure and mechanical reliability of tin-based solder joints has been investigated by Lee[79] and Choudhuri[80]. Their study suggested that TSP additions refined the as-solidified microstructure of SAC305. Optical micrographs comparing the effects of 2wt% TSP additions on the bulk microstructure of SAC305 have been presented in Figure 1-6. TSP addition resulted in smaller sized dendritic arms as compared to the control specimen. TSP additions were also found to influence the morphology and size of IMCs (Ag_3Sn and Cu_6Sn_5) present in microstructure of SAC305. Figure 1-7 (a) shows the backscattered electron image (BEI) ternary eutectic region in the as-solidified microstructure of SAC305, while Figure 1-7 (b) present the BEI of the ternary eutectic regions in SAC305+TSP. In SAC305, large (~30µM) rod and needle shaped Cu_6Sn_5 and Ag_3Sn IMCs are observed in the ternary eutectic region, while specimens containing TSP show a refined ternary eutectic microstructure with relatively spheroidal morphology. In general addition of TSP results in a more uniform microstructure. This suggests that such addition influences the growth of IMCs within the liquid phase during solidification.

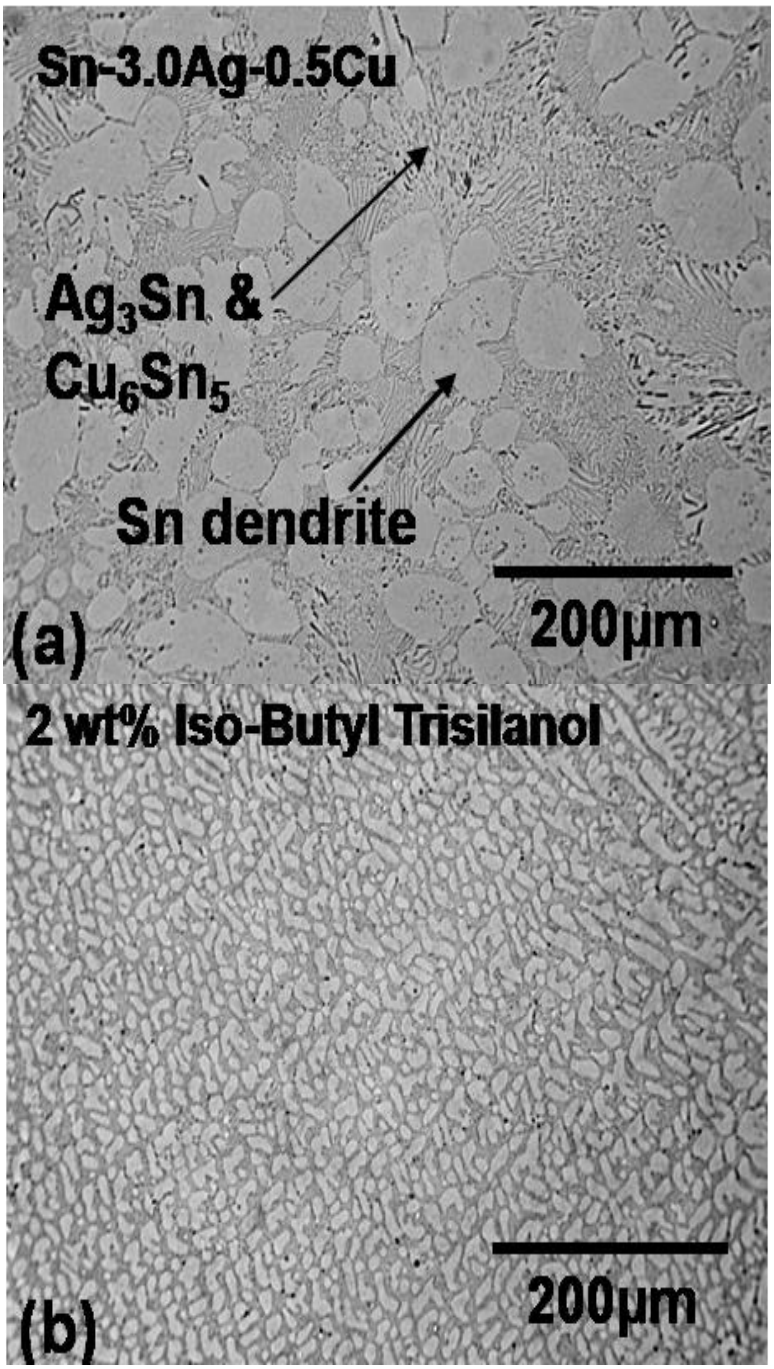

Figure 1-6 Optical micrographs showing the effects of 2wt% TSP additions on the as-solidified microstructures of SAC305.[80]

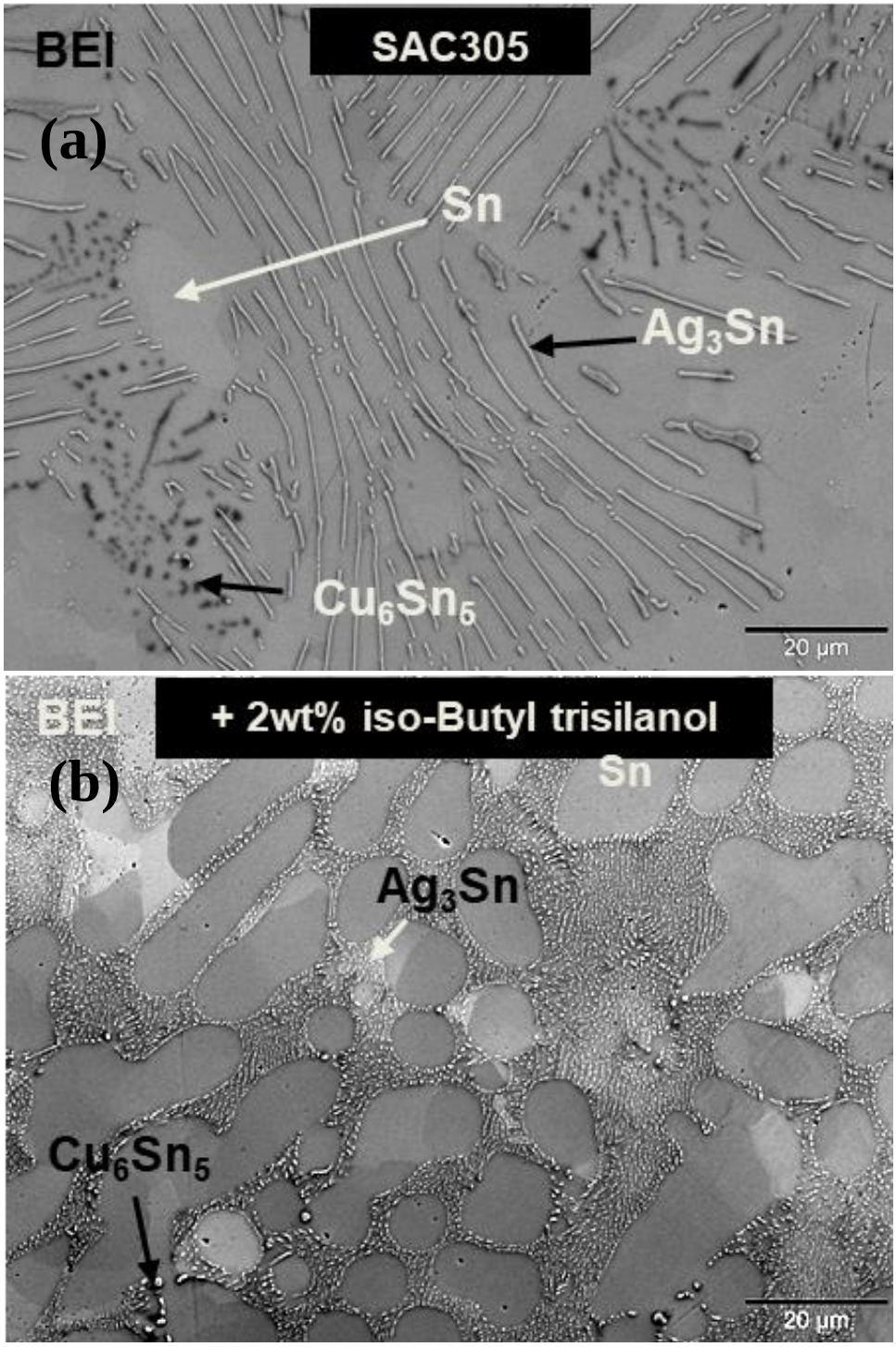

Figure 1-7 High magnification BEI showing sizes and morphology of Cu6Sn5 and Ag3Sn IMCs in the ternary eutectic regions in (a) SAC305, and (b) SAC305 + 2wt% TSP.[80]

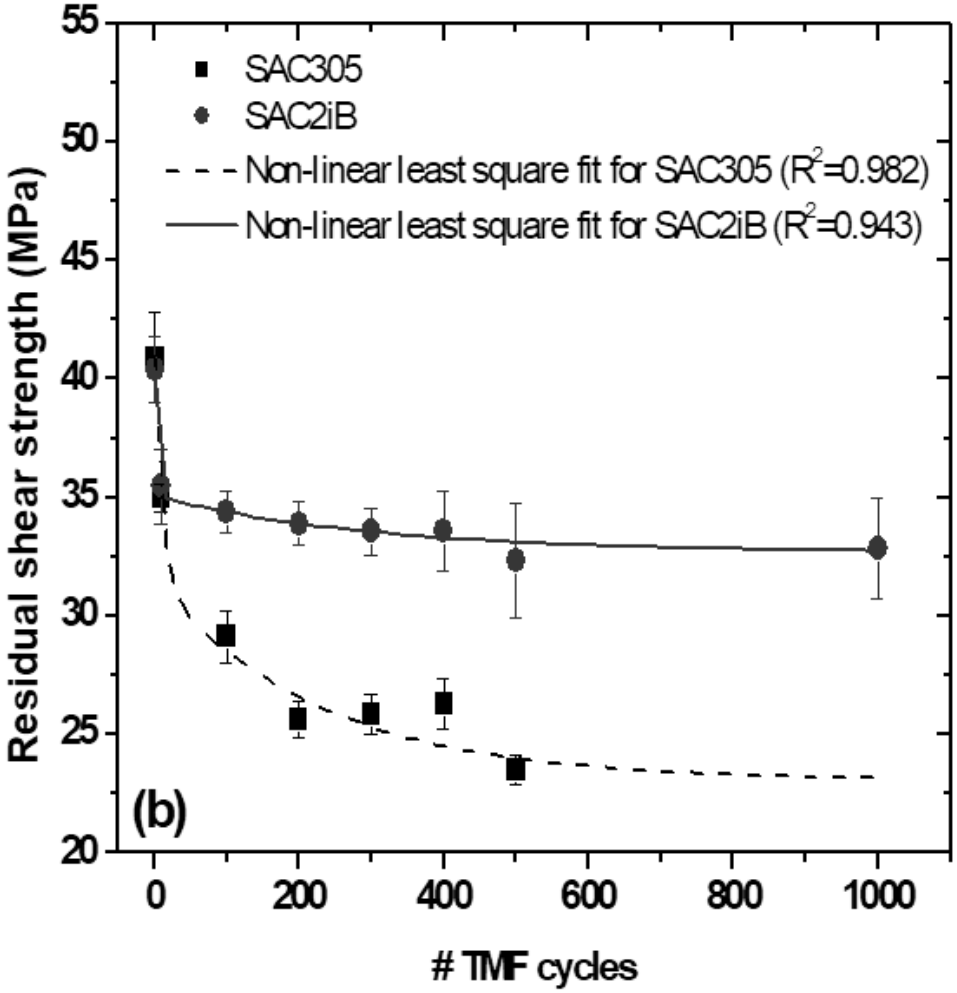

Figure 1-8 Comparison of residual shear strengths of SAC305 and SAC2iB solder joints. Error bars show 95% confidence intervals. Second order exponential non-linear least square fits have also been shown. [80]

The refined IMCs and SDAS with TSP addition results in the residual mechanical improvement of SAC305 solder joints within the number of TMF cycles chosen as shown in Figure 1-8. Such an improvement indicates that TSP reinforcements retard the microstructural damages responsible for the deterioration in the mechanical strength of control joints.

In summary, TSP additions refine microstructure of both the primary Sn and the Cu6Sn5 intermetallic compounds (IMC). More importantly, TSP prevents coarsening at elevated

temperature for microstructural stability of Sn-based solders, and also significantly improves the thermomechanical fatigue life of solder joints by pinning Sn grain boundaries from sliding and enhancing the IMC/Sn bonding.

The objectives for this thesis are to achieve microstructure refinement and stability with TSP additions, leading to significant mechanical property enhancement for cast Al alloys. Presence of silanol groups in TSP facilitates the bonding between TSP and Al. Once this bonding is achieved to form a closed Si-O-M cage, the cage structure can be maintained a temperature higher than 1000^{o}C without thermal degradation due to the inert nature of POSS inorganic core. Because of these unique feathers, poisoning and fading issues in cast Al alloys with the incorporation of TSP would not occur.

1.3.3 Fundamental Idea and Specific Aims

A nanostructured chemical based on trisilanol polyhedral silsesquioxane (TSP) was used as a chemical modifier to modify the microstructure of Al-Si based casting alloys. This study focuses on increasing the ductility of Al-Si casting alloys by modifying the microstructure of eutectic Si crystals in the as-cast condition while maintaining the strength of the unmodified alloy.

Specific aims of this project include the following:

1) Study the impact of TSP additions on the microstructure and mechanical properties of Sn based binary and ternary alloys. The relationships between the structure and properties of the material were investigated to design microstructure with a predetermined set of material properties.

2) Investigate the effect of TSP additions on the solidification of Al-Si casting alloys to understand how their microstructures are produced during phase transformation. The role of phase transformations in the microstructure development of TSP modified Al-Si were addressed to propose the modification mechanism.

3) Develop an optimized process to obtain a TSP master modifier to avoid the fading issues of current modifiers. By controlling the TSP incorporation method and TSP content in the master, the designed master modifier is demonstrated to function in hypoeutectic Al-Si for structural applications.

4) Use the TSP master alloy to modify the microstructure of Al-Si binary and commercial alloys with improved mechanical properties. Microstructural and thermal characterizations have been performed to ascertain the role of the TSP master alloy in the strength and ductility changes.

This study addresses fundamental questions on how the addition of TSP influences microstructure and solidification behavior of Al-Si based casting alloys and provides solutions to reinforce aluminum alloys with high ductility and strength for automotive industry.

Chapter 2 Sn-Cu Binary Alloys Refinement

2.1 Background

Tin (Sn) based lead-free alloys have been widely used as industrial solders to fabricate solder joints in recent years.[81] Tin-silver-copper (SAC) alloys are considered as the preferred substitute for Sn-Pb solder in solder joint applications.[82, 83] However, Sn-Cu binary alloys, such as Sn-0.7wt.%Cu and Sn-3wt.%Cu, have been drawn more and more attentions as the prevailing alloy system due to slightly higher service temperature and lower cost as compared to SAC solder alloys. The microstructure of Sn-Cu alloy is determined by the chemical composition of Cu in Sn. In the case of eutectic Sn-0.7Cu, the microstructure is typically formed with intermetallic compound (IMC) particles embedded in Sn-rich matrix, while hypereutectic Sn-Cu contains proeutectic Cu_6Sn_5 phase besides eutectic constituent. Unfortunately, because of the short thermo-mechanical fatigue lifetime, Sn-Cu alloys have poor strength and creep resistance[84], and hence limits their solder joint applications.

The limiting mechanical performances are mainly due to the size and texture of Sn-rich grains, the size and dispersion of Cu_6Sn_5 IMC during processing[85, 86], and coarsening of IMC during service[87, 88]. Currently, there are two major approaches to solve these problems: alloying and composite approaches. For alloying approach, it has been reported that Ni[89-91], Co[89], Al[92], Zn[93, 94], In[95], and/or rare earth elements[96] are added as grain refiner of Sn-rich grains. The potential issue is that the addition of minor alloying elements cannot prevent IMC coarsening during services. For composite approach, additional IMC are incorporated by either in-situ or mechanical mixing methods.[97, 98] The drawbacks of IMC incorporation are the big size of reinforcements (several microns) resulting in poor mechanical properties, as well as coarsening of reinforcements during service. Another composite approach is to incorporate inert reinforcements by mechanical mixing method.[99, 100] Lack of bonding between solder and

reinforcements[101], clustering of particles with pores in-between agglomerated particles, and interfacial cracking due to the required mechanical work to break up clusters are the unavoidable issues.

Polyhedral oligomeric silsequioxanes (POSS) are silsequioxane-based nano-structural chemicals.[74, 75] These chemicals are cage like structures with repeated monomer units of $RSiO_{1.5}$ where Si is the element silicon, O is oxygen, and R is hydrocarbon group, e.g. ethyl, isobutyl, phenyl etc. Partial cage-like POSS with multiple silanol (Si-OH) functionalities are produced by replacing a Si atom at the corner of POSS to form silanol bonds. TriSilianol phenyl POSS (TSP) is used in this study. These silanol bonds have revealed to form thermodynamically stable Si-O-M bonds with metals (e.g. Sn).

The objective of this study is to investigate creep resistance and strength, and correlate above mentioned mechanical properties changes with microstructure alterations of Pb-free Sn-Cu solder alloys with addition of nanostructured silanols.

2.2 Experimental

2.2.1 Preparation of Sn/Cu Solder Wires

TriSilanolphenyl Polyhedral Oligomeric Silsesquioxane (TSP), obtained from Hybrid Plastics, Inc. (Hattiesburg, MS), was used in this study as nano-structured modifier. Nearly eutectic, Sn-0.7Cu, and hypereutectic, Sn-3Cu, alloys were manufactured by Johnson Manufacturing with their standard industrial alloy practice. For a comparative study of creep resistance and microstructures of TSP-treated Sn-Cu alloys, both Sn-0.7Cu and Sn-3Cu alloys containing 0.5wt% TSP were prepared using the same alloying approach.

Nearly eutectic and hypereutectic Sn-Cu alloys without and with 1wt% TSP addition were cast to 38 mm by 178 mm billet form according to the established ISO procedures by Johnson

Manufacturing. 0.8 mm diameter solid solder wires were then extruded from billet using a 100 Ton Collin Press.

2.2.2 Coil Creep Testing

The creep behavior of solder wires was characterized by coil creep test. A 20-turn coil of Sn-Cu solder wire was wound on a cylindrical aluminum tube with 25.4 mm in diameter as shown in Figure 2-1 (a). The creep test of a self-loaded coil in Figure 2-1 (b) was conducted in a temperature-controlled column at 40, 50, 60, and 70°C. Stretch rate was evaluated through dividing the spacing between the 1st and the 10th turns by time at specific temperature for all wires, which can be used as an indicator of creep rate.

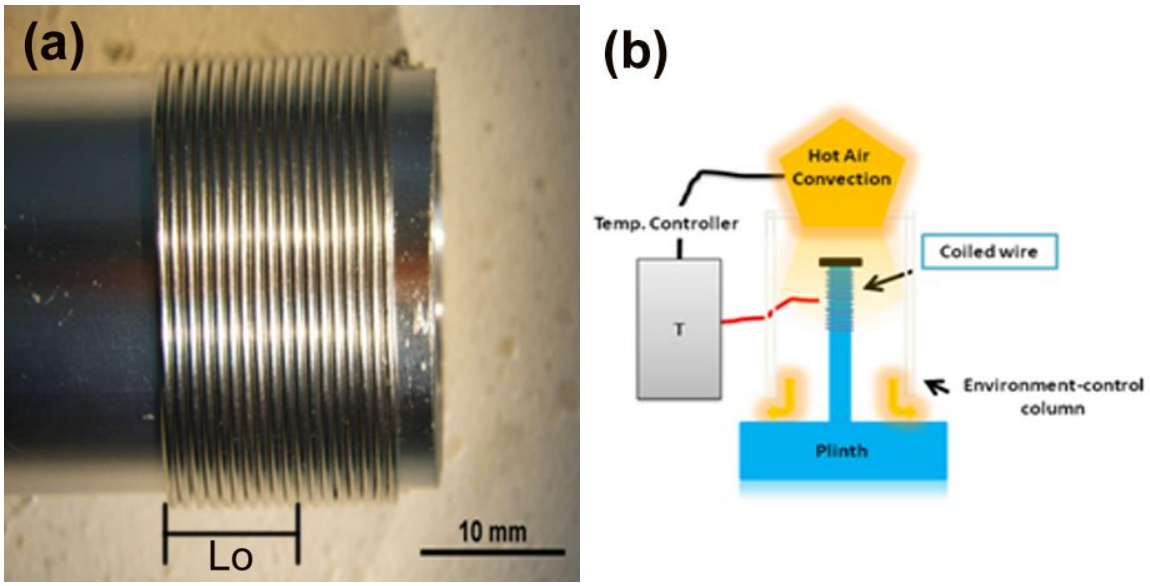

Figure 2-1 Creep Experimental Setup: (a) Stereo Micrographs of Wire Winding and (b) Schematic of Coil Creep Setup.

2.2.3 Polarized Optical Microscopy

Four pieces of each specimen were cut from four different regions and mounted with epoxy resins in such a way that wires orientated in the extrusion direction. The wire mount was ground

until wire surface reached the center, and then polished. Polarized optical micrographs were taken using an inverted metallographic microscope, Nikon ECLIPSE MA200.

2.2.4 Differential Scanning Calorimetry

Thermal characteristics were performed using a TA Instrument Q2000 equipped with a mechanical cooling system under N_2 atmosphere. Sn-Cu wires, about 15mg, were placed in a TZero^{TM} aluminum pan made for thermal analysis of solid samples. All samples were heated to 350°C and kept for 1 min to ensure complete melting, then cooled to 150°C at a constant cooling rate of 10°C/min and then reheated to 350°C at a heating rate of 10°C/min. Onsite of the exothermic solidification peak was denoted as the crystallization temperature, T_c, and the onsite of the endothermic melting peak was denoted as the melting temperature, T_m.

2.2.5 Indentation Microhardness

Microhardness of the polished wire in the epoxy mount was measured with a Clark CM-800 Knoop tester at 25 gf applied load with 15 seconds dwell at room temperature.

2.2.6 Orientation Imaging Microscopy

The Sn crystal orientation of the polished wire in the epoxy mount was evaluated using a CamScan field-emission gun (FEG) secondary electron microscopy (SEM) equipped with electron backscatter diffraction (EBSD) analysis systems. The accelerating voltage used was 20 kV. A 3-μm step size was used for EBSD scans. To reduce the charging effects inside the SEM from the nonconductive epoxy mount, the mounted sample was mostly covered by Cu tape, and the areas surrounding the wires were covered with conductive carbon paint. EBSD c-axis orientation maps, texture, and pole figure plots were generated using orientation imaging microscopy (OIM) Data analysis software.

2.3 Results and Discussions

2.3.1 Creep Behavior

The addition of TSP improved creep resistance of both Sn-0.7Cu and Sn-3Cu wires. Stretch rates of both Sn-0.7Cu and Sn-3Cu solder wires without and with TSP addition at various temperatures were plotted in Figure 2-2. It is well known that there are typically three stages with distinctive strain-time feather during creep: primary, steady-state, and tertiary creep. In the solder coil study, steady-state creep dominates the creep behavior due to the time-independent strain rate at all testing temperatures. Diffusion creep and dislocation creep are basically two general mechanisms by which steady-state creep occurs. The melting points of eutectic Sn-Cu alloy was around 500K[102], so the homologous temperature at room temperature (300K) is approximately 0.6. The homologous temperatures during coil creep testing were greater than 0.6. Therefore, the dominate creep mechanism is diffusion creep.

Comparing Figure 2-2 (a) with Figure 2-2 (b), without TSP addition, Sn-3Cu solder wire had a higher creep resistance than Sn-0.7Cu. The higher creep resistance of Sn-3Cu over Sn-0.7Cu suggested that the diffusion creep behavior in Sn-Cu alloys was controlled by the microstructure and spatial distribution of Cu_6Sn_5 IMCs, similar to precipitation hardening[103]. The results in this study were consistent with the work done by Subramanian et al.[101], where in-situ Cu_6Sn_5 IMCs reinforced eutectic Sn-Ag showed better creep resistance than the control eutectic Sn-Ag at room temperature because of the longer time for a dislocation to climb during diffusion creep. In Figure 2-2, the stretch rate of both Sn-Cu wires at four different temperatures was reduced due to the addition of TSP. More importantly, effect was more significant for Sn-0.7Cu. Thus, Sn-Cu alloys with TSP addition exhibited higher resistance to creep, especially for eutectic Sn-0.7Cu solder wire. This improved creep resistance can be explained by the microstructure change of Cu_6Sn_5 IMCs with TSP addition.

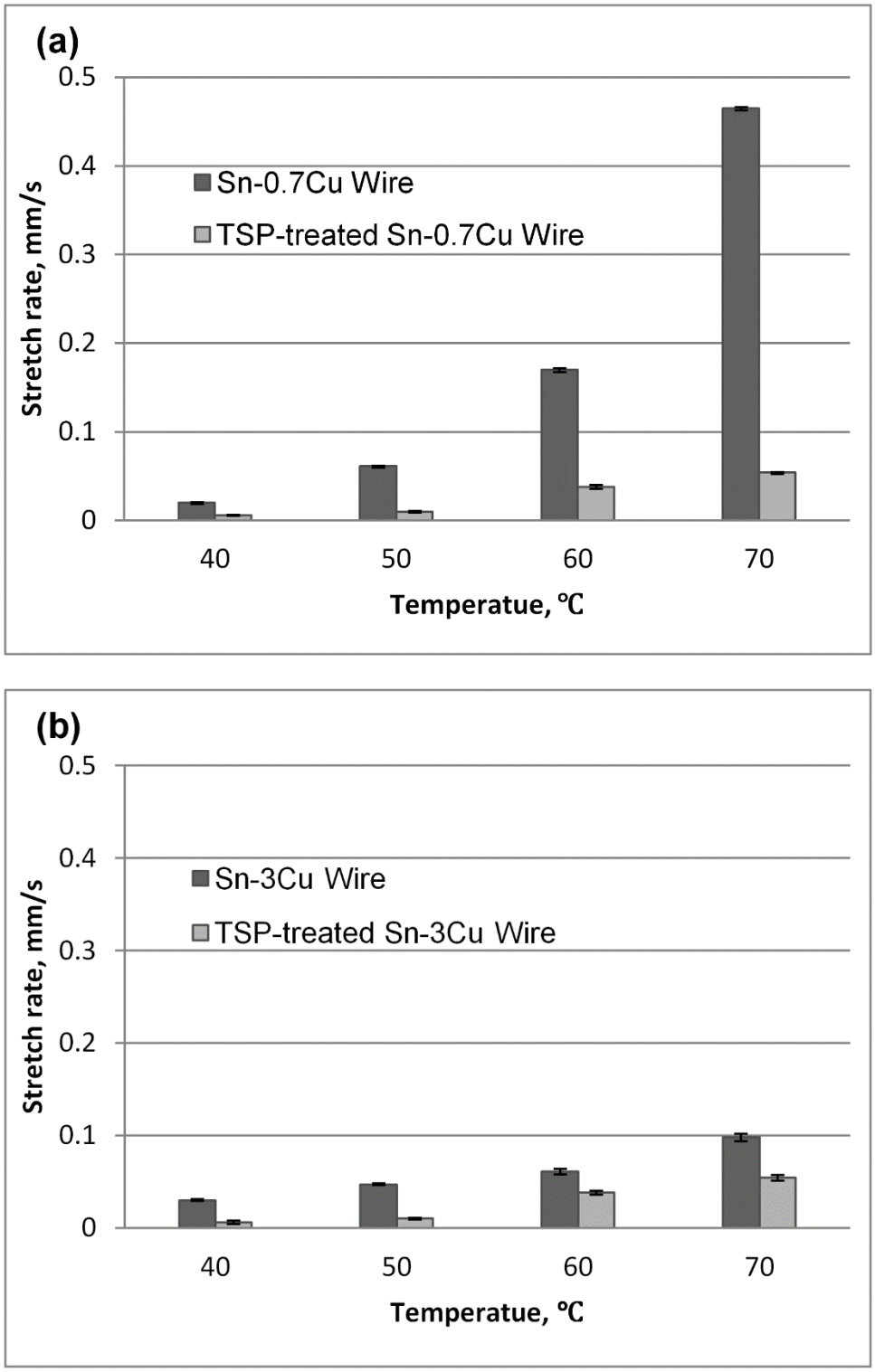

Figure 2-2 Stretch Rates at Various Temperatures: (a) Sn-0.7Cu Wire without and with TSP Additions and (b) Sn-3Cu Wire without and with TSP Additions.

2.3.2 Microstructure

TSP addition to the solder refined the intermetallic compound in the solder matrix. The microstructure of eutectic Sn-0.7Cu solder was shown in Figure 2-3 (a) with dot-shaped Cu_6Sn_5 IMC particles embedded in Sn-rich matrix, whereas the microstructure of hypereutectic Sn-3Cu solder was shown in Figure 2-3 (b) with proeutectic rod-shaped Cu_6Sn_5 phase and eutectic constituent. Figure 2-2 showed that the creep resistance of Sn-3Cu wire was much higher than Sn-0.7Cu. This can be explained by the presence of the large and rod-shaped IMCs in Figure 2-3 (b), which hindered dislocation climb and improved the steady-state creep.

Under the same wire extruding conditions, Cu_6Sn_5 IMC particles in both TSP-treated Sn-Cu alloys appeared to be smaller and well distributed as compared to control, as shown in Figure 2-3 (c) and 2-3 (d). TSP-treated Sn-Cu alloys with smaller IMCs and closer spacing between IMCs exhibited higher resistance to creep. Cu_6Sn_5 IMC particles size in Sn-3Cu was larger than those in Sn-0.7Cu, resulting in less improvement of creep resistance for Sn-3Cu with TSP incorporation as compared to Sn-0.7Cu.

The addition of TSP also caused a refined Sn-rich morphology in eutectic Sn-0.7Cu. Comparing Figure 4a with Figure 4c, the Sn-rich grain size in TSP-treated Sn-0.7Cu was smaller than that in Sn-0.7Cu control. Based on how paths change during diffusion creep, diffusion creep can be classified into two main classes: Nabarro-Herring creep and Coble creep, where the diffusion paths in Nabarro-Herring creep are predominantly through the main body of the grains at relative high temperature, and the diffusion paths in Coble creep are predominantly through the grain boundaries at relative low temperature. With TSP addition, both the finely dispersed IMC particles within Sn-rich grains and the refined Sn-rich grains improved creep resistance, especially for Sn-0.7Cu, suggesting that the dominance of diffusion creep in Sn-Cu system is supported by Nabarro-Herrring creep. Nevertheless, the improved creep resistance for both Sn-0.7Cu and Sn-

3Cu was attributed to the smaller IMCs and closer spacing between IMCs with TSP incorporation. This changed microstructure can be explained by thermal analysis.

2.3.3 Solidification of Eutectic Constituent

The addition of TSP reduced the extent of undercooling for eutectic solidification reaction in both Sn-0.7Cu and Sn-3Cu. Effect of TSP addition on the eutectic solidification reaction of Sn-0.7Cu and Sn-3Cu were examined using Differential Scanning Calorimetry (DSC). Table 2-1 listed the values of the crystallization temperature, Tc, the melting temperature, Tm, and the undercooling, ΔT, where Tc denoted the onsite of the exothermic solidification peak, T_m denoted onsite of the endothermic melting peak, and ΔT was equal to the difference between Tm and Tc. The melting temperature of eutectic constituent in Sn-0.7Cu and Sn-0.3Cu appeared at 226°C. The melting temperature of eutectic constituent in both alloys did not change with TSP addition. The extent of undercooling, which was determined by the difference between the melting temperature and the cooling temperature, was used to quantify the solidification behavior.

Table 2-1 Comparison of Solidification Temperature, Melting Temperature, and Undercooling for Sn-Cu Wires.

	Tc (°C)	Ts (°C)	Tm (°C)	ΔT (°C)
Sn-0.7Cu	-	202.1	226.5	24.3
TSP-treated Sn-0.7Cu	-	20.8	226.5	21.7
Sn-3Cu	318.9	198.4	226.3	27.9
TSP-treated Sn-3Cu	313.1	217.3	226.3	8.9

*Tc: formation temperature of the proeutectic constituent
Ts: solidification temperature of the eutectic constituent
Tm: melting temperature of the eutectic constituent
ΔT: undercooling for eutectic solidification reaction, Tm-Tc

Based on classical nucleation theory, the additional undercooling supplies a driving force to overcome free energy barrier during solidification reaction. In Table 2-1, the undercooling of

Sn-0.7Cu and Sn-3Cu was around 24 and 28, respectively. These results suggested that eutectic solidification reaction was not affected by the presence of proeutectic Cu_6Sn_5 IMCs, as Sn-0.7Cu is a near eutectic, while Sn-3Cu is hypereutectic. However, the undercooling of TSP-treated Sn-Cu solder alloys for eutectic reaction was reduced in both. These results suggested that TSP addition decreased the interfacial energy between solid and liquid, lowered the energy barrier, and thus aided nucleation of IMCs as nucleation sites during eutectic reaction. Effect of TSP addition on eutectic reaction in Sn-3Cu was significant, which was consistent with results of optical microscopy showing presence of micron-size Cu_6Sn_5 in Sn-rich grains. That indicated that TSP could act as heterogeneous nucleation sites to improve nucleation rate of eutectic reaction and affect the size and spatial distribution Cu_6Sn_5 IMCs.

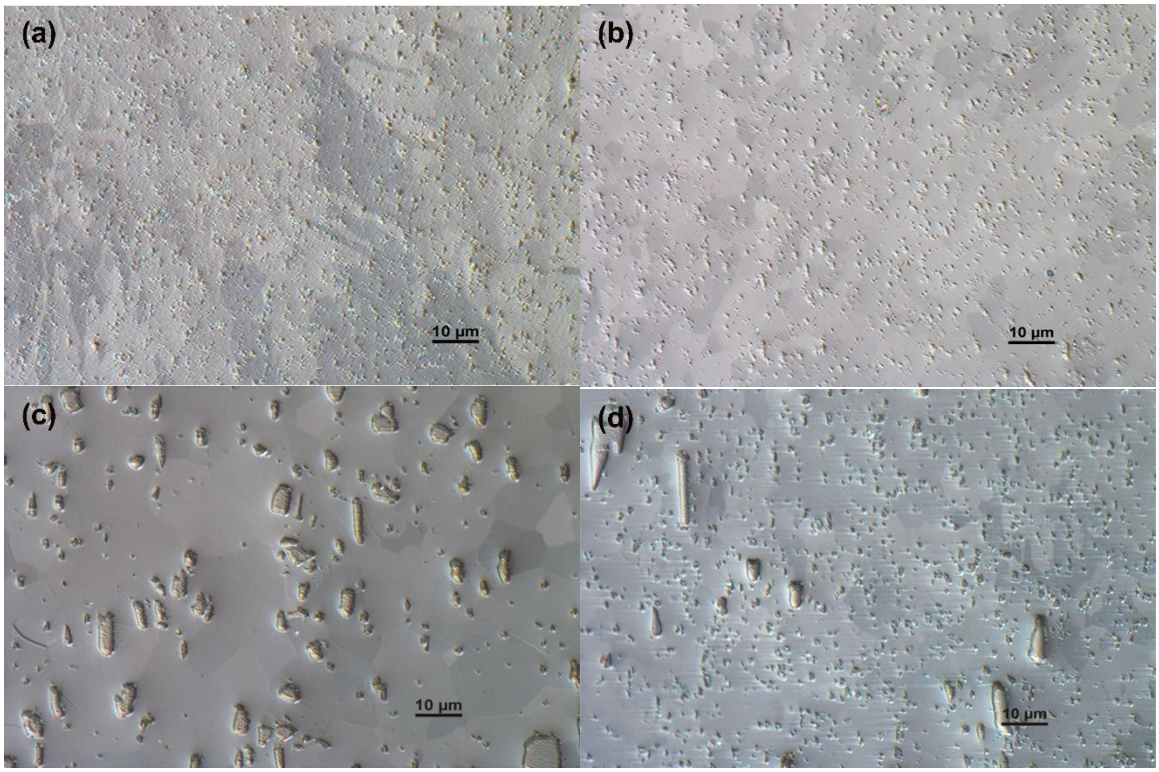

Figure 2-3 Polarized Optical Micrographs of Sn-Cu Solder Wires: (a) Sn-0.7Cu Wire, (b) TSP-treated Sn-0.7Cu Wire, (c) Sn-3Cu Wire, and (d) TSP-treated Sn-3Cu Wire.

2.3.4 Indentation Microhardness

The addition of TSP improved microhardness of both Sn-0.7Cu and Sn-3Cu wires. Knoop hardness values of solder wires made of both Sn-0.7Cu and Sn-3Cu without and with TSP addition were shown in Figure 2-4. Similar hardness values were observed between Sn-0.7Cu and Sn-3Cu, suggesting hardness of Sn-Cu is more sensitive to the microstructure of Sn-rich grains than IMC distribution. Hardness of Sn-3Cu wire increased from 11.9 to 13.1 H_k with TSP incorporation (about 12% improvement). Increase in hardness due to TSP addition in Sn-0.7Cu was about one-half of that in Sn-3Cu. It is clear from indentation microhardness test that the addition of TSP enhances the microhardness of both Sn-0.7Cu and Sn-3Cu wires. These results were also consistent with our previous study on eutectic Sn-Ag[75]. The observed improvement in strength of TSP-treated Sn-Cu wires was further explained by the microstructure change of Sn-rich grains.

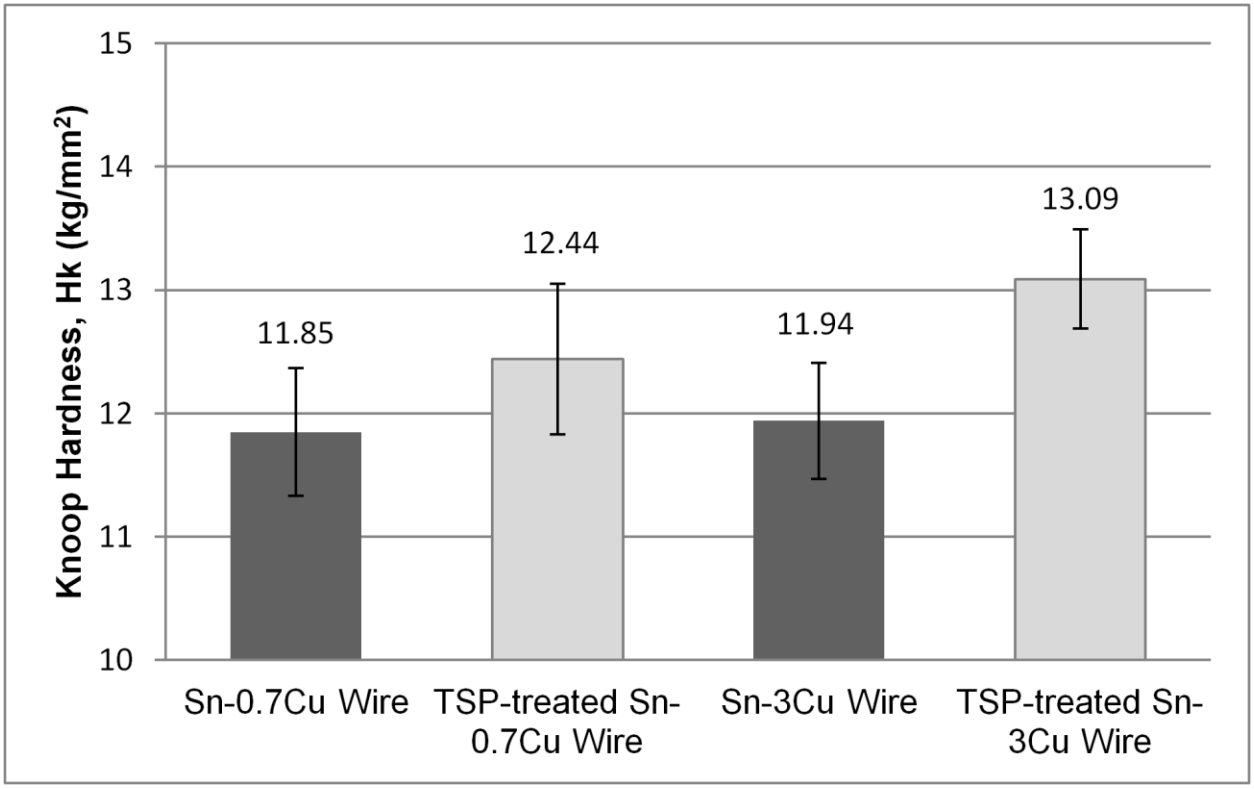

Figure 2-4 Knoop Hardness Values of Sn-Cu Wires.

2.3.5 EBSD Results on Tin-rich Grains

TSP addition showed significant effect on the refinement of Sn-rich phase. Figures 8a and 8b were the EBSD Sn crystal c-axis orientation map of solder wires made of Sn-0.7Cu without and with TSP addition. Sn-0.7Cu wire, as shown in Figure 2-5 (a), exhibited a non-uniform grain size distribution due to extrusion process. Under the same extruding process, Sn-0.7Cu wire with TSP addition in Figure 2-5 (b) exhibited a more uniform grain size distribution as compared to control. The EBSD Sn c-axis orientation maps of solder wires made of Sn-3Cu without and with TSP addition were shown in Figure 2-5 (c) and 2-5 (d), respectively. Sn-3Cu wire exhibited a more uniform grain size distribution as compared to Sn-0.7 due to the presentence of proeutectic Cu_6Sn_5 phase. However, average size of Sn-rich grains in Sn-3Cu was reduced with TSP incorporation.

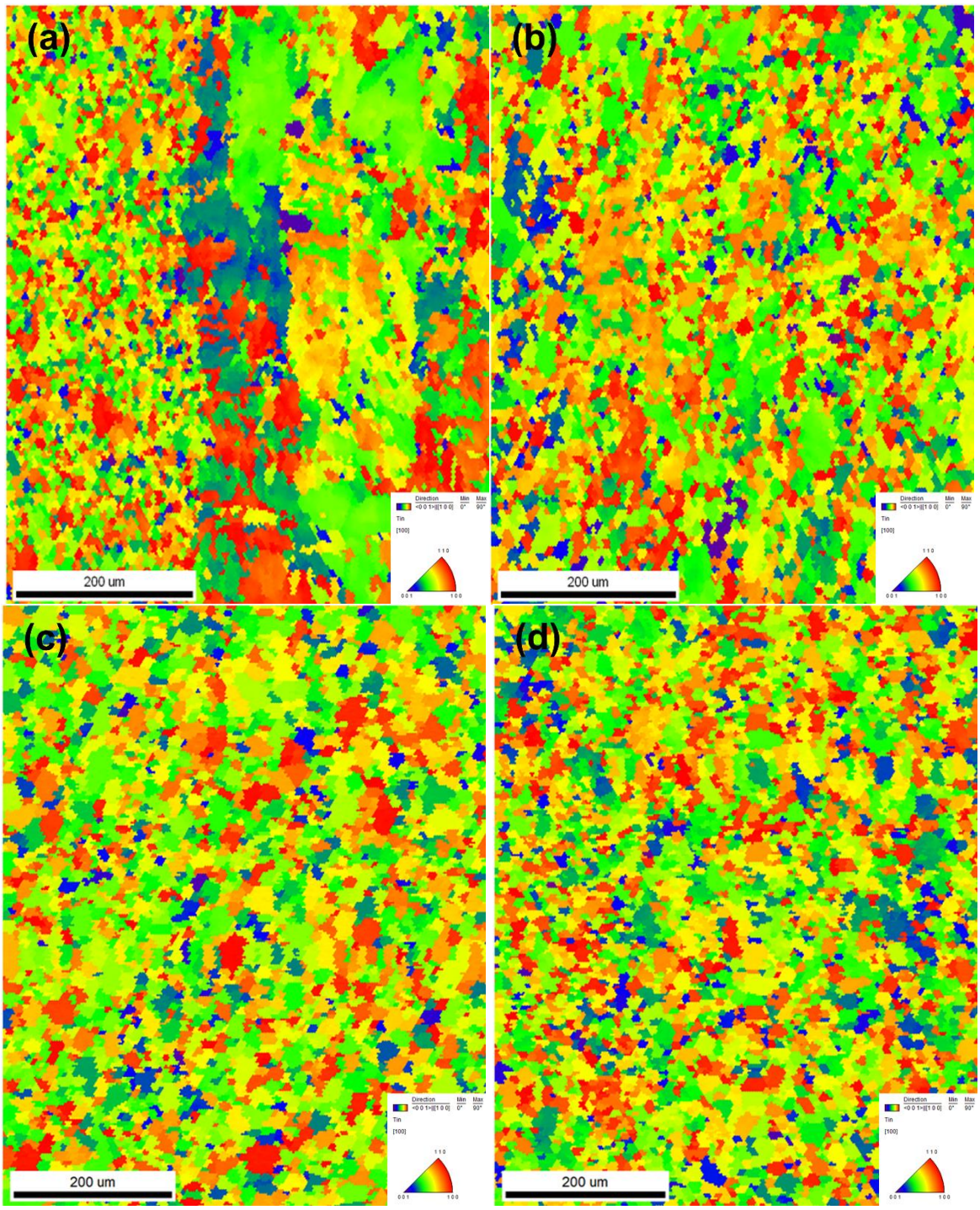

Figure 2-5 C-axis orientation maps of Sn-Cu solder wires: (a) Sn-0.7Cu wire, (b) TSP-treated Sn-3Cu wire, (c) Sn-3Cu wire, and (d) TSP-treated Sn-3Cu wire

These results corresponded well with the Hall-Petch equation which gives the relationship between the yield strength σ_y and grain size:

$$\sigma_y = \sigma_0 + k_y d^{-1/2} \qquad (1)$$

where d is the average grain diameter, and σ_0 and k_y are constants. Therefore, the reduced grain size can be explained by the improvement of strength with TSP incorporation. The reinforcement mechanism of lead-free solder by TSP in previous study[75] was proposed that the improvement of thermomechanical fatigue performance results from the grain boundary pinning effect of TSP. In this study, effect of TSP on the strength of Sn-Cu solid solder wire also supports the proposed reinforcement mechanism.

2.3.6 Texture of Tin-rich Grains

The texture intensity of both Sn-0.7Cu and Sn-3Cu wires was reduced with TSP incorporation. Both discrete and density pole figures in Figure 2-6 were plotted from the Sn c-axis orientation maps in Figure 2-5. The pole figures in Figure 2-6 (a) showed that observed orientations were represented by a cluster of poles near upper left of the (001) discrete pole figure and a maximum value of 7.079 in the (001) density pole figure, indicating a preferred crystal orientation. With TSP addition, the texture intensity was reduced from 7.079 to 6.042, as shown in Figure 2-6 (b). Similarly, the pole figures in Figure 2-6 (c) showed that observed orientations were represented by a cluster of poles near lower left of the (001) discrete pole figure and a maximum value of 10.343 in the (001) density pole figure, indicating a strongly preferred crystal orientation. With TSP addition, the texture intensity was reduced from 10.343 to 6.314, as shown in Figure 2-6 (d). The reduced texture intensity of both Sn-0.7Cu and Sn-3Cu wires can be attributed to the changed microstructure, size, and spatial distribution of Sn-rich grains and Cu_6Sn_5 IMCs with TSP incorporation.

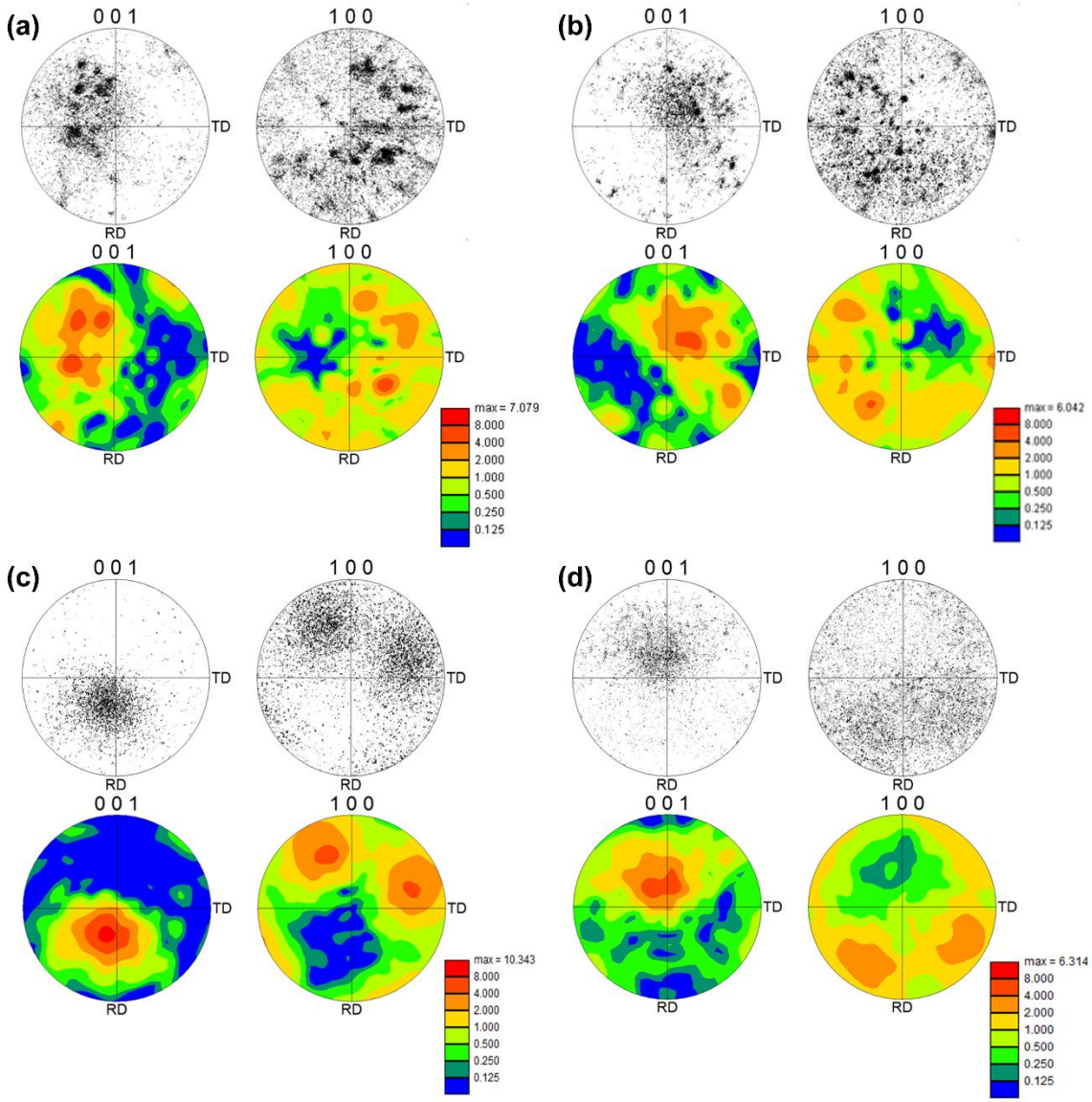

Figure 2-6 (001) and (100) discrete and density pole Fig.s of Sn-Cu solder wires: (a) Sn-0.7Cu wire, (b) TSP-treated Sn-3Cu wire, (c) Sn-3Cu wire, and (d) TSP-treated Sn-3Cu wire

2.4 Conclusions

In summary, sets of experiments were carried out on both nearly eutectic Sn-0.7wt%Cu and hypereutectic Sn-3wt%Cu solid solder wires to identify the effect of nanostructured silanols addition on creep resistance and microstucture of Sn-Cu solder wires. The following conclusions can be made from the current work:

1. The extent of undercooling for eutectic solidification reaction was reduced for both Sn-Cu wires with TSP addition, affecting the microstructure, size and spatial distribution, of Sn-rich grains and Cu_6Sn_5 IMCs.
2. Addition of TSP improved uniformity of Sn-rich grains and reduced the texture intensity of Sn-rich grains of both Sn-Cu wires.
3. Addition of TSP reduced size and improved spatial distribution of Cu_6Sn_5 IMCs in both Sn-Cu wires.
4. The decreasing size of Sn-rich grains was due to the grain boundary pinning effect of TSP, whereas nano-sized cage structure of -Si-O-Sn served as heterogeneous nucleation sites for Cu_6Sn_5 IMCs to reduce IMC size and improve IMC distribution.
5. These microstructure changes in Sn-0.7Cu significantly improved its creep resistance, with minimal increase in hardness, while in Sn-3Cu significantly increased the hardness, with minimal increase in creep resistance.

Chapter 3 Sn-based Ternary Alloys

3.1 Background

To further improve mechanical properties of cast alloys, the evolution of secondary phases, such as precipitates or IMCs, also needs to be fully optimized. Because some properties, such as strength, stiffness, creep, and fatigue, strongly depend on the microstructure of secondary phase. In previous study, TSP is added into Sn-Cu binary alloys to improve creep resistance of solid solder wires. The improved creep behavior is due to the controllable size and distribution of IMCs in Sn-Cu alloys with TSP additions.

Sn-rich ternary alloys have attracted considerable attention due to their good solderability and wetting properties. It is important to inverstiage how TSP additions affect their as-cast microstructure as well as creep resistatance.

Many Sn based ternary alloy systems with different alloying elemnts such as Ag, Cu, Zn, and Sb have been developed.

The secondary creep state or steady state is of the greatest engineering importance since in this regime plastic flow will occur while the stress and temperature are held constant and the strain rate (dƐ/dt) dependence can be expressed as the following equation describes:

$$\frac{d\varepsilon}{dt} = A\,\sigma^{n} e^{-\frac{Q}{RT}} \qquad \text{equation 3-1}$$

where σ is the applied stress, ‘n’ is the stress exponent, and ´Q´ is the activation energy. The value of stress exponent, n, is related to operative creep mechanisms, while the activation energy, Q, correlates to the activation energy for diffusion.

3.2 Experimental

3.2.1 Preparation of Solid Wires

TriSilanolphenyl Polyhedral Oligomeric Silsesquioxane (TSP), obtained from Hybrid Plastics, Inc. (Hattiesburg, MS), was used in this study as nano-structured modifier. Pure tin and three ternary alloys were manufactured by Johnson Manufacturing with their standard industrial alloy practice as shown in Table 3-1. For a comparative study of creep resistance and microstructures of 0.5%TSP-treated alloys were prepared using the same alloying approach. All alloys with and without 0.5wt% TSP addition were cast to 38 mm by 178 mm billet form according to the established ISO procedures by Johnson Manufacturing. 0.8 mm diameter solid solder wires were then extruded from billet using a 100 Ton Collin Press.

Table 3-1 Chemical Composition in wt% of All Wires.

Material	Cu	Ag	Sb	Zn	Sn
Pure Sn	-	-	-	-	99.9
Sn-4.7Ag-1.7Cu	1.7	4.7	-	-	Balance
Sn-3.5Cu-7.5Sb	3.5	-	7.5	-	Balance
Sn-15Cu-3Zn	15	-	-	3	Balance

3.2.2 Coil Creep Testing

The creep behavior of solder wires was characterized by coil creep test. A 20-turn coil of solder wire was wound on a cylindrical aluminum tube with 25.4 mm in diameter as shown in Figure 2-1 (a). The creep test of a self-loaded coil in Figure 2-1 (b) was conducted in a temperature-controlled column. Different temperatures were used to keep the testing temperature within 0.4-0.7 range of their melting temperatures. Stretch rate was evaluated through dividing the spacing between the 1^{st} and the 10^{th} turns by time at specific temperature for all wires, which

can be used as an indicator of creep rate. To evaluate the stress exponent ´n´ and the activation energy ´Q´ of different alloys, ln (strain rate) was plotted against ln (σ) to generate a set of data points on the graph, with a linear regression, the gradient of the straight line would be n - the stress exponent. Similarly, by plotting ln (strain rate) against the reciprocal of temperature, the gradient of the plot should be - Q/R. Using this method, activation energy of each material could be obtained from the plot.

3.2.3 Polarized Optical Microscopy

Four pieces of each specimen were cut from four different regions and mounted with epoxy resins in such a way that wires orientated in the extrusion direction. The wire mount was ground until wire surface reached the center, and then polished. Polarized optical micrographs were taken using an inverted metallographic microscope, Nikon ECLIPSE MA200.

3.3 Results and Discussions

3.3.1 Pure Tin

The addition of TSP improved creep resistance of pure Sn wires dramatically. Stretch rates of Sn wires with and without TSP additions at two temperatures were plotted in Figure 3-1. The stretch rate of tin wires at two different temperatures was reduced due to the addition of TSP. As it can be observed in Table 3-2, the calculated stress exponents are between 2 and 6, which is consistent with the fact that this is dislocation creep. However, TSP additions increase creep activation energy from 2.4 to 85.2 KJ/mol, resulting in high creep resistance.

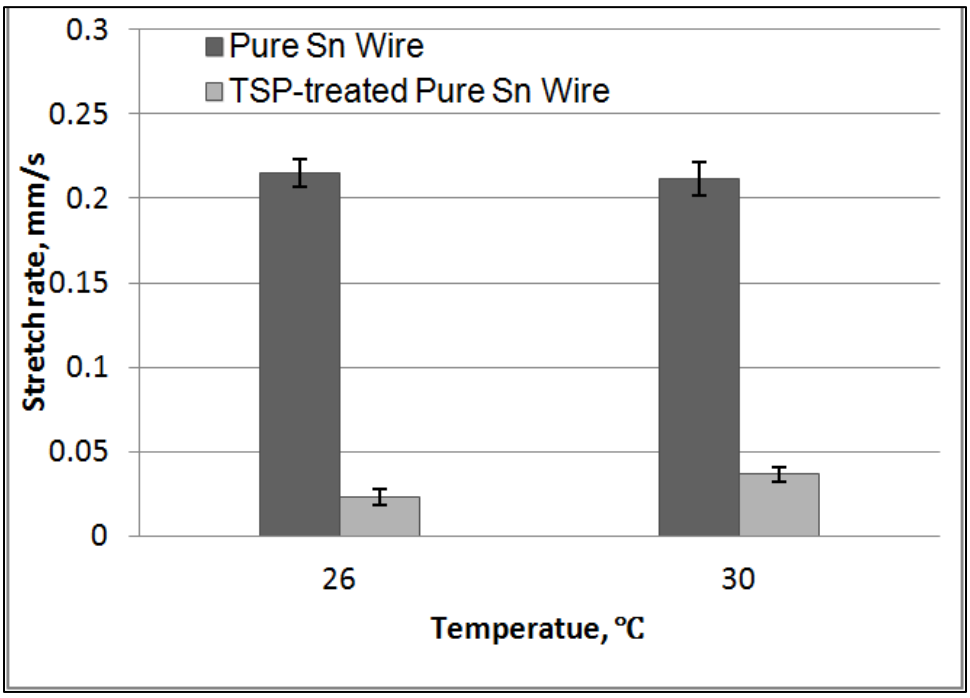

Figure 3-1 Stretch Rates of Pure Sn and TSP-treated Sn Wires at Various Temperatures.

Table 3-2 Stress Exponent and Activation Energy of Pure Sn and TSP-treated Sn Wires.

Material	Temperature (°C)	Stress Exponent	Activation Energy (KJ/mol)
Pure Sn	26	6.1	2.4
	30	5.6	
TSP-treated Sn	26	2.8	85.2
	30	2.7	

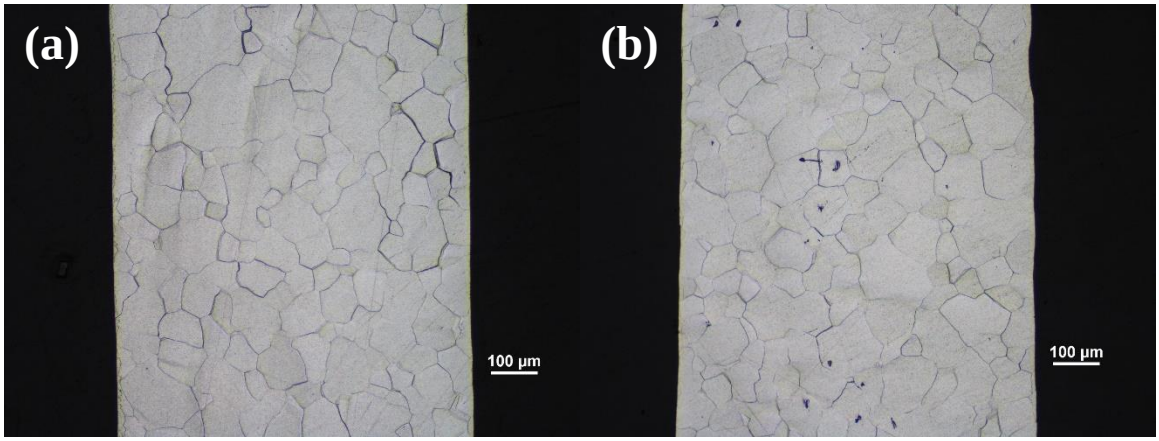

Figure 3-2 Optical Micrographs of Pure Tin Solder Wires: (a) Pure Sn Wire and (b) TSP-treated Sn Wire.

Figure 3-2 shows the microstructure of pure Sn wires with and without TSP additions. As it is a pure material, pure Sn, all the grains that appear on the image are Sn grains with different grain size. Analyzing the modified sample, it can be observed almost no variation on the microstructure of Sn.

3.3.2 Sn-Ag-Cu Alloys

The addition of TSP also improved creep resistance of Sn-Ag-Cu ternary wires dramatically. Stretch rates of Sn-4.7Ag-1.7Cu wires with and without TSP additions at four temperatures were plotted in Figure 3-3. The stretch rate of tin wires at four different temperatures was reduced due to the addition of TSP. As it can be observed in Table 3-3, the calculated stress exponent is about 1 in all the samples, which is consistent with the fact that it is diffusion creep, being the main mechanism is these solder specimens over this temperature range. However, TSP additions increase creep activation energy from 62.4 to 150.7 KJ/mol, resulting in high creep resistance.

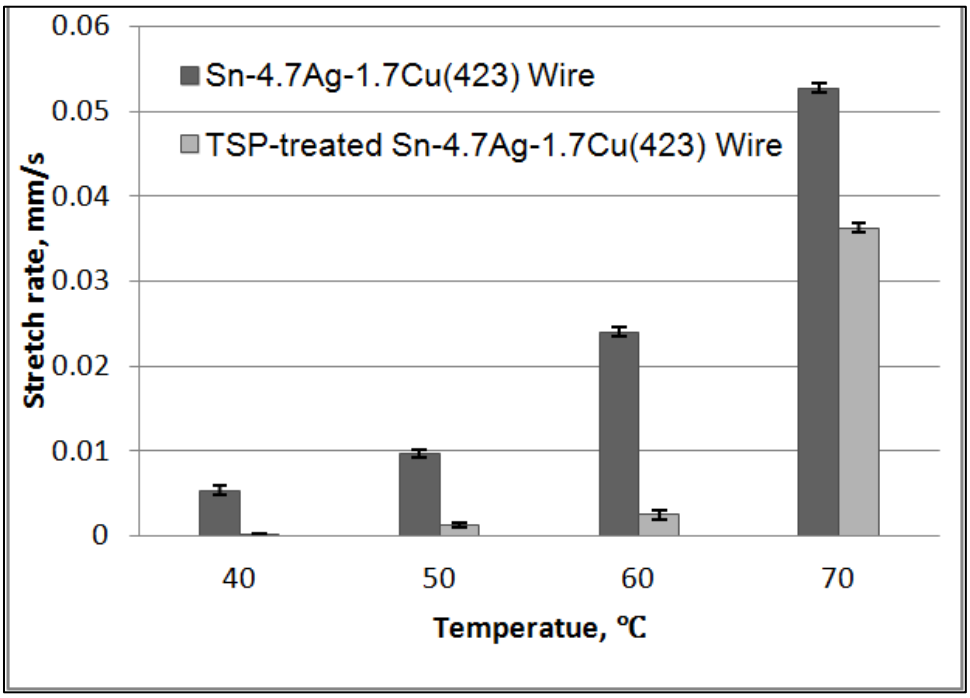

Figure 3-3 Stretch Rates of Sn-4.7Ag-1.7Cu and TSP-treated Sn-4.7Ag-1.7Cu Wires at Various Temperatures.

Table 3-3 Stress Exponent and Activation Energy of Sn-4.7Ag-1.7Cu and TSP-treated Sn-4.7Ag-1.7Cu Wires.

Material	Temperature (^{o}C)	Stress Exponent	Activation Energy (KJ/mol)
Sn-4.7Ag-1.7Cu	40	0.6	62.4
	50	0.7	
	60	0.6	
	70	0.8	
TSP-treated Sn-4.7Ag-1.7Cu	40	1.0	150.7
	50	1.9	
	60	1.8	
	70	1.0	

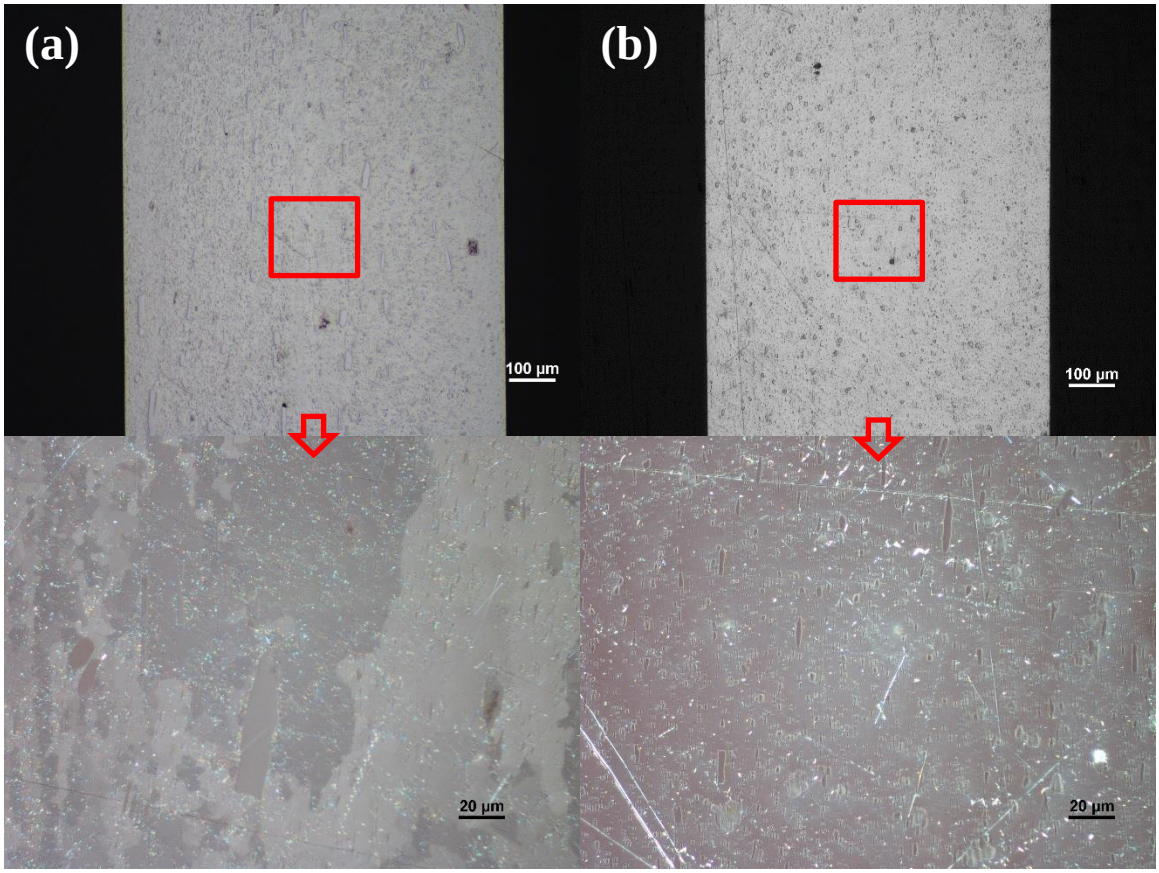

Figure 3-4 Optical Micrographs of Sn-4.7Ag-1.7Cu Solder Wires: (a) Sn-4.7Ag-1.7Cu Wire and (b) TSP-treated Sn-4.7Ag-1.7Cu Wire.

Figures 3-4 illustrates the microstructure of Sn-4.7Ag-1.7Cu wires with and without TSP additions. Three phases were observed in Sn-4.7Ag-1.7Cu wire. The primary Sn phases, Cu6Sn5 and Ag3Sn intermetallic compounds. With TSP additions, both grain size of primary Sn and IMCs size decreased. This refinement with TSP additions is associated with the increased activation energy and creep resistance.

3.3.3 Sn-Cu-Sb Alloys

The addition of TSP improved creep resistance of Sn-Cu-Sb ternary wires dramatically. Stretch rates of Sn-3.5Cu-7.5Sb wires with and without TSP additions at four temperatures were plotted in Figure 3-5. The stretch rate of Sn-Cu-Sb wires at four different temperatures was reduced due to the addition of TSP. As it can be observed in Table 3-4, the calculated stress

exponent is about 1 in all the samples, which is consistent with the fact that it is diffusion creep, being the main mechanism is these solder specimens over this temperature range. However, TSP additions increase creep activation energy from 111.6 to 123.7 KJ/mol, resulting in high creep resistance.

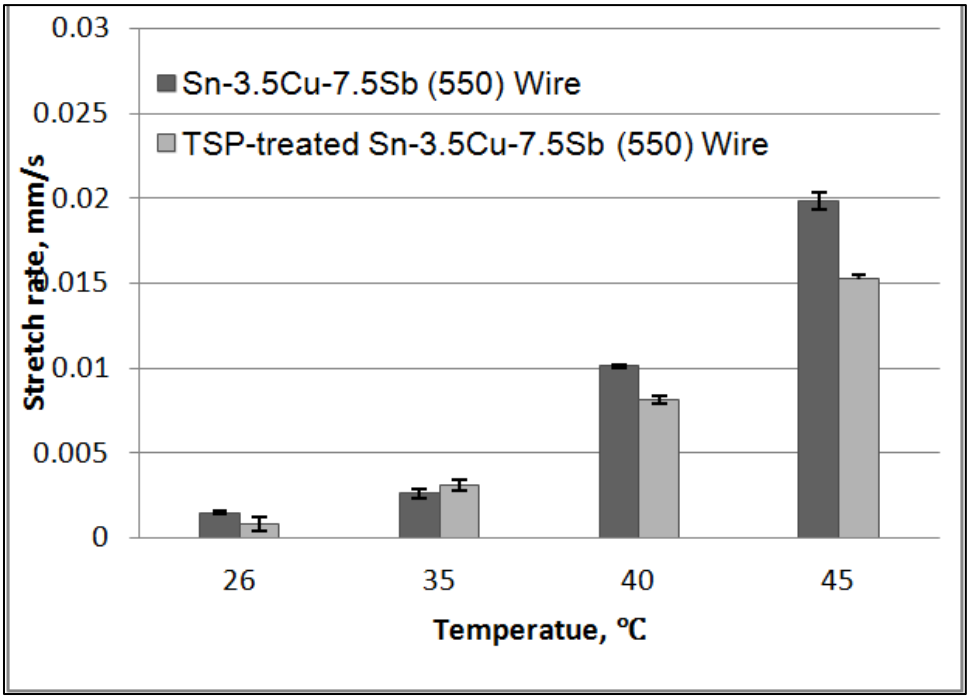

Figure 3-5 Stretch Rates of Sn-3.5Cu-7.5Sb and TSP-treated Sn-3.5Cu-7.5Sb Wires at Various Temperatures

Table 3-4 Stress Exponent and Activation Energy of Sn-3.5Cu-7.5Sb and TSP-treated Sn-3.5Cu-7.5Sb Wires.

Material	Temperature (°C)	Stress Exponent	Activation Energy (KJ/mol)
Sn-3.5Cu-7.5Sb	26	1.2	111.6
	35	1.0	
	40	1.0	
	45	1.6	
TSP-treated Sn-3.5Cu-7.5Sb	26	0.9	123.7
	35	0.7	
	40	1.2	
	45	1.6	

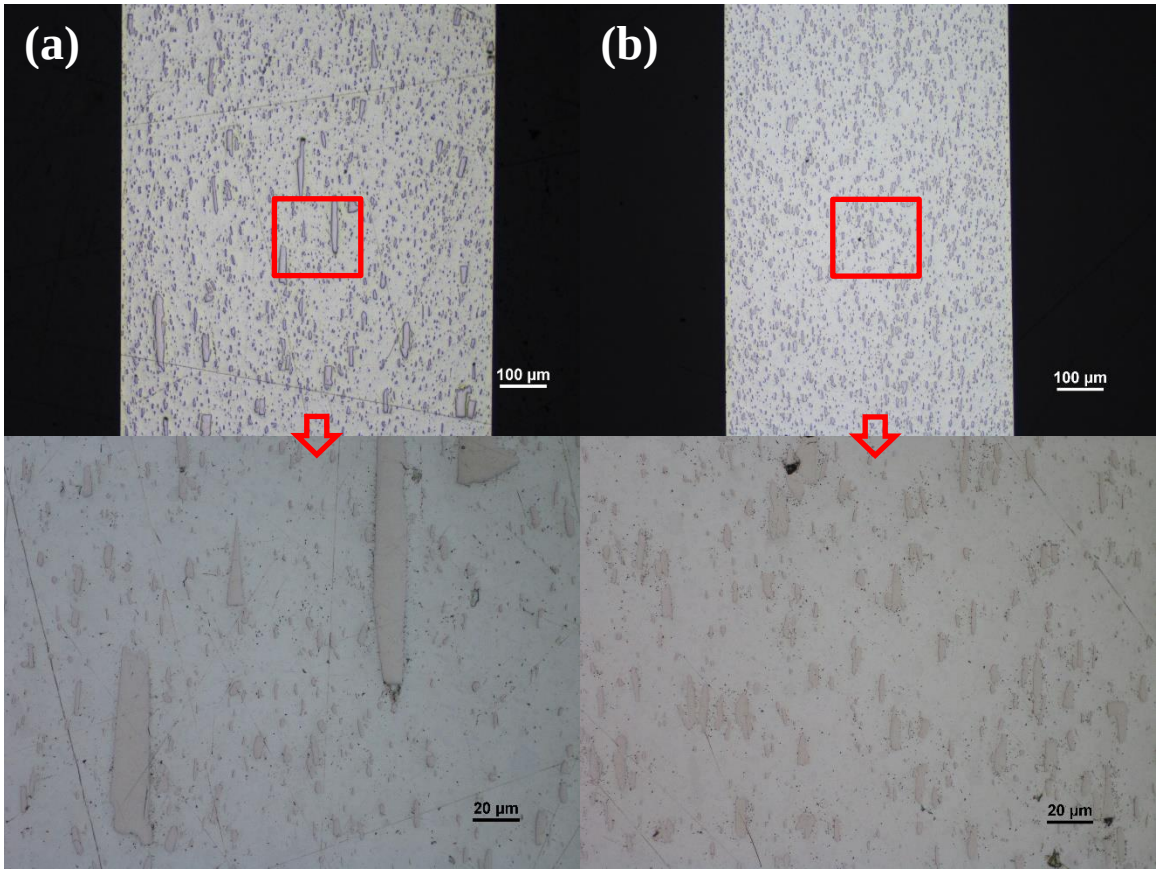

Figure 3-6 Optical Micrographs of Sn-3.5Cu-7.5Sb Solder Wires: (a) Sn-3.5Cu-7.5Sb Wire and (b) TSP-treated Sn-3.5Cu-7.5Sb Wire.

Figures 3-6 illustrates the microstructure of Sn-3.5Cu-7.5Sb wires with and without TSP additions. Three phases were observed in Sn-3.5Cu-7.5Sb wire. The primary Sn phases, Cu3Sn and SbSn3 intermetallic compounds. With TSP additions, both grain size of primary Sn and IMCs size decreased. This refinement with TSP additions is associated with the increased activation energy and creep resistance.

3.3.4 Sn-Cu-Zn Alloys

The addition of TSP reduced creep resistance of Sn-Cu-Zn ternary wires. Stretch rates of Sn-15Cu-3Zn wires with and without TSP additions at three temperatures were plotted in Figure 3-7. The stretch rate of Sn-Cu-Zn wires at four different temperatures was increased due to the addition of TSP. As it can be observed in Table 3-5, the calculated stress exponent is about 1 in

all the samples, which is consistent with the fact that it is diffusion creep, being the main mechanism is these solder specimens over this temperature range. However, TSP additions decrased creep activation energy from 118.7 to 88.7 KJ/mol, resulting in low creep resistance.

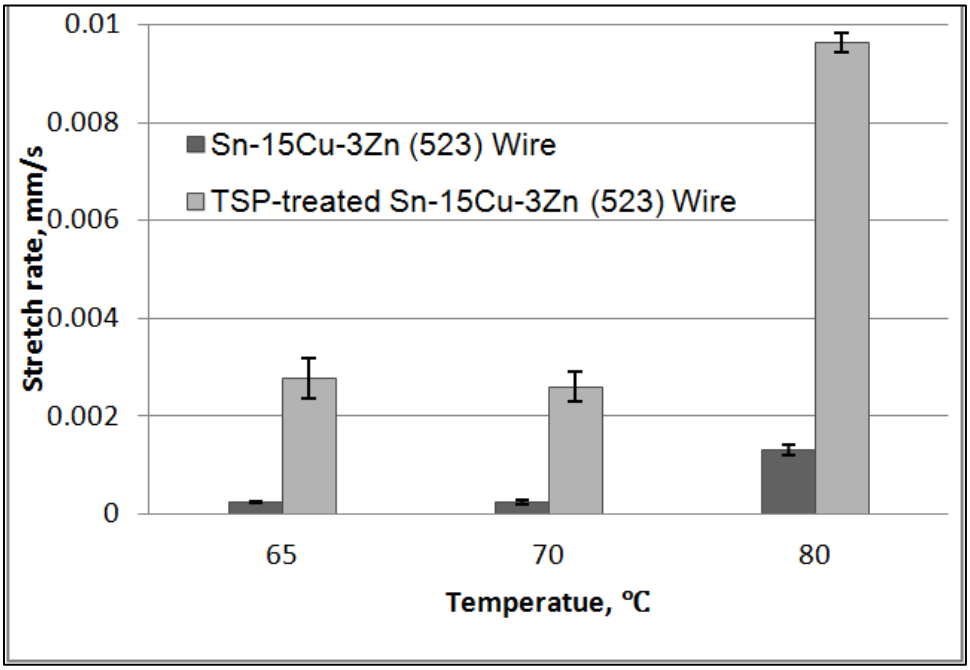

Figure 3-7 Stretch Rates of Sn-15Cu-3Zn and TSP-treated Sn-15Cu-3Zn Wires at Various Temperatures.

Table 3-5 Stress Exponent and Activation Energy of Sn-15Cu-3Zn and TSP-treated Sn-15Cu-3Zn Wires.

Material	Temperature (^{o}C)	Stress Exponent	Activation Energy (KJ/mol)
Sn-15Cu-3Zn	65	0.8	118.7
	70	0.8	
	80	0.8	
TSP-treated Sn-15Cu-3Zn	65	0.3	88.8
	70	0.6	
	80	0.8	

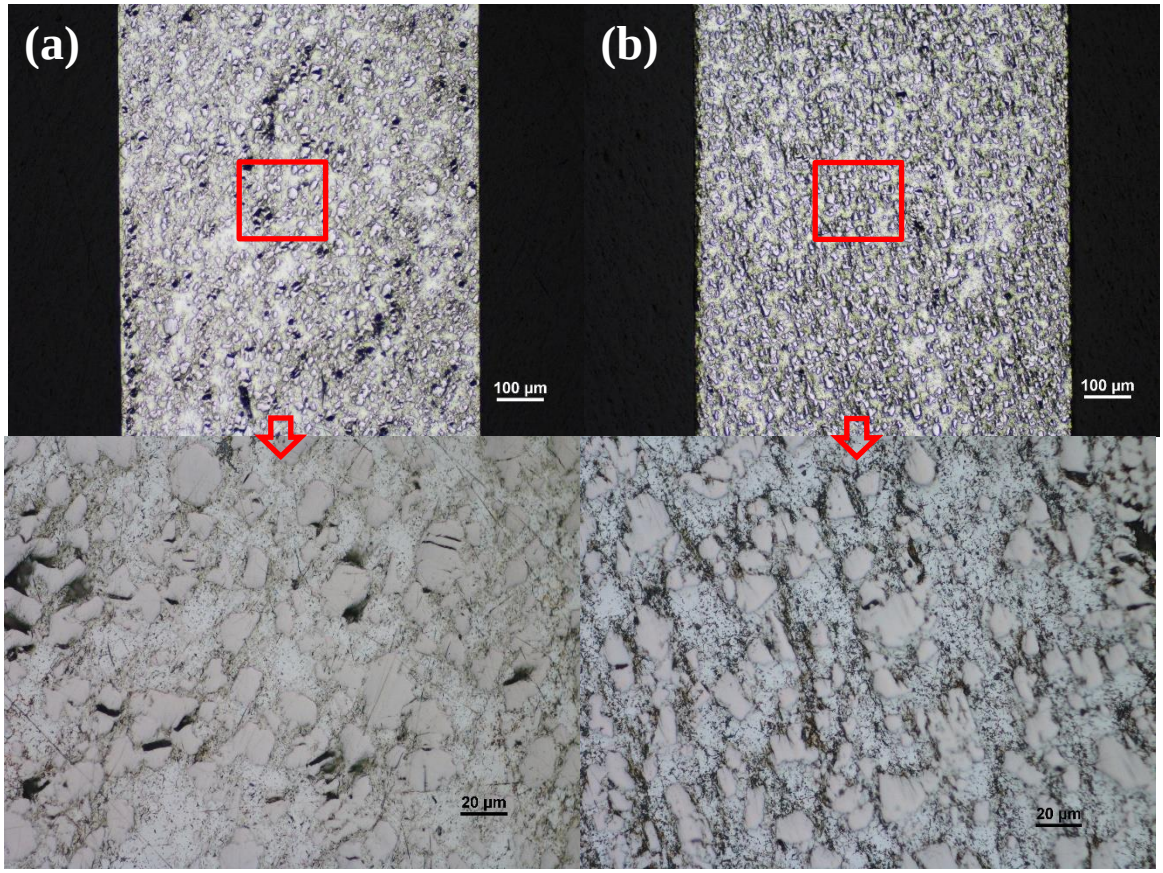

Figure 3-8 Optical Micrographs of Sn-15Cu-3Zn Solder Wires: (a) Sn-15Cu-3Zn Wire and (b) TSP-treated Sn-15Cu-3Zn Wire.

Figures 3-8 illustrates the microstructure of Sn-15Cu-3Zn wires with and without TSP additions. Three phases were observed in Sn-15Cu-3Zn wire: primary Sn and (Cu,Zn)3Sn phases. With TSP additions, (Cu,Zn)3Sn size become smaller. This refinement with TSP additions is associated with the reduced activation energy and creep resistance.

3.4 Conclusions

TSP additions improved creep activation energy of pure tin, Sn-Ag-Cu and Sn-Cu-Sb alloys without altering the creep deformation mechanism. The improved creep resistance with TSP additions for Sn-Ag-Cu and Sn-Cu-Sb ternary alloys is due to refined secondary phases. TSP additions also caused the refinement of the secondary phase of Sn-Cu-Zn alloys, however, the refined microstructure causes the reduction of creep resistance.

Chapter 4 Al-12Si Alloys with TSP Treatment

4.1 Background

Aluminum silicon based casting alloys have structural applications that are directly linked their light-weight and low life-cycle costs, in industries such as automotive, military, aerospace, and alternative energy [1, 4]. However, conventional Al-Si based casting alloys exhibit low ductility as a concession for high strength, since the presence of irregular flakes like eutectic Si crystals in the as-cast condition promote crack initiation and propagation.

In order to improve the overall mechanical performance of cast aluminum alloys, chemical modifiers, such as Na [45], Sr [50, 52], Ba [46], P [104], and Ti/ B [105], are added into alloys in trace levels to modify the microstructure morphology. For example, the presence of Sr changes the morphology of eutectic Si crystals from flaky to fibrous form. However, the fading and poisoning effects of Sr additions remain two major concerns in industrial practice [56]. Specifically, the microstructure of a Sr-modified Al-Si alloys cannot be maintained after the second melt, which is referred to as fading. Other trace elements have been used to improve the performance of cast aluminum alloys, i.e. Ti and B were used to refine the primary Al phase in hypoeutectic Al-Si [105], while P was used to refine the primary Si phase in hypereutectic Al-Si [104]. However, the effectiveness of eutectic modifiers can be diminished if a hypo/hypereutectic modifier is present, i.e. P can coarsen the eutectic structure by reacting with Sr [56]. This poisoning issue of extraneous reactions, due to the presence of trace elements in Al-Si based alloys, limits their potential in applications. Therefore, there is a need for a universal modifier that can be used in a larger range of Si contents to change the morphology of Al-Si based casting alloys and enhance their ductility.

The objective in this chapter is to investigate if TSP can serve a purpose similar to the commonly used chemical modifiers without the disadvantage of the potential “fading” and

"poisoning" issues from other elements. To test this hypothesis, the TSP-treated Al-12Si powders were melted and cast into ingots. Solidification, microstructure, and mechanical properties were evaluated.

4.2 Experimental

4.2.1 Materials

SO1458-trisilanolphenyl polyhedral oligomeric silsesquioxane (Ph-TSP), obtained from Hybrid Plastics, Inc. (Hattiesburg, MS), was used in this study. The 50 μm A4047 powder, with a nearly eutectic composition (nominal wt. %) of Al-12Si, was manufactured by Johnson Manufacturing (Princeton, IA).

4.2.2 Surface Treatment of A4047 powders

To treat the A4047 powders with TSP, the oxides from the powder surfaces were first removed by soaking the powder in 8 wt% HCl for 5 minutes at room temperature. The clean powers then were soaked in 1wt%TSP ethanol solutions for 24 hours to get the TSP-treated powders.

4.2.3 Preparation of A4047 Ingots

Dried TSP-treated A4047 powders were melted at 1088 K (815°C). The molten melt was poured by gravity into a permanent graphite mold to form a rectangular ingot of 25 mm x 50 mm x 12 mm in size and cooled in air. An A4047 ingot, which was made using the same casting approach from the clean A4047 powder without TSP treatment, was benchmarked as a control sample.

To study the TSP effectiveness in A4047, the TSP-treated A4047 ingot was designated as the master alloy and was added into untreated, molten A4047 at 1088 K (815°C) to get the diluted ingot with a different TSP concentration. Table 4-1 shows the overall composition of TSP in the A4047 ingots before and after sequential dilution.

Table 4-1 Overall Composition of TSP in the A4047 Ingots.

Samples	PPM of TSP
A4047 control	0
TSP-treated A4047	10,000
50% untreated A4047 + 50% TSP-treated A4047	5000
75% untreated A4047 + 25% TSP-treated A4047	2500
94% untreated A4047 + 6% TSP-treated A4047	600
98.5% untreated A4047 + 1.5 % TSP-treated A4047	150

4.2.4 Microscopy

The cast ingot was cut, exposing the middle interior region of the sample, and mounted with epoxy resins. Metallographic samples were prepared by grinding with SiC paper and then polishing with 0.3 μm alumina slurry and 0.02 μm colloidal silica suspension. Optical micrographs were taken using a Nikon ECLIPSE MA200 inverted metallographic microscope. Scanning electron microscopy (SEM) was performed with a LEO 1450VP SEM.

4.2.5 Tensile Test

Cylindrical tensile specimens of the Al-based alloys were machined from ingots with a gauge diameter of 4 mm and gauge length of 30 mm, according to ASTM-E8 standard for room temperature testing.

4.2.6 Indentation Microhardness

Microhardness of the eutectic microconstituent of the polished sample in the epoxy mount was measured with a Clark CM-800 Vickers tester using 100 gf applied load with 15 seconds dwell at room temperature. Ten measurements for each sample were performed to obtain average and standard deviation values.

4.2.7 Thermal Analysis

Twelve-gram ingots of the A4047 samples were melted in a furnace at 1088 K (815 °C) for 5 minutes. After the samples were in the liquid state, the molten metal was poured into a ceramic crucible to solidify at room temperature. The ceramic crucible was connected to a Protek^{TM} 506 digital thermometer using an N-type thermocouple wire. The time-temperature data was recorded using Protek^{TM} 506 software until the alloy completely solidified.

4.3 Results and Discussion

4.3.1 Mechanical Properties

A4047 powders with and without TSP treatment were used to make ingots for mechanical property measurement. The set of the ingots was made from the same powders without TSP treatment and was benchmarked as control samples. Tensile tests were conducted on the tensile bars machined from the ingots as described earlier. The ultimate tensile strength (UTS), and elongation to failure are summarized in Figure 4-1.

Elongation to failure increased from 5% with no TSP treatment to 18% when treated with TSP. However, the ultimate tensile strength did not decrease with the increase of elongation. Instead, it was slightly higher with TSP treatment. This is opposite to the common practice of material development – increasing elongation usually causes decreases in the strength.

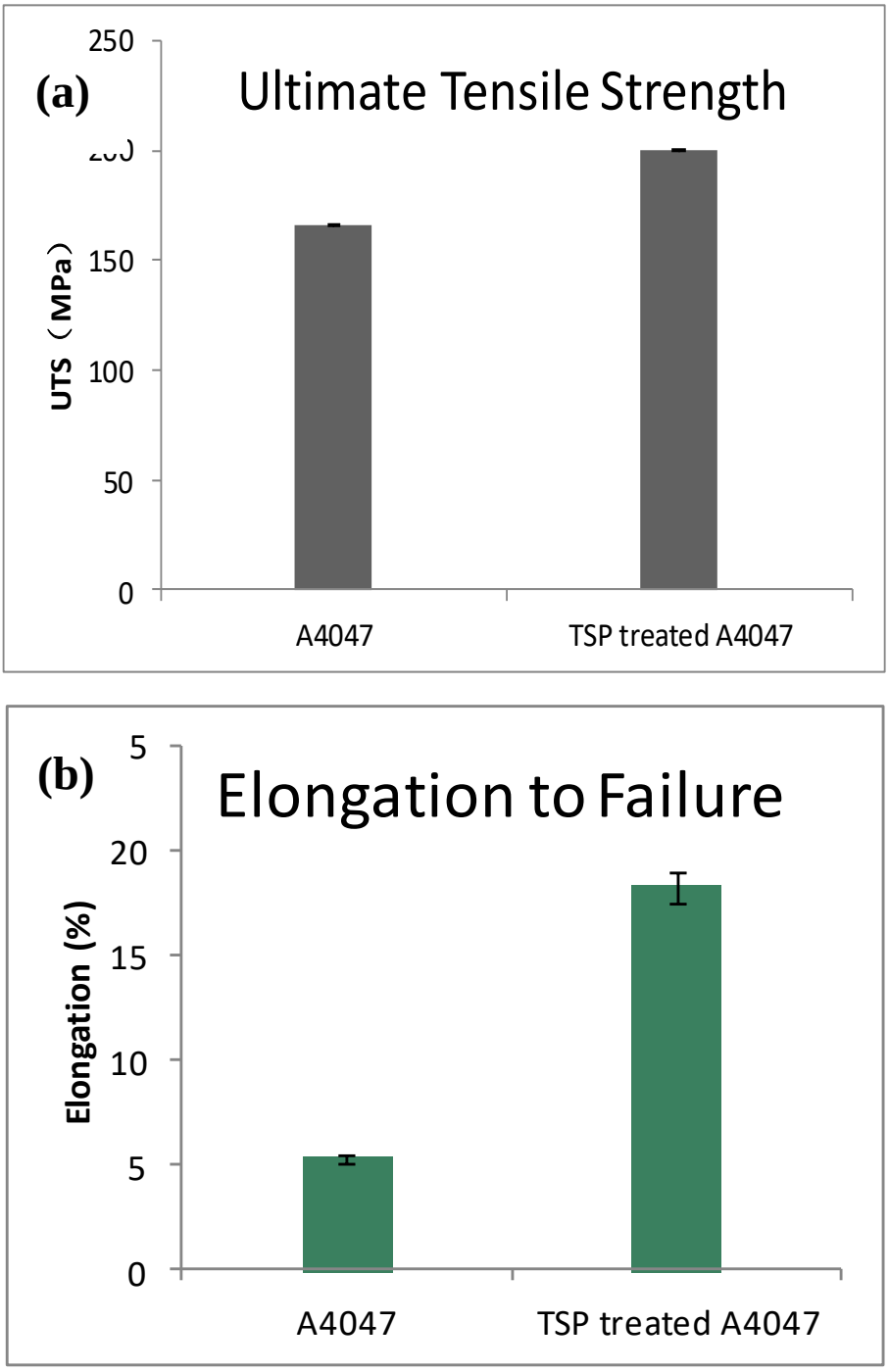

Figure 4-1 Ultimate Tensile Strength (a) and Elongation to Failure (b) of Ingots Made of A4047 Powders without and with TSP Treatment.

4.3.2 As-cast Microstructure

The improved mechanical properties of samples with TSP treatment can be explained by the microstructure. TSP treatment resulted in a significant refinement of both the primary Al and eutectic microconstituent in A4047 alloys. Figures 4-2 (a) – (f) show optical micrographs of the ingots made from the A4047 powder without and with the TSP treatment. A4047 has a near-eutectic Al-Si composition, with the primary Al phase and eutectic microconstituent. Figure 4-2 (a), (c), and (e) display the microstructure of the A4047 control with the objective lens of 5x, 20x and 100x, respectively, showing Al dendrites and irregular Si flakes. With TSP treatment, under the same casting and cooling conditions, the primary Al phase was gradually refined, as shown in Figure 4-2 (b) and (d), and the Si flakes in the eutectic colonies were broken down to very fine fibrous phase, as shown in Figure 4-2 (f).

The secondary dendrite arm spacing (SDAS) of A4047 ingots was gradually reduced with TSP treatment. The SDAS values of primary Al in both A4047 and TSP-treated A4047 were measured using the ImageJ software as shown in Figure 4-3. The SDAS of primary Al in A4047 control was 44.9 μm while the average SDAS in TSP-treated A4047 was decreased to 15.3 μm. The reduced SDAS with TSP treatment corresponds with the improved tensile strength.

In addition, the size of the eutectic Si phase in the A4047 ingots was significantly reduced with TSP treatment. The values of the eutectic Si size in both A4047 and TSP-treated A4047 were measured using the ImageJ software, as shown in Figure 4-4. The average grain size of eutectic Si in the A4047 control was 9.36 μm^2 while the average grain size of eutectic Si in TSP-treated A4047 was decreased to 1.01 μm^2. Therefore, the improved elongation of samples with TSP treatment can be explained by the modification of Si morphology from flaky to fibrous.

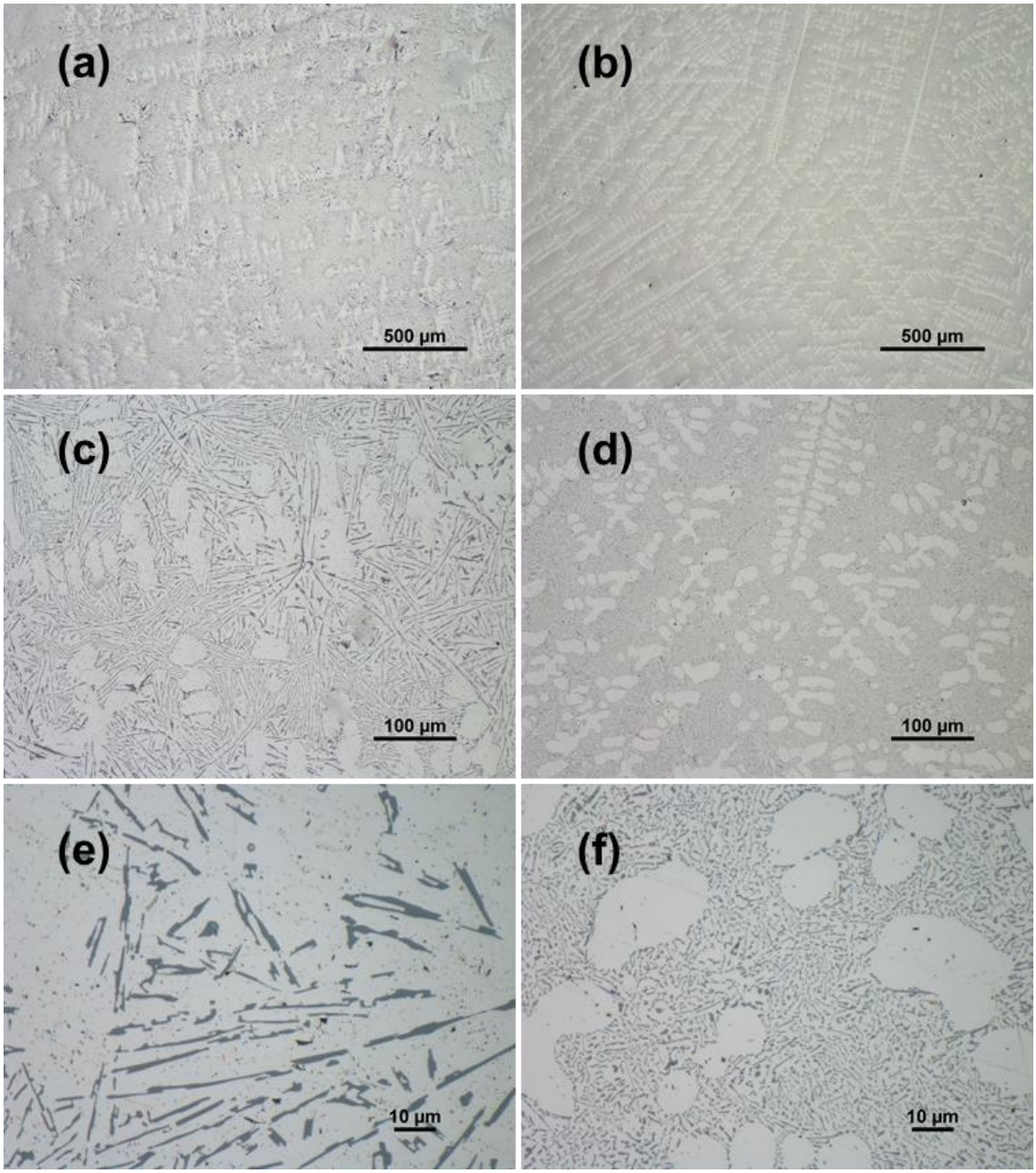

Figure 4-2 Optical Micrographs of Al-Si Alloys Showing the Effect of TSP on the Primary Al and Eutectic Si Morphology of the as-Cast Ingot: (a) The A4047 Control with an Objective Lens of 5x, (b) The TSP-treated A4047 with an Objective Lens of 5x, (c) The A4047 Control with an Objective Lens of 20x, (d) The TSP-treated A4047 with an Objective Lens of 20x, (e) The A4047 Control with an Objective Lens of 100x, and (f) The TSP-treated A4047 with an Objective Lens of 100x.

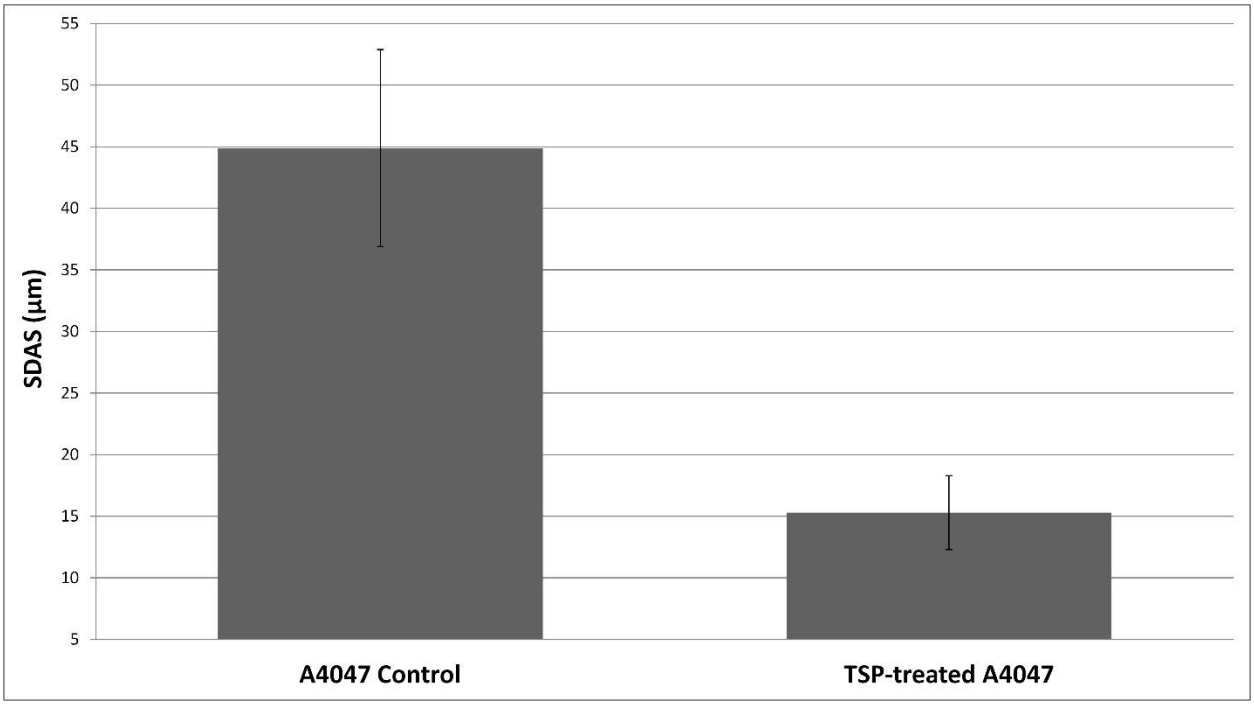

*100 dendrites per condition were measured to get an average and standard deviation values. Each dendrite with at least four arms was select.

Figure 4-3 Effect of TSP Treatment on the Secondary Dendrite Arm Spacing (SDAS) of the A4047 Ingots.

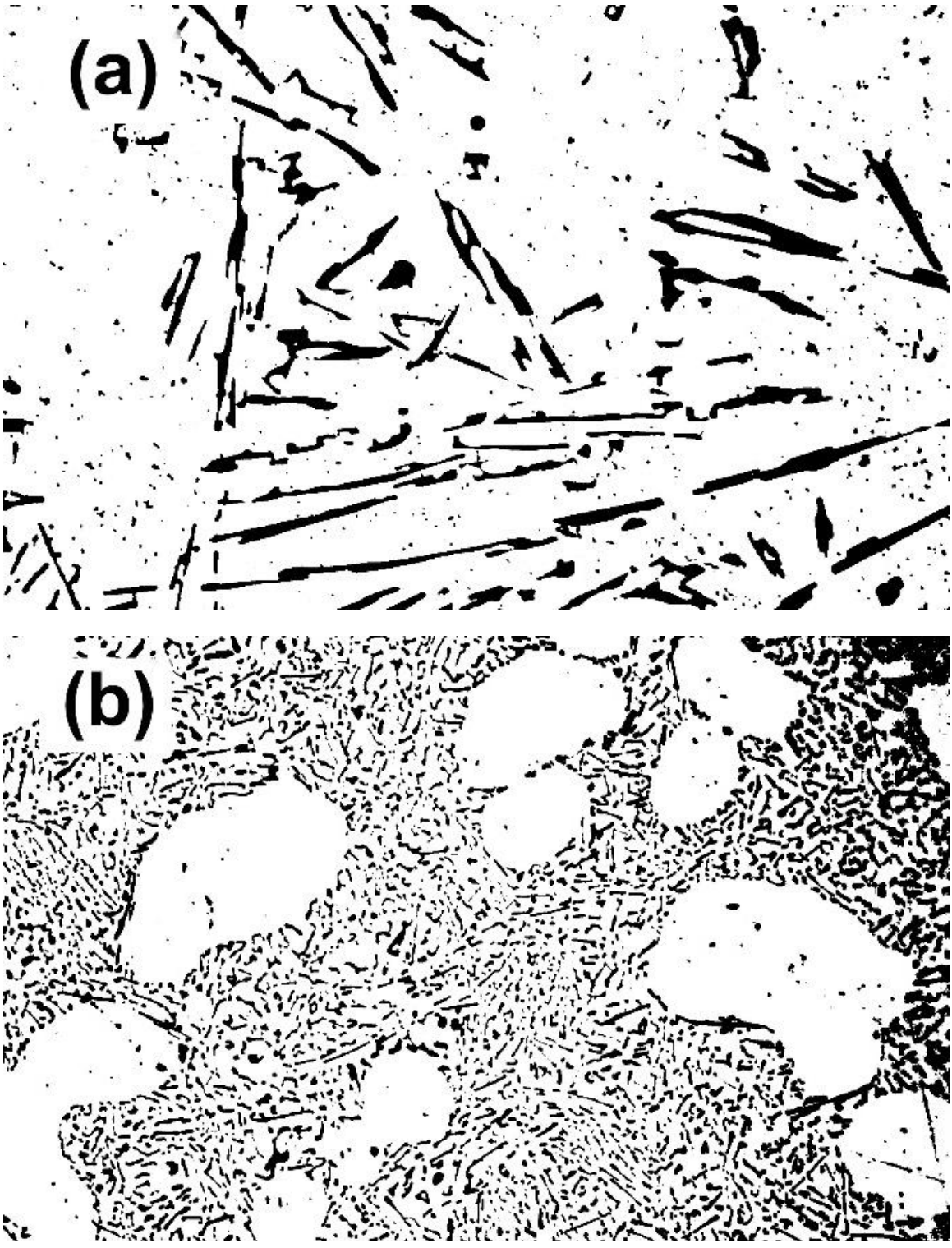

Figure 4-4 ImageJ Analysis of (a) the A4047 Ingot and (b) the TSP-treated A4047 Ingot.

4.3.3 Fracture Surface

Si platelets are shown in Figure 4-2 (e) contribute to the brittle fracture and low ductility as the crack propagates through the interface between Si platelets and the primary Al phase. In contrast, a continuous Al matrix with dispersed Si cuboids, shown in Figure 4-2 (f), resulted in higher ductility when the crack propagated through the mixture of ductile primary Al and Si phases. Fractured samples made of the A4047 alloys, after tensile testing, without and with TSP were imaged are shown in Figures 4-5 and 4-6, respectively.

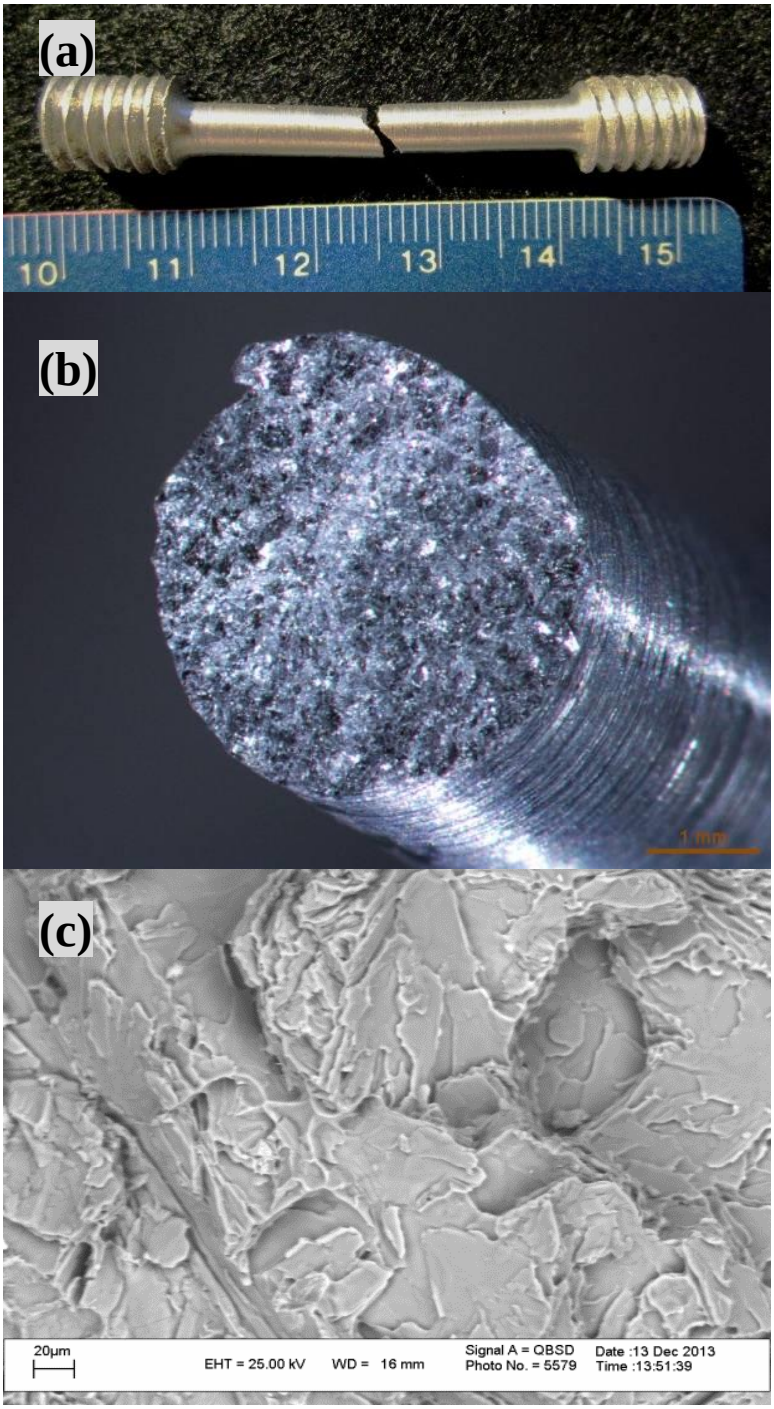

Figure 4-5 A Fractured A4047 Tensile Bar: (a) Photograph of Fractured Sample, (b) Stereo Photograph of Fracture Surface, and (c) Back-scattered Electron Micrograph of Fracture Surface.

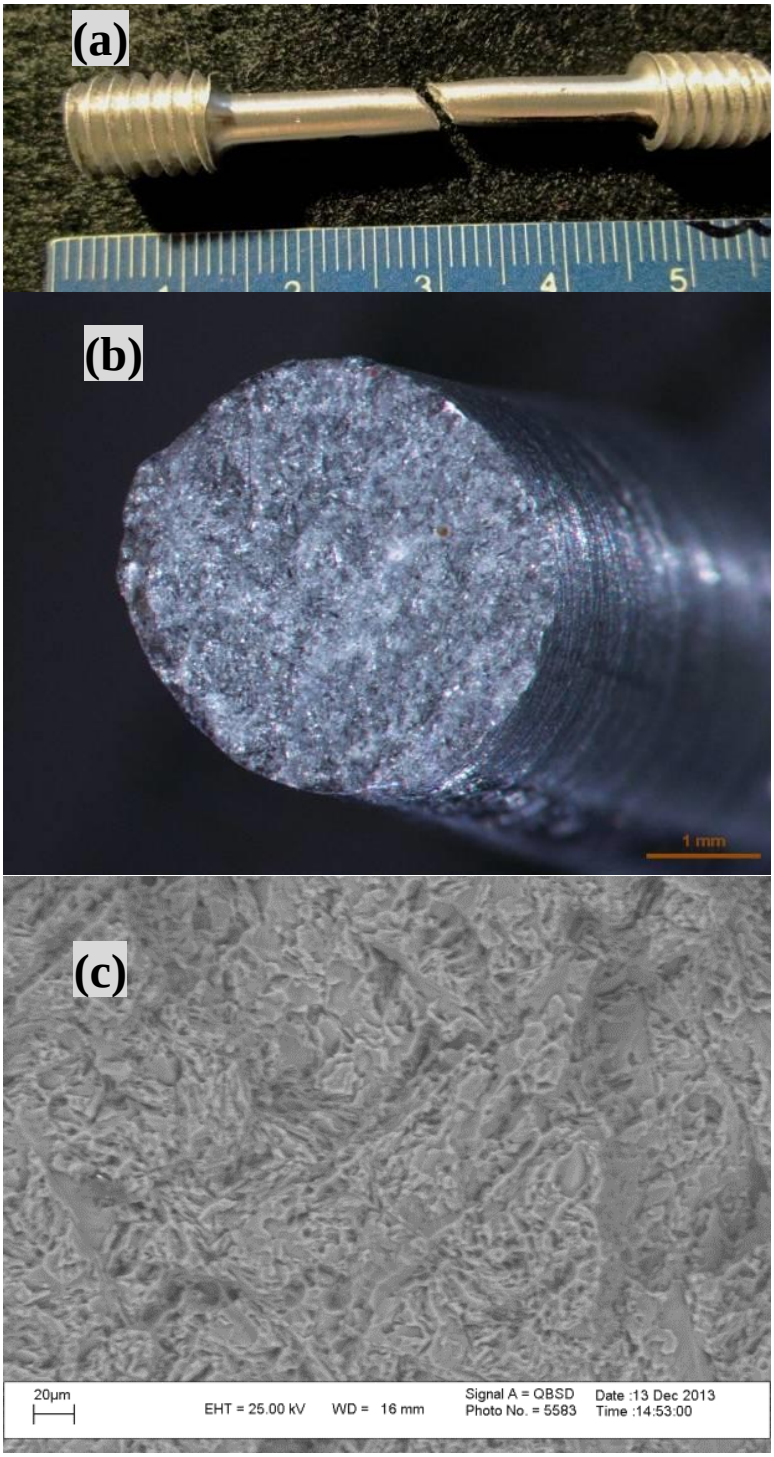

Figure 4-6 A Fractured TSP-treated A4047 Tensile Bar: (a) Photograph of Fractured Sample, (b) Stereo Photograph of Fracture Surface, and (c) Back-scattered Electron Micrograph of Fracture Surface.

The subfigures (a) in Figures 4-5 and 4-6 are the photographs of fracture specimens after tensile testing from ingots without and with TSP treatment, respectively. The control sample in Figure 4-5 (a) had a 5% elongation to failure and showed very little deformation at the fracture. The TSP-treated sample, shown in Figure 4-6 (a), with an 18% elongation to failure, clearly showed a necking phenomenon at the fracture point.

Further indications of brittle failure of the sample without TSP treatment were evidenced by the shining surface in the stereo photograph of figure 4-5 (b) and large cleavage in the electron micrograph (Figure 4-5 (c). In comparison, failure sample with TSP treatment showed dull fracture surface in Figure 4-6 (b), and denser dimples in Figure 4-6 (c).

In summary, cleavage-like brittle fractures were observed on the fracture surface of A4047 in Figure 4-5 (b). However, the cleavage-like facets became smaller or the larger cleavage-like facets are replaced by dimples with the addition of TSP in Figure 4-6 (b), which makes the surface much rougher and thus results in higher elongation to failure.

4.3.4 Solidification

TSP depressed the undercooling and reduced the growth temperature during the Al-Si eutectic reaction. The cooling curves of the A4047 ingots with and without TSP treatment are shown in Figure 4-7. The characteristic temperatures for the eutectic reactions obtained from these curves are shown in Table 4-2. As shown in Table 4-2, the undercooling in the A4047 control was about 3 K, while there was no undercooling with the TSP treatment. Moreover, the eutectic temperature shown in the A4047 control was 848K (575°C), which is the typical Al-Si eutectic temperature[7]. The TSP-treated alloy showed the eutectic temperature decreased to 831 K (558 °C). These results contrast with Sr-modified samples, which show a decrease in eutectic temperatures with increased undercooling temperatures.

The increase of the undercooling with Sr modification can be explained by the restricted nucleation theory. The Sr addition decreases the number of Si-Si covalent bonds, reducing the number of silicon nuclei in the melt, and increases the undercooling, due to the hindrance eutectic silicon nucleation [63, 106]. The decrease of the eutectic growth temperature can be explained by two restricted growth theories. One of them [26, 68] refers to the poisoning of re-entrant edges. Sr sits at re-entrant edges, acting as a deactivator to inhibit Si growth rather than a nucleation site to promote the growth process. Instead of the Si growing along <112> directions anisotropically, the isotropic growth behavior along multiple directions takes place in the modified Al-Si eutectic colonies. Lu and Hellawell [70] claimed that Sr is expelled into the liquid ahead of the solidification front, because of the extremely low solubility of Sr in both aluminum and silicon. Therefore, Sr elements at trace levels are absorbed onto the silicon layers, which can induce twinning by poisoning silicon growth ledges. The morphology change of Si crystals from flakes to fibers can be explained by the poisoning of the re-entrant edges and/or growth ledges to induce Si twinning. Therefore, the increased undercooling and depressed eutectic growth temperature during solidification of Sr-modified Al-Si alloys can be explained by the presence of additional Sr.

However, the undercooling of A4047 was depressed significantly with TSP incorporation. Instead of increasing the interfacial energy between the eutectic liquid and solid, as in the case of Sr addition, TSP molecules act as heterogeneous nucleation sites during the eutectic reaction to decrease the interfacial energy during the eutectic reaction, lower the energy barrier, and thus aid the nucleation of eutectic Si. The A4047 eutectic temperature was also depressed with TSP incorporation. The higher nucleation density and a flaky-fibrous transition in the silicon morphology leads to a large solid-liquid interfacial area during solidification, resulting in the diffusion of Si atoms at the interface and requiring relatively low temperature

during crystal growth. In summary, on the basis of the observed refinement of both the primary Al and eutectic Si microconstituents, the proposed modification mechanism for Al-Si alloys with TSP incorporation is that the nano-sized cage structure of TSP serves as a heterogeneous nucleation site to refine primary Al and modify eutectic Si.

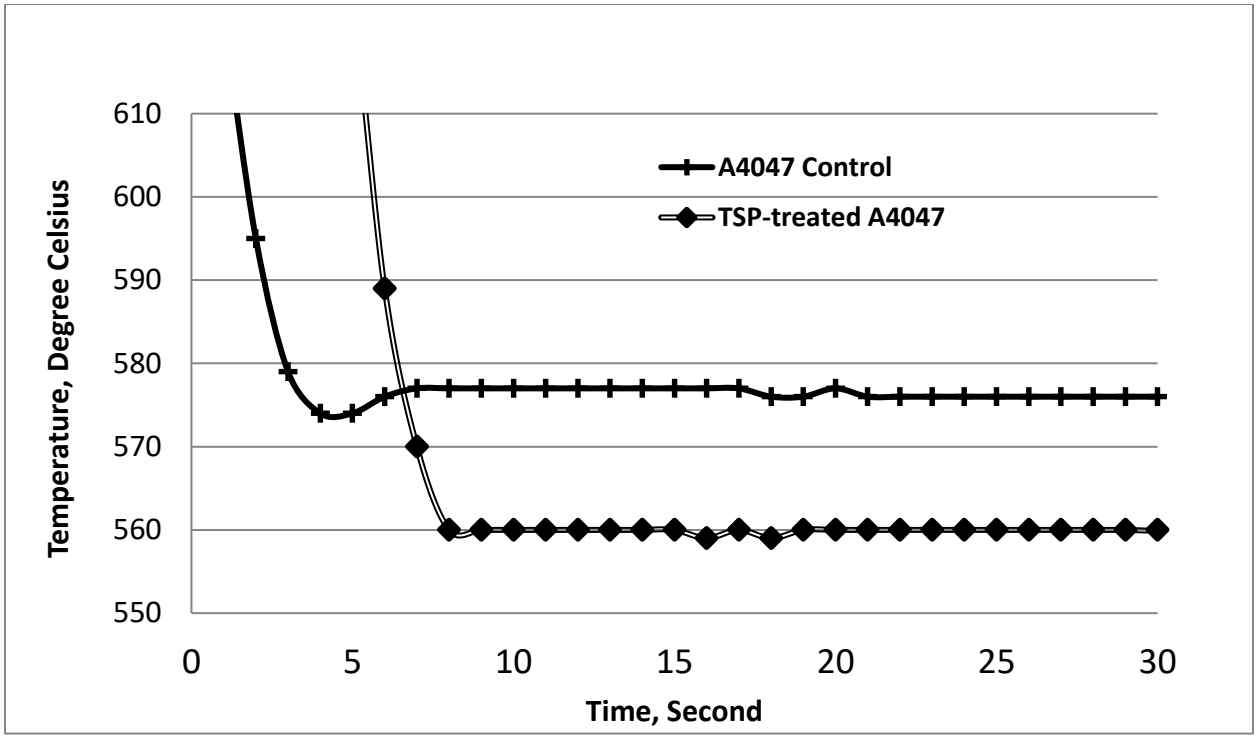

Figure 4-7 Cooling Curves of A4047 and TSP-treated A4047 Alloys.

Table 4-2 Eutectic Reaction Temperatures for A4047 with and without TSP Extracted from Cooling Curves.

TSP-treated System	T_{Min} [K(°C)]	T_G [K(°C)]	ΔT [K(°C)]
A4047 Control	845 K (572°C)	848 K (575°C)	3 K (3°C)
TSP-treated A4047	831 K (558°C)	831 K (558°C)	0 K (0°C)

* T_{Min}: the minimum eutectic reaction temperature of Al-Si;
T_G: the eutectic growth temperature of Al-Si;
ΔT: the undercooling. Temperature difference between T_{Min} and T_G.

4.3.5 Influence of Treatment Time

To investigate the reaction kinetics of A4047 powders and TSP, the effect of dwell time of A4047 powders in TSP ethanol solution was studied. The step 1 and step 3 in section 3.2.2 were kept the same. However, step 2 was changed by varying the dwell time of A4047 powders in TSP solution. Clean A4047 powders were soaked in TSP solutions for 4, 8, 24 hours, and 9 days.

Figure 4-8 shows optical micrographs of ingots made of A4047 powders with different treatment times in TSP solution. There was no change in the morphology of Si eutectic after 4-hour treatment over the control sample. The morphology of eutectic colonies was refined after 8-hour treatment. 8-hour, 24-hour, and 9-day treatment showed the similar refined eutectic morphology. This microstructure change suggests that the reaction between A4047 and TSP is kinetically controlled by the time.

The hardness improvement is corresponding with the changes in microstructures. Table 4-3 lists the Vickers hardness values of the ingots made of the powders with different treatment time. Still, there was no change in hardness after 4-hour treatment over the control. Hardness improvements after 8-hour, 24-hour, and 9-day treatments were observed, which was consistent with the refined morphology.

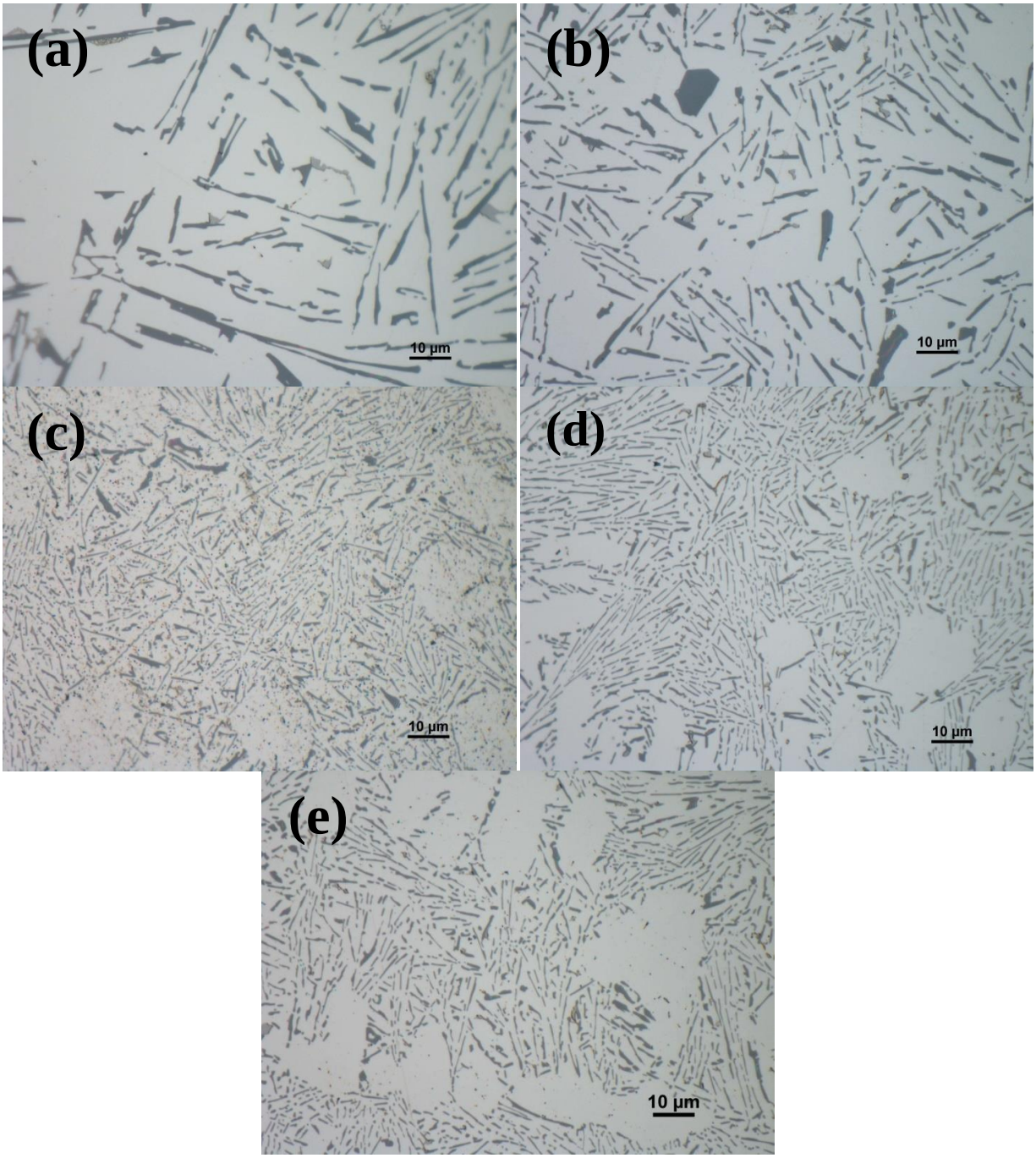

Figure 4-8 Optical Micrograph of an Ingot Made of the A4047 Powders: (a) without TSP Treatment, (b) 4-hour Treatment, (c) 8-hour Treatment, (d) 24-hour Treatment, and (e) 9-day Treatment.

Table 4-3 Microhardness of the TSP-treated A4047 Alloys.

Samples	Vickers Hardness (kg/mm^2)
A4047 control	61.75 ± 2.50
4h-TSP-treated A4047	61.40 ± 1.83
8h-TSP-treated A4047	65.93 ± 2.20
24h-TSP-treated A4047	67.65 ± 2.93
9d-TSP-treated A4047	68.28 ± 1.17

* The applied force and dwell time were 100gf and 15 second, respectively. 10 measurements for each sample were performed to obtain the average and standard deviation values.

4.3.6 Sequential Dilution

1) Indentation microhardness

The microhardness of the eutectic microconstituent of the A4047 ingots improved with TSP treatment. Vickers hardness values of the ingots made from A4047 powder with and without TSP treatment are shown in Table 4-4. The hardness of the A4047 ingot increased from 61.75 to 69.78 Hv with TSP treatment (about 13% improvement). These results are consistent with tensile properties that show that the ultimate tensile strength and ductility increased to 15% and 250% with TSP treatment, respectively. Table 3 also illustrates the microhardness values of sequentially diluted TSP-treated A4047 ingots. The ingot made of 50% untreated + 50% untreated A4047 with the hardness value of 62.60 Hv showed the similar hardness property with the A4047 control while the average hardness values of sequentially diluted TSP-treated A4047 were higher than that of A4047 control. Moreover, the hardness of the A4047 ingot with only 150 ppm TSP increased to 64.33 Hv, suggesting that 150 ppm TSP can show enhancement in the hardness of eutectic colonies of Al-Si alloys.

Table 4-4 Microhardness of the Diluted A4047 Alloys.

Samples	Vickers Hardness (kg/mm^2)
A4047 control	61.75 ± 2.50
TSP-treated A4047	69.78 ± 1.83
50% untreated A4047 + 50% untreated A4047	62.60 ± 2.20
50% untreated A4047 + 50% TSP-treated A4047	69.78 ± 2.93
75% untreated A4047 + 25% TSP-treated A4047	68.60 ± 1.17
94% untreated A4047 + 6% TSP-treated A4047	64.65 ± 1.33
98.5% untreated A4047 + 1.5 % TSP-treated A4047	64.33 ± 1.96

* The applied force and dwell time were 100gf and 15 second, respectively. 10 measurements for each sample were performed to obtain the average and standard deviation values.

2) Microstructure

The modified microstructure of the eutectic microconstituent of TSP-treated A4047 was maintained after sequential dilution. Figure 4-9 shows optical micrographs of sequentially diluted ingots. The control one with 50% untreated A4047 addition in Figure 4-9 (a) was under the same casting process, which showed the similar morphology to untreated A4047 ingot in Figure 4-2 (e). However, the ingots with 50% TSP-treated A4047 and 50% untreated A4047 in Figure 4-9 (b) maintained the same refined morphology as the TSP-treated A4047 master alloy in Figure 4-2 (f). The modified morphology for all the diluted ingots was maintained as shown in Figures 4-9 (b)-(e). The morphology of the eutectic colonies in A4047 with 150 ppm TSP was still refined. Therefore, the improved hardness in the sequentially diluted TSP-treated ingots in Table 4-4 corresponds to the maintained morphology after dilution in Figure 4-9. These results also suggested that TSP can survive after multiple re-melting in 800°C furnace, which possessed a great potential for recycling applications.

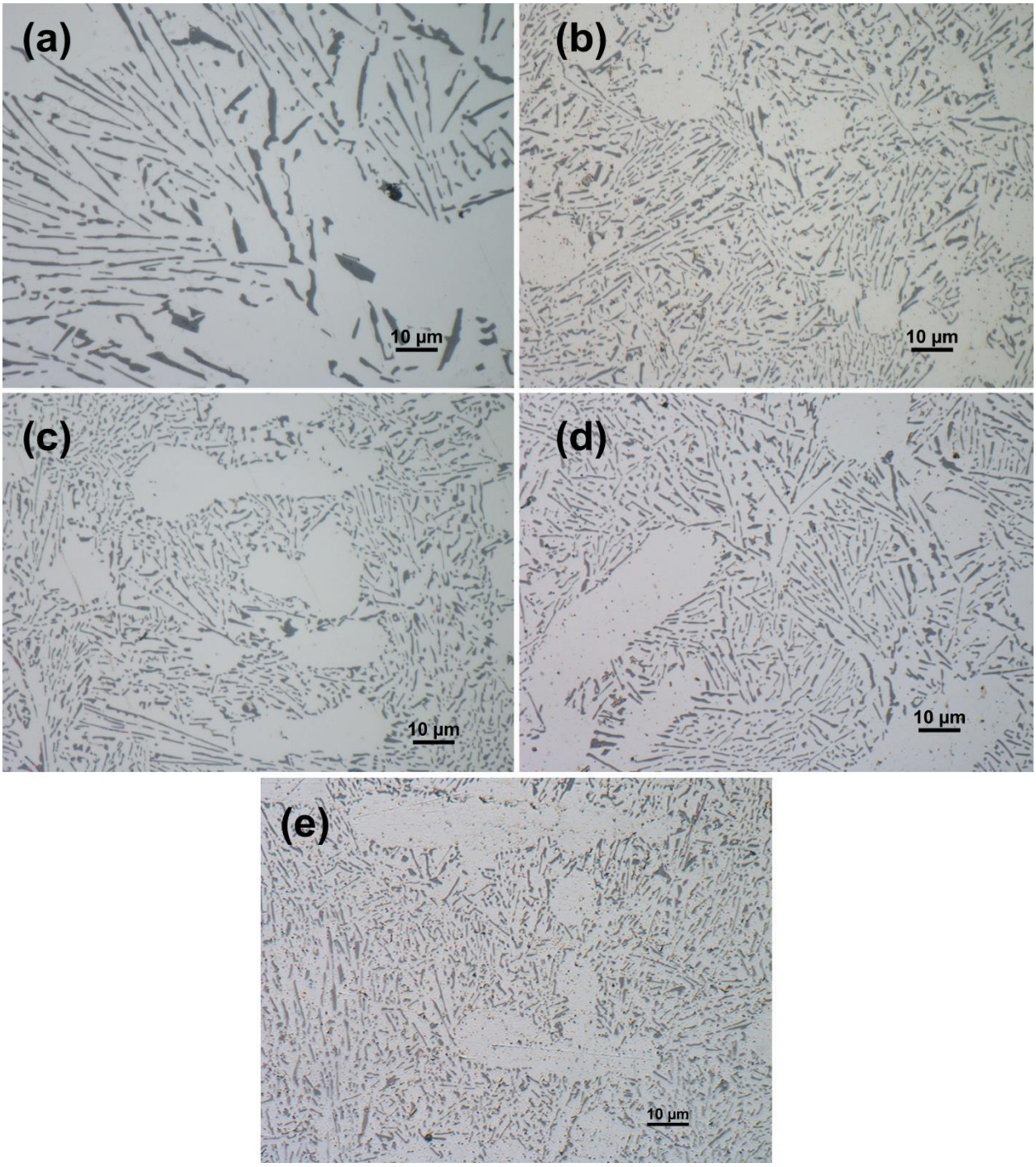

Figure 4-9 Optical Micrographs of Diluted A4047 Ingots: (a) 50% Untreated A4047 + 50% Untreated A4047, (b) 50% Untreated A4047 + 50% TSP-treated A4047, (c) 75% Untreated A4047 + 25% TSP-treated A4047, (d) 94% Untreated A4047 + 6% TSP-treated A4047.

3) Solidification

TSP depressed the undercooling and reduced the growth temperature during Al-Si eutectic reaction, as shown in Figure 4-7. More interestingly, the depressed undercooling and eutectic temperature were dependent on the TSP level. The cooling curves of A4047 after sequential dilution are shown in Figure 4-10. The cooling curves of TSP-treated A4047 have been overlaid along the time-axis for clarity. The characteristic temperatures for the eutectic reactions obtained from these curves are shown in Table 4-5. As shown in Table 4-5, the undercooling in the A4047 control was about 3 K, while there was no undercooling with TSP treatment. Moreover, the eutectic temperature shown in the A4047 control was 850 K (577°C). The TSP-treated alloy showed the eutectic temperature decreased to 833 K (560 °C). The depressed undercooling and eutectic temperature were dependent on the TSP level in Al-Si ingots in Table 4-5. The undercooling increased as the TSP level decreased. These results give a further indication that TSP reduces the solid-liquid interfacial energy to modify eutectic Si.

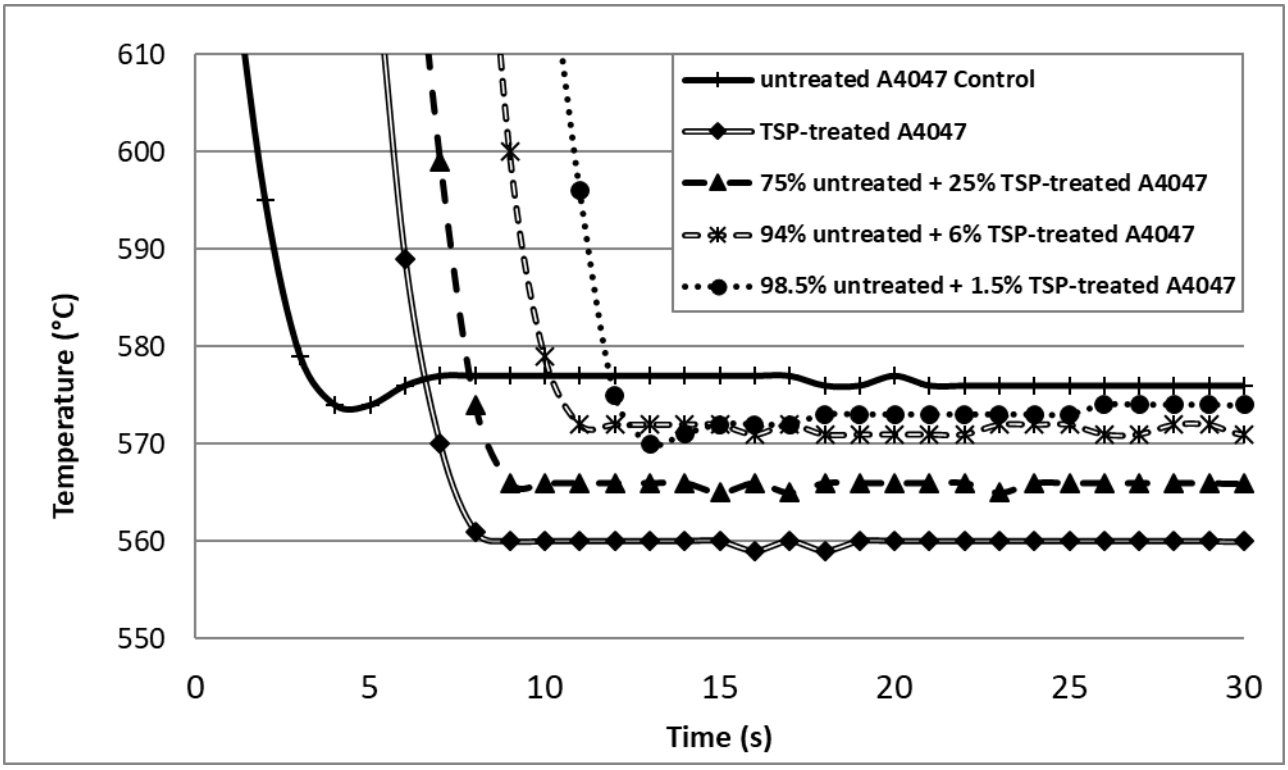

*The cooling curves of the TSP-treated A4047 have been overlaid along the time-axis for clarity.

Figure 4-10 Cooling Curves of Diluted TSP-treated A4047 ingots.

Table 4-5 Eutectic Reaction Temperatures Extracted from Cooling Curves.

TSP-treated System	T_{Min} [K(°C)]	T_G [K(°C)]	ΔT [K(°C)]
A4047 control	846.5 K (573.5°C)	850.0 K (577.0°C)	3.5 K (3.5°C)
TSP-treated A4047	833.0 K (560.0°C)	833.0 K (560.0°C)	0 K (0°C)
75% untreated A4047 + 25% TSP-treated A4047	839.5 K (566.5°C)	839.5 K (566.5°C)	0 K (0°C)
94% untreated A4047 + 6% TSP-treated A4047	844.5 K (571.5°C)	845.0 K (572.0°C)	0.5 K (0.5°C)
98.5% untreated A4047 + 1.5 % TSP-treated A4047	843.5 K (570.5°C)	846.0 K (573.0°C)	2.5 K (2.5°C)

* T_{Min}: the minimum eutectic reaction temperature of Al-Si;
T_G: the eutectic growth temperature of Al-Si;
ΔT: the undercooling. Temperature difference between T_{Min} and T_G.

4.3.7 Proposed Modification Mechanism

With TSP addition, the morphology of Si crystals is modified to the form of a fibrous structure, resulting in improved ductility. The undercooling of the Al-Si eutectic decreases with the addition of TSP and was inversely proportional to the amount of TSP in the melt. The change in undercooling during solidification can be explained by nucleation, which involves the formation of silicon nuclei. The free energy barrier for heterogeneous nucleation can be represented by Eq 4-1

$$\Delta G_{het}^{*} = \frac{16\pi\gamma_{SL}^{3}}{3\Delta s_f^2 (\Delta T)^2}[(2+\cos\theta)(1-\cos\theta)^2/4]$$

Equation 4-1

In Eq. 3-1, Θ is the wetting angle of the melt on pre-existing solid particle, γ is the solid/liquid interfacial energy, ΔT is the undercooling, and ΔS_f is the entropy of fusion. Eq. 4-1 states that the energy barrier for nucleation decreases with decreasing interfacial energy. The presence of a pre-existing solid particle will reduce the interfacial energy only if Si can easily form on particle surface. In general, the lattice mismatch between a pre-existing particle and solute have to be less than 10% to facilitate the nucleation process[107]. The Si-O-Si cage structure in TSP is in the form of cubic cluster with a diameter of 5.343 Å (the lattice parameter of Si is 5.413 Å), where the Si-O-Si angles are in the range of 145-152^{o}, Si-O bond length is 1.55-1.65Å, and atomic radius of Si and O are 1.176 and 0.60Å. Therefore, TSP has a low lattice mismatch with the Si crystal, suggesting that the TSP can reduce the interfacial energy during Si nucleation process. Table 4-5 shows that addition of TSP to an Al-Si eutectic alloy is accompanied by reduced undercooling, which supports the fact that TSP aids nucleation of the eutectic silicon by decreasing the interfacial energy of the melt. Hence, the presence of TSP in nearly eutectic Al-Si alloys aids the nucleation of eutectic Si due to low lattice mismatch with eutectic Si.

Growth begins after nucleation. In un-modified Al-Si eutectic alloys, the Si crystal is bounded by 111 habit planes with two parallel twins [108]. The 141° re-entrant corner is the most favorable site for Si crystals to nucleate, and eutectic Si grows along <112> directions at the reentrant corner, as shown in Figure 4-11. This growth mechanism is well known as twin plane re-entrant edge (TPRE) [108].

What happens after adding the TSP? The addition of the TSP decreased the eutectic growth temperature. The eutectic Si growth temperature was inversely proportional to the amount of TSP in the melt. Combining the solidification results and the TPRE mechanism in the unmodified Al-Si system, a restricting TPRE growth theory with TSP addition is proposed: TSP bonds with Al to slow down the Al segregation from Al-Si melt during eutectic reaction, leading to the microstructural refinement of Al-Si eutectic.

To summarize, TSP modification of eutectic Si crystals in Al-Si alloys is associated with two mechanisms: reducing the interfacial energy to aid nucleation and slowing down the Al segregation from Al-Si melt to suppress Si growth, which leads to morphological transformation and mechanical enhancements.

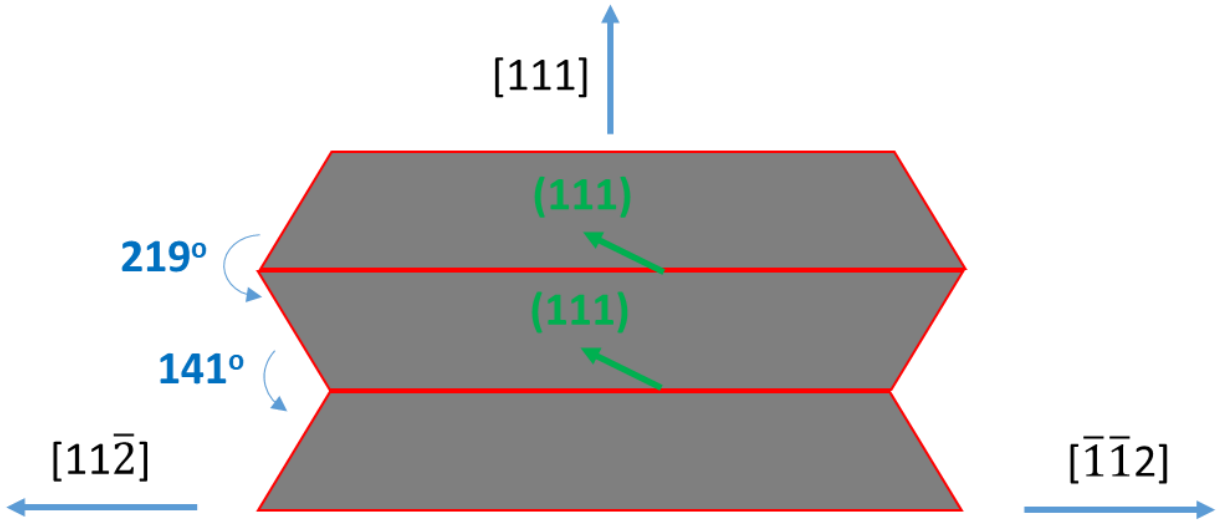

Figure 4-11 Schematic Illustrating 2D View of the Twin Plane Re-entrant Edge Growth Mechanism.

4.4 Conclusions

In this chapter, a new process was developed to enable the in-situ kinetic reaction of TSP and A4047. The microstructure of the eutectic microconstituent of A4047 with TSP treatment was modified, which was still maintained with only 150 ppm TSP after sequential dilution, shedding light on the Sr fading issues. A modified microstructure was created due to the diminishment of undercooling, while the eutectic temperature changed from 850 K (577°C) to 833 K (560 °C) with TSP treatment during solidification. The change of morphology with TSP treatment was associated with mechanical enhancement of the A4047 alloy. These results suggest that TSP aids nucleation of eutectic Si by decreasing the interfacial energy of the melt, while inhibits Si growth by slowing down the Al segregation from Al-Si melt, leading to morphological transformation and mechanical enhancement.

Chapter 5 Development of Al-Si-TSP Master Alloys

5.1 Background

TriSilanol POSS (TSP) as a novel chemical modifier was used to modify the microstructure of Al-Si based casting to increase the ductility without sacrificing the strength of the unmodified alloy. In chapter 3, microstructure modification was obtained in a nearly eutectic alloy, A4047(Al-12Si), after melting TSP-treated A4047 powders at laboratory scale. The objective in this chapter is to develop a TSP master, which can be easily incorporated into base alloy in aluminum foundries at large scale. Two important goals need to be achieved: 1) the master must meet the temperature range of the thermal stability of TSP; 2) the master must assure that the reaction between TSP and Al occurs efficiently to refine microstructure.

There are three types of A4047-TSP master in this study: loose powder, cold-pressed puck and pre-melted ingot. At the laboratory scale, highly modified Si in A4047 after sequential dilution was obtained as shown in chapter 3. However, the A4047-TSP master in the form of cold-pressed puck or ingot will be more practicable to be added into the molten alloy at larger scale. The A4047-TSP master in the form of powder requires fast-heating-rate furnace and narrow process window to allow TSP to react with Al, which is difficult to process in aluminum foundries. Therefore, two types of A4047-TSP master, cold-pressed puck and pre-melted ingot, were used in this study. Besides the form of master, TSP concentration and relative amount of master alloys were investigated at 25-kg laboratory scale. Al-12Si and Al-7.5Si were selected as base alloys to study the effectiveness of the A4047-TSP master.

5.2 Experimental

5.2.1 Materials and Melt Preparation

Pure Al ingot consists of >99.5% Al. Al-50Si master ingot. Chemical composition (nominal %): 50 Si, balance Al. A4047 powder -325 mesh (44 μm or less) from Johnson Manufacturing (Princeton, IA). Chemical composition (nominal %): 12 Si, balance Al. Trisilanolphenyl-POSS (TSP), obtained from Hybrid Plastics, Inc. (Hattiesburg, MS), was used in this study.

The materials in the form of 5-kg ingots were melted in 35-kg capacity silicon carbide crucibles, using an electric melting furnace. In each cast, the melt temperature was maintained at 720^{o}C before sampling.

5.2.2 TSP Incorporation Process

1) Cold-pressed Puck

The TSP was dissolved in base alloy via puck, where the TSP is combined with A4047 powder then pressed to form a cylindrical puck. A puck is 24.5 mm in diameter and pressed with a force of 40~45 KN (which is about 78 ~ 88 MPa) at 200^{o}C and hold for 20 min.

2) Pre-melted Ingot

The TSP-treated A4047 ingot as the master alloy was added into base alloy at 720°C to get the Al-7.5Si ingot with about 1000 ppm level of TSP. The A4047-TSP master alloy was prepared by melting the A4047-TSP mixture at 720°C.

5.2.3 Casting

27 kg of alloy was prepared by adding pure Al and Al50Si master alloy to melt to achieve composition. The melt was degassed through 2 min injection flux followed by 7 min N_2 purge. The molten alloy was poured to a torpedo-shaped steel mold to form torpedo shape sample. The mold was maintained at 175^{o}C using the heated oil.

5.2.4 Characteristics

1) Optical Emission Spectrometry

A sample of molten alloy was poured to a spectrometer disk to perform qualitative and quantitative analysis of the elements with the SPECTROMAXx arc spark OES metal analyzer. At least six measurements of each sample were performed.

2) Metallography

The cast ingot was cut, exposing the middle interior region of the sample, and mounted with epoxy resins. Metallographic samples were prepared by grinding with SiC paper and then polishing with 5/0.3 μm alumina slurry and 0.05 μm colloidal silica suspension. The polished mount was etched using Keller's solution for 30s prior to imaging. Optical micrographs were taken using the inverted metallographic microscope, Nikon ECLIPSE MA200, with the magnification up to 1,000X.

5.3 Results and Discussion

5.3.1 Melt Characterization

The base alloys used for this chapter were prepared from commercially-pure aluminum ingot with Al-50Si master alloy addition to achieve the composition listed in Table 5-1. The Al-7.5Si base alloy composition is very similar to 300 series casting alloys except for Mg and Cu additions. The two base alloys contain 0.15% Fe due to it being a secondary alloy.

Table 5-1 Chemical Composition in wt% of the Al-7.5Si Base Alloy.

Base Alloy	Si	Fe	Al
Al-7.5Si	7.51	0.15	Balance
Al-12Si	12.07	0.16	Balance

5.3.2 Form of Master

Table 5-2 summaries the alloys prepared using two types of A4047-TSP master. Two base alloys are used in this study, Al-12Si and Al-7.5Si. The master forms include cold-pressed puck and pre-melted ingot. The A4047-TSP master contains 2wt% TSP in A4047 matrix.

Table 5-2 Naming Conventions of All Cast Specimens for Master Form Study.

Name	Master	Amount of master (wt%)	Master form
Al-12Si-P	A4047	25	Cold-pressed puck
Al-12Si-TSP-P	A4047-2TSP	25	Cold-pressed puck
Al-12Si-I	A4047	25	Pre-melted ingot
Al-12Si-TSP-I	A4047-2TSP	25	Pre-melted ingot
Al-7.5Si-P	A4047	25	Cold-pressed puck
Al-7.5Si-TSP-P	A4047-2TSP	25	Cold-pressed puck
Al-7.5Si-I	A4047	25	Pre-melted ingot
Al-7.5Si-TSP-I	A4047-2TSP	25	Pre-melted ingot

Figure 5-1 shows the optical micrographs of Al-12Si castings with and without TSP via cold-pressed puck process. It can be seen that the eutectic Si exhibit well-modified structure after the addition of TSP pucks. This modified structure is similar to the TSP-treated A4047 alloy via dip coating process. The same Si morphology was observed in the Al-12Si casting with TSP vis pre-melted ingot process in Figure 5-2. In terms of Si morphology, there is no significant difference between the puck-form master and the ingot-form master.

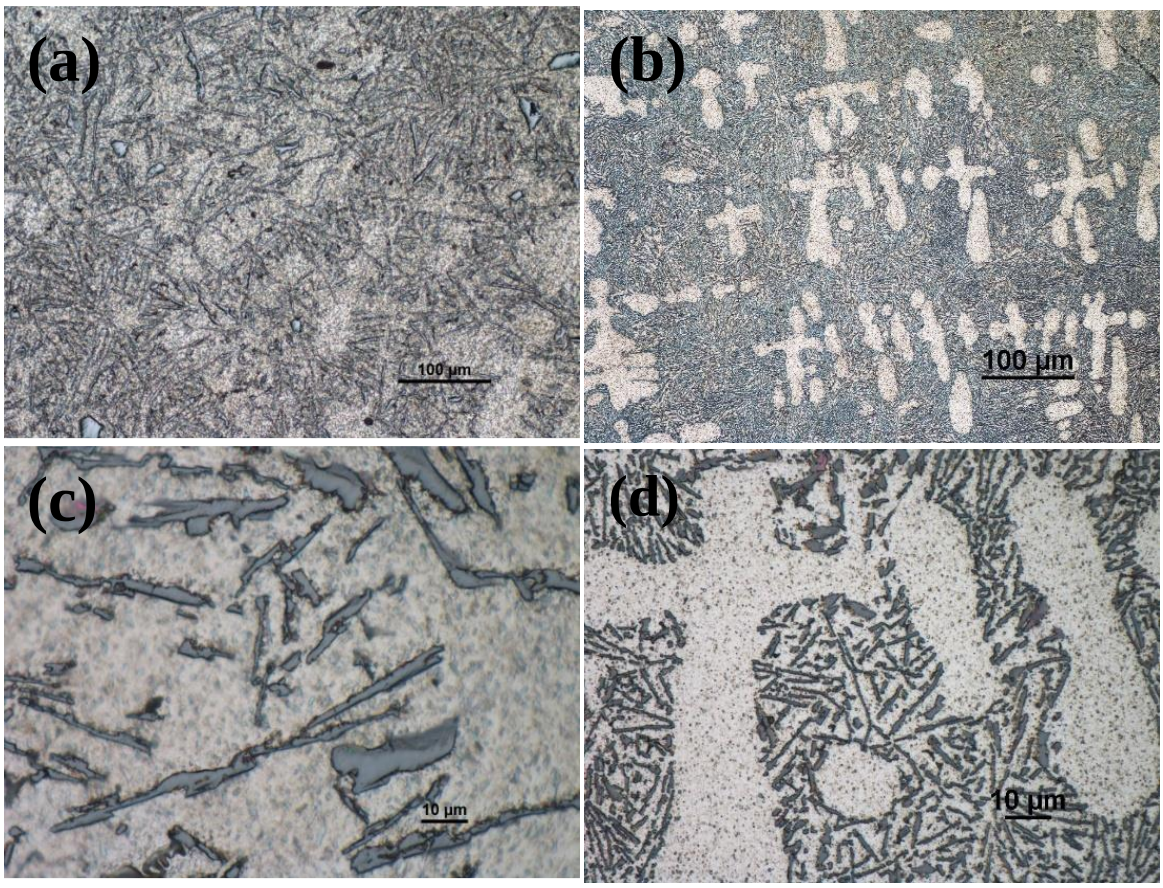

Figure 5-1 Optical Micrographs of As-cast Al-12Si Alloys with and without TSP Using Cold-pressed Puck Process: (a) the Al-12Si-P Base Alloy with the Objective Lens of 20x, (b) the Al-12Si-TSP-P with the Objective Lens of 20x, (c) the Al-12Si-P Base Alloy with the Objective Lens of 100x, and (d) the Al-12Si-TSP-P with the Objective Lens of 100x.

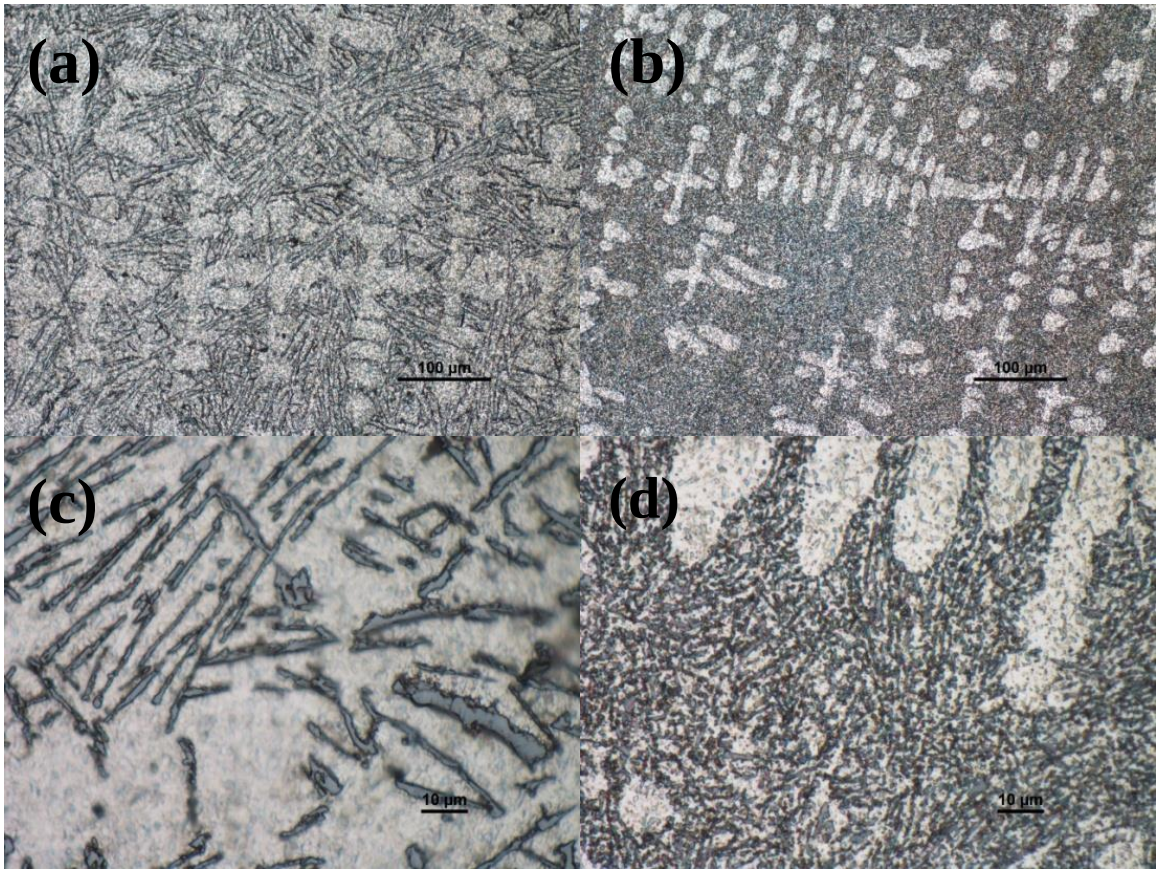

Figure 5-2 Optical Micrographs of As-cast Al-12Si Alloys with and without TSP using Pre-melted Ingot Process: (a) the Al-12Si-I Base Alloy with the Objective Lens of 20x, (b) the Al-12Si-TSP-I with the Objective Lens of 200, (c) the Al-12Si-I Base Alloy with the Objective Lens of 100x, and (d) the Al-12Si-TSP-I with the Objective Lens of 100x.

Table 5-3 SDAS of the Al-12Si Alloys with and without TSP.

Samples	SDAS (μm)
Al-12Si-P	45.0 ± 7
Al-12Si-TSP-P	31.2 ± 5
Al-12Si-I	44.7 ± 8
Al-12Si-TSP-I	15.4 ± 4

* 100 dendrites per condition were measured to get an average and standard deviation values. Each dendrite with at least four arms was select.

The secondary dendrite arm spacing (SDAS) of A4047 ingots was gradually reduced with TSP additions. The SDAS values of primary Al for all castings were measured using the ImageJ software as shown in Table 5-3. The SDAS of primary Al in Al-12Si controls was around 45 μm while the average SDASs in Al-12Si-TSP via cold-pressed puck and pre-melted ingot process were decreased to 31 and 15 μm, respectively. Compared with the Al-12Si-TSP prepared with puck master, the ingot master exhibited even smaller arm spacing. In addition, the dwell time in hot furnace for the Al-12Si-TSP alloy prepared using cold-pressed puck is at least one hour while pre-melted ingot only needs 15 mins to allow TSP to disperse into the melt. In other word, the pre-melted ingot needs much less time to melt than the cold-pressed puck.

Typical phases presented in Al-7.5Si are primary Al and Al-Si eutectic, where eutectic Si appears as dark phase in Figure 5-3 (a,c) and 5-4 (a,c). Well-modified Si morphology was observed with TSP addition via cold-pressed puck in Figure 5-3 (b,d) or pre-melted ingot in Figure 5-4 (b,d). In the Al-7.5Si-TSP-P casting, it took one hour to melt the TSP pucks in 720 ^{o}C furnace. Less than 20 mins is needed to melt the pre-melted ingots to cast Al-7.5Si-TSP-I alloys. Therefore, pre-melted ingot was chosen as TSP master to modify Al-Si alloys due to dissolving much quicker, saving energy and production time.

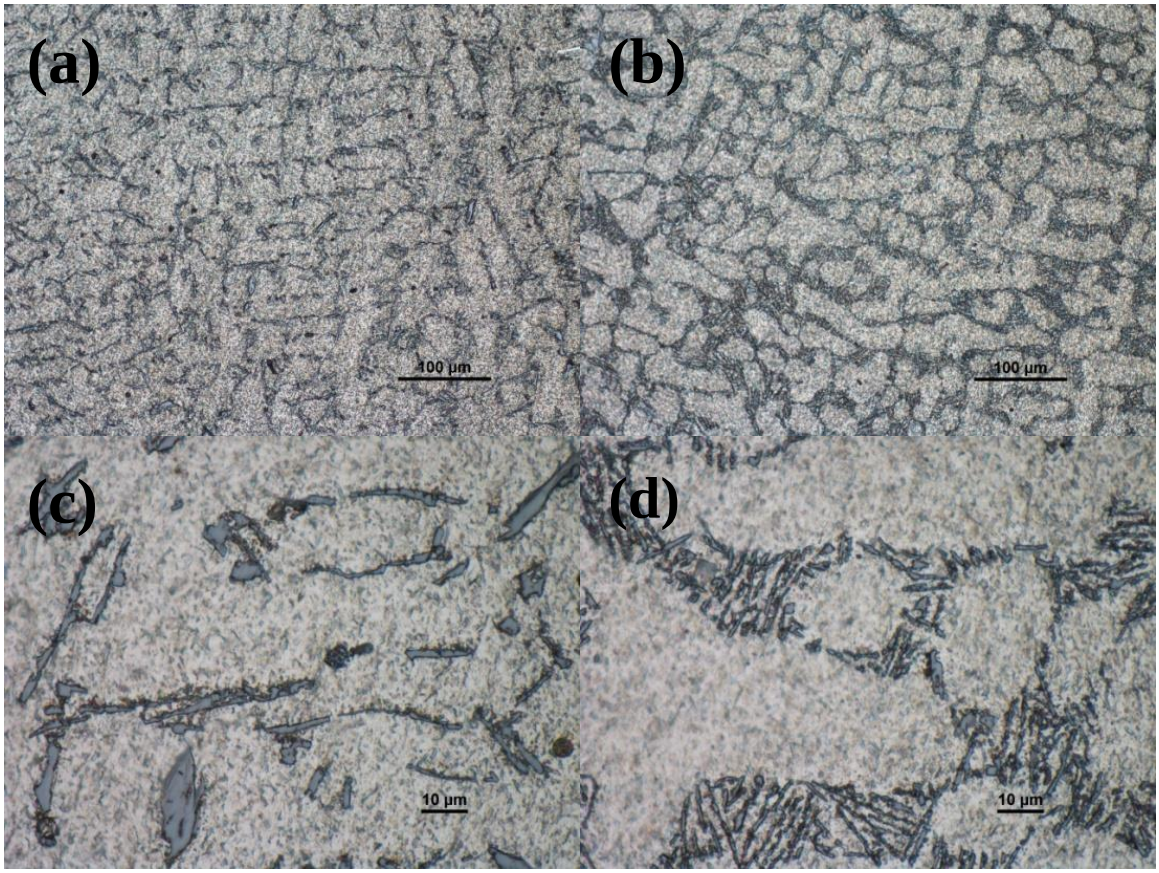

Figure 5-3 Optical Micrographs of As-cast Al-7.5Si Alloys with and without TSP Using Cold-pressed Puck Process: (a) the Al-7.5Si-P Base Alloy with the Objective Lens of 20x, (b) the Al-7.5Si-TSP-P with the Objective Lens of 20x, (c) the Al-7.5Si-P Base Alloy with the Objective Lens of 100x, and (d) the Al-7.5Si-TSP-P with the Objective Lens of 100x.

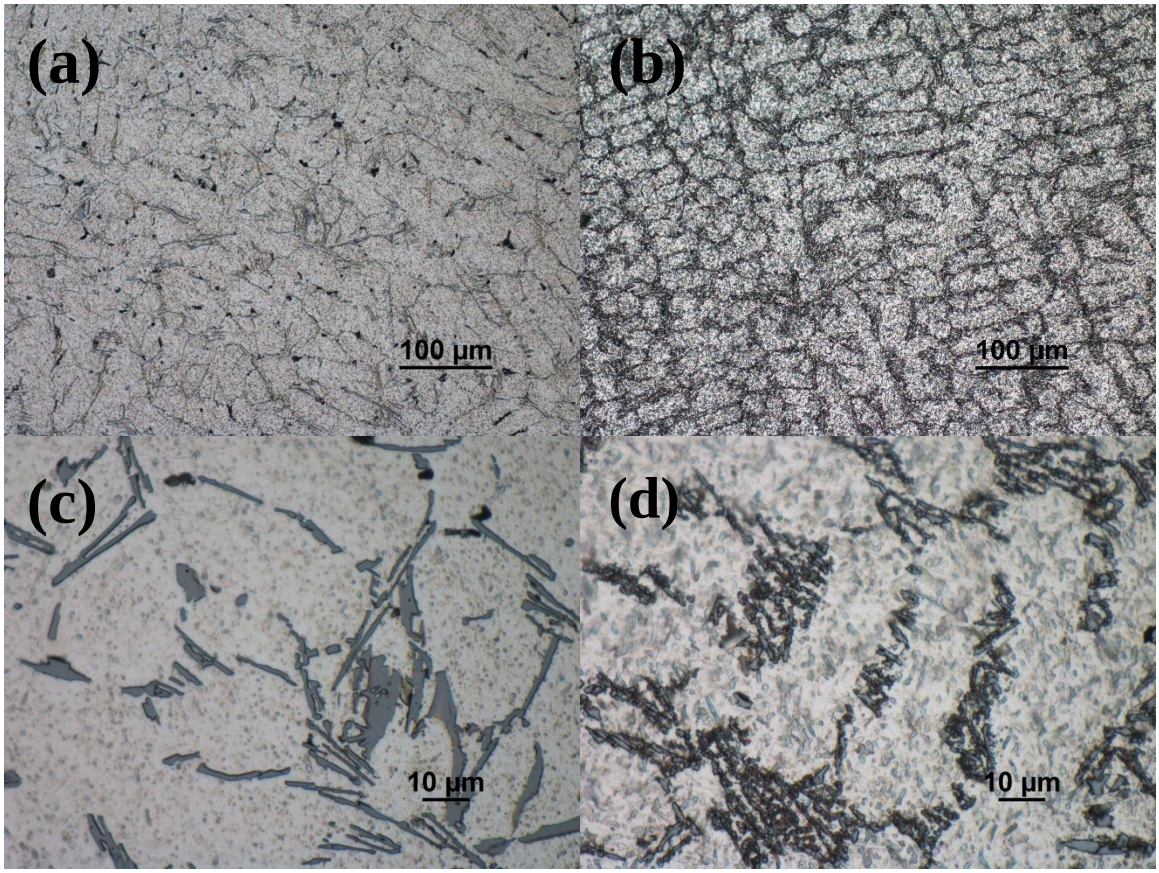

Figure 5-4 Optical Micrographs of As-cast Al-7.5Si Alloys with and without TSP Using Pre-melted Ingot Process: (a) the Al-7.5Si-I Base Alloy with the Objective Lens of 20x, (b) the Al-7.5Si-TSP-I with the Objective Lens of 200x, (c) the Al-7.5Si-I Base Alloy with the Objective Lens of 100x, and (d) the Al-7.5Si-TSP-I with the Objective Lens of 100x.

5.3.3 TSP Concentration in Master

Table 5-4 summarized the Al-7.5Si alloy prepared with different composition of A4047-TSP master. The TSP content in the A4047-TSP master were 2%, 4% and 6%. The A4047-master were prepared vis pre-melted ingot. 25% of A4047-TSP master was added into the Al-7.5Si melt. The entire cast specimens used in the TSP concentration study are listed in Table 5-4.

Table 5-4 Naming Conventions of All Cast Specimens for TSP Concentration Study.

Name	Master	TSP content (wt%) in master	Amount of master (wt%)
Al-7.5Si	A4047	0	25
Al-7.5Si-TSP-i	A4047-2TSP	2	25
Al-7.5Si-TSP-ii	A4047-4TSP	4	25
Al-7.5Si-TSP-iii	A4047-6TSP	6	25

Figure 5-5 showed the optical micrographs of A4047-2TSP, A4047-4TSP and A4047-6TSP masters with two different magnifications. Similar to the microstructure of TSP-treated A4047 using dip coating method in chapter 4, modified Si was observed in the A4047-2TSP master. However, TSP in A4047-4TSP and A4047-6TSP appeared as a form of cluster in Figure 5-5(d) and (f). TSP in master were tending to agglomerate when more than 2% of TSP were added into A4047 base alloy. 6% TSP was the maximum amount of TSP that can be added into A4047 base alloy without sacrificing the overall soundness of the master alloy.

Figure 5-6 illustrated the optical micrographs of Al-7.5Si and Al-7.5Si-TSP-i castings with two different magnifications. 2% TSP addition in the A4047-TSP master modified the eutectic Si from flaky to fibrous form in Figure 5-6 (b,d). Similar modified Si morphology was observed in Al-7.5Si-TSP-ii and Al-7.5Si-TSP-ii from Figure 5-7, where the A4047-TSP master

contains 4% and 6% TSP, respectively. To optimize the modification efficiency, the A4047-6TSP was selected as a master alloy.

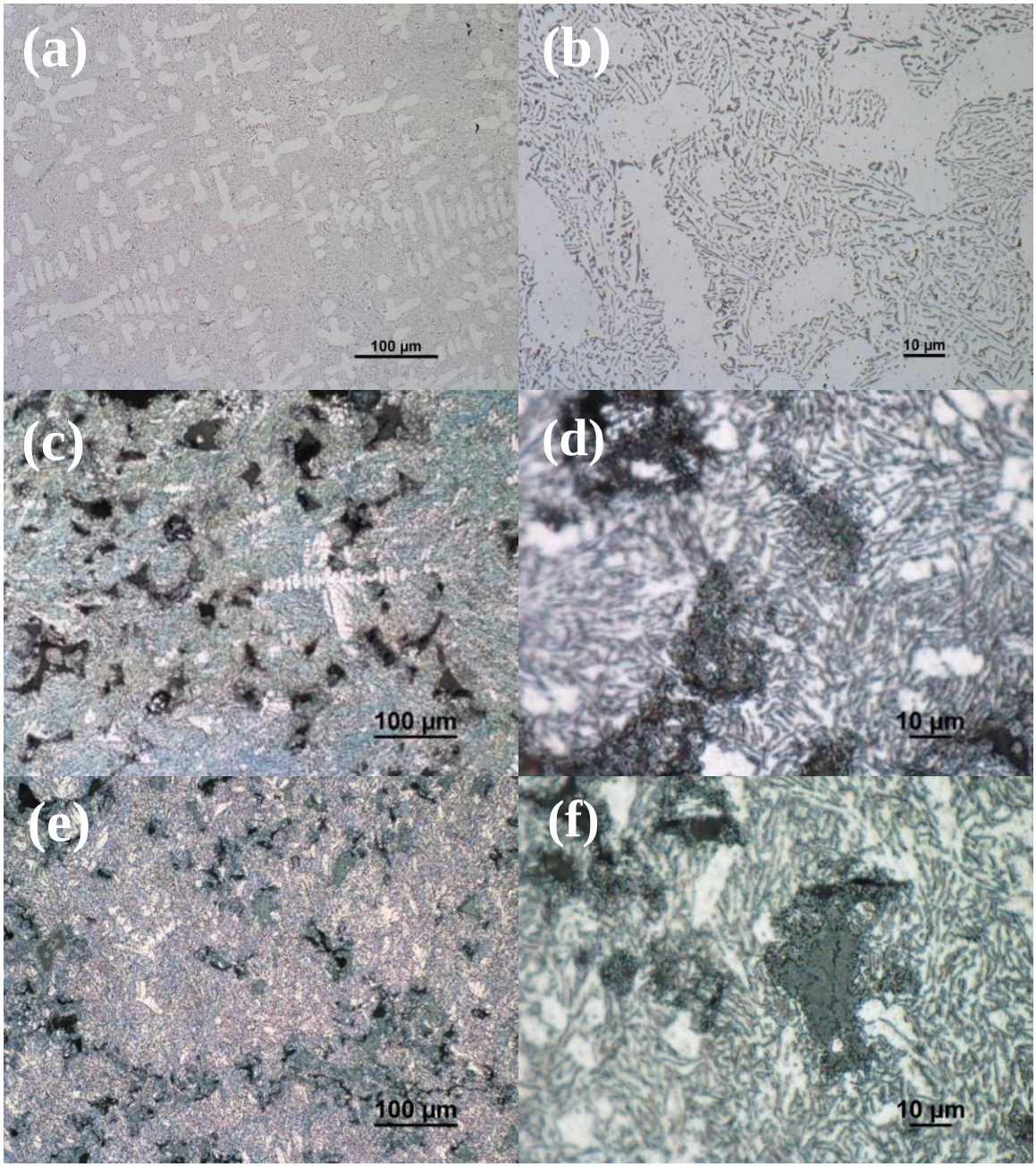

Figure 5-5 Optical Micrographs of the A4047-TSP Master with Different Amount of TSP: (a) the A4047-2TSP with the Objective Lens of 20x, (b) the A4047-2TSP with the Objective Lens of 100x, (c) the A4047-4TSP with the Objective Lens of 20x, (d) the A4047-4TSP with the Objective Lens of 100x, (e) the A4047-6TSP with the Objective Lens of 20x, and (f) the A4047-6TSP with the Objective Lens of 100x.

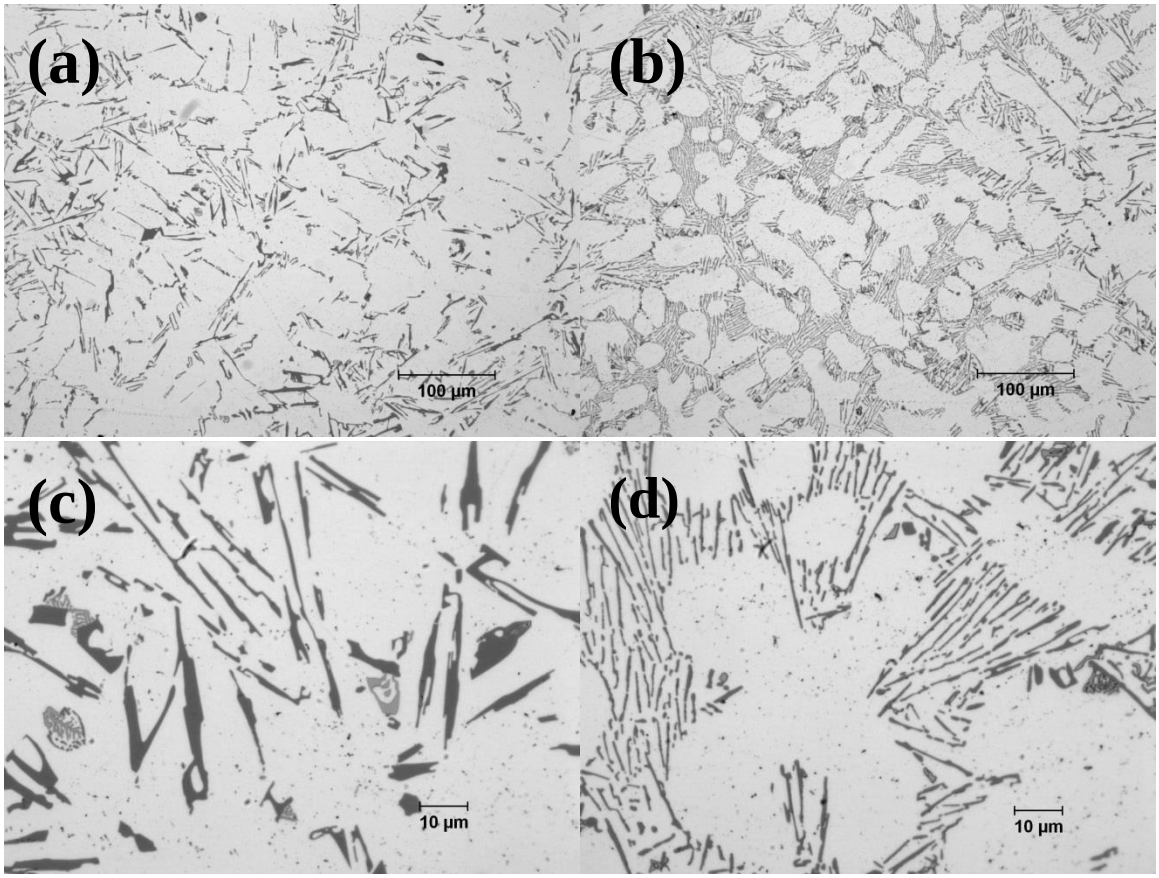

Figure 5-6 Optical Micrographs of As-cast Al-7.5Si Alloys with and without TSP: (a) the Al-7.5Si Base Alloy with the Objective Lens of 20x, (b) the Al-7.5Si-TSP-i with the Objective Lens of 20x, (c) the Al-7.5Si Base Alloy with the Objective Lens of 100x, and (d) the Al-7.5Si-TSP-i with the Objective Lens of 100x.

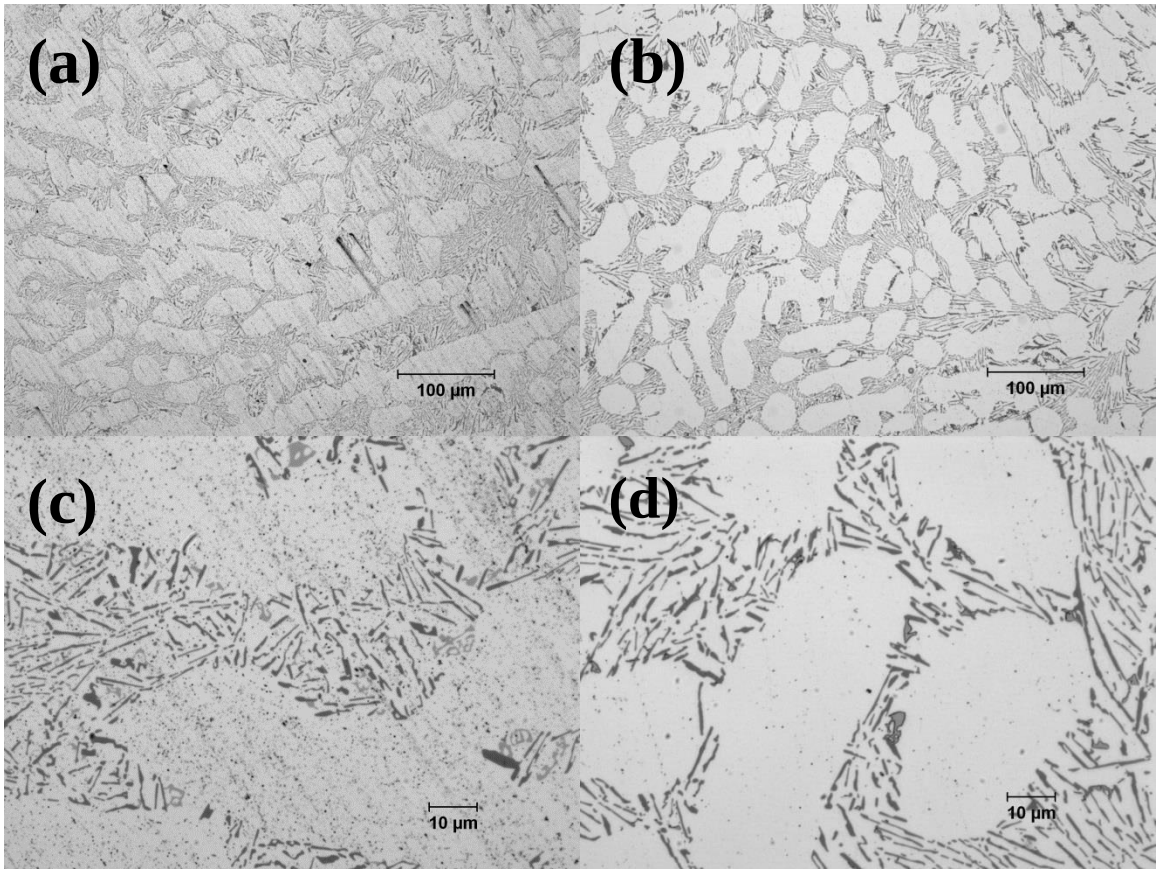

Figure 5-7 Optical Micrographs of As-cast Al-7.5Si Alloys with TSP: (a) the Al-7.5Si-TSP-ii with the Objective Lens of 20x, (b) the Al-7.5Si-TSP-iii with the Objective Lens of 20x, (c) the Al-7.5Si-TSP-ii with the Objective Lens of 100x, and (d) the Al-7.5Si-TSP-iii with the Objective Lens of 100x.

5.3.4 Amount of Master

Three alloys were prepared with A4047-TSP master via pre-melted ingot. The relative amount of master added into base alloy were 5%, 10% and 25%. The microstructure of these three alloys were compared to optimize the amount of master in the base alloy. The entire cast specimens used in the master content study are listed in Table 5-5.

Table 5-5 Naming Conventions of All cast Specimens for Master Content Study.

Name	Master	Amount of master (wt%)
Al-7.5Si	A4047	25
Al-7.5Si-TSP-5	A4047-6TSP	5
Al-7.5Si-TSP-10	A4047-6TSP	10
Al-7.5Si-TSP-25	A4047-6TSP	25

Figure 5-8 shows the optical micrographs of Al-7.5Si and Al-7.5Si-TSP-25 castings with two different magnifications. The Al-7.5Si control has primary Al and Al-Si eutectic microconstituents, where eutectic Si appears as dark phase in Figure 5-8 (a,c). Well-modified Si morphology was observed with TSP addition using 25% A4047-6TSP master in Figure 5-8 (b,d). Similar modified Si morphology was observed in Al-7.5Si-TSP-10 from Figure 5-9 (a,c), where the relative amount of the A4047-6TSP master is 10%. However, the Si became coarse with only 5% A4047-6TSP in the Al-7.5Si base alloy as shown in Figure 5-9 (b,d), suggesting that more than 5% of A4047-6TSP is needed to effectively modify Si in the Al-7.5Si alloy.

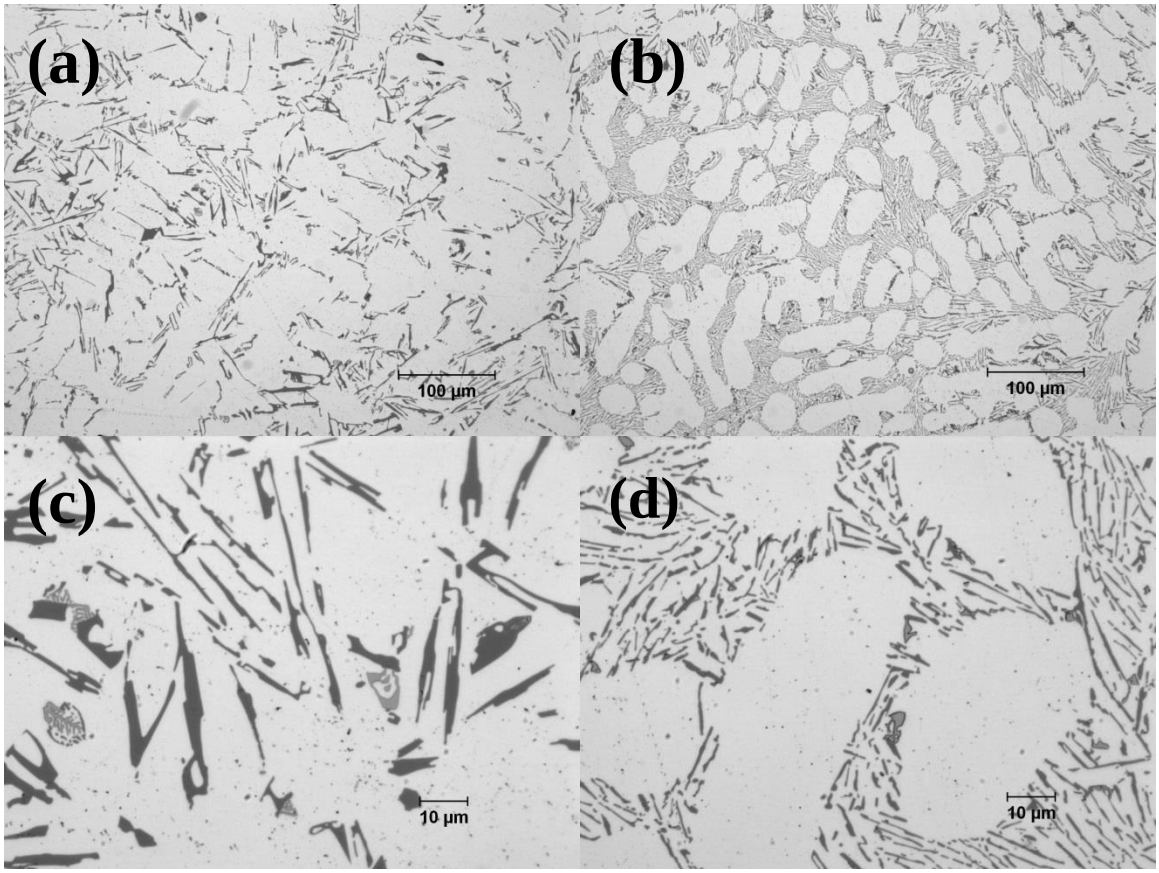

Figure 5-8 Optical Micrographs of As-cast Al-7.5Si alloys with TSP: (a) Al-7.5Si with the Objective Lens of 20x, (b)Al-7.5Si-TSP-25 with the Objective Lens of 20x, (c) Al-7.5Si with the Objective Lens of 100x, (d) Al-7.5Si-TSP-25 with the Objective Lens of 100x.

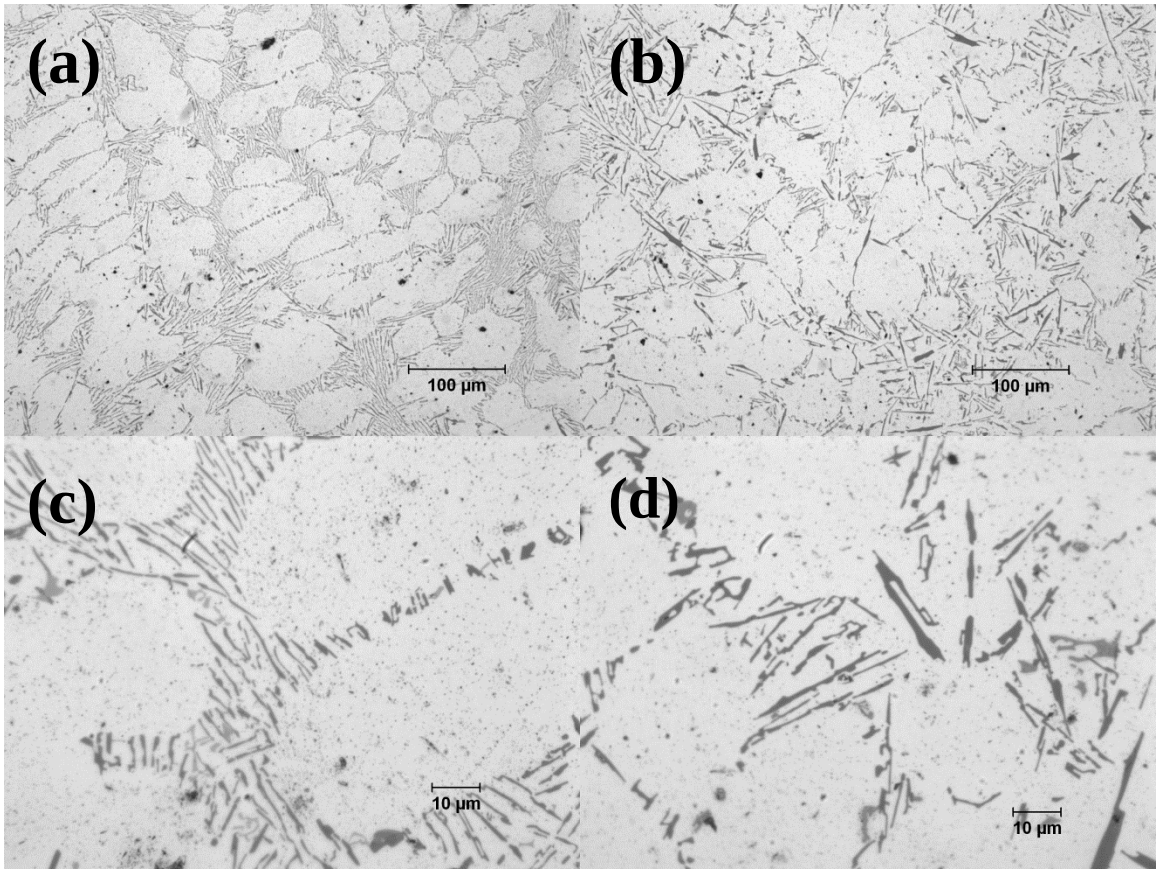

Figure 5-9 Optical Micrographs of As-cast Al-7.5Si Alloys with TSP: (a) Al-7.5Si-TSP-10 with the Objective Lens of 20x, (b) Al-7.5Si-TSP-5 with the Objective Lens of 20x, (c) Al-7.5Si-TSP-10 with the Objective Lens of 100x, (d) Al-7.5Si-6TSP-5 with the Objective Lens of 100x.

5.5 Conclusions

The eutectic Si exhibited well-modified structure after the addition of both cold-pressed pucks and pre-melted ingots. The modified structure was similar to the TSP-treated Al-12Si alloys via dip coating process. Pre-melted ingots were chosen as the optimized TSP master form due to dissolving much quicker, saving energy and production time. Besides the form of master, TSP concentration and relative amount of master alloys were investigated at 25-kg laboratory scale. Similar modified Si morphology was observed in the based alloy with the A4047-TSP masters containing 2, 4 and 6% TSP. To optimize the modification efficiency, the A4047-6TSP was selected as a master alloy. Well-modified Si morphology was observed with TSP addition using both 25% and 10% A4047-6TSP master. However, the Si became coarse with only 5% A4047-6TSP in the Al-7.5Si base alloys, suggesting that more than 5% of A4047-6TSP is required to effectively modify Si in the Al-7.5Si alloy.

Chapter 6 Aluminum Silicon Binary Alloys Modification

6.1 Background

Al-Si based casting alloys have been used in automobile industry to improve energy efficiency by reducing vehicle bodyweight. However, as compared to steel, Al-Si casting alloys have shown relatively low strength and ductility, which limit their applications as structural components. To improve their overall mechanical, grain refiner or chemical modifier has been added into base alloy, which enhances the overall mechanical properties through microstructure refinement. For example, titanium (Ti)/ boron (B) can react with Al to form intermetallic compounds (IMCs) [72], such as Al_3Ti and TiB_2. These IMCs serve as heterogeneous nucleation sites of primary Al, resulting in refined grain size. The addition of strontium (Sr) can poison the re-entrant corner or growing ledge of eutectic Si in order to modify the morphology of eutectic Si from flaky to fibrous form[62, 70]. However, as the Si content is greater than 3%, the effect of the Al-Ti-B grain refiner on changing Al grain size diminishes significantly [39, 73], which is resulting from the formation of TiSi and $TiSi_2$. Sr also suffers from an accelerated oxidation at casting temperature [56], leading to the loss of Si modification in Al-Si alloy after the second melt. Therefore, the issues of Ti poisoning and Sr fading after the addition of refiners/modifiers become major concerns for aluminum foundries and researchers.

To avoid the issues listed above, TSP has been used as a novel chemical modifier to modify the microstructure of the Al-Si eutectic alloys in our previous study at laboratory scale [109]. This chapter focuses on increasing the ductility of Al-Si casting alloys via microstructure refinement in the as-cast condition using master alloy approach at 40-kg scale, while maintaining the strength of the unmodified alloy.

6.2 Experimental

6.2.1 Materials

Commercially-pure aluminum ingot (P 0506), consists of >99.5% Al. Al-50Si master ingot. Chemical composition (nominal %): 50 Si, balance Al. A4047 powder -325 mesh (44 µm or less) from Johnson Manufacturing (Princeton, IA). Chemical composition (nominal %): 12 Si, balance Al. Trisilanolphenyl-POSS (TSP), obtained from Hybrid Plastics, Inc. (Hattiesburg, MS), was used in this study.

6.2.2 TSP Master Alloy Preparation

Two stage process is used to produce the TSP master alloy, A4047 powders with 6wt% TSP were pressed to form a cylindrical puck. The powders were pressed with a force of 40~45 KN at 180 ^{o}C and held for 10 minutes to produce a puck 31.75 millimeter in diameter. The TSP puck was melted at 700°C in a 3-kg capacity graphite crucible, using an electric melting furnace to homogenize the master alloy.

6.2.3 Casting

40 kg of the base alloy was prepared from pure Al with Al-50Si master alloy additions in an electric resistance furnace with a clay-graphite crucible at 720^{o}C. A 4-kg A4047-6TSP master alloy was added into the molten base alloy and stirred for dispersion. The molten alloy was poured into a steel mold to form torpedo shape sample. The metal mold temperature was maintained at 150^{o}C using the heated oil.

To study TSP high-temperature and remelt stability, samples were cast after 1.5 and 4 hours hold time at 720 ^{o}C. The remaining alloy was removed from the furnace. The TSP treated metal was remelted and an additional four samples were cast using 720 ^{o}C melt temperature and hold time of 24, 48, 72, and 192 hours. The entire cast specimens are listed in Table 6-1.

Table 6-1 Naming Conventions of All Cast Specimens.

Name	Holding time, hrs	Remelting	Holding time after remelting, hrs
Al-7.5Si	-	-	-
Al-7.5Si-TSP-1.5h	1.5	No	-
Al-7.5Si-TSP-4h	4	No	-
Al-7.5Si-TSP-4h-R-24h	4	Yes	24
Al-7.5Si-TSP-4h-R-48h	4	Yes	48
Al-7.5Si-TSP-4h-R-72h	4	Yes	72
Al-7.5Si-TSP-4h-R-192h	4	Yes	192

6.2.4 Characteristics

1) Optical Emission Spectrometry

A sample of molten alloy was poured to a spectrometer disk to perform qualitative and quantitative analysis of the elements with the SPECTROMAXx arc spark OES metal analyzer. For repeatablility, three measurements of the base alloy were performed.

2) Cooling Curve Analysis

An aluminum MeltLab system was used to conduct cooling curve analysis on all alloys. A steel cup with 150-gram molten sample was placed on an insulated stand and a thermocouple was position in the center of the melt. Temperature versus time data was recorded at 10 points per second till the alloy completely solidified. For repeatablility, three cooling curves were collected for each alloy.

3) Differential Scanning Calorimetry

A TA Discovery DSC250 was used to analyze the alloy. The as-cast alloy, around 8mg, was placed in a 40 μL alumina pan, and melted at 725 °C at a heating rate of 10°C/min and kept for 1 min; after pre-melting the sample was cooled to 450°C at a cooling rate of 20°C/min and then reheated up to 725°C at a heating rate of 10°C/min. Endothermic melting data was recorded as a function of temperature. For repeatablility, three samples were analyzed per condition.

4) Metallography

The cast torpedo bar was cut, exposing the middle interior region of the sample, and mounted with epoxy resins. Metallographic samples were prepared by grinding with SiC paper and then polishing with 5/0.3 μm alumina slurry and 0.05 μm colloidal silica suspension. Optical micrographs were taken using the inverted metallographic microscope, Olympus GX51, with the magnification up to 1,000X.

5) Tensile Testing

Cylindrical tensile specimens were machined from the torpedo rod with a gauge diameter of 6.35 mm and gauge length of 25.4 mm, per ASTM-B557-15 standard for room temperature testing.

6.3 Results and Discussion

6.3.1 Melt Characterization

Table 6-2 shows the average composition measured after each melt treatment. It is the challenging using a spark emission spectrometer to measure exactly TSP concentration in the alloy. However, the Si concentration was increased by 0.1 to 0.2 wt% for the samples containing TSP due to the Si element in TSP. Future study will be necessary to develop an alternative approach to characterize the TSP concentration in the alloy.

Table 6-2 Chemical Composition in wt% of the Al-7.5Si Alloy with and without TSP.

Alloy	Si	Fe	Al
Al-7.5Si	7.51	0.15	Balance
Al-7.5Si-TSP	7.59	0.14	Balance

6.3.2 Solidification and Melting

1) Cooling Curve Analysis

TSP depressed the first arrest of Al-7.5Si alloy during cooling. The cooling curves of the Al-7.5Si alloy with and without TSP are shown in Figure 6-1. Two major temperature arrests are observed on the cooling curve of the Al-7.5Si base alloy in Figure 6-1a. The first arrest represents the solidification of primary Al dendrites, while the second arrest represents the solidification of the Al-Si eutectic. In order to quantitatively compare the solidification behavior of these alloys, the first derivative was plotted in Figure 6-1. Selected characteristic temperatures taken from cooling curves are listed in Table 6-3. It can be noted that the nucleation, local minimum, and maximum temperatures of primary Al were reduced by 9, 5, and 6 °C with TSP addition. Also, the undercooling, which is equal to the difference between nucleation and local minimum, was changed from 7°C for the base alloy to 3°C for the alloy containing TSP. The undercooling and arrest temperature during the formation of the Al-Si eutectic was reduced with TSP additions, which can be explained by the restricted TPRE growth mechanism.

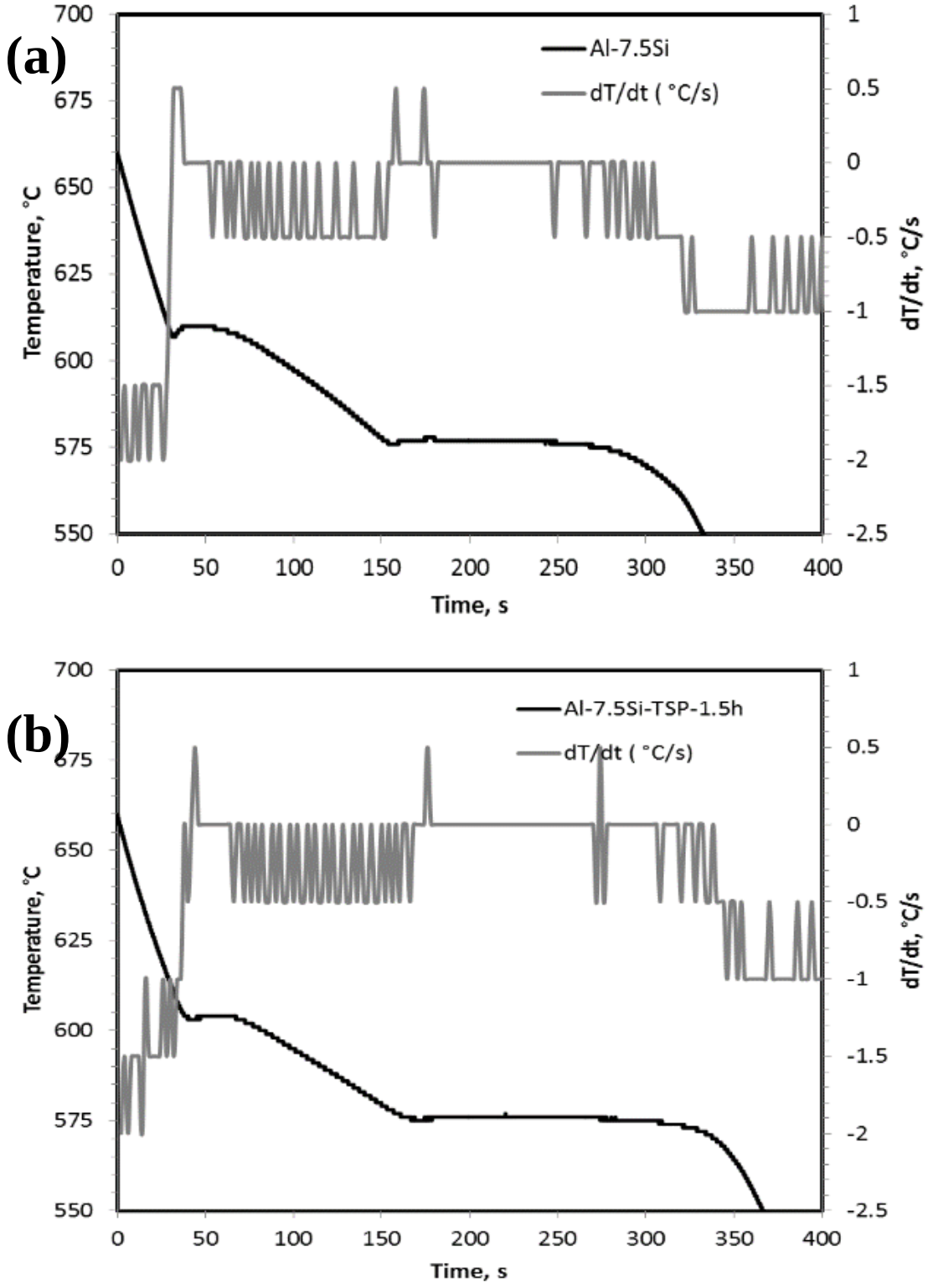

Figure 6-1 Cooling Curve and its First Derivative of (a) Al-7.5Si and (b) Al-7.5Si-TSP-1.5h.

Table 6-3 Selected Characteristic Temperatures Taken from Cooling Curves.

Alloy	TAl nuc (°C)	TAl min (°C)	TAl max (°C)	TAl-Si nuc (°C)	TAl-Si arr (°C)
Al-7.5Si	615	608	610	577	577
Al-7.5Si-TSP-1.5h	606	603	604	574	574

*Each value in the table is the average of three measurements.

2) Differential Scanning Calorimetry Analysis

DSC heating curves of the Al-7.5Si alloy with and without TSP are shown in Figure 6-2. Onset and peak melting temperature of the Al-Si eutectic are listed in Table 5-4. TSP additions did not change the onset and peak melting temperatures of the Al-Si eutectic, suggesting that the formation of Al-Si eutectic with TSP additions are thermodynamically stable. However, there is a noticeable shoulder at around 578°C observed from the alloy with TSP additions, which supports the proposed nucleation mechanism: TSP aids nucleation of eutectic Si due to low lattice mismatch. The peak melting temperature of primary Al and the total enthalpy during the melting are also listed in Table 6-4. TSP addition reduced the peak melting temperature of primary Al by about 5 °C, which is consistent with the cooling curves results.

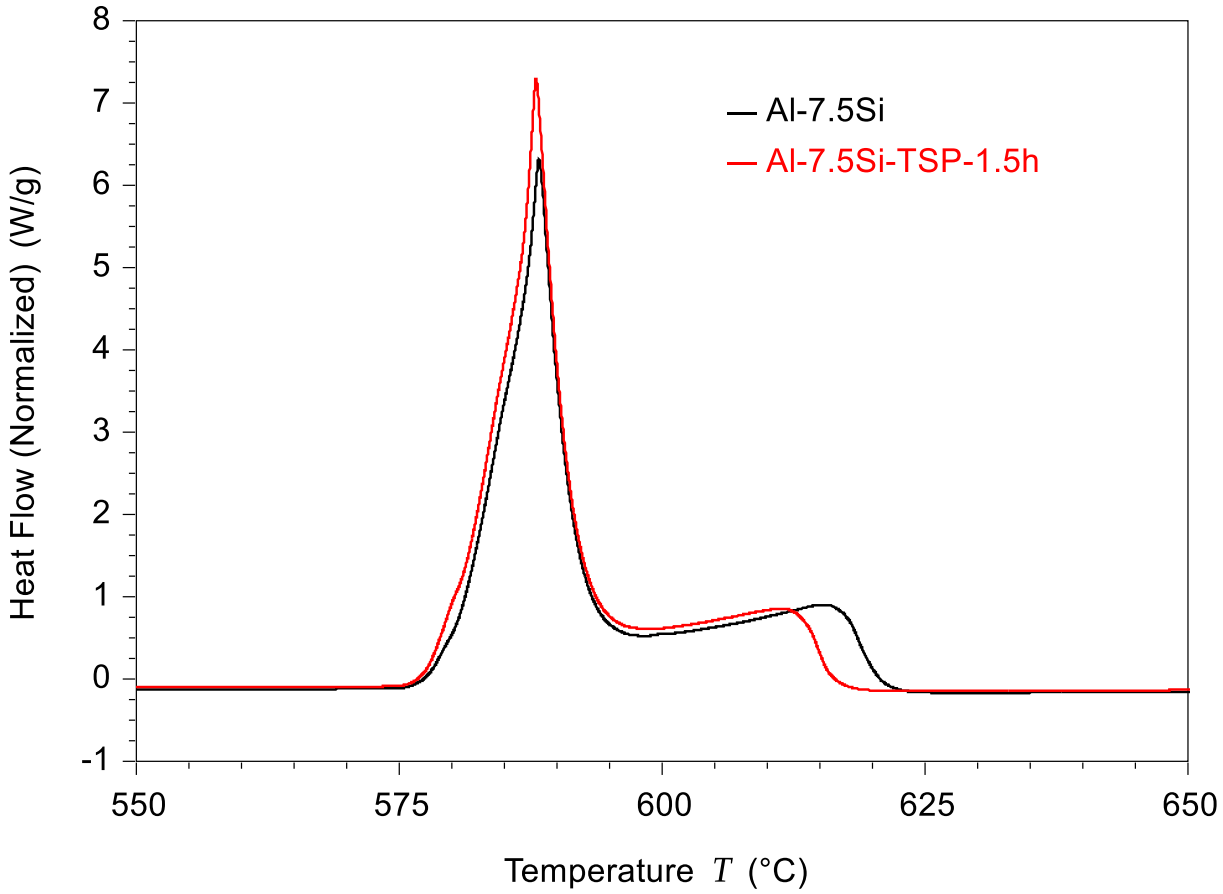

Figure 6-2 DSC Heating Curves of the Al-7.5Si Alloy with and without TSP.

Table 6-4 Selected Characteristic Temperatures Taken from DSC Heating Curves.

Alloy	TAl-Si onset (°C)	TAl-Si peak (°C)	TAl peak (°C)	Enthalpy (J/g)
Al-7.5Si	577	588	616	386
Al-7.5Si-TSP-1.5h	577	588	611	402

*Each value in the table is the average of three measurements.

6.3.3 As-cast Microstructures

Typical phases presented in Al-7.5Si are primary Al and Al-Si eutectic, where eutectic Si appears as dark phase in optical micrographs. Figure 6-3 shows optical micrographs of the Al-7.5Si alloy with and without TSP additions. It is widely known that Sr modified the eutectic Si through poisoning the re-entrant corner or growing ledge. The arrest temperature of the Al-Si eutectic after Sr addition is decreased, while the undercooling is increased significantly. In our case, TSP serves the same role in modifying Si morphology as Sr in terms of microstructure. However, there might be a completely new mechanism for the Al-Si alloys with TSP addition based on the thermal analysis. Since there is a barely change in the undercooling of the Al-Si eutectic during solidification, TSP gets involved during the eutectic reaction. There is also a small shoulder observed in the DSC melting curve near the onset melting of the Al-Si eutectic, suggesting that TSP might offer an aiding effect on the nucleation of eutectic microconstituents during solidification.

The secondary dendrite arm spacing (SDAS) of the Al-7.5Si alloy was slightly reduced with TSP additions. The SDAS values of primary Al in both Al-7.5Si and Al-7.5Si-TSP were measured using the ImageJ software. The SDAS of primary Al in the Al-7.5Si base alloy was 25 μm while the average SDAS in Al-7.5Si-TSP-1.5h was decreased to 18 μm. The reduced SDAS with TSP additions can be due to the decreased nucleation, growth temperatures during the solidification of primary Al. After the TSP addition, the primary Al arrest exhibited much less amount of undercooling as the base alloy suggesting that TSP can aid the nucleation process of primary Al as well.

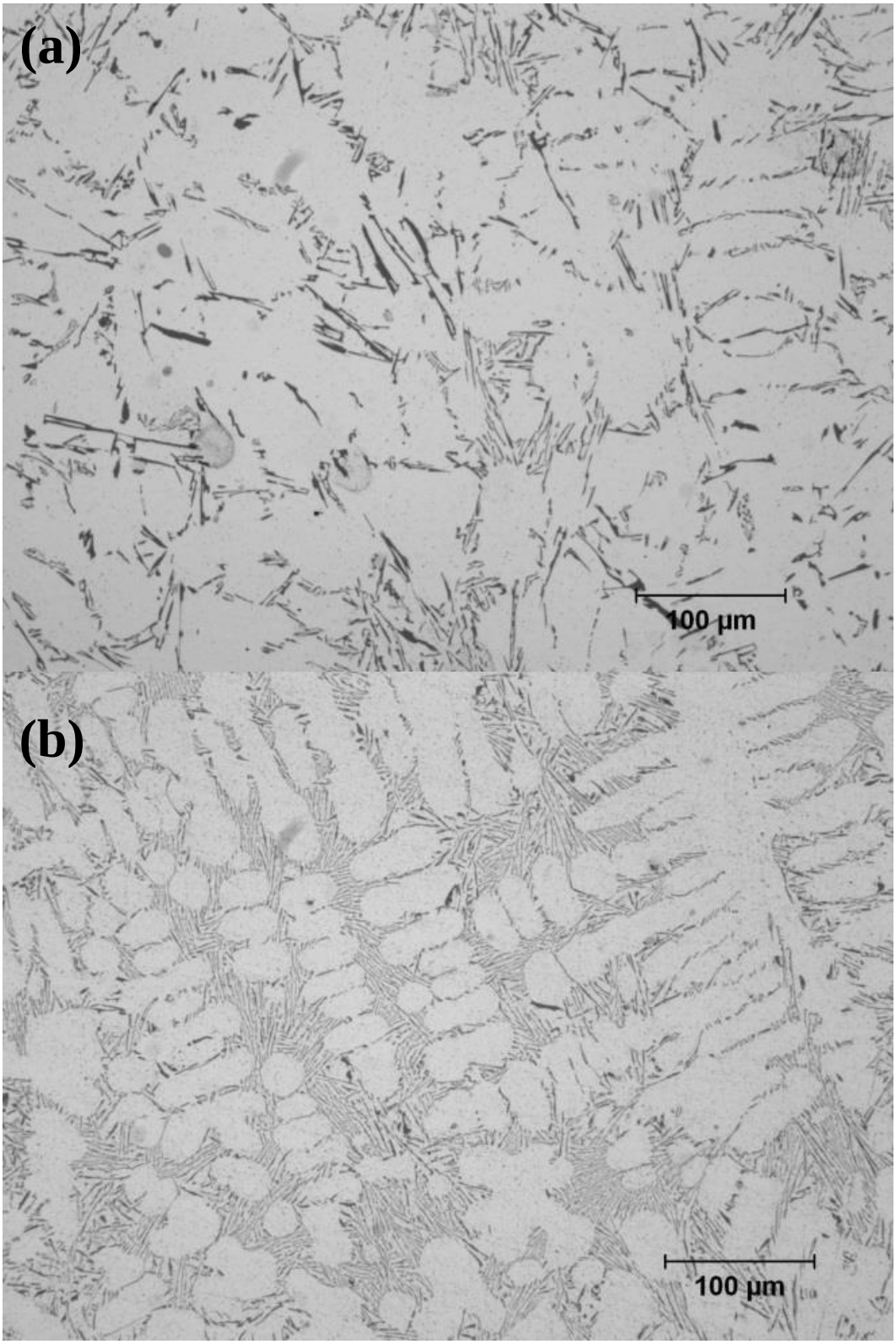

Figure 6-3 Optical Micrographs of the Al-7.5Si Alloy with and without TSP: (a) Al-7.5Si, (b) Al-7.5Si with TSP Additions after 1.5-hour Hold in 720 ^{o}C Furnace.

6.3.4 Tensile Properties

The tensile properties of the Al-7.5Si alloy were improved with TSP additions. The engineering stress-strain curves of the Al-7.5Si alloy with and without TSP additions at room temperature are given in Figure 6-4. Ductility increased from 4.5% with no TSP additions to 6% with TSP additions. The addition of TSP increased the ductility of the Al-7.5Si alloy by 50% without sacrificing the strength. Ultimate tensile strength and ductility as determined from the stress-strain curves are shown in Figure 6-5. The increase in ductility is due to the modified Si morphology from flaky to fibrous form after TSP additions.

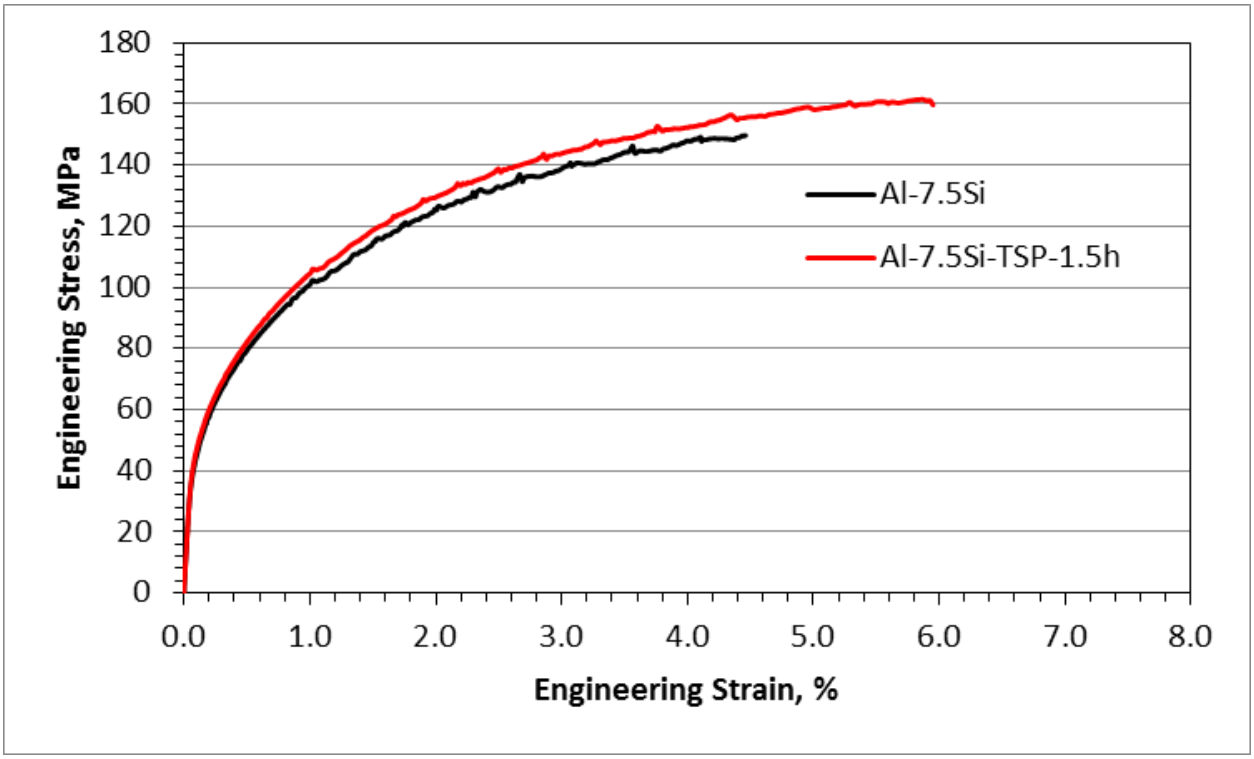

Figure 6-4 Stress-strain Curves of the Al-7.5Si Alloy with and without TSP at Room Temperature.

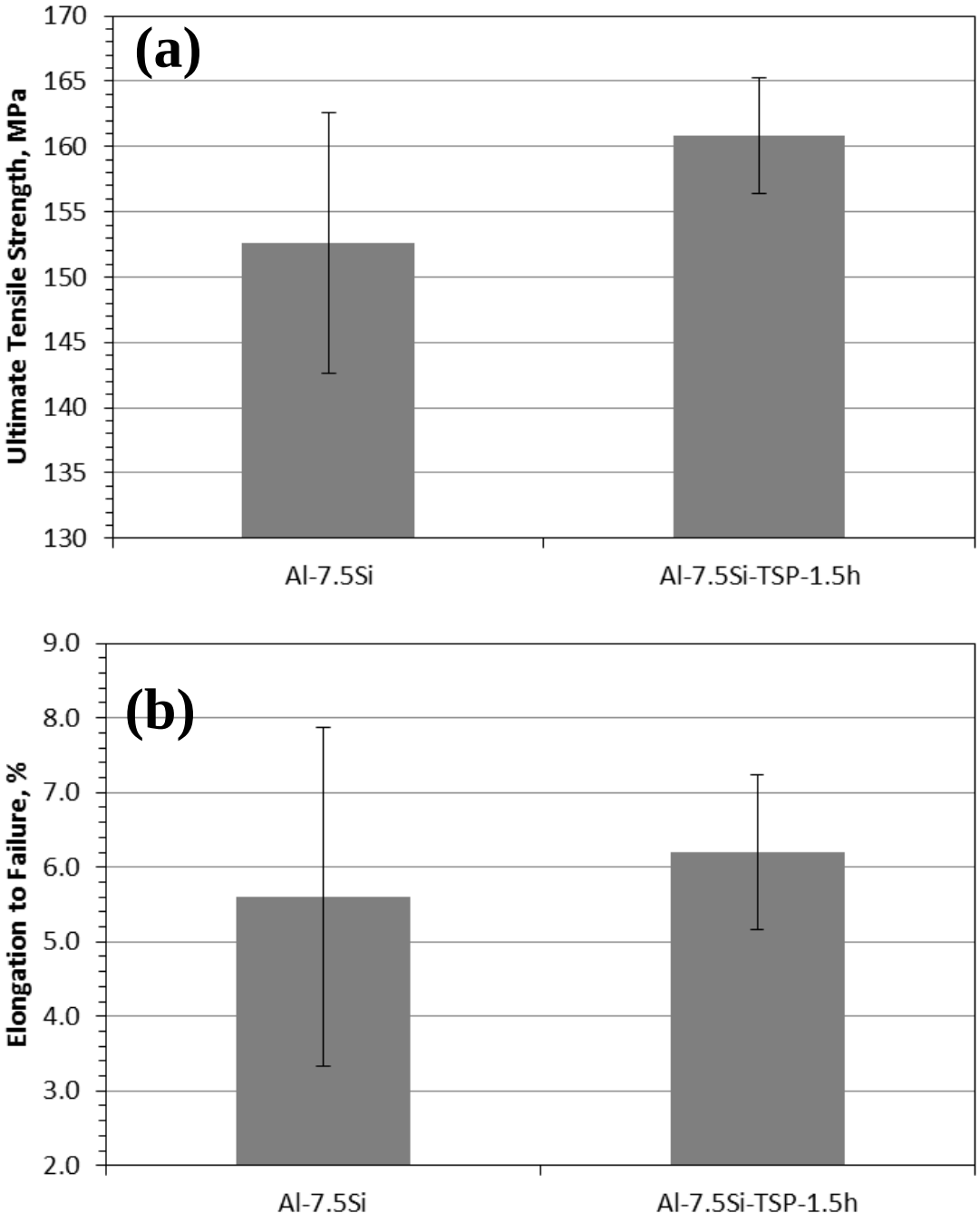

Figure 6-5 Tensile Strength (a) and Ductility (b) of the Al-7.5Si Alloy with and without TSP.

6.3.5 Additive Stability

1) Effect of Holding Time

Both solidification and melting behavior of the Al-7.5Si alloy with TSP addition are maintained after 1.5- and 4-hours furnace hold at 720 ^{o}C. Figure 6-6 shows MeltLab cooling curves and Figure 5-7 shows the DSC heating curves of the Al-7.5Si, Al-7.5Si-TSP-1.5h, and Al-7.5Si-TSP-4h alloys. In Figure 6-6, reduced undercooling and depressed arrest temperature of both proeutectic and eutectic microconstituent still appear after hold TSP in 720 ^{o}C furnace for 4 hours. Also, the Al-7.5Si-TSP-4h alloy still shows a small shoulder near the Al-Si eutectic onset. Typically, the level of Sr present in the melt decrease with time, which is one of the major disadvantages of Sr usage. It is reported that Sr can completely burns off after holding in the melt for 4 hours as oxidation is the primary mechanism for Sr loss. In our study, both the MeltLab cooling curve and the DSC heating curve of the Al-7.5Si-TSP-4h alloy exhibit the same characteristics as the Al-7.5Si-TSP-1.5h alloy, suggesting that no TSP fading can be observed after 4-hour hold in 720 ^{o}C furnace. More importantly, the modified morphology and improved tensile properties are still maintained as shown in Figure 6-8 and 6-9.

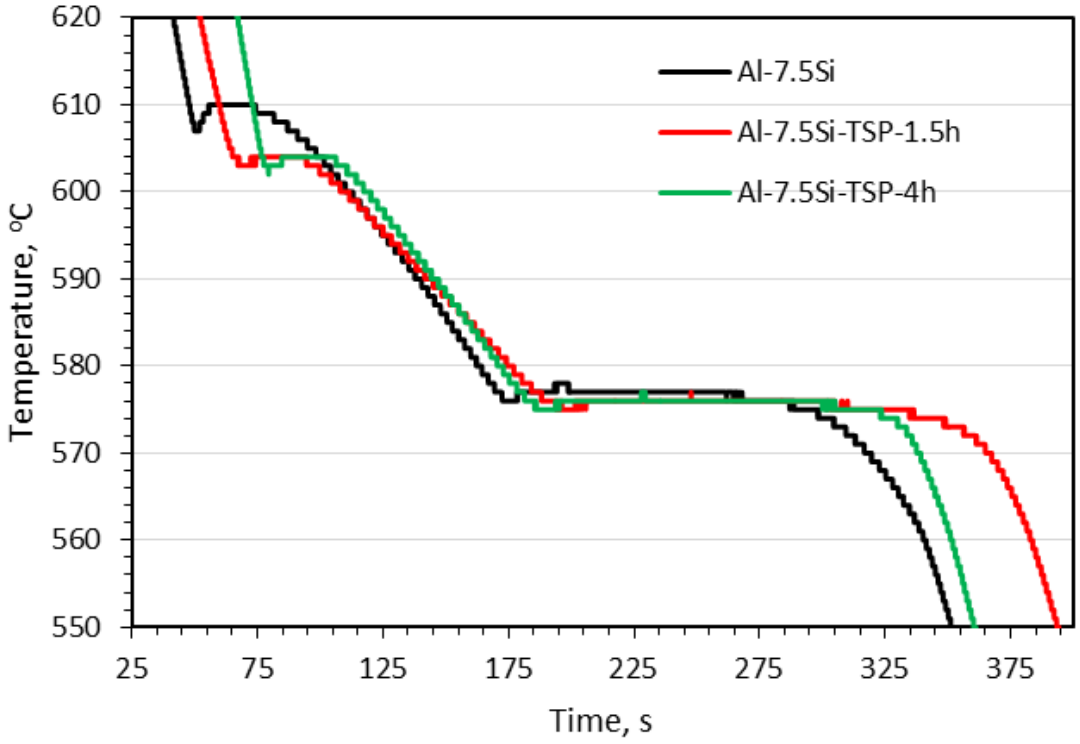

Figure 6-6 Cooling Curves of the Al-7.5Si, Al-7.5Si-TSP-1.5h, and Al-7.5Si-TSP-4h Alloys.

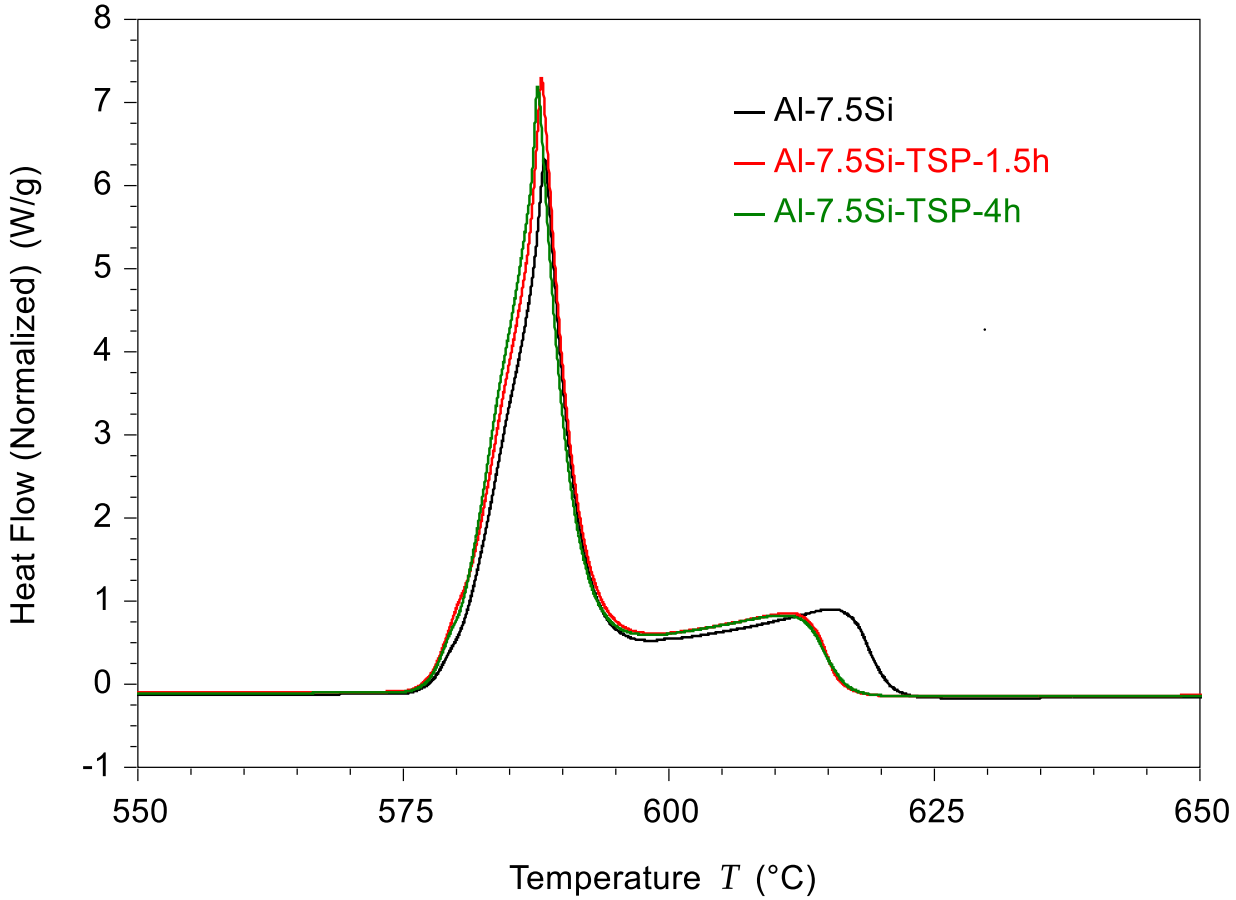

Figure 6-7 DSC Heating Curves of the Al-7.5Si, Al-7.5Si-TSP-1.5h, and Al-7.5Si-TSP-4h Alloys.

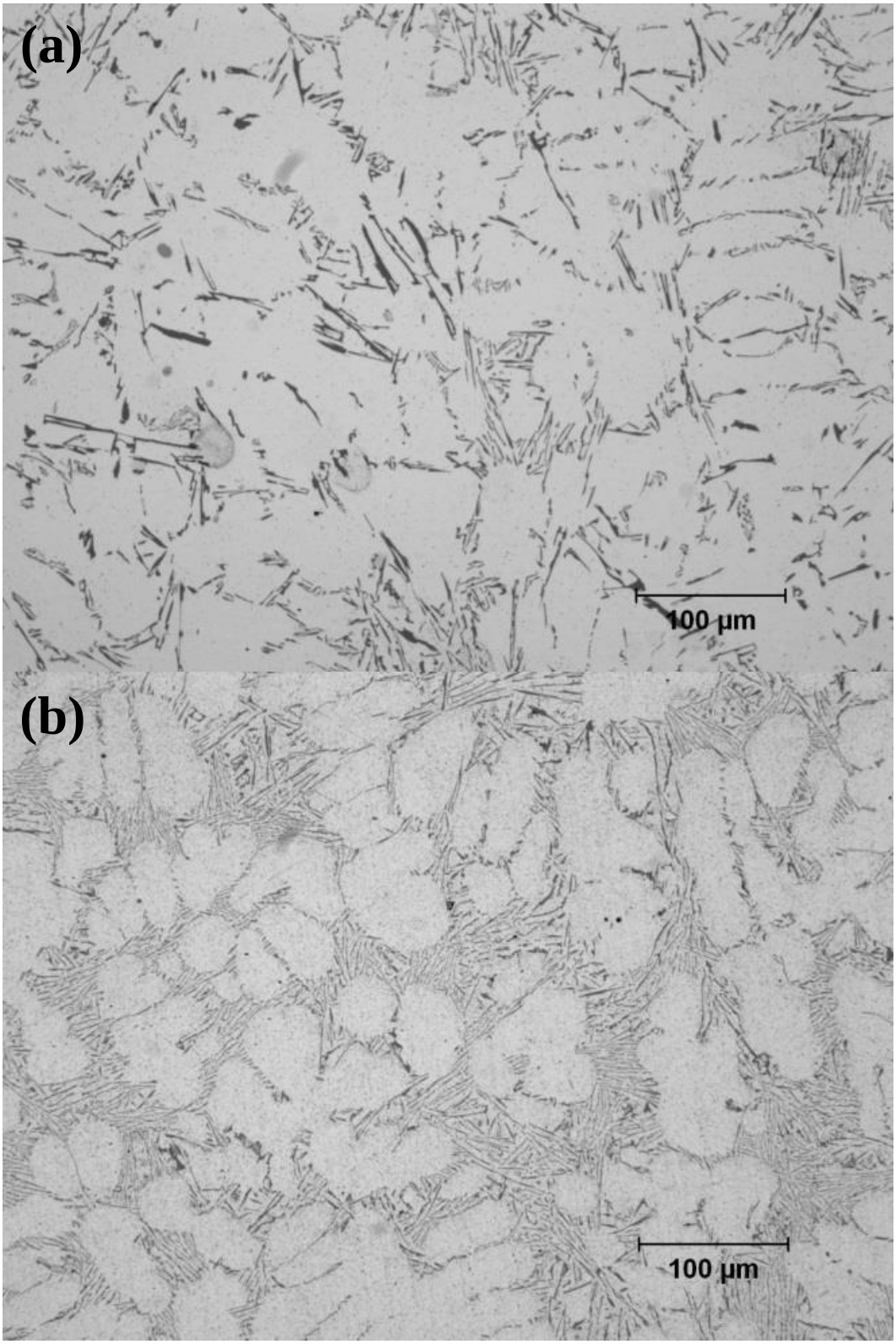

Figure 6-8 Optical Micrographs of the Al-7.5Si and Al-7.5Si-TSP-4h Alloys. (a) Al-7.5Si, (b) Al-7.5Si With TSP Additions After 4-hour Hold in 720 ^{o}C Furnace.

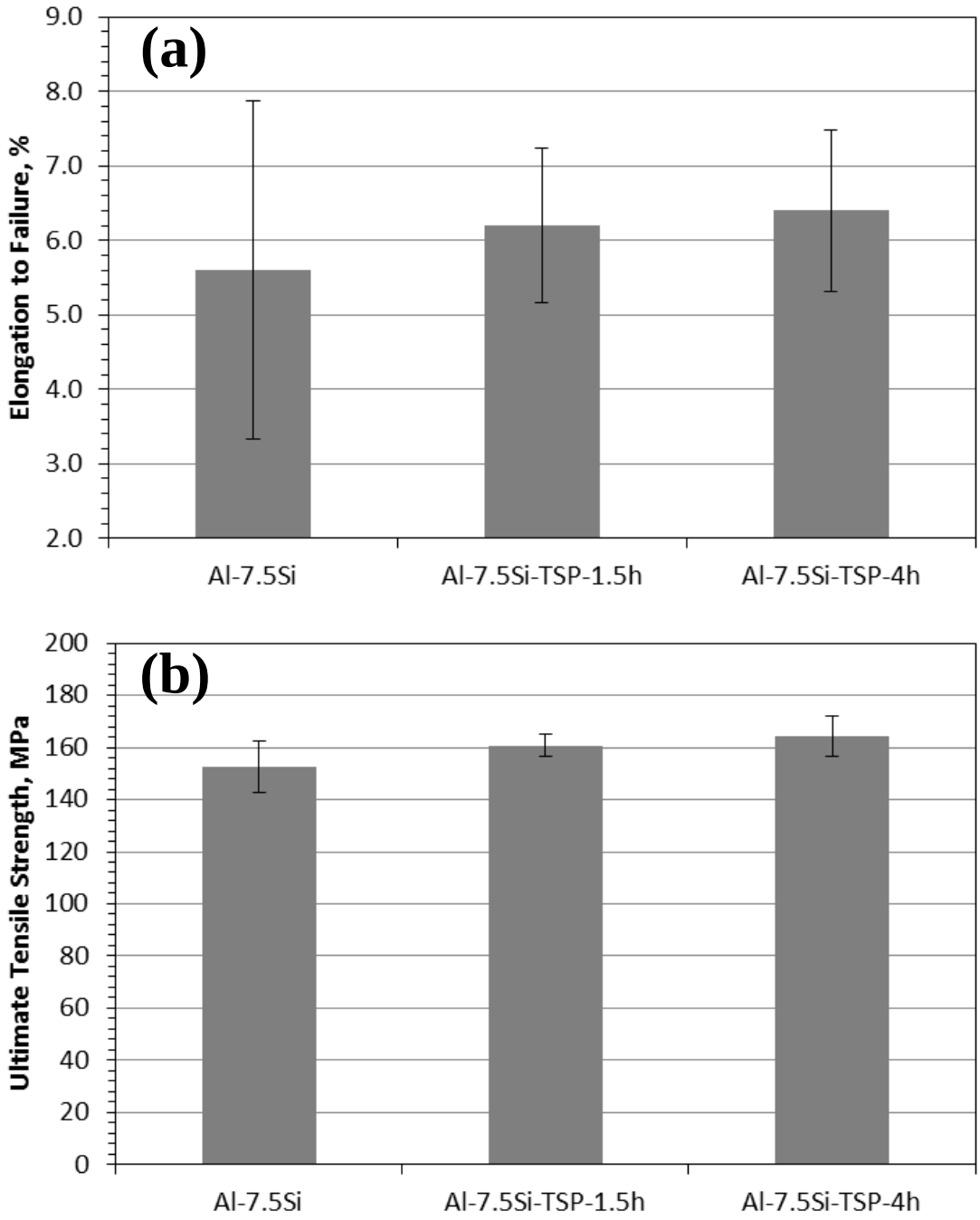

Figure 6-9 Tensile Strength (a) and Ductility (b) of the Al-7.5Si, Al-7.5Si-TSP-1.5h, and Al-7.5Si-TSP-4h Alloys.

2) Effect of Re-Melting

The microstructure modification and solidification behavior of the Al-7.5Si-TSP alloys are still valid after remelting 4-hour-hold Al-7.5Si-TSP alloy and held in the 720 ^{o}C furnace for up to 196 hours. Figure 6-10 shows the cooling curves of all remelted Al-7.5Si-TSP alloys with different furnace holding time. It can be clearly seen that remelting does not change the temperature characteristics of both primary Al and Al-Si eutectic, such as undercooling, and arrest temperatures. Minimal fade was observed after re-melting. In comparison, melt loses 30-50% of Sr on remelting without additional furnace holding [110]. Our study shows the eutectic Si in all remelted Al-7.5Si-TSP alloy still exhibit well-modified Si morphology as shown in Figure 6-11.

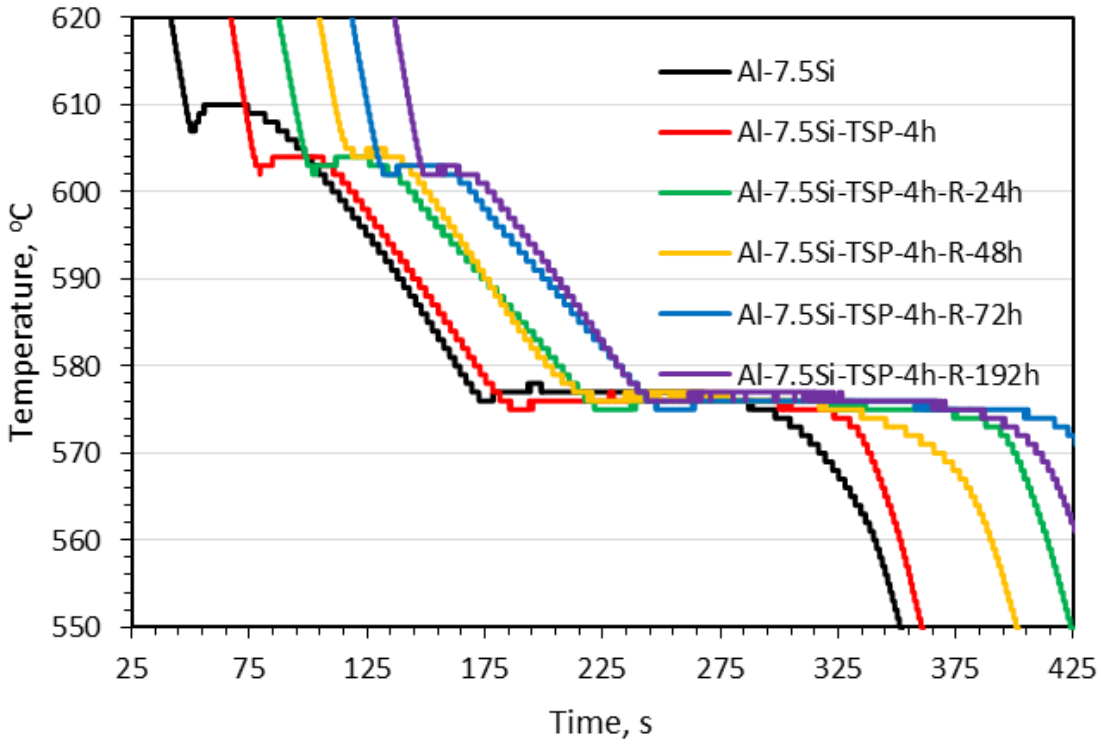

Figure 6-10 Cooling Curves of the Al-7.5Si, Al-7.5Si-TSP-4h, and Al-7.5Si-TSP-4h-R-X. X=24, 48, 72, and 192h.

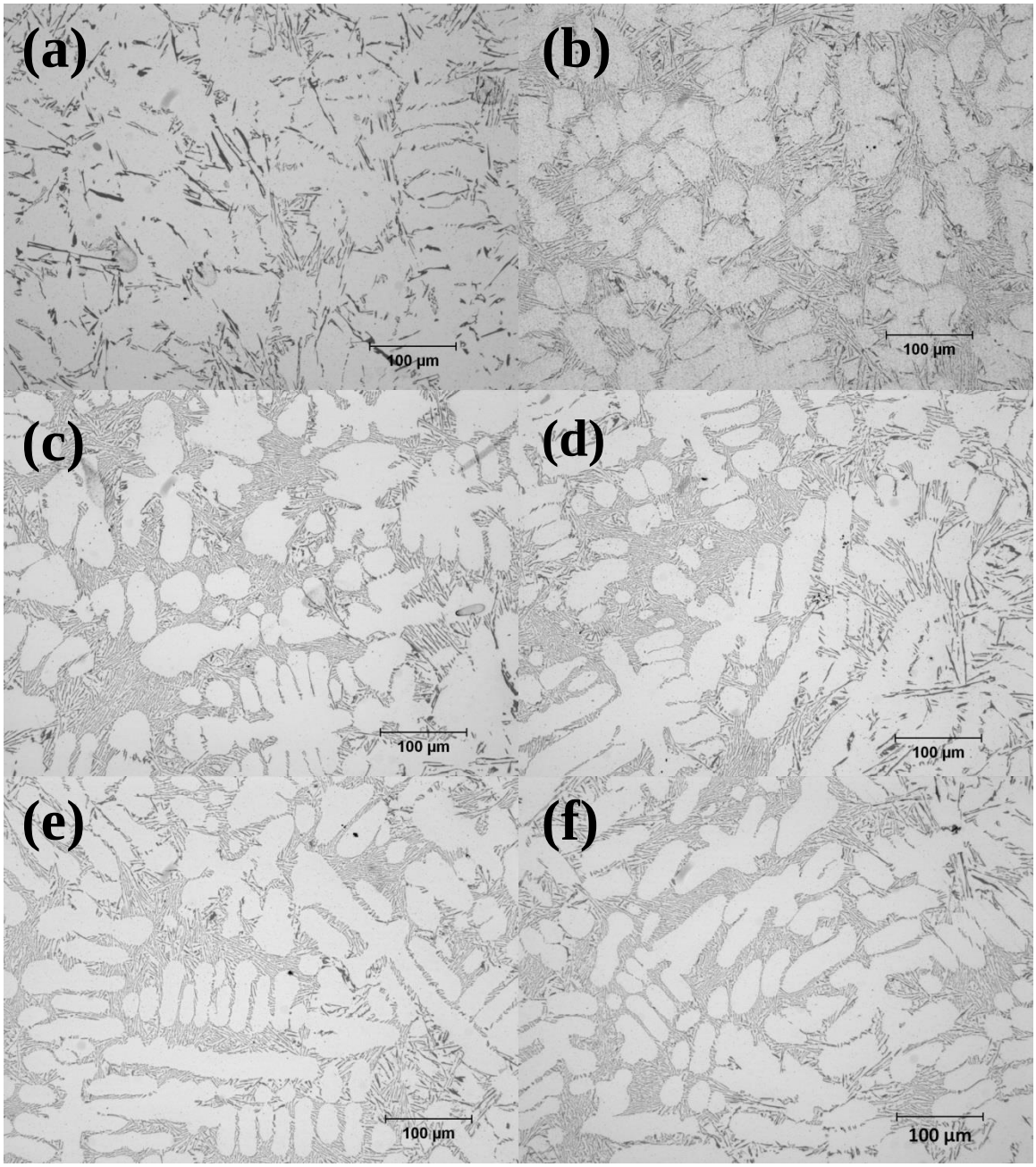

Figure 6-11 Optical Micrographs of the Al-7.5Si, Al-7.5Si-TSP-4h, and Al-7.5Si-TSP-4h-R-X. X=24, 48, 72, and 192h: (a) Al-7.5Si, (b) Al-7.5Si with TSP Additions after 4-hour Hold in 720 ^{o}C Furnace, (c) Al-7.5Si with TSP Additions after Remelting 4-hour-hold Al-7.5Si-TSP Alloy and Additional **24-hour** Hold in 720 ^{o}C Furnace, (d) Al-7.5Si with TSP Additions after Remelting 4-hour-hold Al-7.5Si-TSP Alloy and Additional **48-hour** Hold in 720 ^{o}C Furnace, (e) Al-7.5Si with TSP Additions after Remelting 4-hour-hold Al-7.5Si-TSP Alloy and Additional **72-hour** Hold in 720 ^{o}C Furnace, (f) Al-7.5Si with TSP Additions after Remelting 4-hour-hold Al-7.5Si-TSP Alloy and Additional **192-hour** Hold in 720 ^{o}C Furnace.

6.4 Conclusions

In this study, a novel chemical modifier with extraordinary thermal stability was developed, which shows 50% improvement over the Al-7.5Si alloy in ductility without sacrificing the strength. The microstructure of both primary Al and eutectic microconstituents of the Al-7.5Si alloy with TSP addition was refined, and the modified microstructure was well maintained after remelting with additional 192 hours held in the 720°C furnace. The addition of TSP reduced the undercooling and arrest temperatures of both proeutectic and eutectic microconstituents and caused the formation of a small shoulder near the eutectic onset melting temperature. These results suggest that the presence of TSP in hypoeutectic Al-Si alloys not only has aiding effect on nucleation of both proeutectic and eutectic microconstituents, but also restrict the growth ability of eutectic Si. TSP as a novel high-stable modifier is a further advantageous alternative in recycling operations.

Chapter 7 Commercial Cast Aluminum Silicon Based Alloys Modification

7.1 Background

Lightweight materials, such as aluminum (Al), magnesium (Mg), and titanium (Ti) alloys, are essential for improving fuel economy in automotive industry [111-114]. The ability to integrate into vehicle depends on their properties and the associated manufacturing processes. The mechanical properties are directly related to their microstructures which depend strongly both on the composition and the solidification process. A wide range of alloying elements are added into the alloy as grain refiners, solid solution strengtheners, or intermetallic compounds. The mechanical strength can be enhanced by grain size reduction or precipitation strengthening mechanisms. For example, titanium (Ti)/ boron (B) can react with Al to form intermetallic compounds (IMCs) [72], such as Al_3Ti and TiB_2. These IMCs serve as heterogeneous nucleation sites of primary Al, resulting in refined grain size. Mg and Si were added into Al to increase strength by solid solution strengthening and precipitation hardening mechanism with the formation of Mg_2Si IMCs. Cu was added into Al alloy to increase strength and fatigue life with the formation of Al_2Cu IMCs as well. Therefore, 319-type Al-Si-Cu casting alloys are widely used in automotive industry in the production of engine blocks, cylinder head and body panel [115]. To further reduce body weight, high performance alloys were designed specifically for structural applications. High amount of Si offers very good fluidity. High-Si containing Aural^{TM} 2-type alloys are well suited to the casting of thin and large structural components, such as shock towers, crash system, and space frames [116].

However, ductility is dramatically sacrificed when an alloy is strengthened with the alloying elements additions. This study focuses on the effects of TSP additions on the casting, solidification and mechanical properties of cast Al-Si based commercial alloys at 40-kg scale.

The alloys used for this study are based on Aural^{TM} 2 and Ford-W319, which are used in the production of structural components and engine parts respectively.

7.2 Experimental

7.2.1 Materials

Commercially-pure aluminum ingot (P 0506), consists of >99.5% Al. Commercially-pure Cu rod, consists of >99.9% Cu. Commercially-pure Mg ingot, consists of>99.9% Mg. Al-50Si master ingot. Chemical composition (nominal %): 50 Si, balance Al. Al-10Mn master ingot. Chemical composition (nominal %): 10 Mn, balance Al. Al-6Ti master ingot. Chemical composition (nominal %): 6 Ti, balance Al. A4047 powder -325 mesh (44 μm or less) from Johnson Manufacturing (Princeton, IA). Chemical composition (nominal %): 12 Si, balance Al. Trisilanolphenyl-POSS (TSP), obtained from Hybrid Plastics, Inc. (Hattiesburg, MS), was used in this study.

7.2.2 TSP Master Alloy Preparation

Two stage process is used to produce the TSP master alloy. A4047 powders with 6wt% TSP were pressed to form a cylindrical puck. The powders were pressed with a force of 40~45 KN at 180 ^{o}C and held for 10 minutes to produce a puck 31.75 millimeter in diameter. The TSP puck was melted at 700°C in a 3-kg capacity graphite crucible, using an electric melting furnace to homogenize the master alloy.

7.2.3 Casting

40 kg of the base alloy was prepared from pure Al with master alloy additions in an electric resistance furnace with a clay-graphite crucible at 720^{o}C. A 4-kg A4047-6TSP master alloy was added into the molten base alloy and stirred for dispersion. The molten alloy was poured into a steel mold to form torpedo shape sample. The metal mold temperature was maintained at 150^{o}C using the heated oil.

7.2.4 Characteristics

1) Optical Emission Spectrometry

A sample of molten alloy was poured to a spectrometer disk to perform qualitative and quantitative analysis of the elements with the SPECTROMAXx arc spark OES metal analyzer. For repeatability, three measurements of the base alloy were performed.

2) Scanning Electron Microscopy

To examine the three-dimensional nature of the eutectic Si, a polished specimen was deep etched in 1wt% NaOH solution for 30 min at 333 K. A deep-etched microstructure was characterized in the as-cast condition using a JSM-6610LV scanning electron microscopy (SEM).

In addition, the Al grain size of the polished sample in the epoxy mount was evaluated using a JSM-6610LV SEM equipped with electron backscatter diffraction (EBSD) analysis systems. The accelerating voltage used was 20 kV. A 3-μm step size was used for EBSD scans. To reduce the charging effects inside the SEM from the nonconductive epoxy mount, the areas surrounding a sample were covered with conductive carbon paint.

3) Cooling Curve Analysis

An aluminum MeltLab system was used to conduct cooling curve analysis on all alloys. A steel cup with 150-gram molten sample was placed on an insulated stand and a thermocouple was position in the center of the melt. Temperature versus time data was recorded at 10 points per second till the alloy completely solidified. For repeatability, three cooling curves were collected for each alloy.

4) Differential Scanning Calorimetry

A TA Discovery DSC250 was used to analyze the alloy. The as-cast alloy, around 8mg, was placed in a 40 μL alumina pan, and melted at 725 °C at a heating rate of 10°C/min and kept

for 1 min; after pre-melting the sample was cooled to 450°C at a cooling rate of 10°C/min and then reheated up to 725°C at a heating rate of 10°C/min. Endothermic melting data was recorded as a function of temperature. For repeatability, three samples were analyzed per condition.

5) Metallography

The cast torpedo bar was cut, exposing the middle interior region of the sample, and mounted with epoxy resins. Metallographic samples were prepared by grinding with SiC paper and then polishing with 5/0.3 μm alumina slurry and 0.05 μm colloidal silica suspension. Optical micrographs were taken using the inverted metallographic microscope, Olympus GX51, with the magnification up to 1,000X.

6) Heat Treatment

Prior to mechanical testing, all samples were subjected to a T7-type heat treatment. The heat treatment is of considerable practical importance since it has a strong effect on the ductility of the material. The procedure for this heat treatment is as follows:

Step 1. Each sample was solutionized at 723 K for 90 minutes;

Step 2. After solutionization the sample was quenched in room temperature water;

Step 3. The sample was then artificially aged at 498K for 90 minutes.

7) Mechanical Property Testing

a. Tensile Testing

Cylindrical tensile specimens were machined from the T7- heat treated torpedo bar with a gauge diameter of 6.35 mm and gauge length of 25.4 mm, per ASTM-B557-15 standard for room temperature, 150℃, and 300℃ testing. Five samples per alloy condition were tested and averaged to determine yield stress, ultimate tensile stress, and elongation to failure for each alloy.

b. Fatigue Testing

Cylindrical fatigue specimens were machined from the T7- heat treated torpedo bar with a gauge diameter of 6.35 mm and gauge length of 25.4 mm, per ASTM-E466 standard for room temperature testing. The room temperature high cycle fatigue (HCF) test was performed under stress control on a servohydraulic testing machine. For each alloy there were 24 samples tested to develop the staircase (16 specimens) and in addition, the incremental stress tests (8 specimens). The HCF data were processed in-house using Random Fatigue Limit model.

7.3 Results and Discussion

7.3.1 Melting Characterization

Tables 7-1 and 7-2 shows the average composition of Aural^{TM} 2 and W319 measured after each melt treatment. Aural^{TM} 2 base alloy contains 11wt% Si with 0.3% Mg, 0.5wt% Mn, and 0.2 wt% Fe additions. W319 base alloy comprises 7.8 wt% Si, 3.3wt% Cu, 0.2 wt% Mg, and 0.1wt% Ti. The Sr level in both of Sr-containing alloys was about 125 ppm.

Table 7-1 Chemical Composition in wt% of the Aural™ 2 Alloys.

	Si	Mg	Mn	Fe	Sr (ppm)	Al
Aural™ 2	11.12	0.31	0.54	0.20	-	Balance
Aural™ 2-TSP	10.94	0.34	0.53	0.27	-	Balance
Aural™ 2 - Sr	10.78	0.26	0.53	0.27	125	Balance

Table 7-2 Chemical Composition in wt% of the W319 Alloys.

	Si	Cu	Mg	Ti	Fe	Sr (ppm)	Al
W319	7.7	3.3	0.2	0.11	0.12	-	Balance
W319-TSP	8.0	3.2	0.2	0.13	0.13	-	Balance
W319-Sr	7.7	3.3	0.2	0.13	0.15	125	Balance

7.3.2 Casting Properties

One of the casting defects occur during solidification is solidification shrinkage. Figure 7-1 shows the top-view images of Aural™ 2 castings: Aura™l 2 base alloys, Aural™ 2 – TSP alloys, and Aural™ 2 – Sr alloys. Aural™ 2 base alloys shrink when they solidify, and the riser of torpedo-shaped castings is to supply the feed metal. Solidification cracks were observed on the top of Aural™ 2 base alloys in Figure 7-1. This is due to the volumetric change during solidification. This volumetric change was significantly reduced with Sr addition. TSP addition also reduced solidification shrinkage of Aural™ 2 alloys.

Similar effect on solidification shrinkage with TSP additions was observed on W319 alloys. Figure 7-2 shows a top-view image of W319 castings with and without TSP additions. Same amount of W319 melt was poured into steel mold. The casting with TSP additions shows less surface shrinkage as compared to the W319 base alloys.

Figure 7-1 A Top-view Image of Aural™ 2 Castings: Aural™ 2 Control, Aural™ 2 – TSP, and Aural™ 2 – Sr Alloys.

Figure 7-2 A Top-view Image of W319 Castings: W319 Control and W319-TSP Alloys.

7.3.3 Solidification and Melting

1) Aural™ 2 Alloys

Figure 7-3 shows the DSC endothermic and exothermic curves of Aural™ 2 alloys. The corresponding constituents, such as primary Al and Al-Si eutectic, are indicated on these curves. In the Aural™ 2 base alloy, two major temperature arrests are observed on the exothermic curve of the Aural™ 2 base alloy. The first arrest represents the solidification of primary Al dendrites, and the second arrest represents the solidification of the Al-Si eutectic. However, only one major temperature arrest appears on the endothermic curve. This is primarily due to the casting history, resulting in an overlap of these two microconstituents. Figure 7-4 overlays the DSC data plots of Aural™ 2, Aural™ 2 with TSP additions, and Aural™ 2 with Sr additions. There is no significant change observed on the endothermic curves for the alloys with and without TSP/Sr addition. However, TSP additions depress the Al-Si eutectic arrest temperature by about 8 °C, suggesting TSP restricts the TPRE growth of Si eutectic. The depressed temperature also appears on the exothermic curve of Aural™ 2 – Sr.

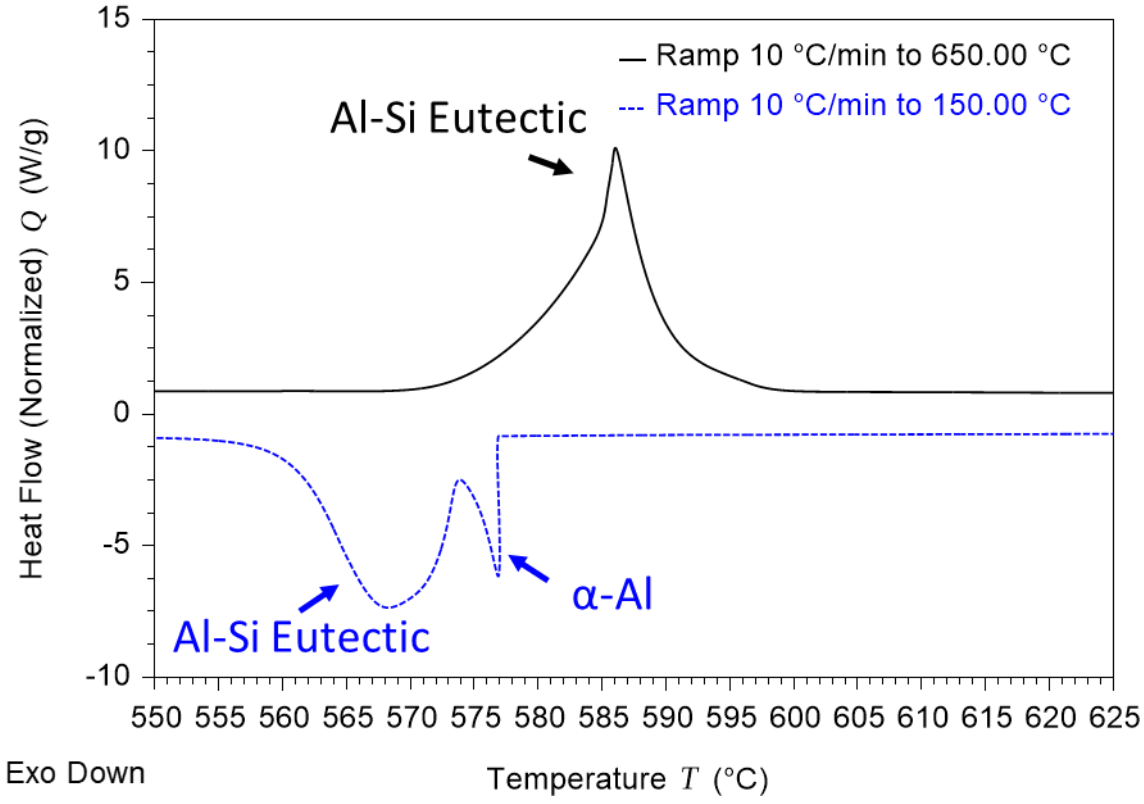

Figure 7-3 Typical DSC Endothermic (Top) and Exothermic (Bottom) Curves of Aural™ 2, Containing the Primary Al and Al-Si Eutectic Microconstituent.

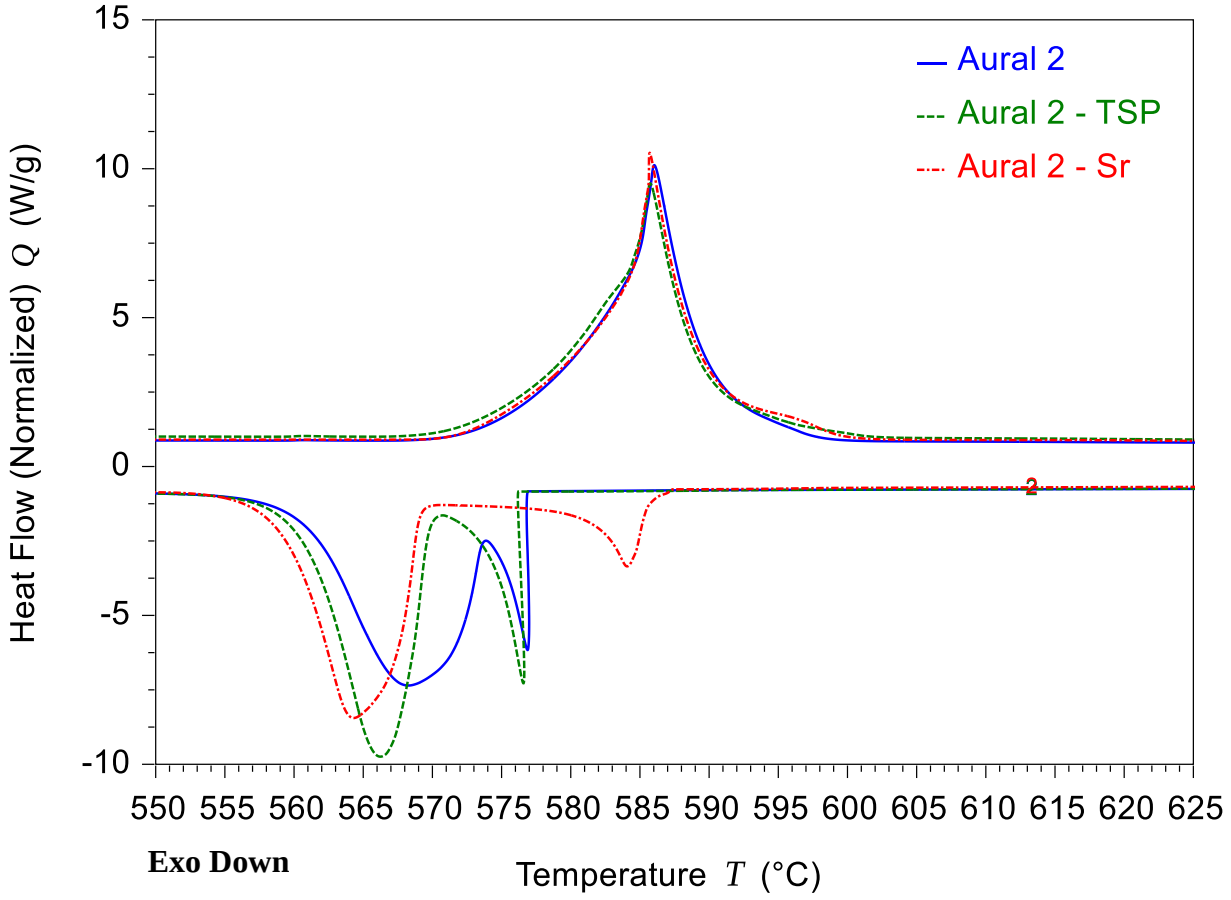

Figure 7-4 DSC Results of Aural™ 2 (Blue), Aural™ 2-TSP(Red), and Aural™ 2 -Sr (Green) during Heating (Top) and Cooling (Bottom) Cycles.

2) W319 Alloys

TSP depressed primary Al arrest and increased the Cu precipitate nucleation temperature of W319 alloy during solidification. The cooling curves of the W319 alloy with and without TSP are shown in Figure 7-5. The typical constituents in W319 are primary Al, Al-Si euetectic, Al_2Cu (θ), $Al_4Cu_2Mg_8Si_7$ (Q) and $Al_{15}(Fe, Mn)_3Si_6$ (α-Fe). Three major temperature arrests are observed on the cooling curve of the W319 base alloy in Figure 7-1(a). The first arrest represents the solidification of primary Al dendrites, the second arrest represents the solidification of the Al-Si eutectic, and the third arrest mainly represents the solidification of Cu IMCs which contain θ and Q phases. To quantitatively compare the solidification behavior of these alloys, the first derivative was plotted in Figure 7-5. Six characteristic temperatures are noted on the first derivative curves as follows:

$T_{Al\ nuc}$: the primary Al nucleation temperature

$T_{Al\ min}$: the primary Al temperature minimum (dT/dt=0).

$T_{Al\ max}$: the primary Al temperature maximum (dT/dt=0).

$T_{Al\text{-}Si\ nuc}$: the Al-Si eutectic nucleation temperature.

$T_{Al\text{-}Si\ arr}$: the Al-Si eutectic arrest temperature.

$T_{sol\ nuc}$: The Cu IMCs nucleation temperature.

Selected characteristic temperatures taken from cooling curves are listed in Table 7-3. It can be noted that the nucleation, local minimum, and maximum temperatures of primary Al were reduced by 4, 3, and 3 °C with TSP additions. Reduced Al-Si eutectic arrest temperature was observed with TSP additions. However, the Cu IMCs nucleation temperature was increased by 4 °C with TSP additions. A higher slope of Cu IMCs in the cooling curves was observed with TSP additions, suggesting TSP might change the Cu IMCs evolution during solidification.

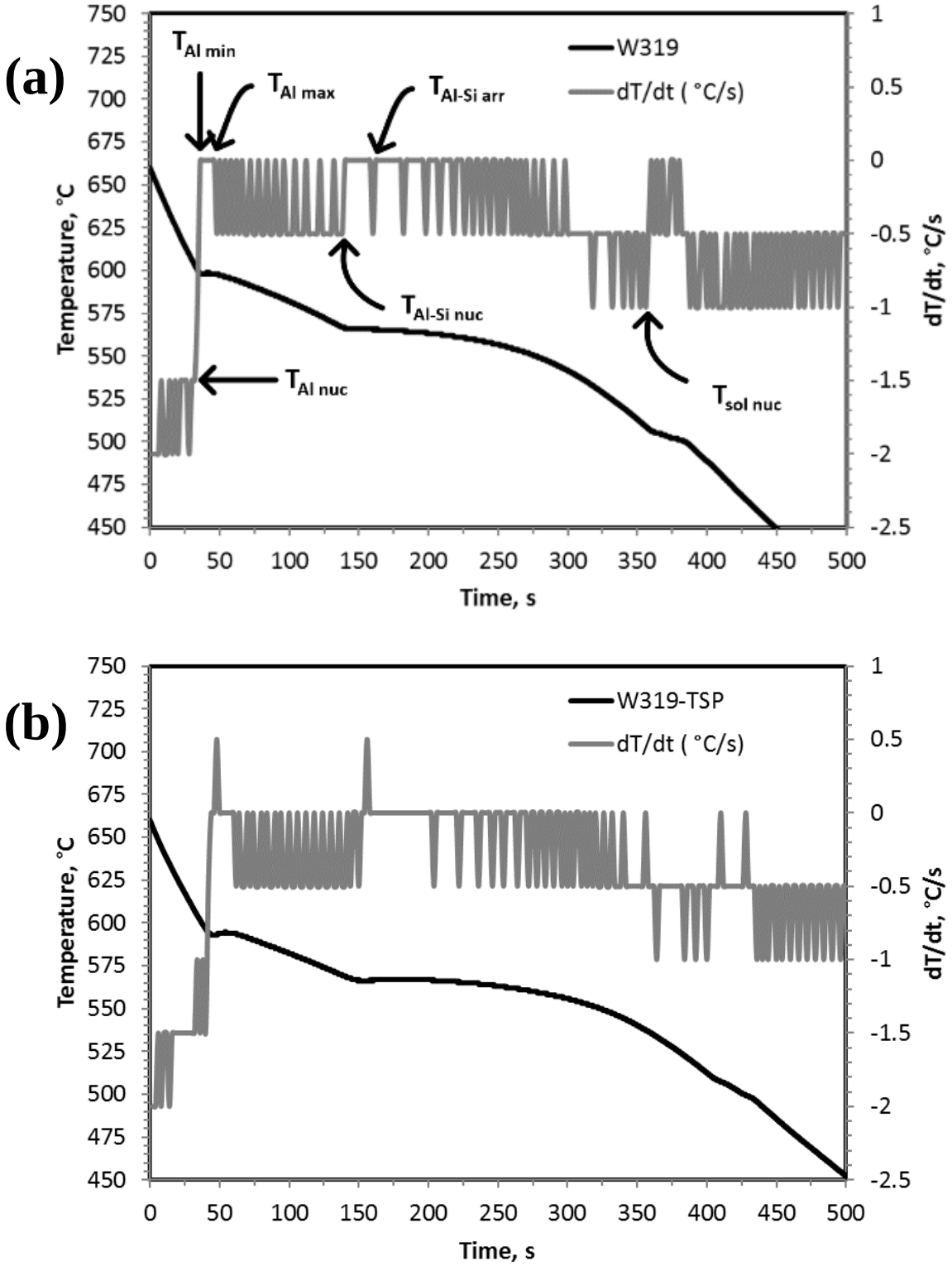

Figure 7-5 Cooling Curve and its First Derivative of (a) W319 and (b) W319-TSP.

Table 7-3 Selected Characteristic Temperatures Taken from Cooling Curves.

Alloy	TAl nuc (°C)	TAl min (°C)	TAl max (°C)	TAl-Si nuc (°C)	TAl-Si arr (°C)	Tsol nuc (°C)
W319	603	598	598	567	566	509
W319-TSP	599	595	595	563	562	513

*Each value in the table is the average of three measurements.

Figure 7-6 shows the DSC heating plot of W319. The corresponding constituents, such as Q, θ, α-Fe, Al-Si eutectic, and primary Al, are indicated on the heating curve. Figure 7-7 overlays the DSC data plots of W319, W319 with TSP additions, and W319 with Sr additions. In the W319 base alloy, Cu IMCs, which contains Q and θ, appears as a single Q peak with a small θ shoulder. TSP additions exhibited two distinct peaks, suggesting two eutectic reactions are occurring at slightly different temperatures. Interestingly, TSP additions also increased the θ peak temperature and the ratio of θ and Q in W319, while Sr additions reduced the peak temperatures of both Q and θ without changing the θ-to-Q ratio. Therefore, TSP changes the Cu IMCs to favor the formation of θ, which is a more potent strengthen precipitate. TSP additions also reduced the peak melting temperature of primary Al, which is consistent with the cooling curves results.

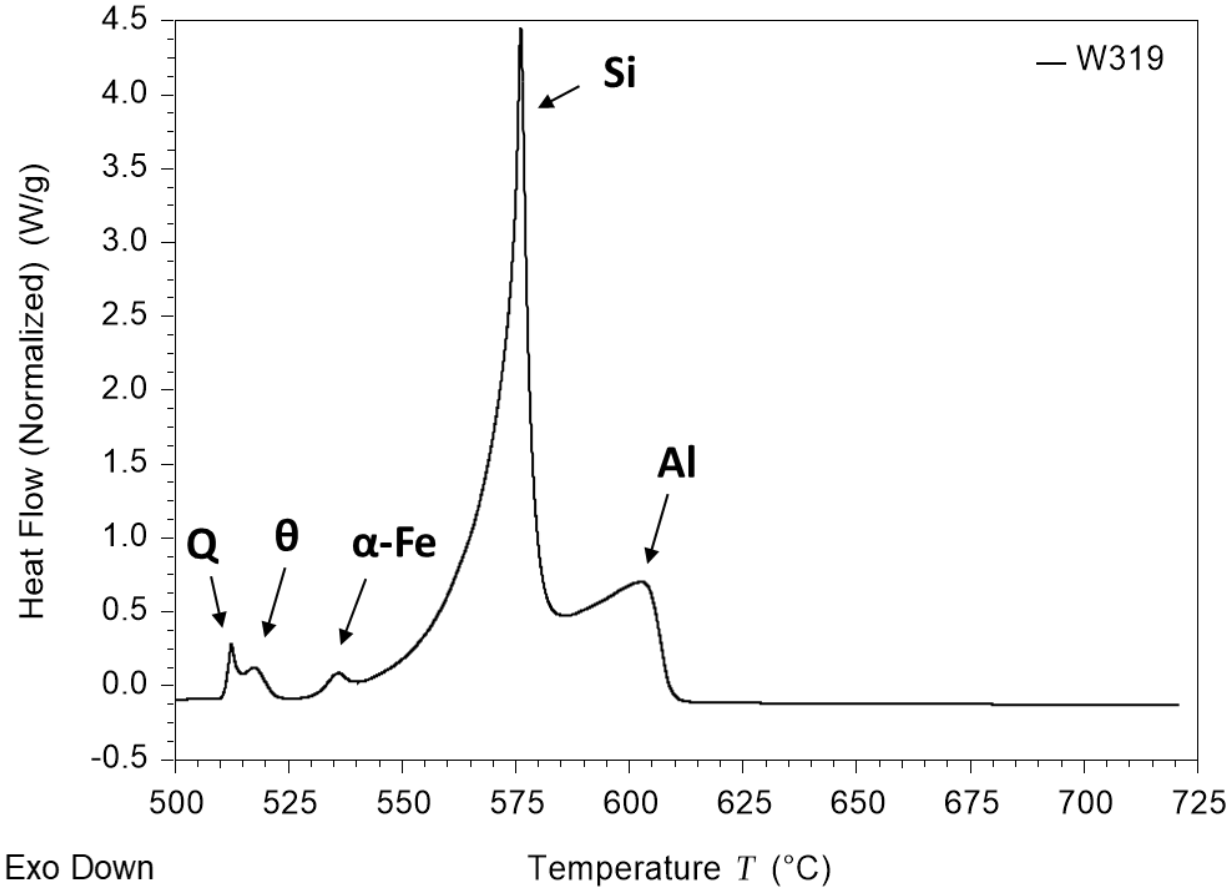

Figure 7-6 Typical DSC Endothermic Curve of W319. Al: The Primary Al, Si: Al-Si Eutectic, θ: Al_2Cu, Q: $Al_4Cu_2Mg_8Si_7$ and α-Fe: $Al_{15}(Fe, Mn)_3Si_6$.

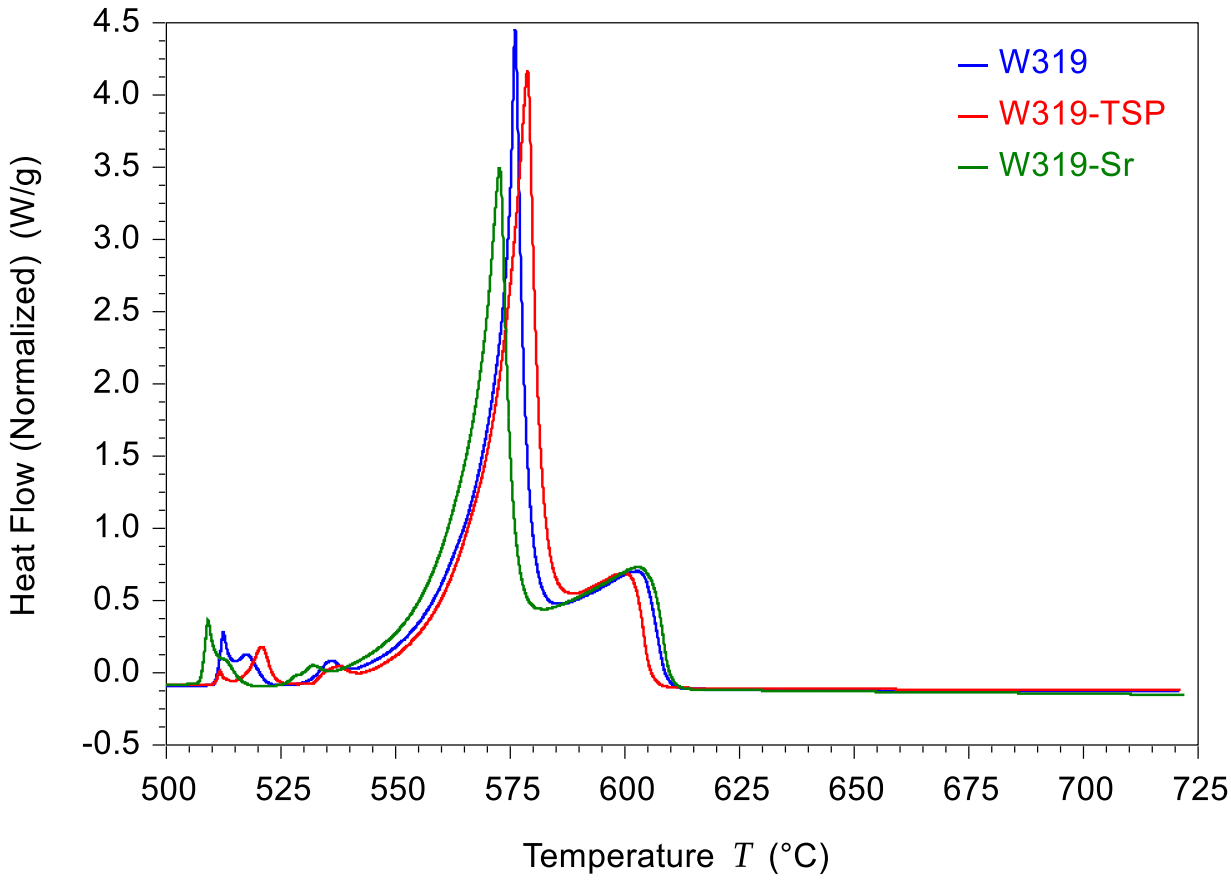

Figure 7-7 DSC Results of W319 (Blue), W319-TSP(Red), and W319-Sr (Green) during Heating Cycle.

7.3.4 As-cast Microstructures

Figures 7-8 shows optical micrographs of the Aural™ 2 alloys in the as-cast condition. The microstructures consisted of primary α-Al dendrite with Al-Si eutectic in the interdendritic regions. There are only small amounts of Mg, Mn, and Fe containing phases in the Aural™ 2 alloys. The Si phase in the unmodified Aural 2™ alloys has the typical coarse morphology as shown in 7-8(a). The Si morphology appeared to be refined with either TSP modification as shown in Figure 7-8(b) or Sr modification, Figure 7-8(c) as compared to the unmodified microstructure. The secondary dendrite arm spacing (SDAS) of all Aural™ 2 alloys was 23±3 µm.

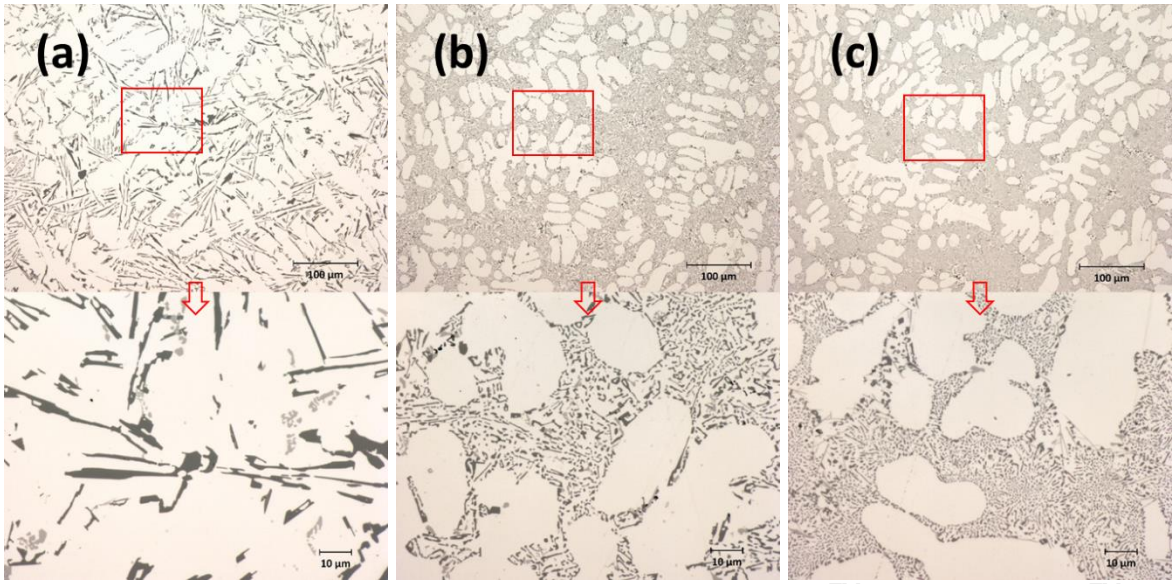

Figure 7-8 Optical Micrographs of the As-cast Condition: (a) Aural™ 2 Base, (b) Aural™ 2 with TSP, and (c) Aural™ 2 with Sr.

To further investigate more details of the modified Si phase, each of the alloys was deep-etched and imaged using SEM as shown in Figure 7-9. The Si phase in both unmodified and TSP-modified Aural™ 2 alloys has a lamellar morphology with the Si in the TSP-modified alloys being more refined. However, the Sr-modified material has a Si morphology in the manner of fibrous form.

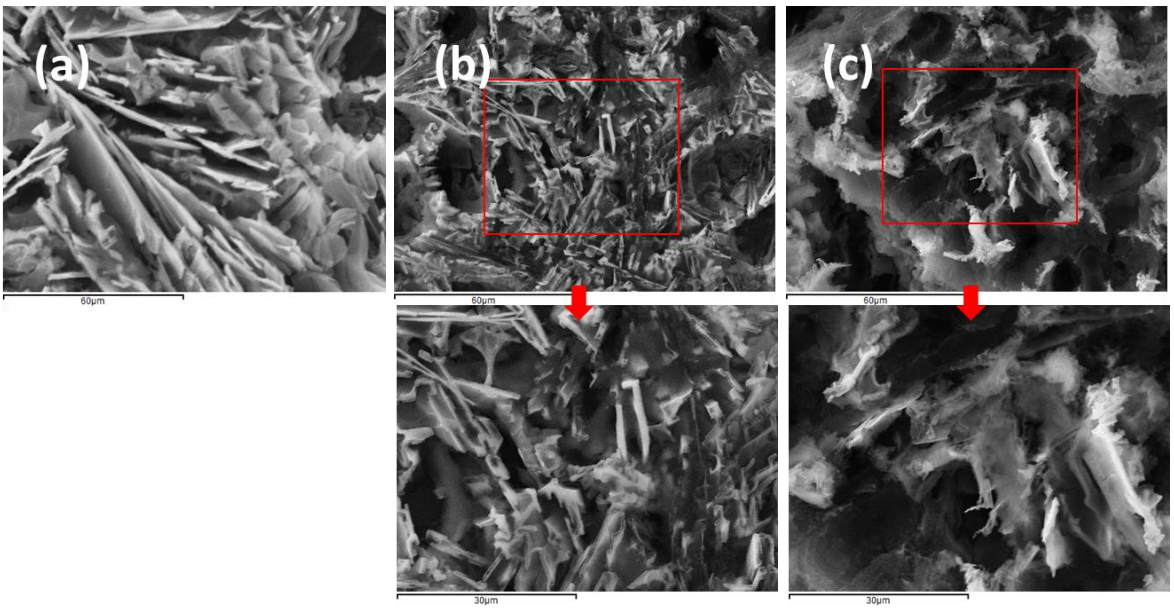

Figure 7-9 SEM Micrographs of the Deep-etched Aural™ 2 Alloys: (a) Aural™ 2 Base, (b) Aural™ 2 with TSP, and (c) Aural™ 2 with Sr.

EBSD samples were prepared for grain size determination. Micrographs for each of the alloys is shown in Figure 7-10. The grain size in the unmodified Aural™ 2 and TSP-modified Aural™ 2 alloys was similar. However, Sr modification significantly increased α-Al grain size.

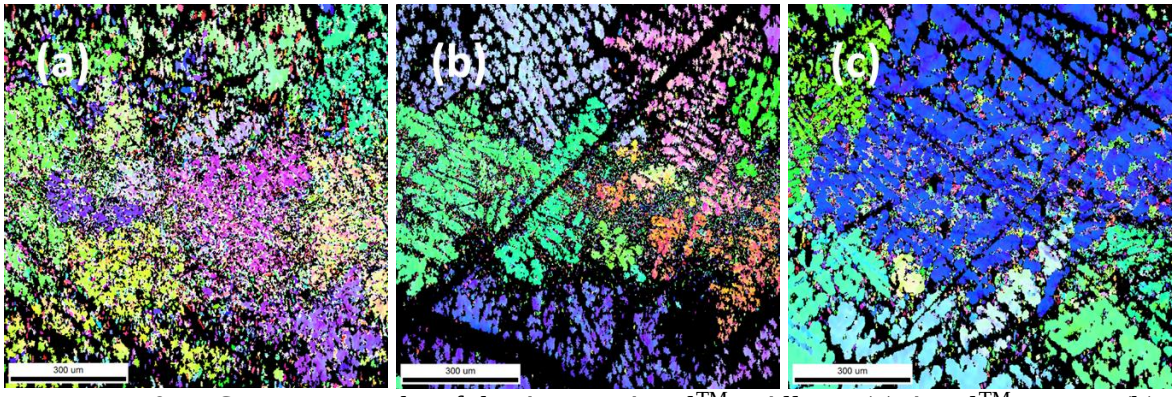

Figure 7-10 EBSD Micrographs of the As-cast Aural™ 2 Alloys: (a) Aural™ 2 Base, (b) Aural™ 2 with TSP, and (c) Aural™ 2 with Sr.

Figures 7-11 shows optical micrographs of the W319 alloys. Similar to Aural™ 2 alloys, TSP additions refined the eutectic Si in the W319 alloys.

In both Aural^{TM} 2 and W319-type alloys, the TSP additions modified the Si eutectic into a lamellar type of structure with similar grain size of primary α-Al while Sr additions modified the Si eutectic into a fibrous morphology and resulted in a much larger α-Al grain size.Further evidence that TSP has aiding effect on the nucleation of eutectic microconstituents comes from the reduced undercooling. More importantly, the arrest temperature of both Sr-modified and TSP-modified AuralTM 2 alloys was decreased; however, the TSP-modified material has a Si morphology in the manner of lamellar form. This suggests that, instead of poisoning the growing ledges of Si, TSP bonds with Al to slow down the Al segregation from Al-Si melt during eutectic reaction, leading to the microstructural refinement of Al-Si eutectic.

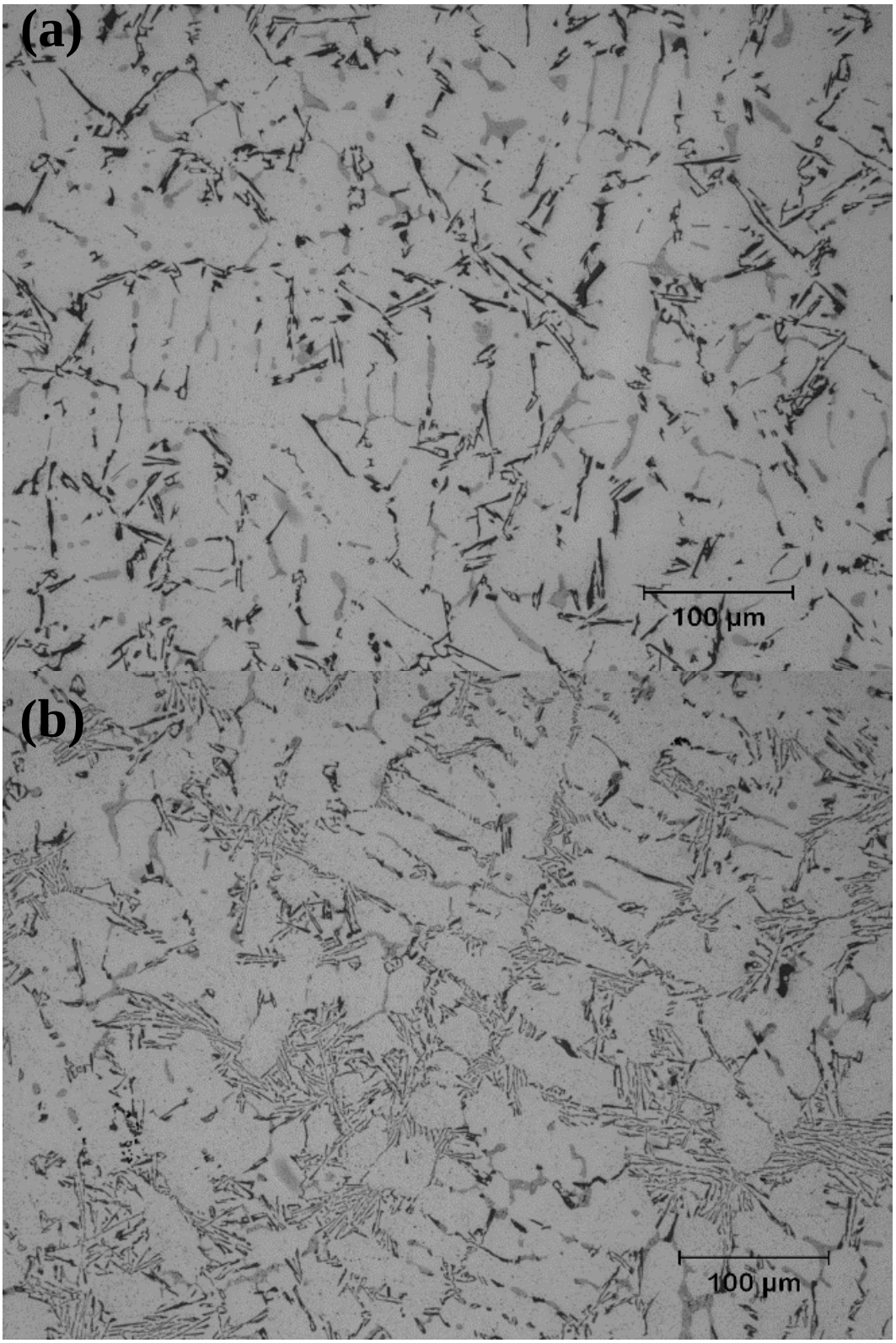

Figure 7-11 Optical Micrographs of the W319 Alloy with and without TSP: (a) W319 and (b) W319 with TSP Additions.

7.3.5 Tensile Properties

The tensile properties of Aural™ 2 alloys at room temperature and 300°C were improved with TSP additions. The engineering stress-strain curves of the Aural™ 2 alloy with and without TSP additions at both room temperature and 300°C are plotted in Figure 7-12. Ductility at room temperature increased from 1% with no TSP additions to 3.5% with TSP additions. Ductility at 300°C increased from 13% with no TSP additions to 26% with TSP additions. Both yield strength and ultimate tensile strength were maintained with TSP addition at room temperature and 300°C elevated temperature. Yield strength, ultimate tensile strength, and ductility as determined from the stress-strain curves at these two testing temperatures are shown in Figure 7-13. The increase in ductility is due to the modified Si morphology from flaky to fibrous form after TSP additions.

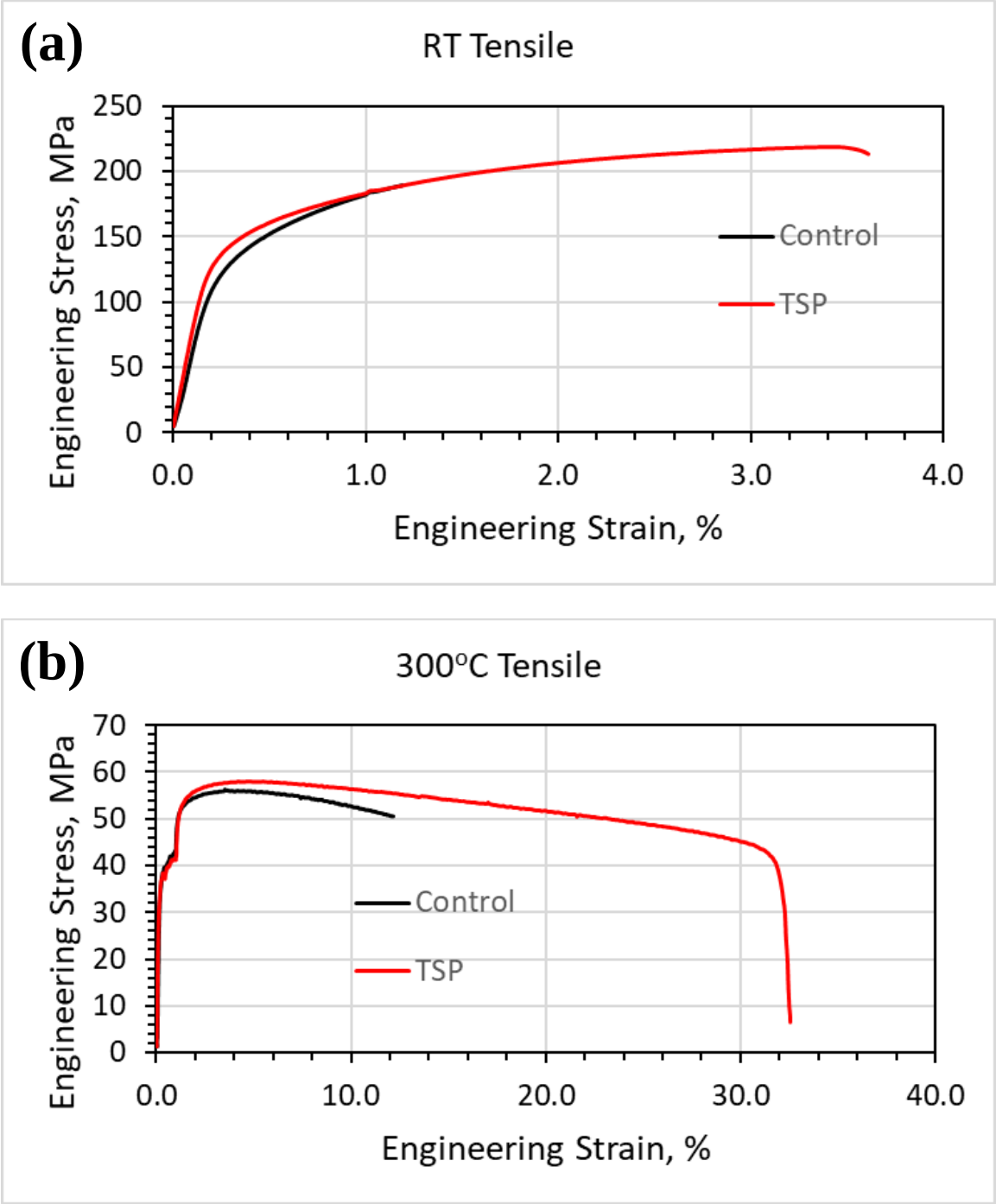

Figure 7-12 Stress-strain Curves of the Aural™ 2 Alloy with and without TSP at (a) Room Temperature and (b) 300°C.

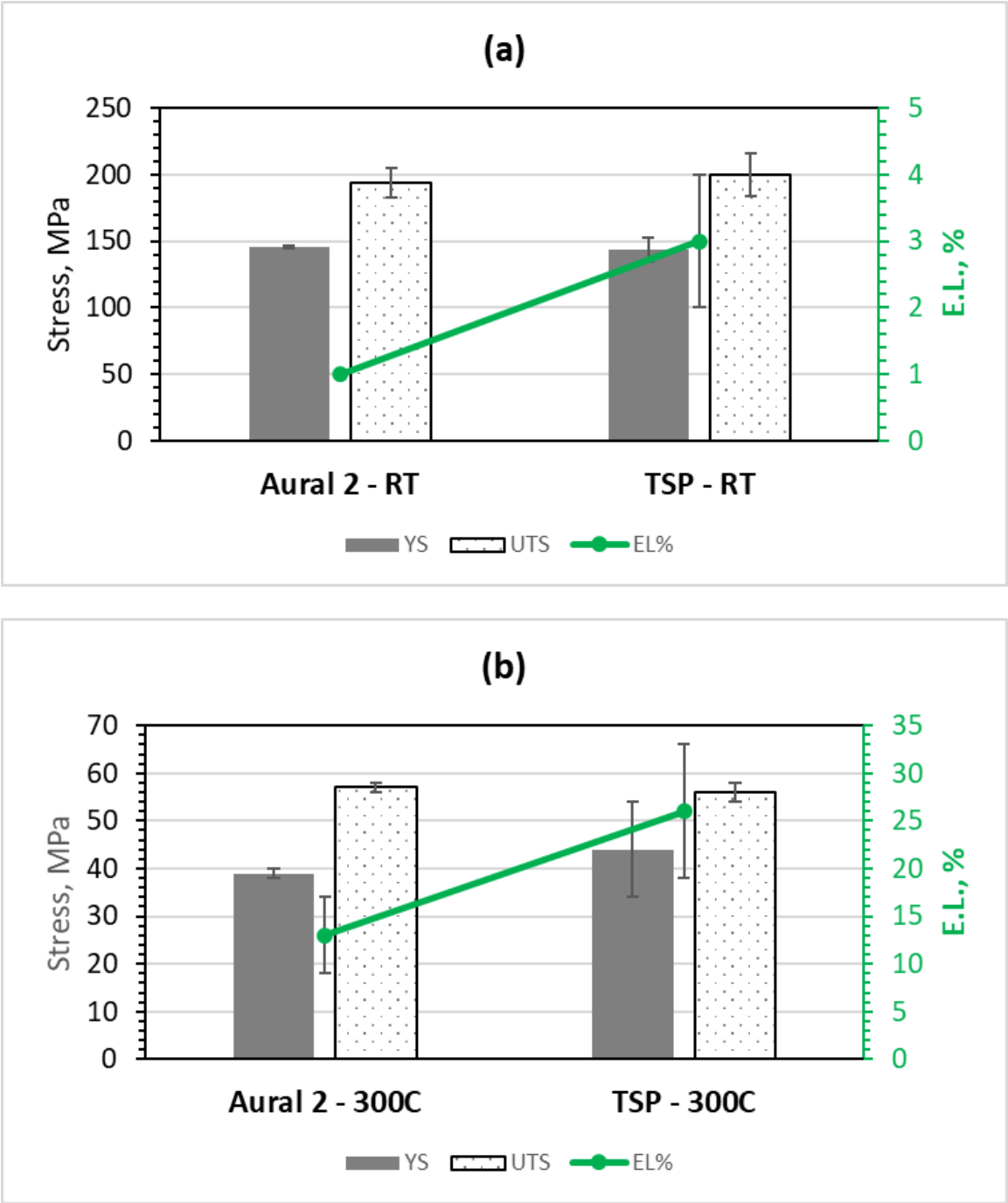

Figure 7-13 Yield Strength, Ultimate Tensile Strength, and Ductility of the Aural™ 2 Alloy with and without TSP Additions at Room Temperature and 300ºC.

7.3.6 High Cycle Fatigue

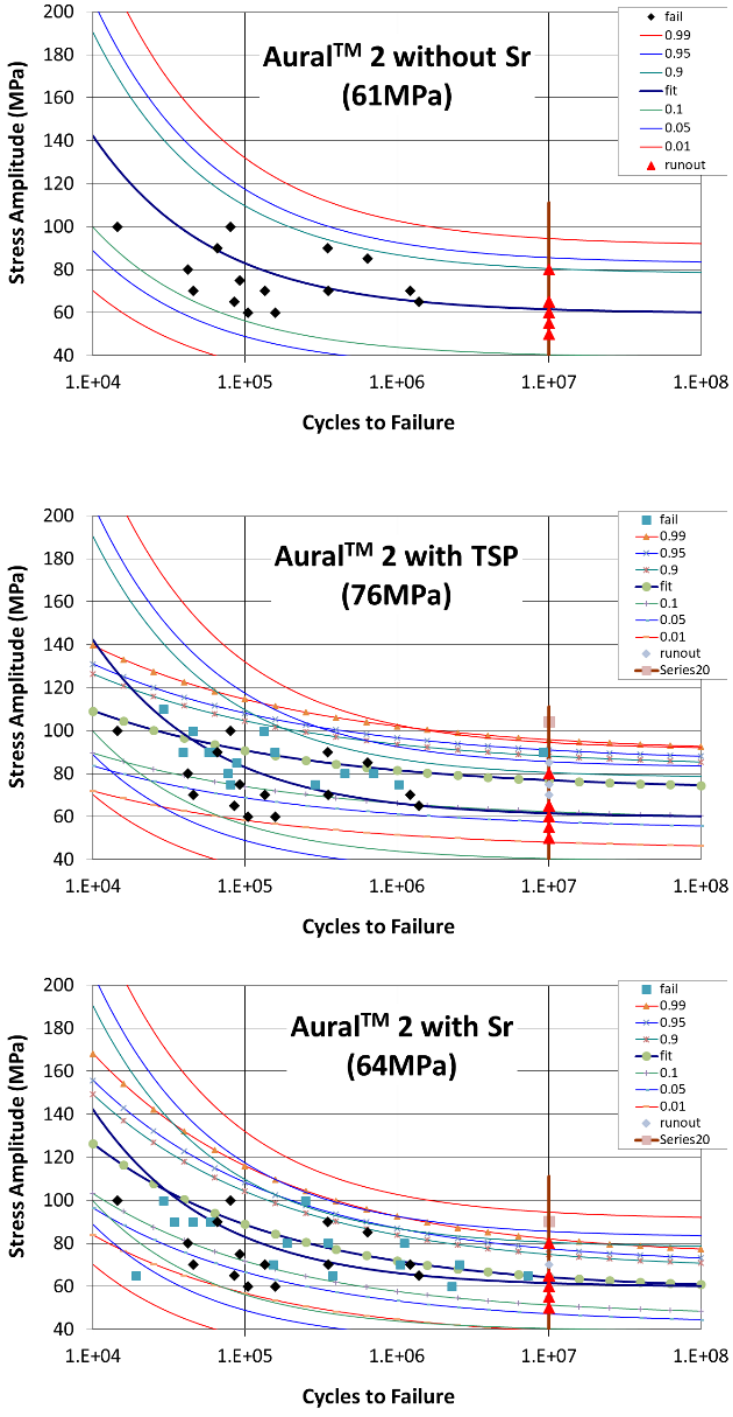

Figure 7-14 S-N Curves of Heat-treated Aural™ 2 Alloys: (a) Aural™ 2 without Sr, (b) Aural™ 2 with TSP, and (c) Aural™ 2 with Sr.

Table 7-4 High Cycle Fatigue Stress of Heat-treated Aural™ 2 Alloys at Room Temperature.

	HCF Stress (MPa)
Aural™ 2 without Sr	61±10
Aural™ 2 with TSP	76±10
Aural™ 2 with Sr	64±9

The high cycle fatigue property of Aural™ 2 alloys at room temperature was improved with TSP additions. Figure7-14 shows S-N curves of all Aural™ 2 alloys. The average HCF stress and standard deviation are listed in Table 7-4. The HCF stress of the unmodified Aural™ 2 alloys was 61 MPa. The HCF stress of the Sr-modified Aural™ 2 alloys was 64 MPa. TSP additions increased the HCF stress from 61 MPa to 74 MPa. The improved fatigue stress with TSP additions resulted from the modified Si without altering Si geometry as well as the overall grain size.

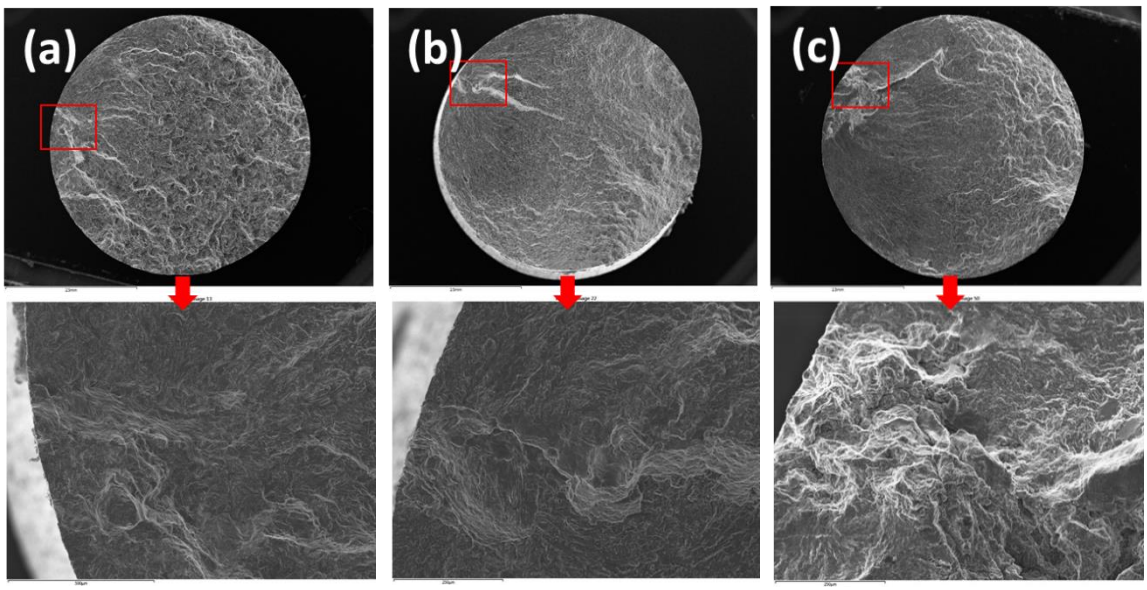

Figure 7-15 Fracture Surface of Fatigue Specimen: (a) Aural 2 without Sr, (b) Aural 2 with TSP, and (c) Aural 2 with Sr Alloys.

Figure 7-15 illustrates the fracture surface of three fatigue specimen. The high magnification images illustrate the initiation site of the fatigue fracture surfaces. There was no porosity on fatigue crack initiation. In addition, No Fe or other IMCs was detected from the initiation site in all three conditions. Therefore, the fatigue properties of all alloys were not influenced by porosity and represented the microstructure of the alloys.

7.4 Conclusions

Nano-structured trisilanol polyhedral oligomeric silsesquioxane (TSP) as a novel chemical modifier was incorporated into Aural^{TM} 2 and W319-type alloys. TSP additions reduced solidification shrinkage during casting. Metallography showed refined Si in the Al-Si eutectic constituent and reduced Al SDAS, resulting in at least 100% improvement in ductility at both room temperature and 300^{o}C elevated temperature without sacrificing the strength. TSP-modified structure improved room temperature high cycle fatigue stress of Aural^{TM} 2 alloys from 64 MPa with Sr additions to 74 MPa with TSP additions, providing solutions to reinforce aluminum alloys in body structures for the environmental and fuel economy benefits. Besides microstructural refinement, the mass fraction of θ increases while Q decreased with TSP addition, suggesting TSP changes the Cu IMCs to favor the formation of θ, which demonstrated its potential as a strengthening precipitate.

Chapter 8 Summary and Future Work

8.1 Summary

Trisilanol polyhedral silsesquioxane (TSP) was first incorporated in Sn-based binary and ternary alloys, leading to microstructure refinement and high creep resistance. The ingot that made of TSP-treated Al-12Si powders exhibited 250% improvement in ductility without the loss of strength as compared to the ingot made of the untreated Al-12Si powders. Microstructure and thermal characteristics confirmed that the improved mechanical was due to the reduced undercooling and arrest temperatures for Al-Si eutectic reaction that resulted in well-modified Si morphology. The TSP-treated A4047 ingots can be further diluted from 10,000 ppm down to 150 ppm TSP without the loss of modified Si structure.

The new TSP master alloy was produced to facilitate the practice addition of TSP to the melt. Different approaches were performed to assess the level of TSP modification and find the optimum content of TSP master. The optimized A4047-TSP master composition is 6%TSP in an A4047 alloy. 10% A4047-6TSP master was used to modify Al-Si binary and commercial alloys using traditional foundry process at a large 100 lbs. scale.

In Al-7.5Si binary alloys, TSP additions increase the ductility from 3.5% with no TSP additions to 6.5% with TSP additions without sacrificing the strength. The microstructure of both primary Al and eutectic microconstituents of the Al-7.5Si alloy with TSP addition was refined, and the modified microstructure was well maintained after remelting with additional 192 hours held in the 720°C furnace. The addition of TSP reduced the undercooling and arrest temperatures of proeutectic and eutectic microconstituents and caused the formation of a small shoulder near the eutectic onset melting temperature. These results suggest that TSP offers aiding effect on the nucleation and bonds with Al to slow down the Al segregation from Al-Si melt during eutectic reaction, leading to morphological transformation.

In Aural^{TM} 2 and W319 -type commercial alloys, TSP additions reduced the solidification shrinkage of castings. Metallography showed refined Si in the Al-Si eutectic constituent and reduced Al secondary dendrite arm spacing (SDAS), resulting in at least 100% improvement in ductility at both room temperature and 300^{o}C elevated temperature without sacrificing the strength. Besides microstructural refinement, the mass fraction of θ (Al_2Cu) increases while Q ($Al_4Cu_2Mg_8Si_7$) decreased with TSP addition, suggesting TSP changes the Cu intermetallic (IMCs) to favor the formation of θ, which demonstrated its potential as a strengthening precipitate.

These findings support the proposed modification mechanism: TSP aids nucleation of eutectic Si by decreasing the interfacial energy of the melt, while bonds with Al to slow down the Al segregation from Al-Si melt during eutectic reaction, leading to morphological transformation and mechanical enhancements.

8.2 Future Work

8.2.1 Understanding modification mechanism with TSP addition.

In this thesis, TSP has shown to reduce primary Al SDAS, modify eutectic Si, and alter the Cu IMCs evolution in cast aluminum. This microstructural change lead to enhanced ductility without sacrificing the strength. However, the detailed mechanism of structural refinement with TSP addition remain unclear. Future study will need to approve the proposed mechanism using high resolution TEM, i.e. the <112> growth directions of Si crystals, thus evidencing an important role of the TSP modifier in the Si growth.

8.2.2 Effect of TSP on the porosity distribution and fatigue in cast aluminum alloys

One of the most significant extrinsic defects in cast aluminum alloys is porosity, which has been shown to have a large impact on fatigue life. Typically, macroporosity with large interconnected pores formed in relatively poor-fed region during casting, resulting in uneven

density distribution at different locations. This is due to a combination of local solidification shrinkage and hydrogen precipitation. Future study on the porosity distribution data will help characterize whether TSP changes density distribution via microstructural refinement to improve fatigue properties.

8.2.3 Application of TSP in foundries

The alloy development in this thesis were performed at 20-kg laboratory scale. Develop trials in different processing methods at larger scale (500kg), including gravity casting and high pressure die casting, is vital to enable application of TSP in cast aluminum foundries. Other future works may include exploration of TSP modification on other lightweight metals, such as magnesium and titanium alloys.

APPENDIX

APPENDIX

Effect of TSP on Crack Propagation in a Near Eutectic Al-Si Alloy

A.1 Background

An important reason to have an understanding why and how cracks propagate and arrest in near eutectic Al-Si alloys is that it helps to explain the ductility improvement with the addition of nano-structured chemicals. The refined microstructure would either enhance or suppress the microcracks initiation near the crack tips and along crack edges [117-121]. To fully understand the facture mechanics associated with microcrack initiation, this appendix focuses on crack propagation in a near eutectic Al-Si alloy with TSP treatment. Four-point bend specimens were deformed using a four-point bend fixture until a crack propagated from a notch. The deformed specimens were characterized with optical and electron microscopy as well as bending beam theory.

A.2 Experimental

A.2.1 Materials and sample preparation

The Al-12Si ingots with and without TSP were prepared with the A4047 powders treated with and without TSP. To treat the A4047 powders with TSP, the oxides from the powder surface were first removed by soaking the powder in 8 wt% HCl for 5 minutes at room temperature. The clean powers were then soaked into the 1wt%TSP ethanol solutions for 24 hours to get the TSP-treated powders. Dried TSP-treated A4047 powders were melted at 1088 K (815°C). The molten melt was poured by gravity to a permanent graphite mold to form a rectangular ingot of 25 mm x 50 mm x 12 mm in size and cooled in air. Four-point bend specimen measuring 24mmx4.5mmx3.5mm was machined using electrical discharge machining from the cast ingots. A 0.5 mm notch was cut using a 0.3mm thick diamond saw as a crack

initiator. The sample was then ground with SiC paper and polished with 0.3 μm alumina slurry and 0.02 μm colloidal silica suspension. Stereomicrographs were taken with an Olympus SZX 16 stereo microscope equipped with a SZX2-RHS transmitted-light stand as shown in Figure A-1.

A.2.2 Four-point bend test

Bending was performed using a four-point flexure fixture as shown in Figure A-2. The specimen was supported with two anvils on the bottom. The force is applied by tightening four screws to push the specimen through two loading anvils. All supporting and loading anvils are hardened steel cylinders, each 4mm in diameter and 40mm long. The supporting and loading span lengths are 5mm and 22mm, respectively. The A4047 and A4047-TSP specimen were bended with an around 2mm crack by tightening 4 screws by 1 ¼ turn. Figure A-3 shows the top and side view of a four-point bend fixture with a bended specimen.

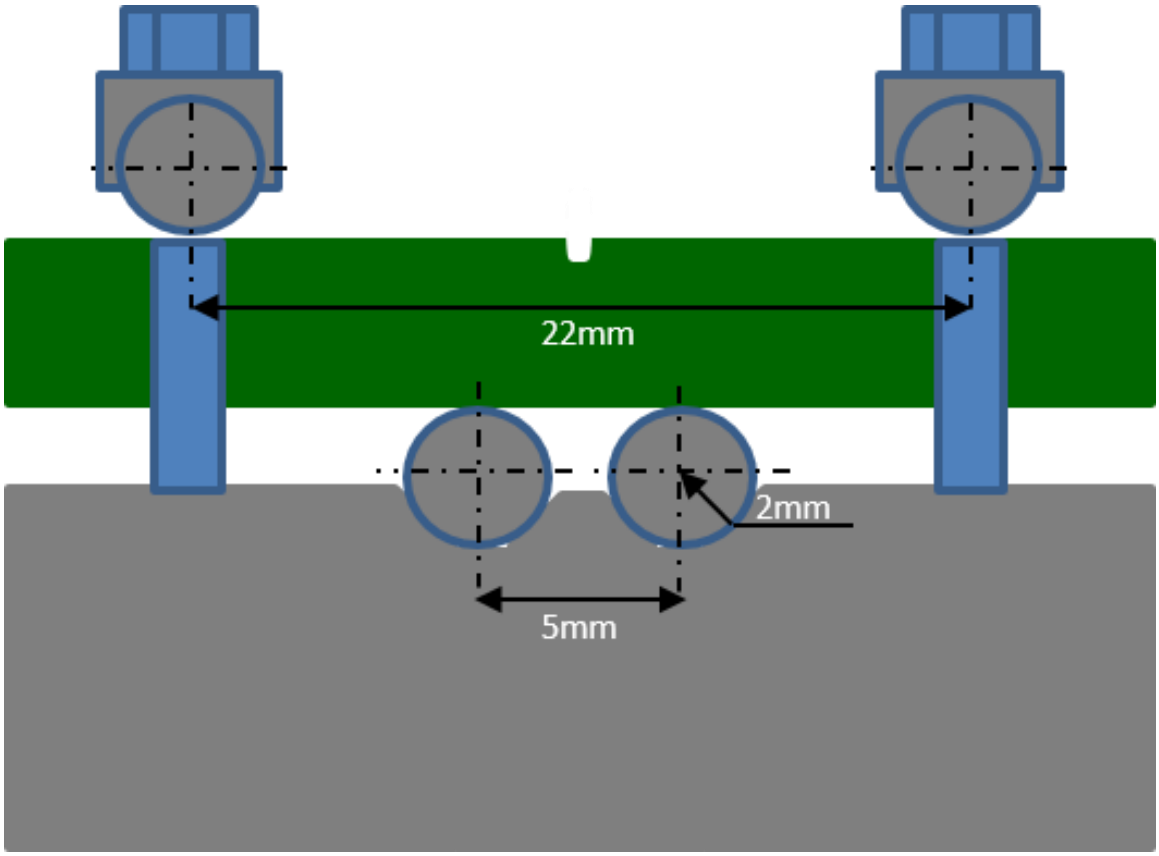

* Force is applied by tightening four screws.
Figure A-1 Cartoon of a Four-point Flexure Fixture.

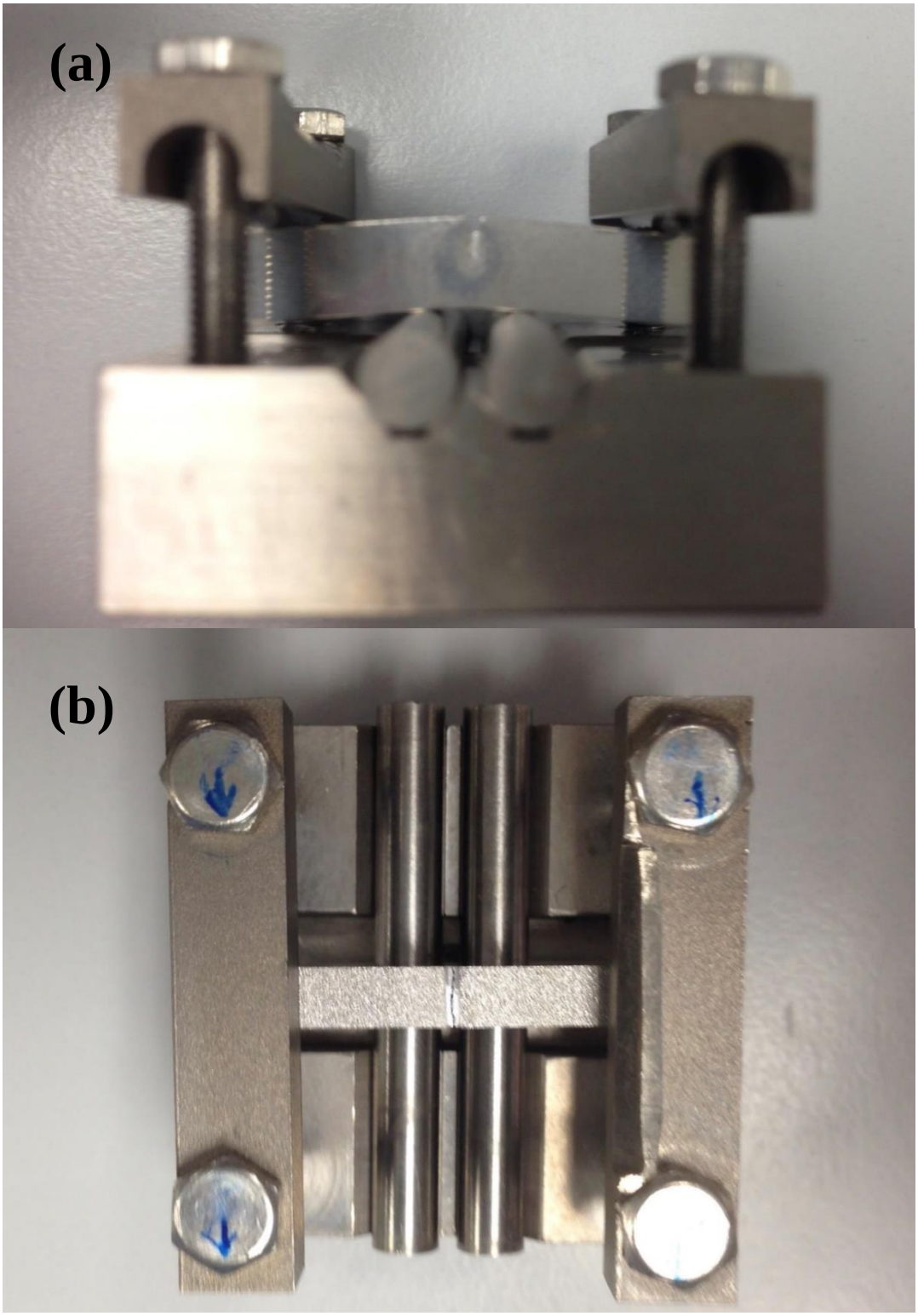

Figure A-2 A Four-point Bend Fixture with a Bended Specimen: (a) Side-view and (b) Top-view.

A.2.3 Microscopy

The Al-12Si alloys with and without TSP were characterized using both optical and scanning electron microcopy. Optical micrographs were taken using the inverted metallographic microscope, Nikon ECLIPSE MA200, with magnification up to 1,000X. SEM micrographs were taken using a MIRA3 TESCAN SEM. Secondary electron (SE) and backscattered electron (BSE) SEM images were captured to compare crack and fracture surface of A4047 with and without TSP treatment.

A.3 Results and Discussion

A.3.1 As-cast Microstructure

A great refinement on both primary Al and eutectic Si microconstituent in A4047 alloys was observed with TSP treatment. Figure A-3 shows stereo micrographs of the 4-point bend specimen. There corresponding microstructures are shown in Figure A-4. Figures A-4 (a) – (d) are the optical micrographs of the ingots made from A4047 powder without and with TSP treatment. Figure A-4 (a) and (b) display the microstructure of the A4047 control with the magnifications of 200x and 1000x, respectively, showing Al dendrites and irregular Si flakes. The primary Al phase was gradually refined with TSP treatment as shown in Figure A-4 (a) and (c), and the Si flakes in the eutectic colonies were broken down to very fine fibrous phase, as shown in Figure A-4 (d).

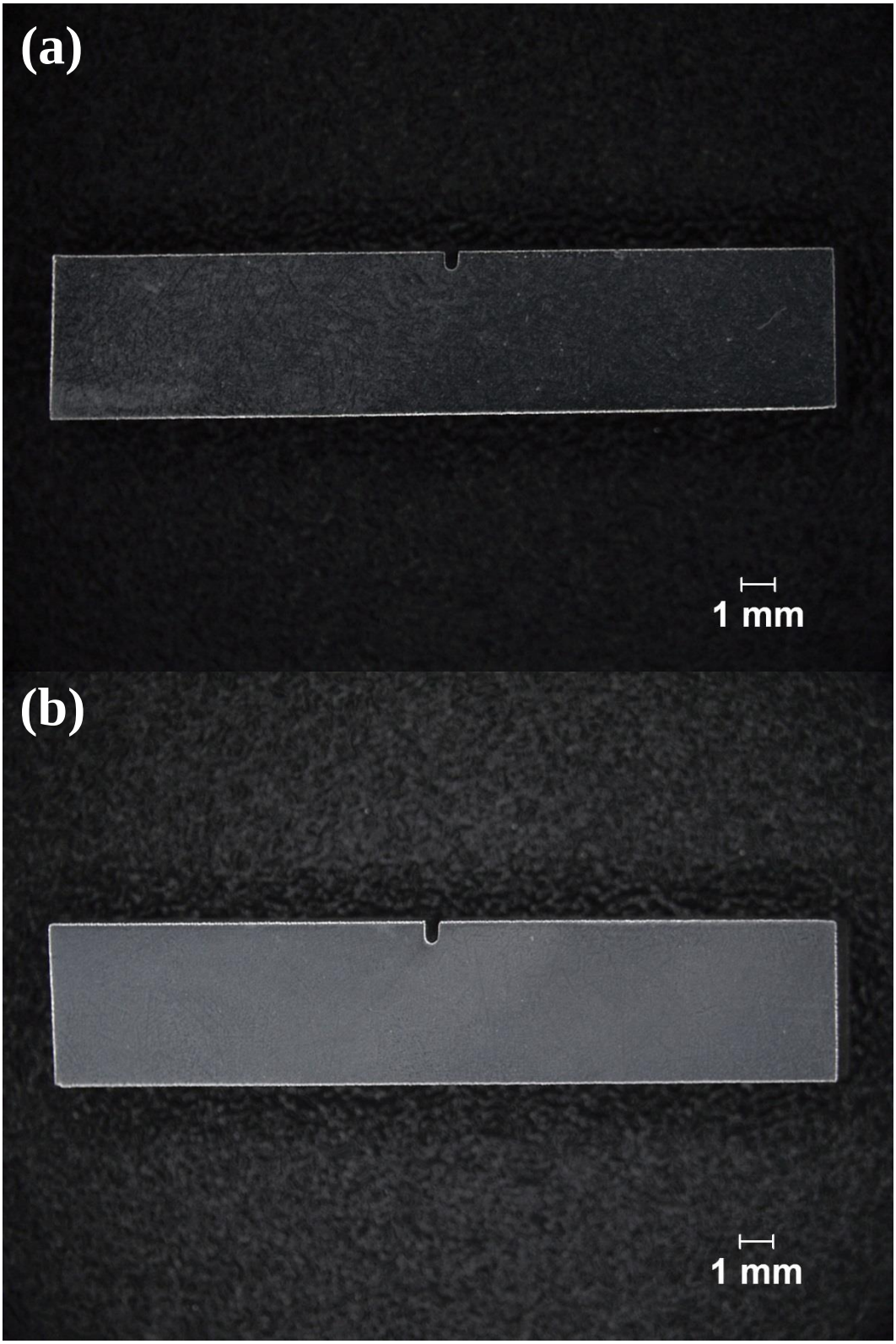

*A 0.5 mm notch was cut using a 0.3mm thick diamond saw.

Figure A-3 Macro of a Four-point Bend specimen: (a) A4047 and (b) A4047-TSP.

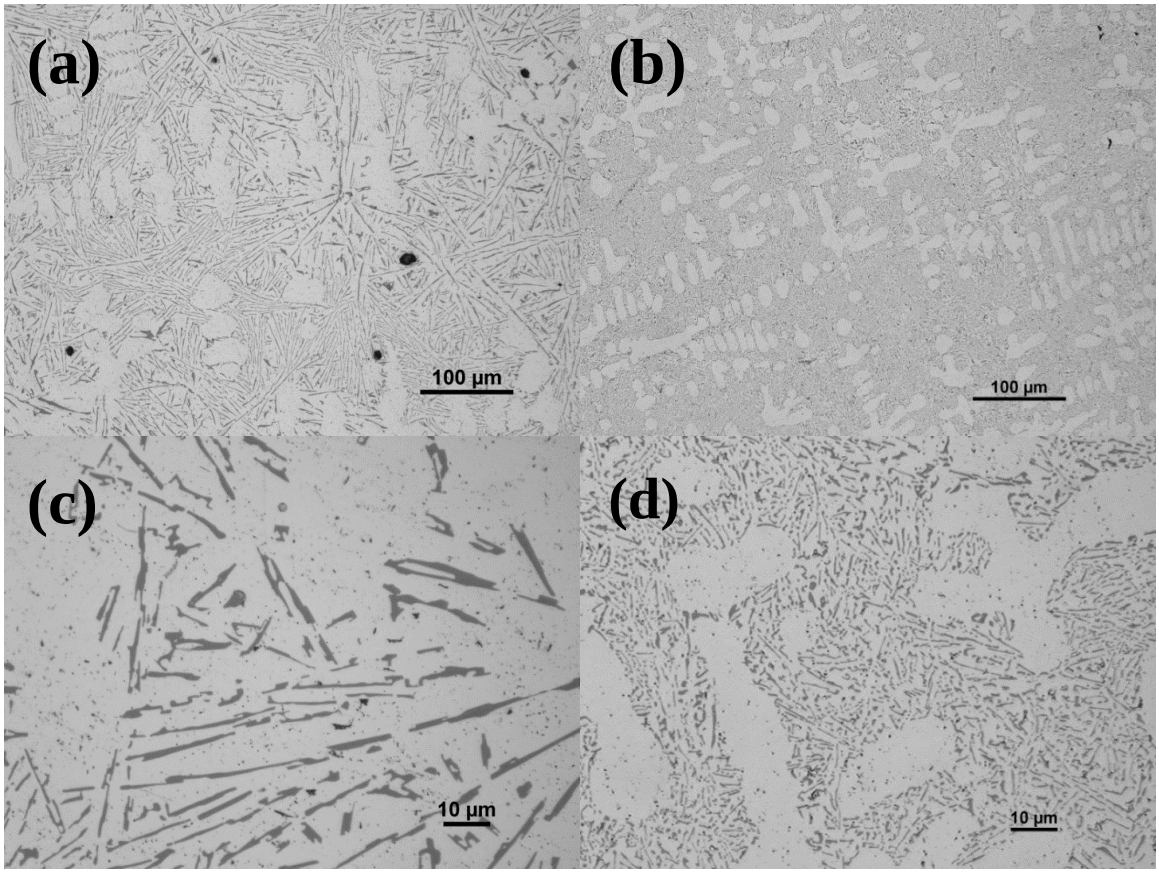

Figure A-4 Opical Micrographs of As-cast A4047 Alloys with and without TSP Treatment Using Dip-coating Process: (a) the A4047 Base Alloy with the Objective Lens of 20x, (b) the T4047-TSP with the Objective Lens of 20x, (c) the A4047 Base Alloy with the Objective Lens of 100x, and (d) the A4047-TSP with the Objective Lens of 100x.

A.3.2 Microstructure after bending

The stereo micrographs after bending were shown in Figure A-5, where cracks propagated right from the 0.5 mm notch.

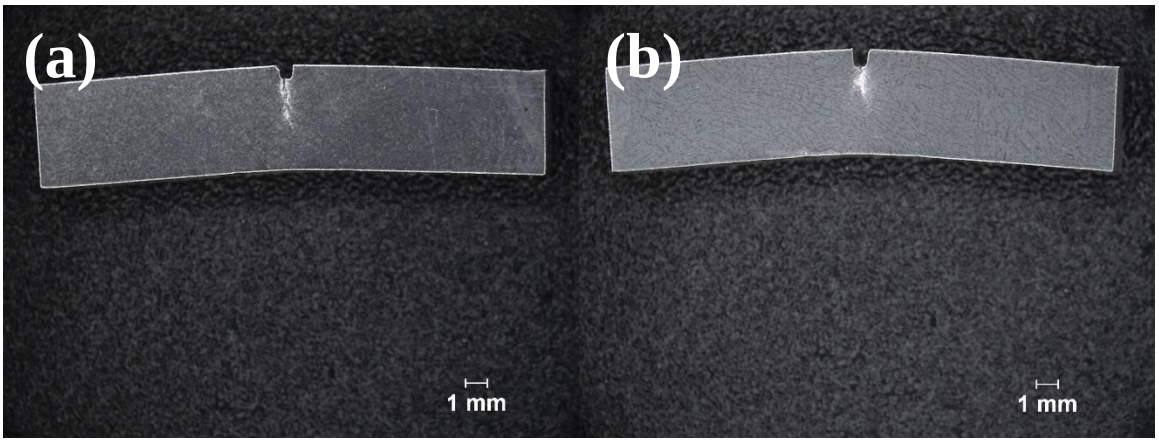

Figure A-5 Stereo Micrographs of Bended A4047 Alloys with and without TSP Treatment Using Dip-coating Process: (a) the A4047 Base Alloy with the Objective Lens of 7x, (b) the A4047-TSP with the Objective Lens of 7x, (c) the A4047 Base Alloy with the Objective Lens of 10x, and (d) the A4047-TSP with the Objective Lens of 10x.

Figure A-6 illustrates the secondary and backscattered electron images of the A4047 alloy. The total crack length was about 1.9 mm from the notch. As can be seen in Figure A-6(a) and (f), all the crack tips were close to the eutectic Si, suggesting a strong resistance to the crack propagation by Si. Also, microcracks were initiated near the tip of the arrested crack, propagated and coalesced with the main crack to cause rupture. Figure A-7 shows the SEM images of the A4047-TSP alloy. The crack length was reduced to 0.78mm from the notch. The increased eutectic density was observed with TSP addition, which absorbed more energy to hinder crack growth. In addition, less amount of microcracks were observed with TSP additions.

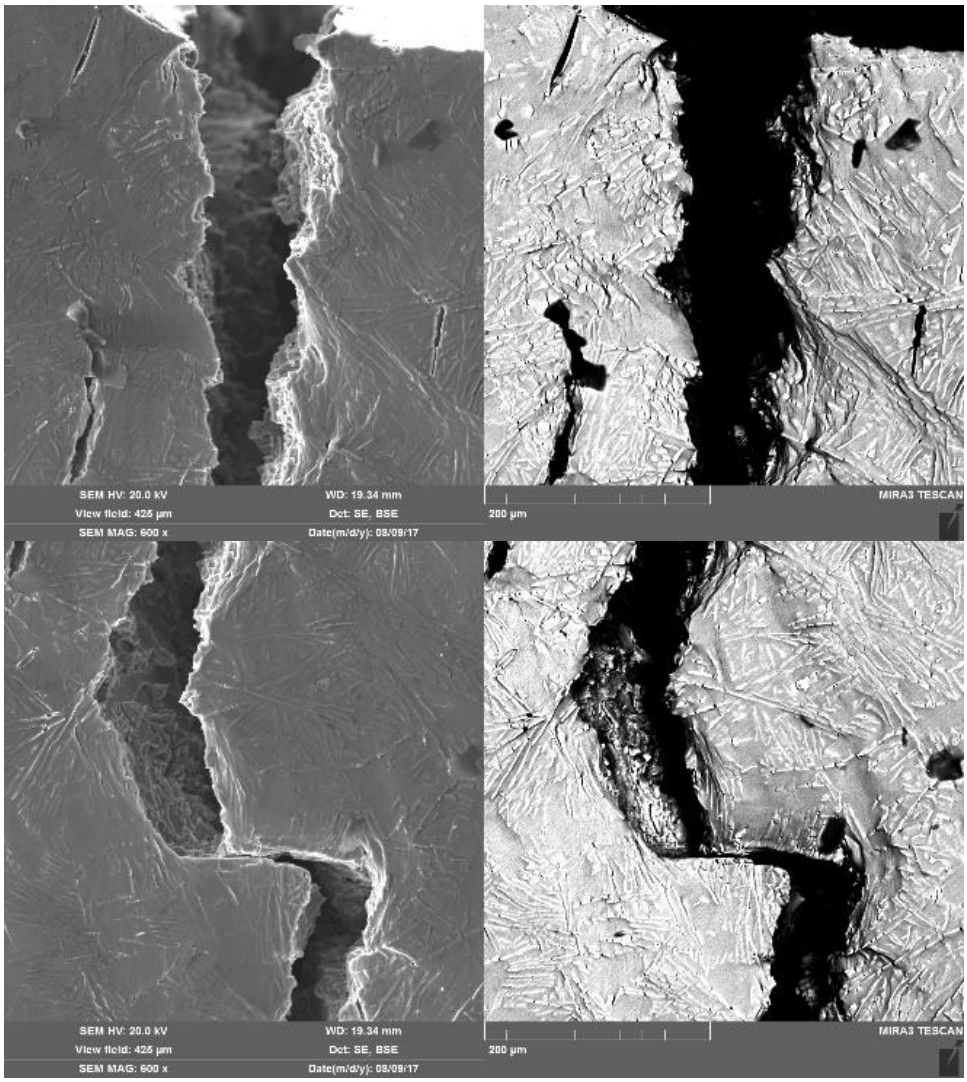

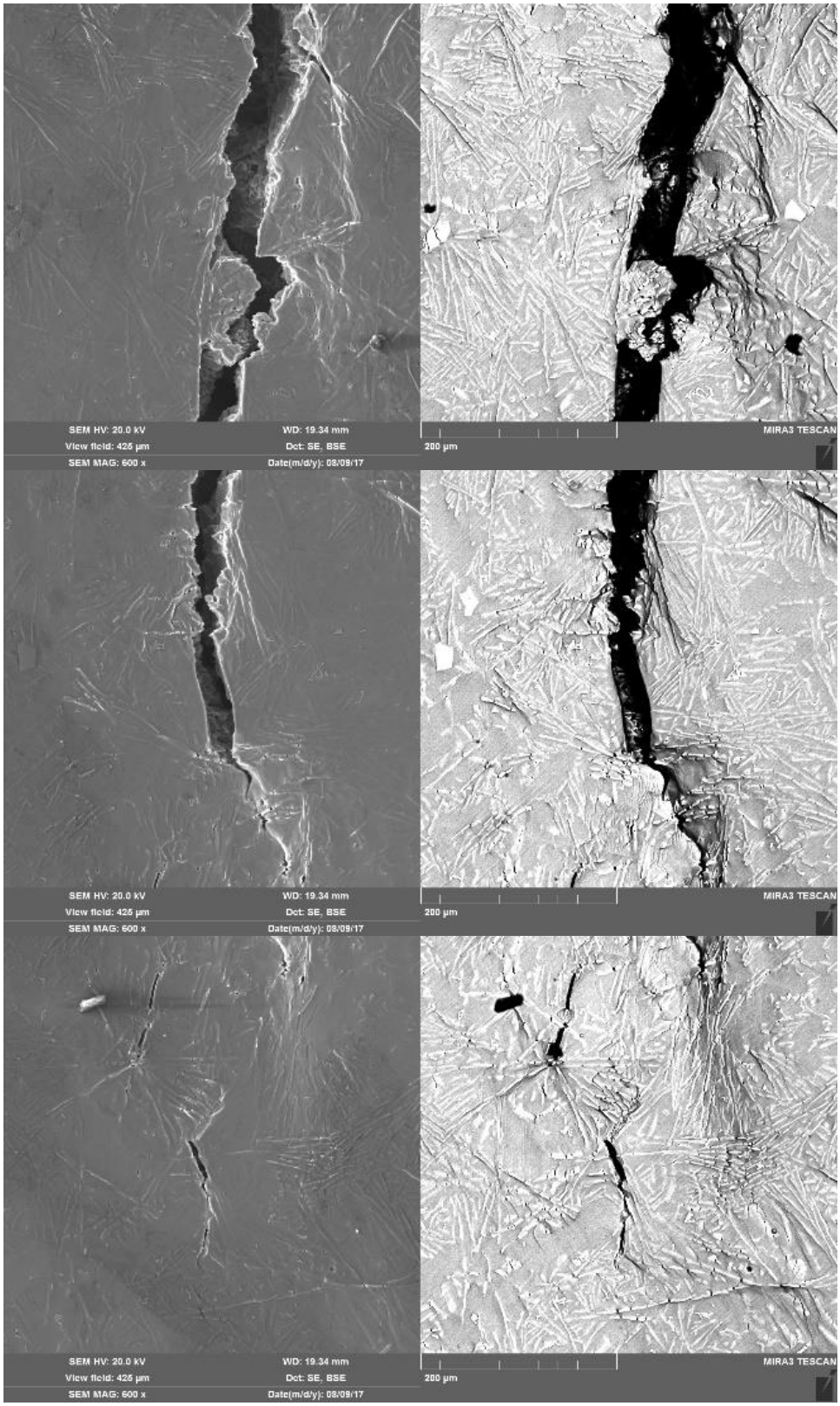

Figure A-6 Secondary (Left) and Backscattered (Right) Electron Images of the A4047 Ingots. A 1.9mm-long Crack was Formed from the Notch.

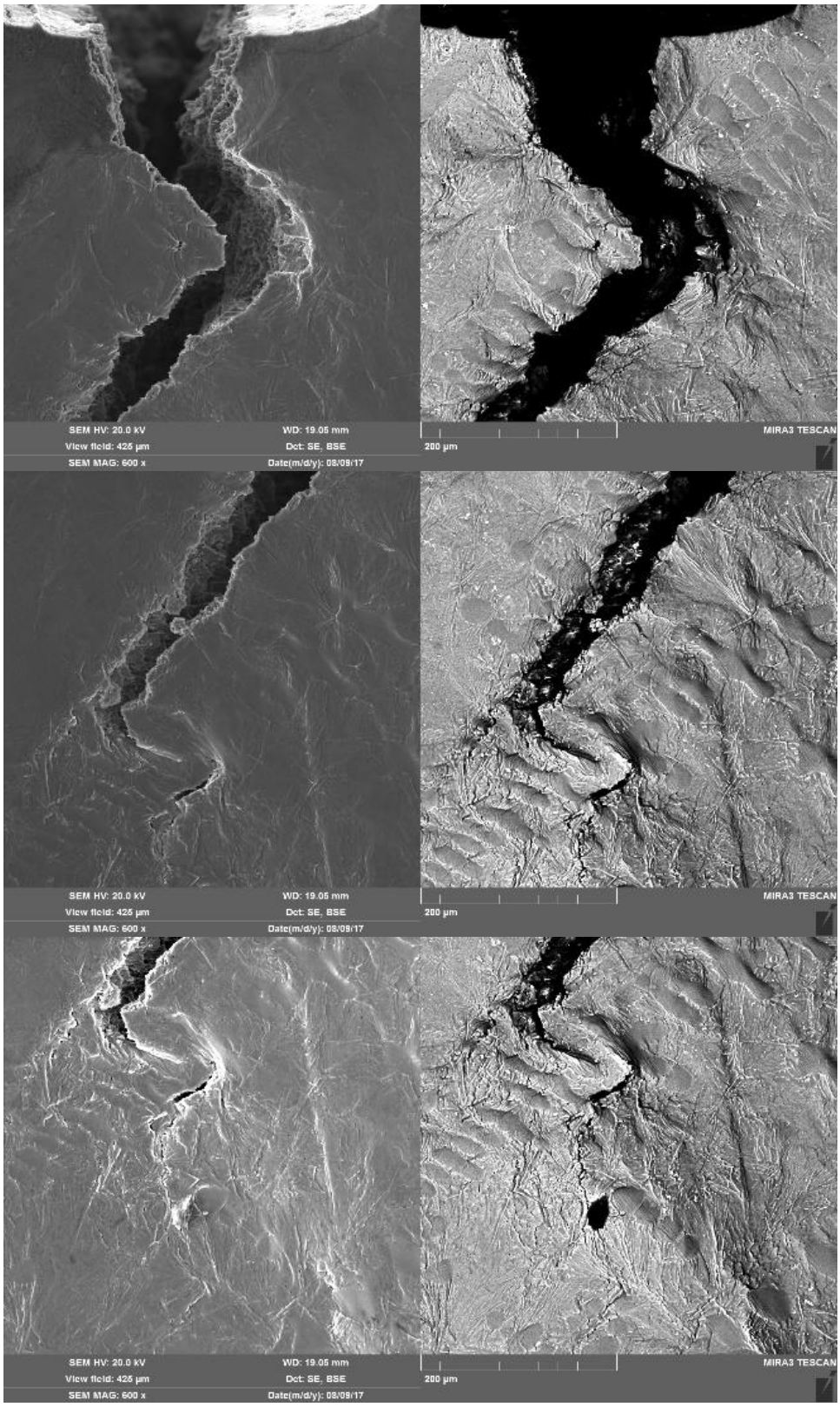

Figure A-7 Secondary (Left) and Backscattered (Right) Electron Images of the TSP-treated A4047 Ingots. A 0.78mm-long crack was formed from the notch.

A.3.3 Strain determination after bending

The bending strains can be determined using classical beam bending theory shown in Figure A-8. As the arc length, L, is related to radius of curvature, R, through $L= R\theta$, where θ is the angle. The radius of curvature at any other radius is (R+Y), where Y is the distance from the neutral axis. Therefore, the final length at any other radius is given by $L=(R+Y)\ \theta$. So, the strain along the length of the beam can be expressed as

$$\varepsilon= L-L0/L0= (R+Y)\ \theta-R\ \theta/R\ \theta=Y/R$$

Where $L0=R\ \theta$.

The radius of curvature for each bended specimen is determined using ImageJ software with a three-point circular ROI plugin. The distance from the neutral axis was measured as well. Figure A-9 showed the results using the images from Figure A-5. As can be seen, 2.53E-4 strain was induced at notch root on A4047 when the crack propagated 1.9mm from the notch, while 3.02E-4 strain was induced at notch root on A4047-TSP when the crack propagated only 0.78mm. TSP incorporation hinders crack growth in near eutectic Al-Si alloys.

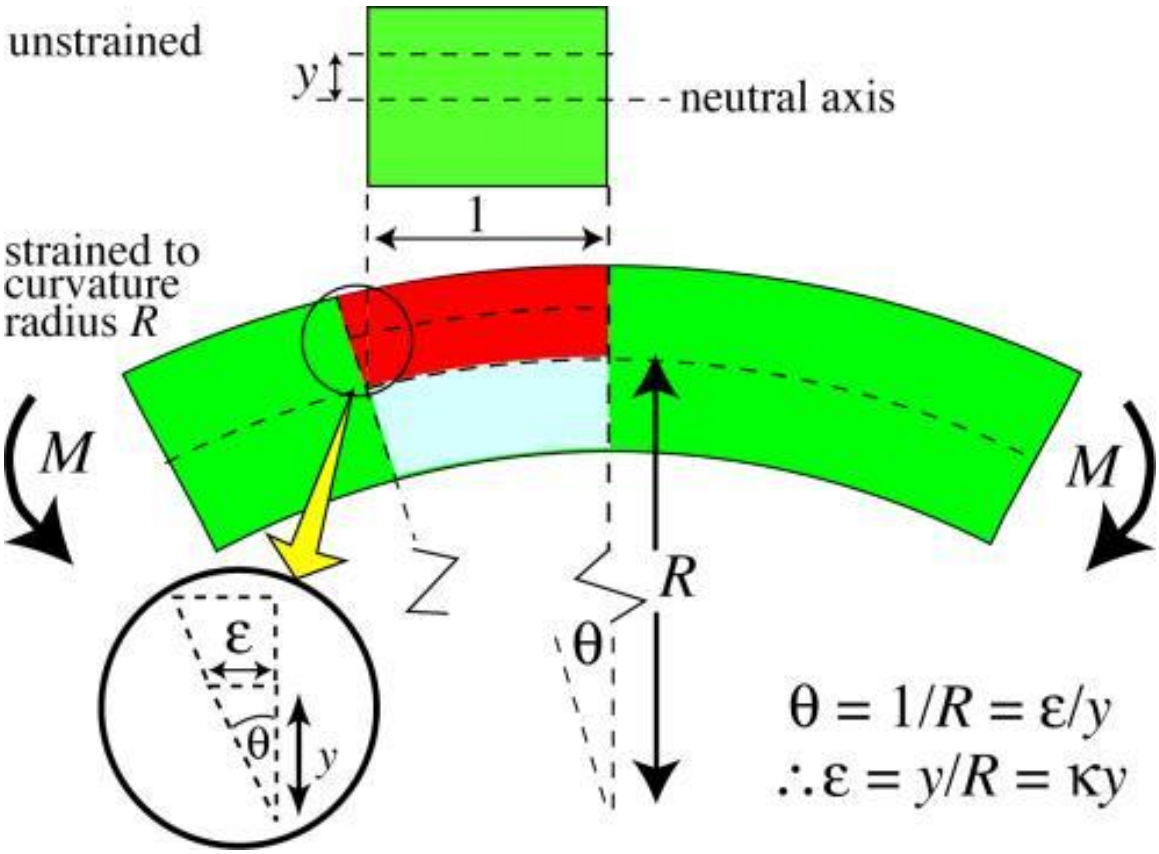

Figure A-8 Strains Induced during Bending of a Beam.

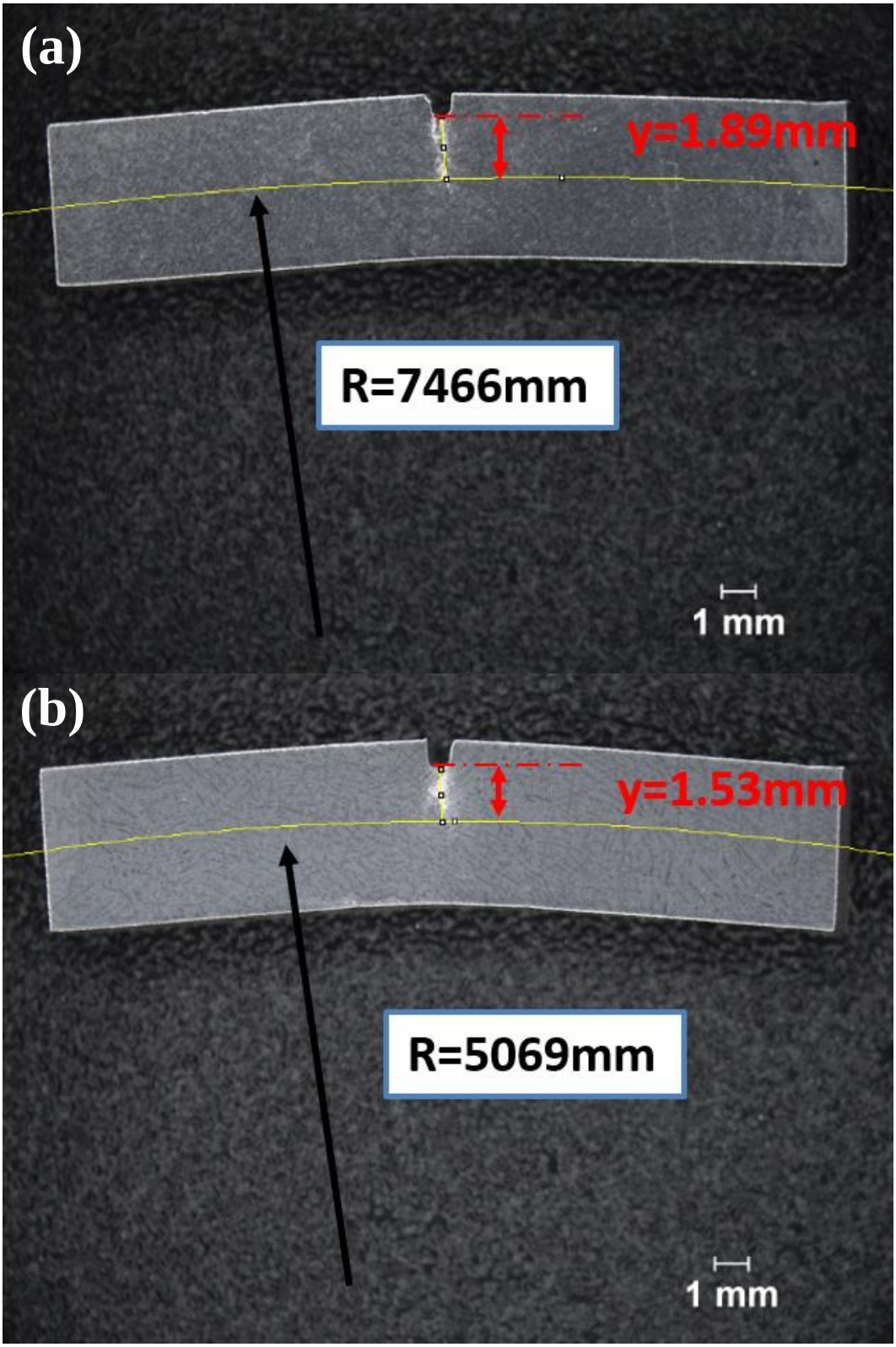

Figure A-9 Stereo Micrographs of (a) the A4047 Ingot and (b) the TSP-treated A4047 Ingot Analyzed by ImageJ.

A.4 Conclusions

The microstructure of both primary Al and eutectic microconstituents of the A4047 alloys made from the TSP-treated A4047 powders was refined. The crack path in a notched specimen was analyzed using a combination of stereo, electron microscopy and beam bending techniques. Eutectic Si tends to act as a barrier to prevent cracks from growth, as all the crack tips were close to Si. The total crack length was reduced from 1.9 mm to 0.78 mm with TSP additions. TSP increased eutectic density to hinder crack growth. In addition, less amount of microcracks were observed with TSP additions.

BIBLIOGRAPHY

BIBLIOGRAPHY

1. Mikell PG: **Fundamentals of modern manufacturing: materials, processes, and systems**. In.: John, Wiley & Sons, Inc; 1999.

2. Trans Tech Publications.: **Technologies and Properties of Modern Utility Materials XXIII Selected, peer reviewed papers from the XXIII Conference on Technologies and Properties of Modern Utility Materials (TPMUM 2015), May 15, 2015, Katowice, Poland**. In. Switzerland: Trans Tech Publications Ltd; 2016: 304 p.

3. Zhou B, Kang Y, Qi M, Zhang H, Zhu G: **R-HPDC Process with Forced Convection Mixing Device for Automotive Part of A380 Aluminum Alloy**. *Materials* 2014, **7**(4):3084-3105.

4. Lovik AN, Modaresi R, Muller DB: **Long-term strategies for increased recycling of automotive aluminum and its alloying elements**. *Environmental science & technology* 2014, **48**(8):4257-4265.

5. Murray JL: **The aluminium-copper system**. *International metals reviews* 1985, **30**(1):211-234.

6. Murray JL: **The Al− Mg (Aluminum− Magnesium) system**. *Bulletin of Alloy Phase Diagrams* 1982, **3**(1):60-74.

7. Murray J, McAlister A: **The Al-Si (aluminum-silicon) system**. *Bulletin of Alloy Phase Diagrams* 1984, **5**(1):74-84.

8. Mollard FR, Flemings MC, Niyama EF: **Aluminum fluidity in casting**. *JOM Journal of the Minerals, Metals and Materials Society* 1987, **39**(11):34-34.

9. Wang J, Guo Z, Song JL, Hu WX, Li JC, Xiong SM: **Morphology transition of the primary silicon particles in a hypereutectic A390 alloy in high pressure die casting**. *Sci Rep* 2017, **7**(1):14994.

10. Murray JL, Mcalister AJ: **Phase-Diagrams for Industry - the Al-Si Binary**. *Met Prog* 1985, **128**(8):38-&.

11. Meyrick G, Powell GW: **Phase transformations in metals and alloys**. *Annual Review of Materials Science* 1973, **3**(1):327-362.

12. Turnbull D, Fisher JC: **Rate of Nucleation in Condensed Systems**. *J Chem Phys* 1949, **17**(1):71-73.

13. Jreidini P, Kocher G, Provatas N: **Classical nucleation theory in the phase-field crystal model**. *Phys Rev E* 2018, **97**(4-1):042802.

14. Grant M, Gunton JD: **Theory for the nucleation of a crystalline droplet from the melt**. *Physical review B, Condensed matter* 1985, **32**(11):7299-7307.

15. Pratt S: **Nucleation theory for matter far from equilibrium**. *Physical review A, Atomic, molecular, and optical physics* 1990, **42**(12):7447-7451.

16. Granasy L, Borzsonyi T, Pusztai T: **Nucleation and bulk crystallization in binary phase field theory**. *Phys Rev Lett* 2002, **88**(20):206105.

17. Berdichevsky VL, Le KC: **Theory of charge nucleation in two dimensions**. *Physical review E, Statistical, nonlinear, and soft matter physics* 2002, **66**(2 Pt 2):026129.

18. Nadykto AB, Yu F: **Simple correction to the classical theory of homogeneous nucleation**. *J Chem Phys* 2005, **122**(10):104511.

19. Christian JW: **The theory of transformations in metals and alloys**: Newnes; 2002.

20. Porter D, Easterling K: **Phase transformations in metals and alloys**. 1992.

21. Porter DA, Easterling KE, Sherif M: **Phase Transformations in Metals and Alloys, (Revised Reprint)**: CRC press; 2009.

22. Robinson AL: **Crystal Anisotropy Directs Solidification: Simplified mathematical models of solidification elevate crystalline anisotropy to main player in selecting dendritic growth patterns**. *Science* 1984, **224**(4653):1085-1087.

23. Fujiwara K, Maeda K, Usami N, Nakajima K: **Growth mechanism of Si-faceted dendrites**. *Phys Rev Lett* 2008, **101**(5).

24. Henry S, Minghetti T, Rappaz M: **Dendrite growth morphologies in aluminium alloys**. *Acta Mater* 1998, **46**(18):6431-6443.

25. Elliott R: **Eutectic Solidification**. *Mater Sci Eng* 1984, **65**(1):85-92.

26. Day MG, Hellawel.A: **Microstructure and Crystallography of Aluminium-Silicon Eutectic Alloys**. *Proc R Soc Lon Ser-A* 1968, **305**(1483):473-&.

27. Jones GP, Pearson J: **Factors affecting the grain-refinement of aluminum using titanium and boron additives**. *Metallurgical Transactions B* 1976, **7**(2):223-234.

28. Callister WD, Rethwisch DG: **Materials science and engineering**, vol. 5: John Wiley & Sons NY; 2011.

29. Sigworth GK: **The grain refining of aluminum and phase relationships in the Al-Ti-B system**. *Metallurgical and Materials Transactions A* 1984, **15**(2):277-282.

30. Backerud L: **How Does a Good Grain Refiner Work**. *Light Metal Age* 1983, **41**(9-10):6-&.

31. Sigworth G, Guzowski M: **Grain refining of hypoeutectic Al-Si alloys**. *AFS Transactions* 1985, **93**(172):907-912.

32. Sigworth GK, Kuhn TA: **Grain refinement of aluminum casting alloys**. *International Journal of Metalcasting* 2007, **1**(1):31-40.

33. Cibula A, Ruddle R: **The effect of grain-size on the tensile properties of high-strength cast aluminium alloys**. *J I Met* 1949, **76**(4):361-+.

34. Cibula A: **The grain refinement of aluminium alloy castings by additions of titanium and boron**. *J Inst Metals* 1951, **80**.

35. Marcantonio J, Mondolfo L: **Nucleation of aluminium by several intermetallic compounds**. *J Inst Metals* 1970, **98**(1):23-27.

36. Easton M, StJohn D: **Grain refinement of aluminum alloys: Part II. Confirmation of, and a mechanism for, the solute paradigm**. *Metallurgical and Materials Transactions A* 1999, **30**(6):1625-1633.

37. Johnsson M, Bäckerud L: **Nucleants in grain refined aluminium after addition of Ti- and B-containing master alloys**. *Zeitschrift für Metallkunde* 1992, **83**(11):774-780.

38. Johnsson M, Backerud L, Sigworth GK: **Study of the mechanism of grain refinement of aluminum after additions of Ti-and B-containing master alloys**. *Metallurgical and Materials Transactions A* 1993, **24**(2):481-491.

39. Kori S, Murty B, Chakraborty M: **Influence of silicon and magnesium on grain refinement in aluminium alloys**. *Mater Sci Tech-Lond* 1999, **15**(9):986-992.

40. Dyzia M: **Aluminum Matrix Composite (AlSi7Mg2Sr0.03/SiCp) Pistons Obtained by Mechanical Mixing Method**. *Materials* 2017, **11**(1).

41. Zhang X, Chen T, Qin H, Wang C: **A Comparative Study on Permanent Mold Cast and Powder Thixoforming 6061 Aluminum Alloy and Sicp/6061Al Composite: Microstructures and Mechanical Properties**. *Materials* 2016, **9**(6).

42. Tosborvorn S, Cheechareon S, Ruttanuchun K, Sirivedin S, Rhienumporn C: **Mechanical evaluation of aluminum alloy ring fixator**. *Journal of the Medical Association of Thailand = Chotmaihet thangphaet* 2006, **89**(11):1896-1901.

43. Cook SD, Weinberg LA: **The effect of aging and surface modification on the mechanical properties of dense aluminum oxide**. *Biomaterials, medical devices, and artificial organs* 1984, **12**(1-2):67-74.

44. Alkahtani SA, Elgallad EM, Tash MM, Samuel AM, Samuel FH: **Effect of Rare Earth Metals on the Microstructure of Al-Si Based Alloys**. *Materials* 2016, **9**(1).

45. Nolting P: **Modification of Eutectic Structure of Aluminum-Silicon Alloy by Sodium, Phosphorus and Solidification Rate**. *Fond-Fr* 1972, **27**(308):29-&.

46. Knuutinen A, Nogita K, McDonald S, Dahle A: **Modification of Al–Si alloys with Ba, Ca, Y and Yb**. *Journal of Light Metals* 2001, **1**(4):229-240.

47. Kundu AL, Gupt KM, Rao PK: **Morphology of Nonmetallic Inclusions Using Silicon, Aluminum, and Calcium-Silicon Alloy in Steel Melt**. *Metall Trans B* 1989, **20**(5):581-594.

48. Felberbaum M, Dahle A: **Modification and Grain Refinement of Eutectics to Improve Performance of Al‐Si Castings**. *Light Metals 2011* 2011:815-820.

49. McDonald SD, Dahle AK, Taylor JA, StJohn DH: **Eutectic grains in unmodified and strontium-modified hypoeutectic aluminum-silicon alloys**. *Metall Mater Trans A* 2004, **35A**(6):1829-1837.

50. Dahle AK, Nogita K, Zindel JW, McDonald SD, Hogan LM: **Eutectic nucleation and growth in hypoeutectic Al-SI alloys at different strontium levels**. *Metall Mater Trans A* 2001, **32**(4):949-960.

51. Jenkinson DC, Hogan LM: **Modification of Aluminium-Silicon Alloys with Strontium**. *J Cryst Growth* 1975, **28**(2):171-&.

52. Barzani MM, Farahany S, Yusof NM, Ourdjini A: **The Influence of Bismuth, Antimony, and Strontium on Microstructure, Thermal, and Machinability of Aluminum-Silicon Alloy**. *Mater Manuf Process* 2013, **28**(11):1184-1190.

53. Haque MM, Ismail AF: **Effect of superheating temperatures on microstructure and properties of strontium modified aluminium-silicon eutectic alloy**. *J Mater Process Tech* 2005, **162**:312-316.

54. Haque MM: **Strontium Modification of Aluminium-Silicon Eutectic Alloy and the Factors Affecting It**. *Met Forum* 1983, **6**(1):54-56.

55. Hanna MD, Lu SZ, Hellawell A: **Modification in the Aluminum Silicon System**. *Metall Trans A* 1984, **15**(3):459-469.

56. Sigworth G: **The modification of Al-Si casting alloys: important practical and theoretical aspects**. *International Journal of Metalcasting* 2008, **2**(2):19-41.

57. Davis JR: **Aluminum and aluminum alloys**: ASM international; 1993.

58. Hurley T, Atkinson R: **Effects of modification practice on aluminum A356 alloys**. *AFS Transactions* 1985, **93**:291-296.

59. Chung SY, Kim YM, Choi SY, Kim JG: **Capturing heterogeneous nucleation of nanoscale pits and subsequent crystal shrinkage during Ostwald ripening of a metal phosphate**. *Acs Nano* 2015, **9**(1):327-335.

60. Abdelsayed V, El-Shall MS: **Direct observation of metal nanoparticles as heterogeneous nuclei for the condensation of supersaturated organic vapors:**

nucleation of size-selected aluminum nanoparticles in acetonitrile and n-hexane vapors. *J Chem Phys* 2014, **141**(5):054710.

61. Anumol EA, Kundu P, Deshpande PA, Madras G, Ravishankar N: **New insights into selective heterogeneous nucleation of metal nanoparticles on oxides by microwave-assisted reduction: rapid synthesis of high-activity supported catalysts**. *Acs Nano* 2011, **5**(10):8049-8061.

62. Makhlouf M: **On the Mechanism of Modification of the Aluminum-Silicon Eutectic by Strontium: The Role of Nucleation**. *International Journal of Metalcasting* 2010, **4**(1):47-50.

63. Xiufang B, Weimin W, Shujuan Y, Jingyu Q: **Structure factors of modified liquid Al–Si alloys**. *Science and technology of advanced materials* 2001, **2**(1):19-23.

64. Jackson KA, Hunt JD: **Lamellar and Rod Eutectic Growth**. *T Metall Soc Aime* 1966, **236**(8):1129-&.

65. Magnin P, Kurz W: **An Analytical Model of Irregular Eutectic Growth and Its Application to Fe-C**. *Acta Metall Mater* 1987, **35**(5):1119-1128.

66. Guzik E, Kopycinski D: **Modeling structure parameters of irregular eutectic growth: Modification of Magnin-Kurz theory**. *Metall Mater Trans A* 2006, **37A**(10):3057-3067.

67. Hamilton DR, Seidensticker RG: **Propagation Mechanism of Germanium Dendrites**. *J Appl Phys* 1960, **31**(7):1165-1168.

68. Kobayashi KF, Hogan LM: **The Crystal-Growth of Silicon in Al-Si Alloys**. *J Mater Sci* 1985, **20**(6):1961-1975.

69. Fujiwara K, Fukuda H, Usami N, Nakajima K, Uda S: **Growth mechanism of the Si < 110 > faceted dendrite**. *Phys Rev B* 2010, **81**(22).

70. Lu SZ, Hellawell A: **The Mechanism of Silicon Modification in Aluminum-Silicon Alloys - Impurity Induced Twinning**. *Metall Trans A* 1987, **18**(10):1721-1733.

71. Shaulov M, Green K, Harrington R, Mergel J, Pickrell D, Keefe R, Van Schalkwyk J: **2017–2025 Corporate Average Fuel Economy Compliance and Effects Modeling System Documentation**. In.; 2012.

72. Birol Y: **Performance of AlTi5B1, AlTi3B3 and AlB3 master alloys in refining grain structure of aluminium foundry alloys**. *Mater Sci Tech-Lond* 2012, **28**(4):481-486.

73. Greer A: **Grain refinement of alloys by inoculation of melts**. *Philosophical transactions of the Royal Society of London A: mathematical, physical and engineering sciences* 2003, **361**(1804):479-495.

74. Phillips SH, Haddad TS, Tomczak SJ: **Developments in nanoscience: polyhedral silsesquioxane (POSS)-polymers oligomeric**. *Curr Opin Solid St M* 2004, **8**(1):21-29.

75. Lee A, Subramanian KN: **Development of nano-composite lead-free electronic solders**. *J Electron Mater* 2005, **34**(11):1399-1407.

76. Carniato F, Fina A, Tabuani D, Boccaleri E: **Polypropylene containing Ti-and Al-polyhedral oligomeric silsesquioxanes: crystallization process and thermal properties**. *Nanotechnology* 2008, **19**(47):475701.

77. Fina A, Abbenhuis H, Tabuani D, Frache A, Camino G: **Polypropylene metal functionalised POSS nanocomposites: a study by thermogravimetric analysis**. *Polymer Degradation and Stability* 2006, **91**(5):1064-1070.

78. Carniato F, Boccaleri E, Marchese L, Fina A, Tabuani D, Camino G: **Synthesis and characterisation of metal isobutylsilsesquioxanes and their role as inorganic–organic nanoadditives for enhancing polymer thermal stability**. *European journal of inorganic chemistry* 2007, **2007**(4):585-591.

79. Lee A, Subramanian K: **Development of nano-composite lead-free electronic solders**. *J Electron Mater* 2005, **34**(11):1399-1407.

80. Choudhuri D: **Influence of nano-structured chemicals on the microstructures and mechanical reliability of lead-free tin-based solders**: Michigan State University; 2009.

81. Lee A, Choudhuri D, Subramanian K: **Effect of Temperature‐Dependent Deformation Characteristics on Thermomechanical Fatigue Reliability of Eutectic Sn‐Ag Solder Joints**. *Lead-Free Solders: Materials Reliability for Electronics* 2012:273-295.

82. Anderson IE, Cook BA, Harringa J, Terpstra RL, Foley JC, Unal O: **Effects of alloying in near-eutectic tin-silver-copper solder joints**. *Mater Trans* 2002, **43**(8):1827-1832.

83. Miller CM, Anderson IE, Smith JF: **A Viable Tin-Lead Solder Substitute - Sn-Ag-Cu**. *J Electron Mater* 1994, **23**(7):595-601.

84. Wu CML, Huang ML: **Creep Behavior of eutectic Sn-Cu lead-free solder alloy (vol 31, pg 442, 2002)**. *J Electron Mater* 2002, **31**(7):828-828.

85. Tai F, Guo F, Xia ZD, Lei YP, Yan YF, Liu JP, Shi YW: **Processing and creep properties of Sn-Cu composite solders with small amounts of nanosized Ag reinforcement additions**. *J Electron Mater* 2005, **34**(11):1357-1362.

86. Sona M, Prabhu KN: **The effect of reflow time on reactive wetting, evolution of interfacial IMCs and shear strength of eutectic Sn-Cu solder alloy**. *J Mater Sci-Mater El* 2014, **25**(3):1446-1455.

87. Kim KS, Huh SH, Suganuma K: **Effects of intermetallic compounds on properties of Sn-Ag-Cu lead-free soldered joints**. *J Alloy Compd* 2003, **352**(1-2):226-236.

88. Satyanarayan, Prabhu KN: **Reactive wetting, evolution of interfacial and bulk IMCs and their effect on mechanical properties of eutectic Sn-Cu solder alloy**. *Advances in colloid and interface science* 2011, **166**(1-2):87-118.

89. Cheng FJ, Ma ZL, Wang Y, Zou QB: **Creep Behaviors of Sn0.7Cu0.1Co0.05Ni/Cu Soldering Joints**. *Ieee T Comp Pack Man* 2014, **4**(12):2058-2065.

90. Cheung N, Garcia A, Spinelli JE: **Microstructure and Mechanical Properties of Directionally Solidified Unmodified and Ni-Modified Sn-0.7wt%Cu Lead-Free Solder Alloy**. *Recent Advances in Mass Transport in Engineering Materials* 2013, **333**:107-115.

91. El-Daly AA, El-Taher AM, Dalloul TR: **Improved creep resistance and thermal behavior of Ni-doped Sn-3.0Ag-0.5Cu lead-free solder**. *J Alloy Compd* 2014, **587**:32-39.

92. Reeve KN, Anderson IE, Handwerker CA: **Nucleation and Growth of Cu-Al Intermetallics in Al-Modified Sn-Cu and Sn-Ag-Cu Lead-Free Solder Alloys**. *J Electron Mater* 2015, **44**(3):842-866.

93. Zeng G, McDonald SD, Gu QF, Terada Y, Uesugi K, Yasuda H, Nogita K: **The influence of Ni and Zn additions on microstructure and phase transformations in Sn-0.7Cu/Cu solder joints**. *Acta Mater* 2015, **83**:357-371.

94. Mayappan R, Yahya I, Ghani NAA, Hamid HA: **The effect of adding Zn into the Sn-Ag-Cu solder on the intermetallic growth rate**. *J Mater Sci-Mater El* 2014, **25**(7):2913-2922.

95. El-Daly AA, Hammad AE: **Enhancement of creep resistance and thermal behavior of eutectic Sn-Cu lead-free solder alloy by Ag and In-additions**. *Mater Design* 2012, **40**:292-298.

96. Drienovsky M, Trnkova LR, Martinkovic M, Ozvold M, Cernickova I, Palcut M, Janovec J: **Influence of cerium addition on microstructure and properties of Sn-Cu-(Ag) solder alloys**. *Mat Sci Eng a-Struct* 2015, **623**:83-91.

97. Guo F, Lee J, Subramanian KN: **Creep behaviour of composite lead-free electronic solder joints**. *Solder Surf Mt Tech* 2003, **15**(1):39-42.

98. Guo F: **Composite lead-free electronic solders**. *J Mater Sci-Mater El* 2007, **18**(1-3):129-145.

99. El-Daly AA, Al-Ganainy GS, Fawzy A, Younis MJ: **Structural characterization and creep resistance of nano-silicon carbide reinforced Sn-1.0Ag-0.5Cu lead-free solder alloy**. *Mater Design* 2014, **55**:837-845.

100. Zhong XL, Gupta M: **Development of lead-free Sn-0.7Cu/Al(2)O(3) nanocomposite solders with superior strength**. *J Phys D Appl Phys* 2008, **41**(9).

101. Subramanian KN, Bieler TR, Lucas JP: **Microstructural engineering of solders**. *J Electron Mater* 1999, **28**(11):1176-1183.

102. Saunders N, Miodownik A: **The Cu-Sn (copper-tin) system**. *Bulletin of Alloy Phase Diagrams* 1990, **11**(3):278-287.

103. Yang M, Cao Y, Joo S, Chen HT, Ma X, Li MY: **Cu6Sn5 precipitation during Sn-based solder/Cu joint solidification and its effects on the growth of interfacial intermetallic compounds**. *J Alloy Compd* 2014, **582**:688-695.

104. Faraji M, Todd I, Jones H: **Effect of solidification cooling rate and phosphorus inoculation on number per unit volume of primary silicon particles in hypereutectic aluminium-silicon alloys**. *J Mater Sci* 2005, **40**(24):6363-6365.

105. Sritharan T, Li H: **Influence of titanium to boron ratio on the ability to grain refine aluminium-silicon alloys**. *J Mater Process Tech* 1997, **63**(1-3):585-589.

106. Zhang Y, Zheng HL, Liu Y, Shi L, Xu RF, Tian XL: **Cluster-assisted nucleation of silicon phase in hypoeutectic Al-Si alloy with further inoculation**. *Acta Mater* 2014, **70**:162-173.

107. Reinhardt A, Doye JP: **Effects of surface interactions on heterogeneous ice nucleation for a monatomic water model**. *J Chem Phys* 2014, **141**(8):084501.

108. Hamilton D, Seidensticker R: **Propagation mechanism of germanium dendrites**. *J Appl Phys* 1960, **31**(7):1165-1168.

109. Lee A, Lu Y, Roche A, Pan T-Y: **Influence of Nano-Structured Silanols on the Microstructure and Mechanical Properties of A4047 and A359 Aluminum Casting Alloys**. *Int J Metalca St* 2016, **10**(3):338-341.

110. Hess P, Blackmun E: **Strontium as a modifying agent for hypoeutectic aluminum-silicon alloys**. *Paper from" Transactions of the Americal Foundrymen's Society* 1975, **83**.

111. Luk JM, Kim HC, De Kleine R, Wallington TJ, MacLean HL: **Review of the Fuel Saving, Life Cycle GHG Emission, and Ownership Cost Impacts of Lightweighting Vehicles with Different Powertrains**. *Environmental science & technology* 2017, **51**(15):8215-8228.

112. Kim HC, Wallington TJ: **Life Cycle Assessment of Vehicle Lightweighting: A Physics-Based Model To Estimate Use-Phase Fuel Consumption of Electrified Vehicles**. *Environmental science & technology* 2016, **50**(20):11226-11233.

113. Alonso E, Lee TM, Bjelkengren C, Roth R, Kirchain RE: **Evaluating the potential for secondary mass savings in vehicle lightweighting**. *Environmental science & technology* 2012, **46**(5):2893-2901.

114. Peretz JH, Das S, Tonn BE: **Evaluating knowledge benefits of automotive lightweighting materials R&D projects**. *Evaluation and program planning* 2009, **32**(3):300-309.

115. Wiengmoon A, Pearce JT, Chairuangsri T, Isoda S, Saito H, Kurata H: **HRTEM and HAADF-STEM of precipitates at peak ageing of cast A319 aluminium alloy**. *Micron* 2013, **45**:32-36.

116. Taub AI, Krajewski PE, Luo AA, Owens JN: **The evolution of technology for materials processing over the last 50 years: The automotive example**. *Jom-Us* 2007, **59**(2):48-57.

117. Demirtas A, Ural A: **Material heterogeneity, microstructure, and microcracks demonstrate differential influence on crack initiation and propagation in cortical bone**. *Biomechanics and modeling in mechanobiology* 2018.

118. Kang M, Han HN, Kim C: **Microstructure and Solidification Crack Susceptibility of Al 6014 Molten Alloy Subjected to a Spatially Oscillated Laser Beam**. *Materials* 2018, **11**(4).

119. Garza-Villarreal EA, Chakravarty MM, Hansen B, Eskildsen SF, Devenyi GA, Castillo-Padilla D, Balducci T, Reyes-Zamorano E, Jespersen SN, Perez-Palacios P *et al*: **The effect of crack cocaine addiction and age on the microstructure and morphology of the human striatum and thalamus using shape analysis and fast diffusion kurtosis imaging**. *Translational psychiatry* 2017, **7**(5):e1122.

120. Saffar S, Gouttebroze S, Zhang ZL: **The Effect of Microstructure, Thickness Variation, and Crack on the Natural Frequency of Solar Silicon Wafers**. *Journal of solar energy engineering* 2014, **136**(1):0110011-0110018.

121. Chai G, Zhou N: **Study of crack initiation or damage in very high cycle fatigue using ultrasonic fatigue test and microstructure analysis**. *Ultrasonics* 2013, **53**(8):1406-1411.